Electrophysiological characterization of the microbial rhodopsins ReaChR and KR2 and their optogenetic potential

Elektrophysiologische Untersuchung der mikrobiellen Rhodopsine ReaChR und KR2 und ihr Potential für die Optogenetik

DISSERTATION

Zur Erlangung des akademischen Grades
doctor rerum naturalium
(Dr. rer. nat.)

im Fach Biophysik

eingereicht an der
Lebenswissenschaftlichen Fakultät
der Humboldt-Universität zu Berlin

von
Christiane Grimm, M. Sc.

Präsidentin der Humboldt-Universität zu Berlin
Prof. Dr.-Ing. Dr. Sabine Kunst

Dekan der Lebenswissenschaftlichen Fakultät
Prof. Dr. Bernhard Grimm

Gutachter:

1. Prof. Dr. Peter Hegemann
2. Prof. Dr. Franz Bartl
3. Prof. Dr. Georg Nagel

Tag der mündlichen Prüfung: 19. Dezember 2018

"It seems as though people are quick to muddle up
what's a fact and what's an opinion.
Science is about facts."

Francis Collins

Abstract

Microbial rhodopsins are photosensitive proteins, which are utilized by fungi, algae, and prokaryotes to sense light or harness its' energy. The subgroup of ion transporting microbial rhodopsins further initiated the field of optogenetics, where they are applied to render transmembrane ion fluxes light sensitive and control neuronal activity with the spatiotemporal precision of light. Meaningful application relies on the molecular characterization of microbial rhodopsins, which is the premise not only to tailor the protein to the experimental needs by engineering but also for setting up a neuronal experiment purposefully.

The first part of the thesis focused on the electrophysiological characterization of the red-shifted channelrhodopsin ReaChR. Although published with a broad, non-Gaussian shaped action spectrum peaking around 600 nm, the flash action spectra of ReaChR recorded here had a maximum at 535 nm without any peculiarities. With increasing intensities and prolonged illumination the action spectrum broadened and finally peaked around 600 nm similar to the published spectrum. This unique behavior is explained by a pronounced secondary photochemistry of ReaChR, which leads to a complex photocycle with various light-induced transitions especially under constant illumination. Additionally, mutations at key positions like the central gate, DC-pair or counter ions were employed to characterize the properties of ReaChR beyond the published data and engineer new features like changed selectivity or different photocycle kinetics.

In the second part an in-depth electrophysiological characterization of the outward sodium pump KR2 was pursued, which was hitherto hindered by the poor membrane targeting of the pump in mammalian cells. Hence, an enhanced KR2 with improved membrane targeting and 60-fold larger photocurrents in ND7/23 than the wild type was engineered. The selectivity measurements revealed that the stationary photocurrent is primarily carried by sodium with a potential contribution of potassium, while no evidence for active proton transport was gathered. Furthermore, it was demonstrated that at sufficient substrate concentration the stationary photocurrent is independent of the membrane voltage distinguishing KR2 from proton and chloride pumps. Finally, expression in cultured hippocampal mouse neurons enabled reliable and reversible inhibition of action potential firing already at 0.5 mW mm^{-2} green light illumination. Existing rhodopsin-based silencing tools rely on passive chloride or active proton/chloride transport, which can be accompanied by drawbacks like dependence on the variable chloride reversal potential or adverse effects on the chloride distribution or the pH. Inhibiting action potential firing through cation extrusion could be less invasive and poses a complementary way of neuronal silencing in contexts where application of established tools is unfavorable or even impossible.

Zusammenfassung

Mikrobielle Rhodopsine sind lichtsensitive Proteine, die von Pilzen, Algen und Prokaryoten exprimiert werden um Licht wahrzunehmen oder dessen Energie zu nutzen. Die Gruppe der Ionen-transportierenden mikrobiellen Rhodopsine begründete zusätzlich das Feld der Optogenetik. Hier werden sie genutzt um transmembrane Ionenflüsse lichtsensitiv zu machen und neuronale Aktivität mit der zeitlichen und räumlichen Präzision von Licht zu steuern. Eine zielführende optogenetische Anwendung baut dabei auf einer molekularen Charakterisierung der mikrobiellen Rhodopsine auf, nicht nur um sie den Anforderungen des Experiments durch Weiterentwicklungen anzupassen sondern auch um das Experiment selbst sinnvoll zu entwerfen.

Der erste Teil der Arbeit beschäftigt sich mit dem rotverschobenen Kanalrhodopsin ReaChR. Obwohl dieses mit einem breiten, nicht gaussförmigen Aktionsspektrum mit maximalen Photoströmen um 600 nm publiziert wurde, zeigte das hier gemessene Blitzlicht-Spektrum maximale Aktivität bei 535 nm ohne jegliche Besonderheiten. Mit stiegender Intensität und längeren Anregungspulsen verbreiterte sich das Spektrum und zeigte schließlich ein Maximum bei 600 nm, welches sehr ähnlich zum publizierten Spektrum war. Dieses einzigartige Verhalten wird durch eine ausgeprägte sekundäre Photochemie erklärt, welche besonders unter Dauerlicht zu einem komplexen Photozyklus mit zahlreichen lichtinduzierten Übergangen führt. Zusätzlich wurden Mutationen an Schlüsselpositionen wie dem zentralen Tor, dem DC-Paar oder den Gegenionen genutzt, um die Eigenschaften von ReaChR über die publizierten Daten hinaus zu charakterisiern und neue zu generieren wie eine veränderte Selektivität oder andere Photozykluskinetiken.

Im zweiten Teil wurde eine elektrophysiologische Charakterisierung der auswärtsgerichteten Natriumpumpe KR2 angestrebt, welche zuvor von der schlechten Membranständigkeit in Säugetierzellen verhindert wurde. Daher wurde eine verbesserte KR2-Variante mit höherer Membranständigkeit und 60-fach größeren Photoströmen als der Wildtyp erstellt. Selektivitätsmessungen zeigten, dass der stationäre Strom von Natrium- und eventuell Kaliumionen getragen wird, wohingegen nichts auf einen Transport von Protonen hindeutet. Weiterhin zeigte sich, dass der stationäre Strom bei ausreichender Substratkonzentration von der Membranspannung unabhängig ist, was KR2 von Chlorid- oder Protonenpumpen unterscheidet. Schließlich ermöglichte die Expression in hippocampalen Mausneuronen die verlässliche und reversible Unterdrückung von Aktionspotentialen schon bei Anregungslichtintensitäten von $0.5\,\mathrm{mW\,mm^{-2}}$. Bisher nutzen Rhodopsin-basierte inhibitorische Werkzeuge passiven Transport von Chloridionen oder pumpen Chloridionen oder Protonen, was eine Abhängigkeit vom variablen Chloridgradienten bedeutet oder unerwünschte Nebeneffekte auf die Chloridkonzentration sowie den pH-Wert nach sich ziehen kann. Die Inhibierung von Aktionspotentialen durch den Auswärtstransport von Kationen stellt hingegen eine verträgliche Art der Inhibierung dar und bietet einen komplementären Weg neuronale Aktivität zu unterdrücken, wenn etablierte Werkzeuge schlecht oder gar nicht genutzt werden können.

Parts of this thesis are already published:

2018 Grimm C, Silapetere A, Vogt A, Bernal Sierra YA, Hegemann P *Electrical properties, substrate specificity and optogenetic potential of the engineered light-driven sodium pump eKR2*, Scientific reports 8:9316: DOI: 10.1038/s41598-018-27690-w

2017 Wietek J, Rodriguez-Rozada S, Tutas J, Tenedini F, Grimm C, Oertner TG, Soba P, Hegemann P, Wiegert JS *Artificial anion-conducting channelrhodopsins with tuned spectra, modified kinetics and enhanced light sensitivity*, Scientific reports 7:14957, DOI: 10.1038/s1598-017-14330-y

2017 Kaufmann JCD*, Krause BS*, Grimm C, Ritter E, Hegemann P, Bartl FJ *Proton transfer reactions in the red light-activatable channelrhodopsin variant ReaChR and their relevance for its function*, Journal of Biological Chemistry 292: 14205-14216, DOI: 10.1074/jbc.M117.779629

2017 Grimm C*, Vierock J*, Hegemann P, Wietek J, *Whole-cell Patch-clamp Recordings for Electrophysiological Determination of Ion Selectivity in Channelrhodopsins*, Journal of visualized experiments (123), DOI: 10.3791/55497

2017 Krause BS*, Grimm C*, Kaufmann CD, Schneider F, Sakmar TP, Bartl FJ, Hegemann P, *Complex Photochemistry within the Green-Absorbing Channelrhodopsin ReaChR*, Biophysical Journal 112:1166-1175, DOI: 10.1016/j.bpj.2017.02.001

Additional publications during the thesis

2017 Vierock J, Grimm C, Nitzan N, Hegemann P *Molecular determinants of proton selectivity and gating in the red-light activated channelrhodopsin Chrimson*, Scientific reports 7:9928, DOI: 10.1038/s41598-017-09600-8

2015 Schneider F, Grimm C, Hegemann P, *Biophysics of Channelrhodopsin*, Annual Review of Biophysics 44:167-186, DOI: 10.1146/annurev-biophys-060414-034014

*equal contribution

Conferences and meeting contributions

03/2018 Gordon research seminar and conference, Photosensory Receptors and Signal transduction, Lucca, Italy, **Talk (selected from abstract):***"An enhanced KR2 enables electrophysiological characterization and optogenetic application of light-driven microbial sodium pumps"*

10/2017 Annual meeting of CRC1078, Elstal, Germany, **Talk:***"Electrophysiological investigation of a light-driven sodium pump"*

02/2017 Biophysical Society Meeting, New Orleans, Louisiana, USA, **Poster:** Grimm C, Vogt A, Hegemann P: *"Electrophysiological investigation of the sodium pump KR2"*

10/2016 EMBO conference, Retinal proteins, Potsdam, Germany, **Poster:** Grimm C, Vogt A, Hegemann P: *"A KR2 variant with high membrane targeting enables electrophysiological recordings in ND7/23 cells"*

04/2016 Annual meeting of the CRC1078, Schmöckwitz, Germany, **Poster:** Grimm C, Krause BS, Kaufmann JCD, Bartl FJ, Hegemann P: *"Investigation of the red-shifted channelrhodopsin ReaChR and selected mutants"*

01/2016 Gordon research seminar and conference, Photosensory Receptors and Signal transduction, Galveston, Texas, USA, **Poster:** Grimm C, Krause BS, Kaufmann JCD, Bartl FJ, Hegemann P: *"Electrophysiological investigation of the red-shifted channelrhodopsin ReaChR and selected mutants"*

04/2015 Annual meeting of the CRC1078, Goslar, Germany, **Poster:** Grimm C, Schneider F, Hegemann P: *"Electrophysiological investigation of the red-shifted ReaChR and its slow-cycling mutants"*

09/2014 International conference: Channelrhodopsin et al.: Optogenetic Tools and Applications, Würzburg, Germany, **Poster**: Grimm C, Schneider F, Hegemann P: *"Electrophysiological investigation of the red-shifted ReaChR and its slow-cycling mutants"*

Abbreviations

Abbreviations of amino acids follow the common one letter code and mutations are indicated by AxyzB with A and B being replaced and replacing residue and xyz the position.

τ_{app}	apparent kinetic constant
τ_{inac}	kinetic constant for inactivation from peak to stationary current
τ_{off}	kinetic constant for current decay after light-off
*Cr*ChR1	channelrhodopsin 1 of *Chlamydomonas reinhardtii*
*Cr*ChR2	channelrhodopsin 2 of *Chlamydomonas reinhardtii*
*Cs*R	*Coccomyxa subellipsoidea* rhodopsin
E_{rev}	reversal potential
*Hs*SR	Sensory rhodopsin of *Halobacterium salinarium*
I_p	peak photocurrent
I_s	stationary photocurrent
*Vc*ChR1	channelrhodopsin 1 of *Volvox carteri*
*Vc*ChR2	channelrhodopsin 2 of *Volvox carteri*
ACR	anion-conducting channelrhodopsin
AP	action potential
ATP	adenosine triphosphate
BLINK	blue-light-induced K^+ channel
bPAC	*Beggiatoa* photoactivated adenylyl cyclase
C1V1	chimeric channelrhodopsin from *Cr*ChR1 and *Vc*ChR1

CCCP	cyanid-*m*-chlorophenyl hydrazon
ChR	channelrhodopsin
DIV	days *in vitro*
ER	trafficking signal to improve release from the endoplasmatic reticulum
FBS	fetal bovine serum
FP	fusion protein of microbial rhodopsin and fluorophore
FTIR	fourier-transform infrared
GHK	Goldman-Hodgkin-Katz voltage equation
GPCR	G-protein coupled receptors
HEK cell	human embryonic kidney cell
HPLC	high-performance liquid chromatography
KR2	NaR of *Krokinobacter eikastus*
LB	lysogeny broth
LJP	liquid junction potential
LOV sensor	light oxygen voltage sensor
NaR	Na^+-pumping rhodopsin
NKA	Na^+,K^+ ATPase
NMG	N-methyl-D-glucamine
NMR	nuclear magnetic resonance spectroscopy
PBS	phosphate-buffered saline
PCR	polymerase chain reaction
PDL	poly-D-Lysine
POPC	1,2-dioleoyl-*sn*-glycero-3-phosphocholine
R18	octadecyl rhodamine B chloride
RBP	retinal binding pocket

ReaChR	red light activatable channelrhodopsin
RSB	retinal Schiff base
SD	standard deviation
SEM	standard error of the mean
sensor of BLUF	sensor of blue-light using flavin-adenine dinucleotide
TS	trafficking signal for enhanced membrane expression
UVR8	UV RESISTANCE LOCUS 8

Contents

1 Introduction

Throughout all kingdoms of life, light provides a ubiquitous environmental cue or serves as energy source in the habitats of various species. Hence, perception and integration of light signals are crucial abilities for viability of an organism on all evolutionary levels from single-celled microbes to human kind. On a molecular level, integration of light signals is mediated by photoreceptor proteins, which are able to detect light and convert the electromagnetic wave into a cellular signal.

In general, photoreceptors operate over a broad spectral range. On the lower end of the wavelength spectrum there are photoreceptors like plant UV RESISTANCE LOCUS 8 (UVR8)[1] or the nematode photoreceptor LITE-1[2] absorbing UV light while on the other end of the spectrum there are phytochromes from bacteria[3] or plants[4], which are sensitive to light in the near-infrared range. As the protein backbone is intrinsically unable to sense light in the visible spectral range, photoreceptors deploy small organic molecules or side chains with a conjugated π-electron system to carry out that function - chromophores. Based on the chromophore they employ, photoreceptors fall into distinct classes with prominent examples being: UVR8 absorbing light with tryptophane side chains, light-oxygen-voltage (LOV) sensors and sensors of blue-light using flavin-adenine dinucleotide (BLUF) harboring a flavin chromophore, phytochromes from plants and algae as well as cyanobacteriochromes employing linear tetrapyrrols (bilins), and rhodopsins covalently binding retinal. All afore-mentioned photoreceptors are cytosolic proteins with the exception of rhodopsins, which are located to the membrane[a].

Rhodopsins divide into type I and type II rhodopsins according to their phylogenetic distance[5]. On the one hand type II rhodopsins like the well-studied bovine rhodopsin[6–9] are present in higher eukaryotes and involved in visual processes or participate in circadian regulation[10,11]. Type I rhodopsins on the other hand are exclusively found in microbes and either function as photosensitive receptors involved in phototactic and photophobic responses or harness light energy converting it into an electrochemical potential used for the generation of adenosine triphosphate (ATP).

[a] The *C. elegans* photoreceptor LITE-1 seems to be an exception as it does not use a retinal co-factor, hence is no rhodopsin, but still is a membrane-embedded photoreceptor[2].

1.1 Microbial rhodopsins

Microbial rhodopsins spread through all domains of life and are found in bacteria, archaea, fungi and algae living in a vast diversity of habitats[5,12]. All microbial rhodopsins share a common heptahelical transmembrane protein fold and harbor a covalently bound retinal co-factor, which enables light perception[12,13]. Although, microbial rhodopsins mediate very different functions on a molecular level, they can be subdivided into two main classes, because they are either functioning as membrane-embedded photoreceptive sensors[14–19] or light-induced ion transporters[12,13,20,21].

Sensory rhodopsin I and II of *Halobacterium salinarium*[14,15] (*Hs*SRI and II) were the first identified representatives of the non-ion transporting[b] microbial rhodopsins followed by the identification of sensory rhodopsins in other microbes like *Natronobacterium pharaonis*[25] or cyanobacteria from the *Anabena* species[16]. Sensory rhodopsins integrate light signals by protein-protein interaction via modulation of their respective membrane-embedded[13,26–28] or cytosolic transducer proteins[13,16] and can thereby for example initiate photophobic or phototactic responses of the microorganism[14,15,23,27]. Additionally, the group of non-transporting microbial rhodopsins comprises the enzyme rhodopins, which provide light-regulated enzymatic functions[17,18,29–33]. All of them feature a membrane-embedded rhodopsin domain, which perceives the light signal, and cytosolic enzyme domain(s) which can for example be kinase[17,33,34], phosphodiesterase[18,31,35] or cyclase domains[19,29,32].

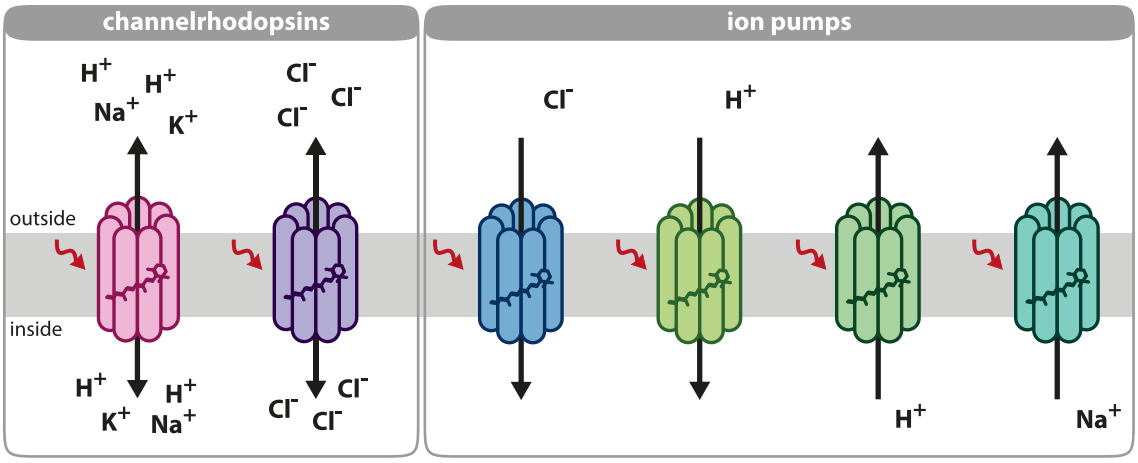

Figure 1.1: Overview of ion transporting microbial rhodopsins, which are subdivided into light-induced channelrhodopsins mediating passive cation or anion flux along the electrochemical gradient and active, light-driven ion pumps actively transporting chloride (inwards), protons (outwards/inwards) or sodium (outwards) upon photon absorption (red).

[b] Later studies found that *Hs*SRI and *Np*SRII can vectorially transport protons in absence of their respective transducer proteins[22–24].

The group of sensory and enzyme rhodopsins is complemented by the group of ion transporting microbial rhodopsins. Light-activated microbial ion transporters fall into two functionally distinct classes, which are illustrated in figure 1.1. On the one hand there are passive light-gated ion channels termed channelrhodopsins (ChR), which allow the passage of ions along an electrochemical gradient upon photoactivation. ChR are either cation channels[36–38] mainly transporting H^+, Na^+, K^+ or anion channels[39–41] allowing the passage of Cl^-. On the other hand there are light-driven ion pumps, which actively transport ions against an electrochemical gradient. The ion pumps selectively transfer one ion per absorbed photon across the membrane either transporting Cl^- from the outside to the inside of the cell[21,42,43], transporting H^+ outwards[20,44,45] or inwards[46,47], or extruding Na^+ from the cell[48]. The group of Na^+-pumping microbial rhodopsins (NaR) was identified recently[48] and the inward-directed H^+-pump was first reported only in 2016[46,47]. Amongst the microbial pumps the inward-directed H^+-pump holds a special position, because in contrast to the other pumps it would degrade the membrane potential and can hence not be used to generate a proton motif force.

1.1.1 Light-driven ion pumps

Bacteriorhodopsin - the prototypical proton pump The proton pump of halophilic archaea *Halobacterium salinarium* (*Hs*BR) was the first reported microbial rhodopsin in 1971[20]. Owing to the fact that it was readily available from the purple membrane patches[49,50] of the microbe and rather stable, it became not only the best investigated microbial rhodopsin but also an exceptionally well-studied membrane protein to date.

Besides *Hs*BR, there exist a lot of other H^+-pumps found in archaea, bacteria or fungi, which are employed to harness light energy converting it into transmembrane potentials for the generation of ATP[13,45]. Microbial H^+-pumps can be clustered into different groups according to a sequence motif comprising three characteristic residues in transmembrane helix3 (TM)[45,51]. In case of *Hs*BR this motif comprises the primary proton acceptor to the retinal Schiff base (RSB) D85, T89 and the proton donor D96, hence *Hs*BR is characterized by a DTD-motif[45] (figure 1.2 A). A second group - the proteo-[44] and xanthorhodopsins[52] - features a glutamate as proton donor and is thus identified by the DTE-motif. Additionally, there is a group of light-driven H^+-pumps, which does not contain a protonatable residue at the proton donor position but a glycin, which are hence classified as DTG rhodopsins[45,53]. Moreover, there are H^+-pumps in Exiguobacteria like *Exiguobacterium sibiricum*, which harbor a lysine at the corresponding position[54–56]. Here, only the structural and functional details of the well-studied *Hs*BR shall be illustrated in detail as it serves as a model for microbial rhodopsins and H^+-pumping.

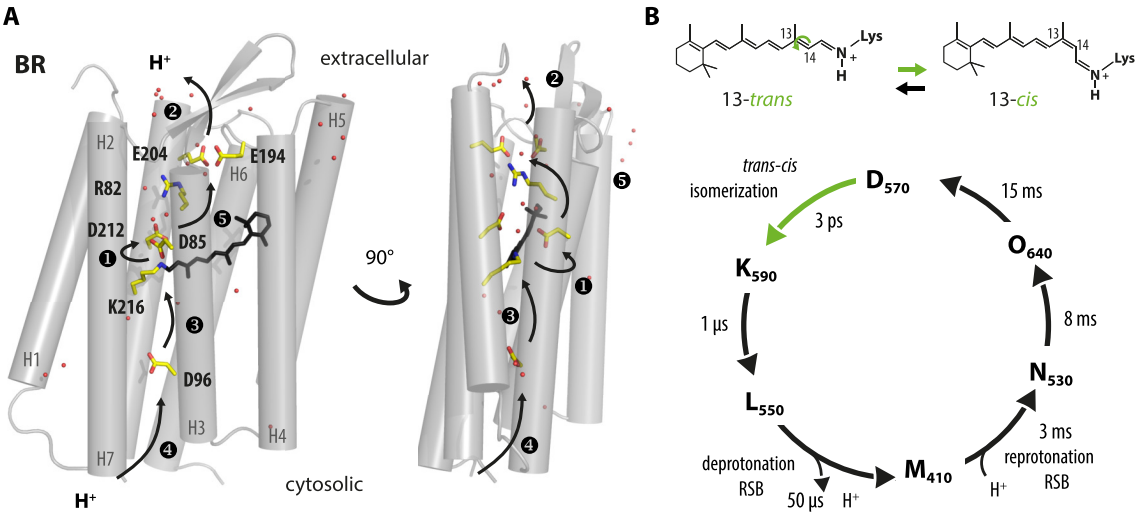

Figure 1.2: Structure and photoactivation of bacteriorhodopsin. A Dark state crystal structure of *Hs*BR (PDB:1C3W) with the retinal (black) covalently bound to K216 in TM7. Side chains of residues important for proton transfer are highlighted with the numbers indicating the sequence of individual steps according to[13]. **B** Photon absorption triggers *trans-cis* isomerization around the C_{13}-C_{14} double bond of the retinal chromophore and initiates the photocycle. Indicatetd time constants according to[57] at neutral pH and 20 °C with the numbers indicating the maximal absorption of the intermediate states.

Many of the functional and structural insights on *Hs*BR and relations thereof were gained using assays on proteoliposomes or spectroscopic techniques. In *Hs*BR and all microbial rhodopsins the absorption of a photon triggers a series of conformation and protonation changes leading to a sequential appearance of spectroscopically distinguishable intermediates during the proteins reversion to the dark state, a process which is referred to as photocycle (figure 1.2 B). In contrast to animal rhodopsins, where a *cis-trans* isomerization triggers the photoreaction[13,58], the photocycle of microbial rhodopsins starts with a *trans-cis* isomerization around the C_{13}-C_{14} double bond[13,58] (figure 1.2 B). Photoisomerization yields the K intermediate on the timescale of picoseconds, which is succeeded by the L state, where the RSB is still protonated[59]. Accompanied by a drastic 140 nm hypsochromic shift of the protein absorption, the RSB proton is transferred to the primary proton acceptor D85 (figure 1.2 A) upon M-state formation[13,60–62], which proceeds with a time constant of 50 µs[57] and represents the first proton transfer step (figure 1.2 A). This is subsequently followed by the release of a H^+ to the extracellular side[13] (figure 1.2 A, step 2). The RSB is reprotonated by the proton donor D96 on the time scale of milliseconds (figure 1.2 A, step 3) via a water chain[59,62] forming the N state with the retinal still in 13-*cis* configuration[63]. The re-isomerization of the retinal to the all-*trans*[64] conformation and the reprotonation of the proton donor D96 happen during the transition from the N to the O state[65] (figure 1.2 A, step 4), which maximally absorbs at 640 nm red-shifted compared to the dark-adapted state. Finally, the O-state reverts to the dark

state within several tens of milliseconds depending on the ambient temperature and pH, which is accompanied by the proton transfer from the primary proton acceptor D85 to the proton release complex constituted by E194 and E204[66] (figure 1.2 A, step 5).

Despite all insights spectroscopic experiments yielded, they provide no means for investigating the transport activity of *Hs*BR at electrochemical load. First investigations of the pumping were performed with the protein reconstituted in vesicles or on black lipid membranes (BLM) already showing that upon illumination, a pH gradient and a proton motif force are established[67–69]. The first direct electrical characterization of the *Hs*BR photocurrents at voltage-clamp conditions was performed in 1995 by Nagel and colleagues promising to yield insights into the voltage dependence of the activity. They heterologeously expressed the protein in the membrane of *Xenopus* oocytes and measured the light-induced currents using two-electrode voltage-clamp[70]. The authors were able to demonstrate that the photocurrent is i) maximal upon illumination in the maximum of the absorption spectrum, ii) always oriented in the same direction, and iii) linearly depends on the applied membrane voltage with more than three-times lower currents at −165 mV than at 60 mV[70].

Sodium pumps - a new member of the microbial rhodopsin family Recently, a new class of microbial rhodopsin was identified in the marine flavobacterium *Krokinobakter eikastus*[c], which supposedly transports Na^+ out of the cell upon illumination[48]. The first identified putative Na^+-pump was named KR2, and since then several homologue rhodopsins have been identified in other marine flavobacteria like *Nonlabens dokdonensis* (*Nd*NaR2)[72], *Nonlabens marinus* (*Nm*NaR)[43], *Nonlabens sp. YIK11* (*N*NaR)[73], the flavobacterium *Gillisia limnaea* (*Gl*NaR) from an antarctic lake[74], the non-flavobacterium *Indibacter alkaliphilus* (*Ia*NaR) from an alkaline halolake[43,75], and *Truepera radiovictrix* (*Tr*NaR1 and 2) from a hot alkaline spring[d,e].

On the sequence level all NaRs share the NDQ-motif[48,51,75] in TM3 (figure 1.3, green boxes), where the bacteriorhodopsin-like H^+ pumps feature the earlier discussed DTD-motif or the Cl^--pump of *Natronomonas pharaonis* (*Np*HR) features the residues TSA. However, Na^+-pump activity has not been experimentally verified yet for all of these pumps exhibiting the NDQ-motif. Interestingly, *Tr*NaR1 stands out from the group of putative Na^+-pumps on the sequence level. Although it exhibits the NDQ-motif rendering it putatively Na^+-pumping, it shows differences on the primary sequence level

[c] The bacterium was reclassified to belong to the genus *Dokdonia* in 2012[71].

[d] Sequences researched together with Arend Vogt.

[e] Even more rhodopsin sequences with the NDQ-motif were identified (GenBank accession number) and tested for activity here[76] from *Flagellimonas* sp_DIK (*F*NaR, KM461123.1), *Desulhohustis* sp. (ESQ10031.1), *Micromonaspora* sp.CNB 394-2 (WP_018784639.1), *Salinarimonas rosea* DSM21201 (*Sr*NaR, WP_052341415.1), *Lynbya aestuarii* (WP_052001698.1).

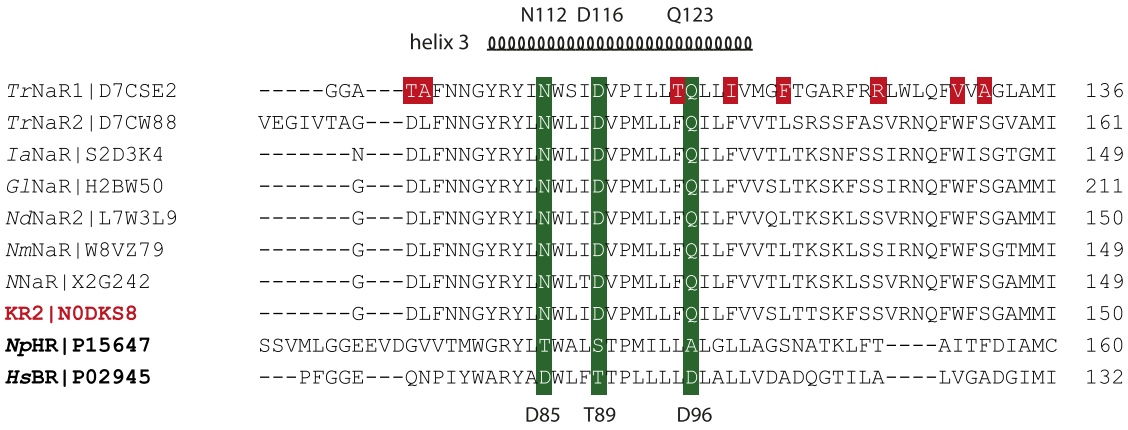

Figure 1.3: Sequence alignment of microbial rhodopsins with NDQ-motif. Sequence alignment around TM3 of the H^+-pump *Hs*BR (DTD-motif), the Cl^--pump *Np*HR (TSA-motif) and microbial rhodopsins with NDQ-motif - putatively pumping Na^+ with respective UniProt ID. *Tr*NaR1 and 2 of *Truepera radiovictrix*, *Ia*NaR of *Indibacter alkaliphilus*, *Gl*NaR of *Gillisia limnaea*, *Nd*NaR2 of *Nonlabens dokdonensis*, *Nm*NaR of *Nonlabens marinus*, *N*NaR of *Nonlabens* sp. YIK11, KR2 of *Krokinobacter eikastus*, *Hs*BR of *Halobacterium salinarum*, *Np*HR of *Natronomonas pharaonis*. The alignment was done using the ClustalOmega[77] online tool and the whole alignment can be found in the appendix A.2.

compared to the other NaRs (figure 1.3). At several positions in TM3 (indicated in red in figure 1.3) and throughout the sequence (see full alignment in appendix A.2) it exhibits different residues compared to the other NaRs sometimes homologue to *Hs*BR.

The assay of choice to monitor activity of NaRs, was recording pH changes in suspension of NaR-expressing *E. coli* upon illumination[48,78,79]. A light-induced, reversible pH increase was observed for KR2 in unbuffered NaCl, NaBr or Na_2SO_4 solution, which was even enhanced when the protonophore carbonyl cyanid-*m*-chlorophenyl hydrazon (CCCP) was added[48]. The insensitivity to CCCP ruled out light-activated H^+ transport at these conditions and rather implied outward-directed Na^+-pumping. However, in KCl, CsCl or RbCl solution the medium was acidified upon illumination, which was abolished after addition of CCCP and thus interpreted as H^+-transport[48,78].

Similar results were obtained *in vitro* for *Ia*NaR, which was reconstituted with an inside-out orientation in proteoliposomes and changes of the intraluminal pH were measured using the pH-sensitive fluorophore pyranine[80]. For *Ia*NaR a light-induced, CCCP-enhanced elevation of the pH inside the vesicle in NaCl solution and a CCCP-abolished acidification in KCl solution was observed[80]. Hence, these *in-vitro* measurements were interpreted similar to the KR2 results with Na^+-pumping in NaCl solution and a switch to H^+-pumping in absence of Na^+. Gushchin and colleagues conducted experiments with KR2-proteoliposomes fused to BLMs[79]. Here, the light-induced current was dependent on the [Na^+] increasing with its concentration, while it was insensitive to the K^+-concentration. Interestingly, the current prevailed even in the absence of Na^+ and

K^+, which was similarly explained by a switch to H^+-transport in absence of Na^+[79]. This selectivity switch was also proposed for *Ia*NaR[80] as mentioned and *Nd*NaR2[81], but excluded for *F*NaR, *N*NaR, and *Sr*NaR[76].

The first identified Na^+-pump KR2 can be readily expressed and purified from *E. coli*, which enabled spectroscopic studies on the purified protein and elucidation of the KR2 photocycle. Inoue *et al.*[48] recorded transient absorption spectra of KR2 reconstituted in 1,2-dioleoyl-*sn*–glycero-3-phosphocholine (POPC) lipid vesicles at pH 8.0 in NaCl and KCl and proposed the two photocycles presented in figure 1.4[48]. In NaCl, formation of the early K state was succeeded by an equilibrium of the L and M state, which rose with a time constant of 26 µs[48]. Subsequently, the O state formed with a kinetic constant of 1 ms accompanied by the proposed uptake of a sodium ion[48]. The O state decayed bi-exponentially with time constants of 7.9 ms and 112 ms, while the slower component only contributed 9.4 % to the decay[48]. In NaCl, the O-state decay was suggested to be accompanied by the release of a sodium ion (figure 1.4, left). Recent step-scan FTIR measurements showed that in the O state the retinal still adopts a 13-*cis* conformation, which would render it rather N-state like[82]. In KCl, the differences in the photocycle were that the K-state decay could not be resolved and that the O state reportedly occurred in equilibrium with the L and M state (figure 1.4, right). The decay of this equilibrium was fitted with three exponential components, yielding time constants of 107 ms, 580 ms and 70 s, which is significantly slower than the main decay component in NaCl[48] (figure 1.4). Further on, the availability of ample amounts of recombinant KR2 from *E. coli* paved the way for crystallization and resolution of the 3D structure only two years after the first report of the pump[78,79]. The plethora of spectroscopic data and the two crystal structures allowed the proposition of a transport mechanism[78,79,83,84], which will be summarized in the following. The two crystal structures and theoretical calculations[83] proposed two sites for transient Na^+ binding, which are sequentially traversed by the transported sodium ion upon photoactivation of KR2 (figure 1.5). The first one is more on the intracellular side between Q123 and the deprotonated counter ion D116 (figure 1.5, green inset)[78,79,83]. D116 hydrogen bonds to the protonated RSB in the dark[78,79]

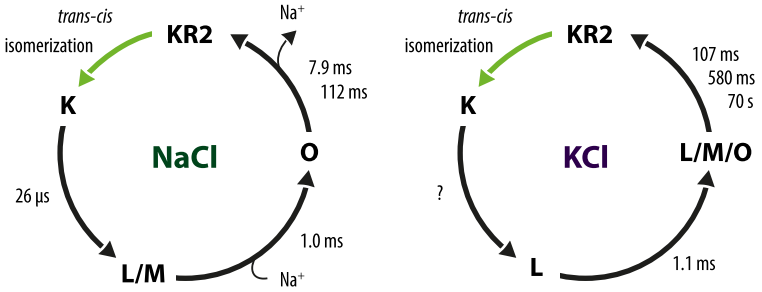

Figure 1.4: Reported spectroscopic photocycles of recombinant KR2 at pH 8.0 reconstituted in lipid vesicles in NaCl (left) and KCl (right) solution according to[48]. Time constants of the respective decay are indicated and taken from[48]. In KCl the time constant of the K-state decay was not resolved[48].

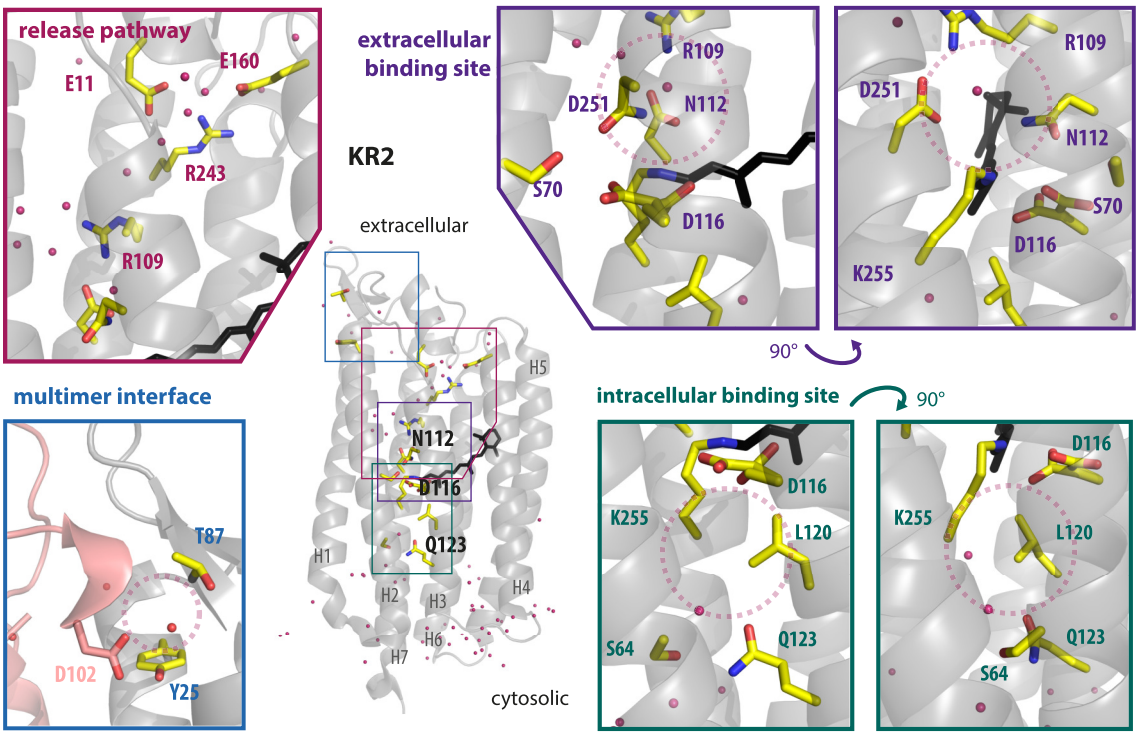

Figure 1.5: Structural insights into KR2. **A** Dark state crystal structure of KR2 (PDB:3X3C)[78] at neutral pH with retinal (black) covalently bound to K255 and water molecules denoted by pink spheres. Green insets show the proposed intracellular transient Na^+ binding site between Q123 and D116 (encircled in red) from two different angles[83]. In the dark D116 forms a hydrogen bond to the protonated RSB[78,79,83]. The second rotamer of D116, which faces S70, was proposed to occur during the M state[78,83]. The purple insets show the transient Na^+ binding site on the extracellular site formed by D251 and N112 (encircled in red) in two different views[83] with the close R109, which is hydrogen bond to D251[78,83]. The red inset shows the potential release pathway for the Na^+-ion formed by a polar cavity, which is filled with water molecules and lined by E11 and E160[84]. The blue inset shows the proposed interface of the protomers in the pentameric multimer (PDB:4XTN)[79] with contributions from Y25 and T85 and D102 (pink) from the neighboring monomer. A non-transported Na^+-ion (encircled in red) is bound at the protomer interface[79,84]; for details the reader is referred to the main text.

and this bond functions as a latch preventing ion passage in the dark[78,83]. Subsequent to photoactivation, the RSB proton is transferred to the deprotonated D116 which then flips towards S70 and N112 forming hydrogen bonds with S70[84]. Effectively, this proton transfer sequesters the positive charge of the protonated RSB from the transport pathway and allows the Na^+-ion to pass the retinal[78]. Upon formation of the O state the proton is transferred back from D116 to the RSB preventing back flow of the ion. Now the Na^+-ion is transiently bound at the second proposed binding site between D251 and N112[83,84] (figure 1.5, purple inset) and then released into the extracellular lumen passing E11 and E160[79,83,84]. Additionally, the structure shows a polar cavity on the extracellular side protruding into the protein up to R109 and containing several water molecules[84] (figure 1.5, pink inset), which could be part of the release pathway for the Na^+-ion.

In the structure published by Gushchin and colleagues[79], a Na^+-ion is resolved

bound on the extracellular side of the protein close to Y25 and T87 (figure 1.5, blue inset), which is not the transported ion itself[78,79,85]. The binding affinity for Na^+ of this site is in the millimolar range with a K_D of 11 mM at pH 8.0[48] and is abolished at pH 3.6[48]. Gushchin and colleagues reported a pentameric oligomeric state of KR2, which was supported by recent atomic force microscopy experiments[86], with this Na^+-ion located at the pentamer interface between Y25 and T87 (figure 1.5, blue inset) in the one protomer and D102, which is located in the extracellular loop 1, of the neighboring protomer[79,84]. Additionally, it was shown that the mutant D102N shows similar activity and kinetics like wt KR2, but reduced thermostability[78]. This further supports that this Na^+-binding is important for protein stability, eventually mediated by oligomerization, but that this Na^+ is not transported.

1.1.2 Light-gated ion channels

Short historical outline In 2002 Nagel and colleagues reported the identification of a directly light-gated cation channel - *Chlamydomonas reinhardtii* ChR 1 (*Cr*ChR1) - in the motile, green freshwater algae *Chlamydomonas reinhardtii*[36]. Although it was known that phototactic responses in green algae are mediated by a rhodopsin[87–89], which initiates electrical currents[90–92] and that photoreception by the rhodopsin and electrical response are tightly linked, this was the first report showing the unification of photoreceptor and channel in one protein - the channelrhodopsin[f]. This finding was backed up by the identification of a second homologue ChR - *Chlamydomonas reinhardtii* ChR 2 (*Cr*ChR2) - from the same alga only one year later accompanied by the results that ChRs are neither coupled to a transducer nor activated by transmitters and thus directly light-gated ion channels[37]. Additionally, this report showed that the transmembrane domain alone provides photoreception as well as channel function and the cytosolic C-terminal domain, naturally present in ChRs, is superfluous to mediate light-activated ion flux[37].

Since the first report of *Cr*ChR1 and *Cr*ChR2, numerous other cation-conducting ChRs[93–95] with distinct characteristics were identified not only in green but also in cryptophyte algae[96]. They feature different biophysical properties with maximal sensitivities spanning the spectral range from 435 nm to 590 nm[97,98], varying kinetics, light sensitivities, and distinct ion selectivities. In 2014, the cation-conducting ChRs were complemented by the engineering of anion-conducting ChRs[39,40] (ACR), which was followed by the identification of naturally occurring anion-conducting ChRs in cryptophyte algae in 2015[41].

[f] Sineschekov *et al.*[92] discussed whether channel function is provided by the rhodopsin itself or the rhodopsin forms a tight complex with a channel, but did not investigate it further in their report.

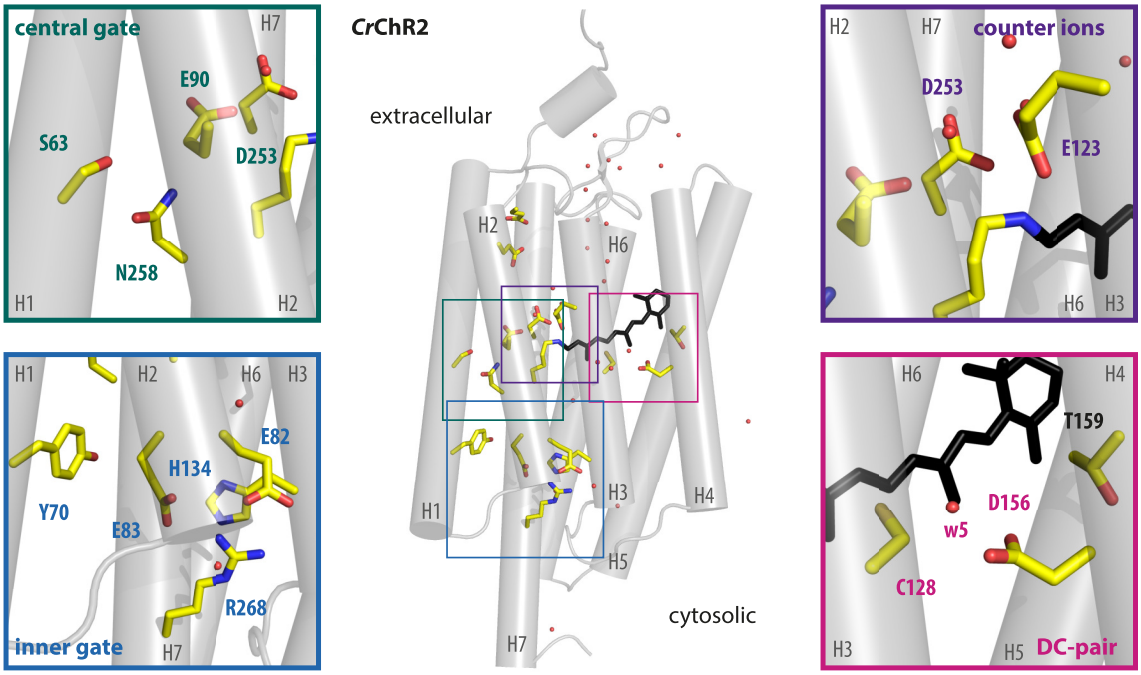

Figure 1.6: Structural overview of *Cr*ChR2. 3D crystal structure of *Cr*ChR2 (PDB: 6EID) showing the seven transmembrane helical fold with the all-*trans* retinal (black) covalently bound to K257 in TM7. The red dots indicate resolved water molecules. Dark green, top left: central gate comprising S63, E90, D253 and N258; purple, top right: counter ion complex with D253 and E123; blue, bottom left: inner gate with Y70, E82, E83, H134, H265 and R268; green, bottom right: DC-pair with C128 and D156 and the bridging water w5, additionally displayed is the close T159.

Crystal structure First attempts to solve the structure of ChR were conducted using cryo-electron microscopy on 2D crystals of *Cr*ChR2 expressed in *Pichia pastoris*, which confirmed the heptahelical structure expected for a microbial rhodopsin at a resolution of 6 Å[99]. The first 3D crystal structure was solved at 2.3 Å for C1C2[100–102] - a chimera of *Cr*ChR1 and *Cr*ChR2[g] - purified from insect cells (*Spodoptera frugiperda*)[103]. Recently, the crystal structure of *Cr*ChR2 was solved at 2.4 Å resolution with protein purified from *Leishmania tarentolae*[104].

To date, all available ChR structures show the dark state conformation, hence structural information of the open state and thus the ion conduction pore is not available yet. However, there is a series of periodical glutamates (E82, E83, E90, E97, E101) in TM2[103–107] along which ion conductance presumably occurs, which would render helices 1, 2, 4, and 7 pore lining. In the dark, a continuous pore through the protein is precluded by two constriction sites located in the center and at the cytosolic side of the protein termed the central and the inner gate[97,103,104]. The central gate comprises the residues S63, E90, D253 and N258, which form a hydrogen bonding network together

[g] All C1C2 chimeras consist of TM1-TM5 of *Cr*ChR1 and TM6 and 7 of *Cr*ChR2. The crystallized chimera from Kato and colleagues additionally contained a modification of the C-terminus as the sequence NKGTGK was removed[103].

with the protonated RSB and connect TM1, 2 and 7 (figure 1.6 top, left)[103,104]. Engaged in the hydrogen bonds of the central gate and protruding into the putative ion conducting pore, E90 is reportedly a major determinant of ion selectivity in *Cr*ChR2[39,106,108]. While replacement of E90 with alanine or glutamine (E90A, E90Q) reduced proton conductance[108], a replacement with lysine or arginine (E90K, E90R) inverted selectivity creating an anion-conducting ChR[39]. The second constriction site is formed by Y70 and the hydrophilic side chains of E82, E83, H134, H265 and R268 engaging in connections bridging helices 1, 2, 3 and 7[97,104] (figure 1.6 bottom, left).

In the dark state *Cr*ChR2, the positive charge of the protonated RSB is balanced by the two counter ions E123 and D253 (figure 1.6 top, right). As replacement of the conserved D253 by non-protonatable residues like asparagine or alanine leads to reduced functionality, D253 was identified as primary proton acceptor to the Schiff base after photoactivation[109,110]. Whether the second, less-conserved counter ion E123 can as well accept the proton remains elusive[111], but mutations of E123 (E123A/T) - the so-called ChETA mutations - were shown to be functional[112] proving that this counter ion is dispensable. However, both substitution by alanine and threonine accelerate channel closing[112,113], implying some role of E123 in proton transfer. Additionally, replacement of E123 by glutamine or alanine (E123Q/A) caused a bathochromic shift of the action spectrum[112,114], supporting the proximity of the deprotonated E123 to the RSB and its contribution to the stabilization of the RSB charge in the dark.

Another functional determinant of ChRs especially regarding kinetics is the so-called DC-pair, which in *Cr*ChR2 comprises C128 and D156 located within the retinal binding pocket (RBP) connecting helices 3 and 4 (figure 1.6 bottom, right). Individually replacing either C128 (C128T/A/S) or D156 (D156A) yielded the so-called step-function opsins (SFO) with closing kinetics of up to five orders of magnitude slower than the wild-type *Cr*ChR2 reaching open state lifetimes in the minutes range for C128S and D156A[115,116]. Combining mutations at both positions (C128S + D156A) synergistically enhanced the effect and yielded an open state stable for more than 30 min[117]. Although, the role of connecting helix 3 and 4 and the involvement of the DC-pair in the closing (kinetics) of *Cr*ChR2 is empirically evident its' molecular structure was debated for several years. It was controversially discussed, whether both residues interact directly[118,119] or are bridged by a water molecule[103,120,121] and whether D156 might function as proton donor for reprotonation of the RSB[110].

The proposition of a direct hydrogen bond evolved from the fact that the homologous residues T90 and D115 in *Hs*BR form a direct hydrogen bond[122,123], which was transferred to *Cr*ChR2 and interpreted into subsequently measured fourier-transform infrared (FTIR) spectroscopy data[118,119]. However, in the crystal structure of C1C2 the residues

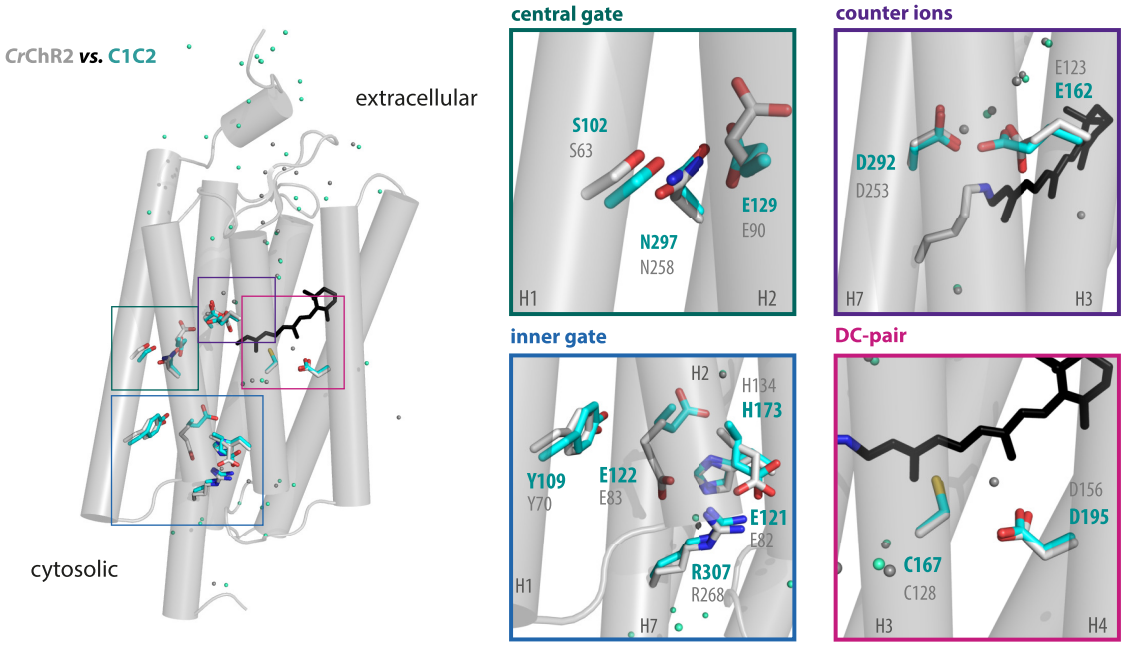

Figure 1.7: Structural comparison of *Cr*ChR2 (6EID)[104] and the chimeric C1C2 (3UG9)[103] with the side chains of *Cr*ChR2 in grey and homologue side chains of C1C2 in green. Insets focus on the residues contributing to the structural key features discussed earlier: central gate (dark green, top left), the counter ion complex (purple, top right), the inner gate (blue, bottom left), and the DC-pair (pink, bottom right). Water is shown by spheres in the respective color.

are separated by a distance of more than 4 Å[103], which is inconsistent with a hydrogen bond[124]. Additionally, a direct hydrogen bond would mediate similar effects of mutations at C128 as well as D156[120], as in both cases formation of the bond would be prevented by mutation, but this is not the case as discussed above. Theoretical calculations support the presence of a water molecule between the DC-pair residues[120] and further showed that the FTIR data, initially used to propose the direct bond of C128 and D156, can as well be interpreted with the indirect bonding via a water molecule[121]. Finally, the *Cr*ChR2 crystal structure ultimately resolved the issue and directly showed the presence of a water molecule between C128 and D156[104].

The second controversial aspect, whether D156 is the proton donor to reprotonate the RSB, was proposed because the kinetics of D156 deprotonation and RSB reprotonation paralleled in FTIR data[110]. However, a sole kinetic correlation is no direct proof for the proton donor function of D156 as the proton could likewise originate from a nearby water. Furthermore, this proposition is challenged by the reported functionality of D156 mutants[113,117] and the insensitivity of the D156 band to H/D exchange in FTIR-measurements[h,126] questioning a contribution to the proton pathway.

Since the *Cr*ChR2 crystal structure was published only in November 2017[104], previous

[h] The insensitivity of the D156 band to H/D exchange was likewise shown for C1C1[125].

structural insights stemmed from homology modeling on *Hs*BR[122] or *Anabaena* sensory rhodopsin[127] and the structure of the C1C2 chimera. Thus, the most evident differences in the *Cr*ChR2 and C1C2 structure regarding the structural elements introduced above will be briefly highlighted here (figure 1.7). As discussed in detail above, one prominent difference is the presence of a water molecule in the DC-pair of *Cr*ChR2, which was not resolved in the C1C2 structure before (figure 1.7, bottom, right). However, the orientations of the cysteine and the aspartic acid are almost identical in both structures with similar distances, allowing that the water might also be present in C1C2 although not resolved. While the central gate glutamic acid (E90 in *Cr*ChR2 and E129 in C1C2) faces towards an asparagine in TM7 (N258 or N297) in C1C2 and presumably forms a hydrogen bond, it faces the primary proton acceptor (D253) in *Cr*ChR2 (figure 1.7, top, left)[104]. Further, the second counter ion adopts different rotamers in both structures (1.7, top, right) and also the inner gate glutamic acids are arranged differently. Most prominently, E83 faces the cytosolic side in *Cr*ChR2 while its homologue E122 in C1C2 faces into the protein (figure 1.7, bottom, right), which could entail conformational differences in the inner gate structure or of ordered water molecules in the vicinity.

Photocycle models Numerous *in-vitro* studies lead to a photocycle for *Cr*ChR2, which evolved over several years and is still extended frequently (see figure 1.8 C). Photoexcitation with blue light (figure 1.8 E) triggers the isomerization of the retinal from the all-*trans* to the 13-*cis* conformation and the excited state decays on the timescale of 400 fs[126] into the relaxed, red-shifted P500 intermediate[128], which is sometimes referred to as P_1. During the formation of the subsequent P390 state (P_2), which rises on the time scale of 25 µs, the RSB deprotonates entailing a distinct blue-shift of the absorption[116,128]. During the transition to the P520 (P_3) state, which occurs within milliseconds and is accompanied by the reprotonation of the RSB, the channel opens. While there is general consensus about P520 being a conducting state[116], the contribution of a late P390 state to ion conduction was proposed as well, because one component of the single turnover photocurrent rises on the time scale of 200 µs; faster than the P520 state, but slower than the P390 state[110,129,130]. From the P520 state the protein reverts to a late P480 state (P_4) within several milliseconds, which is followed by the reversion to the D470 dark state on the time scale of 20 s to 40 s in *Cr*ChR2. Because the protein can be reactivated much faster than after 40 s and the photocurrent does not completely inactivate under continuous illumination, the P480 state was proposed to be photoactivatable with a light-induced conversion to the early P500 state[128].

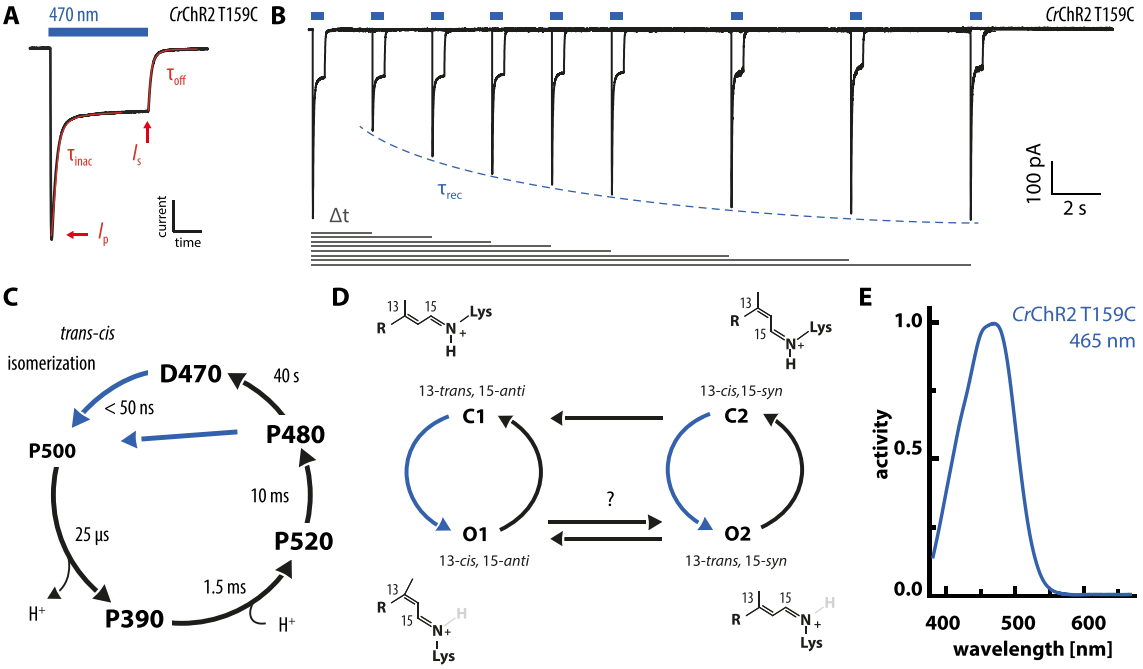

Figure 1.8: *Cr*ChR2 activation and photocycles. **A** Representative photocurrent trace of *Cr*ChR2 T159C recorded under voltage-clamp conditions at E_{hold}=−60 mV from HEK293 cells upon blue-light activation with 470 nm for 500 ms (blue bar). **B** Schematic representation of a peak recovery measurement. Repetitive activation of *Cr*ChR2 T159C with different delays between the light pulses showing the immediate recovery of the stationary but a slow recovery of the full transient current. Raw data kindly provided by Jonas Wietek. **C** Simple spectroscopic photocycle model for *Cr*ChR2 according to Ritter and colleagues[128] with the number denoting the maximal absorption difference to the dark state and the respective time constants. **D** Electrophysiological photocycle model demanding at least two closed and two open states, which were suggested to be populated by different isomerization states of the retinal chromophore. **E** Action spectrum of *Cr*ChR2 T159C at pH 7.2 peaking at 465 nm.

In addition to the spectroscopic results, electrical recordings of the ChR photocurrents impose requirements for the photocycle model as well. Upon photoactivation, the *Cr*ChR2 photocurrent rises to a transient peak I_p, which inactivates with τ_{inac} to a stationary level (I_s) under continuous illumination and decays exponentially with τ_{off} after the light is switched off (figure 1.8 A). The simplest model qualitatively explaining a transient I_p and inactivation to I_s comprises three-states: a closed, an open and a desensitized state, which is closed but does not resemble the dark state[37,131]. However, upon repetitive activation, the full transient I_p only recovers over the time course of seconds, while the complete I_s immediately recovers (figure 1.8 B). This observation could not be explained with the initial three-state model, but introduction of a light-induced transition from the desensitized to the open state enabled the three-state model to also explain this slow recovery of I_p after repetitive stimulation[132].

Nevertheless, the three-state model is not capable of explaining all the features of the photocurrents for example kinetics of τ_{off} and τ_{inac}[131,133], the bi-exponential decay of I_s after light-off[131], and different ion selectivities of I_p and I_s[134]. Thus, a four-state

model comprising two closed (C1 and C2) and two open states (O1 and O2) was introduced (figure 1.8 D)[116,131,133,135]. In that model dark adapted protein resides in C1, which photoconverts to O1 mainly carrying the early transient current I_p. Subsequently, conversion back to C1 or to the second photocycle with a less-conducting open state O2 can occur[131,135]. Consequently, I_s comprises contributions from O1 and O2 under continuous illumination and is carried by an equilibrium of both[131,134]. However, whether there is a direct transition between the open states and whether this transition might be light-induced or the equilibrium of O1 and O2 forms via traversing the dark states is not clear yet. According to the model, the second open state O2 decays to the second closed state C2 and in the dark C2 thermally converts to C1[131,134], but recently photoconversion between the dark states was proposed as well[136].

For dark-adapted *Hs*BR a mixture of retinal conformations comprising 13-*trans*, 15-*anti* and 13-*cis*, 15-*syn* retinal was proposed after retinal extraction followed by high-performance liquid chromatography[137] (HPLC) and nuclear magnetic resonance (NMR) measurements[138]. In *Hs*BR both conformations stabilize the dark state through interactions with the counter ions, but only photoactivation of the 13-*trans*, 15-*anti* isomer leads to the membrane translocation of a H^+[138]. Similar to that and backed up by resonance Raman measurements and retinal extraction experiments[139] a mixture of 13-*trans*, 15-*anti* and 13-*cis*, 15-*syn* retinal isomers was proposed for the *Cr*ChR2 dark state as well. For the slow-cycling *Cr*ChR2 mutant C128T, this mixture of *anti* and *syn* conformers was observed in IR spectroscopy on recombinant *Cr*ChR2 C128T (figure 1.8 D)[140]. Consequently, the open states would be populated by the 13-*cis*, 15-*anti* and 13-*trans*, 15-*syn* isomers. However, experimental evidence combining spectroscopic and electrical measurements to prove that assignment is still lacking.

Spectrally shifted cation-conducting ChRs To date, the blue-light activated *Cr*ChR2 (figure 1.8 E) is the most investigated, best-characterized, and still most frequently used ChR[98]. To enable independent activation of different neuronal cell populations with spectrally distinct ChRs, red-shifted ChRs are indispensable. Ideally, they would have no spectral overlap to minimize cross-talk and enable independent activation. Additionally, delivery of activation light can be a demanding challenge especially in an *in-vivo* context. Regarding this, ChRs which can be activated at wavelengths red-shifted compared to *Cr*ChR2 also pose an advantage, because red-light penetrates deeper into biological tissue than blue light due to reduced scattering and absorption[141–143]. The first naturally occurring red-shifted ChRs were the channelrhodopsin 1 from *Volvox carteri* (*Vc*ChR1)[93,144], *Mesostigma viride* (*Mv*ChR)[145], *Chlamydomonas augustae*[94], and *Chlamydomonas yellowstonensis*[94] (see table 1.1). All of them exhibited significantly red-shifted

action spectra compared to *Cr*ChR2 (see table 1.1) but unified in exhibiting small photocurrents upon light activation, which limited their further usage[94,144–146]. Following the helix shuffling approach of Wang and co-workers[101] the chimeric C1V1 was generated from *Cr*ChR1 and *Vc*ChR1, which overcame the low photocurrents of the natural, red-shifted ChRs[117,147]. C1V1 showed enhanced membrane targeting and higher photocurrents compared to *Vc*ChR1 (and *Cr*ChR1), but preserved the red-shifted activation of the parental *Vc*ChR1 with a maximal sensitivity to 540 nm light[147].

Table 1.1: Natural ChRs with a red-shifted action spectrum compared to *Cr*ChR2 (λ_{max} 465 nm) with organism of origin, maximal sensitivity, year of first report and references of first report and action spectrum.

organism	λ_{max} [nm]	year	reference
V. carteri	535	2009	93,144
M. viride	531	2011	145
C. augustae	520	2012	94
C. yellowstonensis	520	2012	94
S. helveticum	500	2014	95
C. noctigama	590	2014	95

Since then, C1V1 and mutants thereof are successfully applied alternatively to *Cr*ChR2 to elicit AP firing with red-shifted light[117,148,149]. The accelerated mutant C1V1 E122T[147] even enabled light-stimulated action potential (AP) firing upon illumination with 630 nm activation light[117]. Two years later, the lab of Roger Tsien reported a very similar approach and generated a chimera as well based on *Vc*ChR1, which was termed ReaChR, showing even better membrane targeting, higher photocurrents and slightly faster kinetics than C1V1[150]. ReaChR was published with an action spectrum peaking even around 600 nm, but with an unusually broad shape[150].

Although, the enhanced chimeras enabled activation with considerably red-shifted light compared to *Cr*ChR2, all of them retained sensitivity to blue light impairing useful combination of them with blue-light activated ChRs to achieve dual color activation. Finally in 2014, a genome mining approach from the Boyden lab yielded a multitude of new ChRs with very different properties. Amongst them was a ChR from the green freshwater algae *Chlamydomonas noctigama* (*Cn*ChR), which is referred to as Chrimson[95]. Chrimson showed maximal photocurrents upon activation with 590 nm light[95,151] and could be successfully combined with the blue-light activated Chronos, which emerged from the same genome mining approach, to independently excite distinct neuronal populations[95].

1.2 Microbial rhodopsins as optogenetic tools

Already in the first *Cr*ChR2 publication, its application as a tool for light-induced depolarization of the cell membrane was proposed[37]. This idea was rapidly picked up and indeed the photoactivation of various kinds of excitable cells was demonstrated by

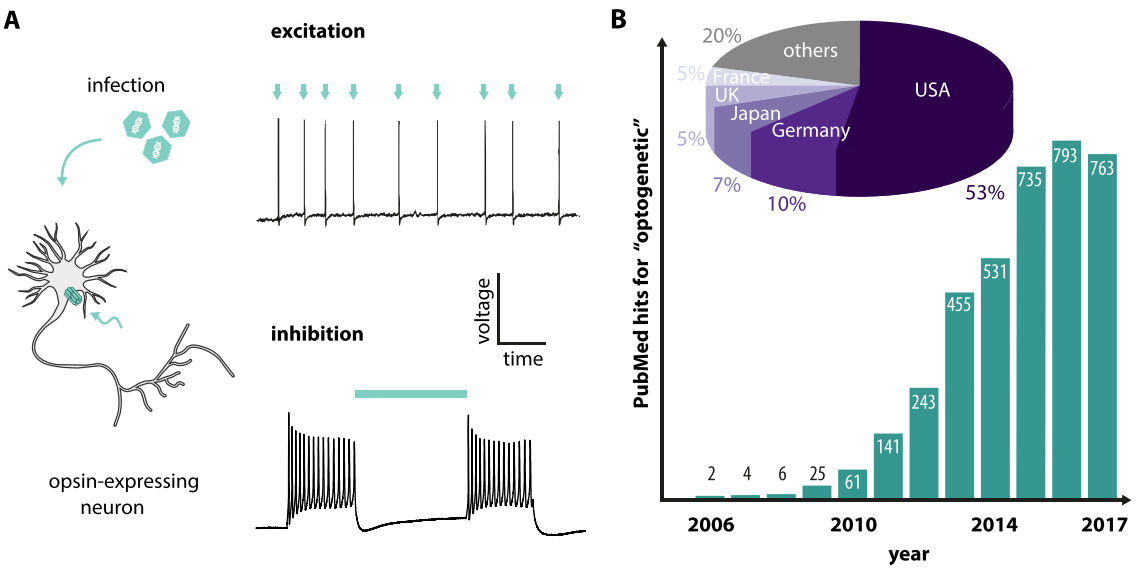

Figure 1.9: Optogenetics. A In a narrower sense optogenetics implies the use of genetically-encoded microbial ion transporters to monitor or control neuronal function with light. Depending on the chosen microbial rhodopsin they allow spatiotemporally defined activation (top, adapted from [153]) or inhibition (bottom) of AP firing using light. **B** PubMed hits (using gopubmed.org) for publications using the term "optogenetic" over the years 2006-2017 and the country of origin for the papers (pie chart).

multiple groups shortly afterwards. The group of Zhuo Pan rendered inner retinal cells light-sensitive attempting to restore visual responses in mice[152], in Karl Deisseroth's lab *Cr*ChR2 was used to trigger neuronal spiking in hippocampal mouse neurons[153], Alexander Gottschalk and colleagues demonstrated light-induced triggering of specific behavioral responses in *C. elegans*[154], Stefan Herlitze and co-workers demonstrated the application of *Cr*ChR2 to light-induced depolarize chicken spinal cord cells[155], and in the lab of Hiromu Yawo *Cr*ChR2 was expressed in brain slices and the rat cell line PC12 rendering the cells light sensitive[156].

The term optogenetics for this kind of experiments was introduced by Karl Deisseroth and colleagues to put the combination of genetic targeting of specific cells and optical methods to monitor and perturb cellular responses under one umbrella[157]. Although the idea to manipulate cells with light was older and there were earlier approaches to modify cellular responses with light[158,159], ChRs made the difference and kicked-off the field such that optogenetics was declared Nature Method of the Year in 2010[160]. ChRs unify photoreception and channel function in one small protein making them perfect candidates for optogenetic manipulations. They rapidly outperformed earlier approaches, which used a combination of different proteins rendering them slow or difficult to handle. Additionally, it turned out that supplementation of retinal is unnecessary in the mammalian brain and easily provided by ingestion in *Caenorhabditis elegans*[154] or *Drosophila melanogaster*[161], which makes *Cr*ChR2 an easy to handle tool.

Shortly after the dawn of optogenetics, depolarizing cation-conducting ChRs where complemented by microbial pumps like the H^+-pump Arch3 or the Cl^--pump *Np*HR, which were used to hyperpolarize the membrane and inhibit neuronal AP firing with light[162–164]. Combining microbial rhodopsins and viral gene delivery to specific neuronal populations, the activation and inactivation of AP firing was now possible with unprecedented spatiotemporal precision (figure 1.9 A). This transformed optogenetics into an incredibly successful technique applied in numerous labs all over the world, which is underlined by the ever growing number of publications using the term optogenetic over the last years (figure 1.9 B).

Initially, neuronal inhibition was slightly handicapped, because the light-driven pumps transport only one charge per photon, thus exhibiting small photocurrents and demanding excellent membrane targeting and higher light intensities for neuronal inhibition than the cation-conducting ChRs need to elicit AP firing. This was overcome by the engineering of Cl^--conducting ChRs[39,40] and the identification of natural anion-conducting ChRs[41], which are now widely used as well[38,165–167] and make the optogenetic toolbox extremely versatile today.

In a narrower sense, optogenetics refers to the application of photoreceptive microbial channels and pumps to investigate and manipulate excitable cells in the neurosciences. Nevertheless, the optogenetic concept can be (and is) applied to a multitude of biological processes and cellular events, which can be put under light control. Prominent examples for light-controlled enzymes are the natural photoactivated adenylyl cyclase of the bacterium *Beggiatoa* (bPAC)[168], the engineered light-activated histidine kinase YF1, which harbors a LOV domain to put kinase activity under light control[169] or the engineered light-activated phosphodiesterase LAPD employing a phytochrome to render a human phosphodiesterase light-sensitive[170]. In further studies, the revolutionary gene-editing tool CRISPR[171] was engineered to be photo-switchable using for example a LOV domain[172] or a photo-dissociable dimeric fluorescent protein[173] to precisely edit DNA in a light-controlled manner. The labs of Alice Ting and Kay Tye engineered FLARE, which is based on a LOV domain combined with calmodulin and enables "Fast Light- and Activity-Regulated Expression" of proteins when rising Ca^+-levels and blue-light illumination occur simultaneously[174]. The light-inducible nuclear localization signal LINuS, which was reported by Niopek and colleagues[175], allows localization of proteins to the nucleus in a light-controlled fashion and its counter part LEXY allows the light-induced export of proteins from the nucleus[176]. This list is not complete and by far only a small selection of cellular processes which were rendered light-controllable over the last years. Nevertheless it emphasizes, that light provides an orthogonal and non-

invasive stimulus in many systems allowing the investigation and control of multiple cellular processes with unprecedented spatiotemporal precision rendering the optogenetic concept extremely versatile.

1.3 Aims of this thesis

Microbial rhodopsins not only provide versatile optogenetic tools, but they also serve as valuable targets for fundamental research. Their structural and functional similarities to animal rhodopsins[12,13] make them valuable models for G-protein coupled receptors (GPCR), which are prominent drug targets in medical research[177,178]. Additionally, their comparably small size makes them easier to investigate promising insights into the structure function relationship of membrane proteins, bioenergetics or photoreception[12]. Ion transporting microbial rhodopsins can further serve as model proteins for membrane transport or ion selectivity. This study aimed at the biophysical investigation of two microbial rhodopsins mainly using electrophysiological techniques, the red-shifted ChR ReaChR and the light-driven ion pump KR2.

The engineered ReaChR[150] was published as the most red-shifted ChR at this time[i]. It was reported to have excellent membrane targeting, high photocurrents and maximal peak photocurrents upon activation with 590 nm light. The action spectrum of I_s was even reported to peak at 630 nm[150] over 150 nm red-shifted compared to *Cr*ChR2[100]. This rendered ReaChR an interesting ChR for further investigation and biophysical characterization as its potential for application was promising. Moreover, the published action spectra were unusually broad and exhibited a non-Gaussian shape, which is uncommon for microbial rhodopsins and drew attention. Thus, this study aims to characterize and re-investigate ReaChR with focus on its spectral sensitivity. Additionally, biophysical features like ion selectivity or kinetics and changes thereof, which were not described in the initial publication[150] should be investigated.

For the Na^+-pump KR2 initial activity assays indicated that it transports Na^+ outwards upon illumination[48]. However, characterization of activity relied on the pH assay in *E. coli* or *in-vitro* measurements on BLMs or proteoliposomes, which have limitations especially regarding the accessibility of the substrate side or characterization of the voltage dependence rendering them unsuitable for a comprehensive investigation of the transport activity. A significant advance would be to investigate KR2 activity via whole-cell voltage-clamp recordings, because this provides control over the ionic composition on the extra- and intracellular side of the pump and additionally over the membrane voltage. However, because expression and membrane targeting of KR2 in mammalian

[i] Chrimson was published one year later in 2014[95].

cells is low, patch-clamp recordings have been hampered so far. Thus, this study aimed at a significant enhancement of the KR2 membrane targeting in mammalian cells to conduct an in-depth electrophysiological characterization. Additionally, this would allow characterization of the substrate specificity of KR2 as early measurements suggested a substrate switch in presence and absence of Na^+ [48]. Finally, a successful expression enhancement in mammalian cells would render KR2 a new optogenetic tool as light-induced sodium extrusion from a neuronal cell would inhibit AP firing. As Na^+-based inhibition neither changes H^+ or Cl^- distribution nor relies on the anion gradient, KR2 could present a valuable alternative where established inhibitory tools are limited.

2 Material and Methods

2.1 Molecular biology

DNA preparation All constructs and variants were expressed as fusion protein (FP) of the microbial rhodopsin with a C-terminally attached fluorophore. Additionally, codon usage was optimized for expression in human or mouse cells. Plasmid DNA encoding for the respective FP was obtained using conventional restriction cloning or genes were commercially synthesized (GenScript, Nanjing, China). To amplify genes from a plasmid, primers (Integrated DNA technologies, USA) were designed according to the flanking regions of the respective gene and the corresponding polymerase chain reaction (PCR) protocol is described in table 2.1. To verify success of the PCR, products of the PCR were loaded onto an agarose gel (1 % w/v) using loading buffer (10 x) and SYBR-Green was used to directly stain the probe (both Sigma-Aldrich, USA). If DNA bands were detected at the expected positions, the PCR products were cut out and DNA was extracted using a gel extraction kit (Macherey-Nagel, Germany).

Table 2.1: Left: Standard reaction mixture for a PCR to amplify a gene from a template vector; Right: Standard reaction cycles for the corresponding amplification PCR; T_m of primers was calculated using the online tool OligoAnalyzer3.1 (Integrated DNA technologies, USA) and the protocol adjusted to it; step two, three and four were performed in 25 to 35 cycles; primer mix contains the forward and reverse primer in a 1:1 ratio diluted to 10 µM

PCR reaction mix		**PCR cycles**	
- ReproFast buffer (10 x)	5 µl	95 °C	5 min
- dNTPs (2 mM)	5 µl	94 °C	40 s
- template DNA (25 ng µl^{-1})	2 µl	2 °C to 5 °C below T_m	30 s
- primer mix	2 µl	72 °C	1 min/kb
- ReproFast polymerase	1 µl	94 °C	30 s
- autoclaved ultrapure water	ad 50 µl	72 °C	10 min
		4 °C	∞

Table 2.2: Standard reaction mixtures for digestion (left) and ligation (right) of DNA or DNA fragments with commercially available enzymes

Digestion mix		**Ligation mix**	
- DNA	1.5 µg	vector	40 ng to 100 ng
- FastDigest buffer (10 x)	3 µl	insert	molar ratio 3:1 or 5:1
- restriction enzyme 1	1 µl	T4 ligase	1 µl
- restriction enzyme 2	1 µl	ligase buffer (10 x)	2 µl
- (alkaline phosphatase)	1 µl	autoclaved ultrapure water	ad 20 µl
- autoclaved ultrapure water	ad 30 µl		

Digestion and Ligation Cleaned PCR products and the target backbone were digested using FastDigest enzymes (Thermo Fisher Scientific, USA) according to the instructions of the manufacturer. If the digested DNA was a vector alkaline phosphatase was added to prevent re-ligation of the backbone. After incubation for an enzyme-specific duration, the reaction was stopped via thermal inactivation of the enzymes at 80 °C (5 min) and the product was purified via gel electrophoresis or DNA clean-up (Macherey-Nagel, Germany) to remove impurities and residual buffer of the previous steps. Table 2.2 shows the standard reaction mixtures for a digestion and the subsequent ligation. After digestion the purified fragments were ligated using T4 ligase (Thermo Fisher Scientific, USA) and its corresponding buffer. Usually, 40 ng to 100 ng of backbone DNA was used and the insert was added in a 3:1 or 5:1 molar excess to enhance ligation efficiency. The ligation mixture was incubated for 1 h at 22 °C, and the ligase was inactivated at 70 °C for 5 min afterwards.

***E. coli* Transformation, inoculation of cultures and DNA purification** Following ligation, a transformation was performed using 8 µl of the ligation mix. Chemocompetent XL1 Blue *E. Coli* cells[a] were used and transformed via the heat shock method. For that, chemocompetent cells were slowly thawed on ice and afterwards plasmid DNA was added. 15 min of incubation on ice was followed by a 42 °C heat shock for 20 s to 90 s, followed by another five minutes on ice. If the kanamycin resistance was used for selection, 200 µl of lysogeny broth (LB) medium without antibiotics were added and cells were incubated for at least 30 min at 37 °C while shaking at 650 rpm to facilitate oxygenation. Afterwards, transformed cells were plated on LB agar plates containing 30 µg ml^{-1} kanamycin or 100 µg ml^{-1} ampicillin and grown at 37 °C over night.

The next day, single colonies were picked from the agar plates, and 4 ml fresh LB medium, which contained 30 µg ml^{-1} kanamycin or 100 µg ml^{-1} ampicillin, was inocu-

[a] For the preparation of unmethylated DNA plasmids the chemically competent strain One Shot INV110 (Thermo Fisher Scientific, USA) was used.

lated with the cells, and incubated over night at 37 °C while shaking at 180 rpm.

Finally, the plasmid DNA was extracted from the cells using a plasmid purification kit (Marcherey-Nagel, Germany) according to the manufacturer's instruction obtaining concentrations of 400 ng µl^{-1} to 700 ng µl^{-1}. In a last step, the plasmid DNA was sequenced with primers binding up- or downstream of the gene (LGC Genomics, United Kingdom) to verify the success of the cloning process.

Site-directed mutagenesis For the site-directed introduction of mutations into the investigated genes the QuikChange site-directed mutagenesis kit (Agilent technolgies, USA) was used according to the instructions of the manufacturer. To introduce a mutation, forward and reverse primers were designed, ordered (Integrated DNA technologies, USA) and used in a PCR described in table 2.3. To get rid of template DNA, it was digested using Dpn1 (Thermo Fisher Sscientific, USA), which cleaves methylated DNA only. For that, 20 µl PCR product was incubated with 0.5 µl of Dpn1 at 37 °C for 1 h. Later on, this DNA was used to transform chemocompetent *E. coli* cells (XL1 Blue). After transformation and inoculation, DNA was purified as described above. Finally, the gene was sequenced to verify the successful introduction of the mutation (LGC Genomics, United Kingdom).

Table 2.3: Reaction mix (left) and PCR cycles (right) for a QuikChange PCR to site-specifically introduce point mutations in a gene. Primer mix contains forward and reverse primer in a 1:1 ratio diluted to 10 µM. Steps two, three and four were repeated in a cycle (18-25 times).

PCR reaction mix		**PCR cycles**	
- Pfu reaction buffer (10 x)	5 µl	95 °C	30 s
- dNTPs (2 mM)	5 µl	95 °C	30 s
- template DNA (40 ng µl^{-1})	2 µl	55 °C	1 min
- primer mix	1.25 µl	68 °C	12 min
- Pfu Turbo polymerase	1 µl	72 °C	10 min
- autoclaved ultrapure water	ad 50 µl	4 °C	∞

2.2 Cultivation of cells

All electrophysiological experiments were carried out on cultured human embryonic kidney (HEK) 293 cells, ND7/23 cells (both Sigma-Aldrich, Germany) or hippocampal neurons. The neuronal cell culture was established by Yinth Andrea Bernal Sierra and maintained by Tharsana Tharmalingam. The HEK239 cell culture was maintained and in most cases performed by Altina Klein or Maila Reh. For the KR2 project, ND7/23 cells[179], which is a hybrid cell line derived from mouse neuroblastoma and rat dorsal

root ganglion cells, was established in the lab. After initial testing and establishment of the culturing conditions for ND7/23 cells, Altina Klein and Maila Reh maintained the cultures.

2.2.1 HEK293 cell culture

Cultivation HEK293 cells were cultivated at 37 °C under 5 % CO_2 atmosphere. The culture was grown using Dulbeccos Modified Eagle medium (Biochrome, Germany) containing 10 % fetal bovine serum (FBS) and 1 % penicillin/streptomycin (100 µg ml^{-1}). Twice a week cells were passaged to a new tissue culture flask (area 25 cm^2, TPP, Switzerland). For that, old medium was removed and after two washing steps with phosphate-buffered saline (PBS) without Ca^+ and Mg^+, new medium was added and the adherent cells were removed from the surface by gentle tapping and rinsing with the medium using a sterilized glass pipette. After counting (Luna automated cell counter, Logos Biosystems, France) $2.5 \cdot 10^5$ cells were seeded in a new flask (5 ml to 8 ml medium) and grown to 70 % to 90 % confluence before splitting or seeding for experiments.

Seeding and transfection for experiments For patch-clamp experiments or confocal imaging cells were seeded into 35 mm petri dishes containing two to three poly-D-Lysine (PDL) coated[180] round glass cover slips[b] and supplemented with all-*trans* retinal at a final concentration of 1 µM. The number of seeded cells was adapted to the time of expression and ranged between $0.5 - 2 \times 10^5$ cells per dish.

One day after seeding, cells were transfected using FuGENE HD transfection reagent (Promega, USA). Per dish the transfection mixture contained 250 µl medium without FBS, 2 µg DNA and 6 µl transfection reagent. After incubation for 15 min at room temperature the mixture was gently added to the cells. The measurements usually took place 24 h to 48 h after transfection.

2.2.2 Establishment of ND7/23 cell culture

To have another mammalian expression system ND7/23 cells (Sigma-Aldrich) were ordered and established in the lab. ND7/23 cells are neuron-like hybrids initially derived from mouse neuroblastoma and rat dorsal root ganglion cells[179]. In contrast to neurons they are immortalized and can be kept in culture like HEK293 cells rendering them an easy to handle expression system closely related to neurons.

According to the supplier's instructions ND7/23 cells can be handled like HEK293 cells, which was verified in the initial weeks of cultivation. Cells were cultivated like

[b] The used procedure is described in detail here[181].

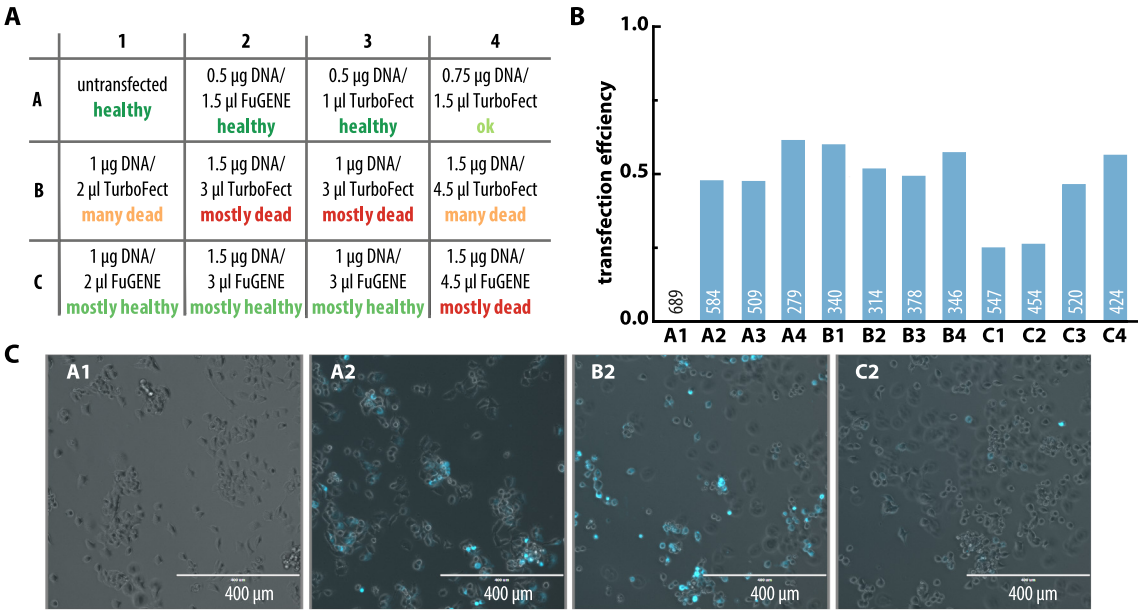

Figure 2.1: Transfection test of ND7/23 cells. **A** Varying amounts of DNA (ReaChR_mCerrulean3) mixed in different ratios with two different transfection reagents - TurboFect and FuGENE - were compared side by side and cell health was evaluated by visual inspection on three images per sample. **B** Transfection efficiency of the respective sample evaluated by counting the fluorescent cells; number indicates evaluated cells. **C** Representative images (overlay of transmitted and epi-fluorescence) of four samples A1 - perfectly healthy, untransfected; A2 - healthy, but low efficiency; B2 - high efficiency, but cell health severely compromised; C2 - very healthy, but low efficiency.

described in section 2.2.1 except that only 5 % FBS was added to the culturing medium. To determine which transfection protocol suits ND7/23 cells best, we tested eleven variations of our standard lipofection protocol. 0.3×10^5 cells per well were seeded in a twelve well plate (3.6 cm^2 growing area) on round cover slips (poly-D-lysine coated) and transfected with different amounts of DNA, different transfection reagents and varying ratios of transfection reagent to DNA (see figure 2.1 A). One day after transfection, images were taken with an EVOS FL (Thermo Fischer Scientific, USA) fluorescence microscope to asses transfection efficiency and viability of the cells (figure 2.1 C). The cell health criterion immediately excluded samples B1, B2, B3, B4 and C4, because viability was severely impaired here already after one day of expression (figure 2.1 A). Apparently, the transfection with higher amounts of TurboFect (B1, B2, B3 and B4) was not well tolerated by the cells, while for FuGENE this effect only occurred at the highest tested amount (C4). For HEK293 cells we obtained good results with FuGENE, thus we chose to use it for ND7/23 cells as well, which excluded samples A2, A3 and A4. Thus, only samples C1, C2 and C3 where left and as C1 and C2 showed only half the transfection efficiency (figure 2.1 B) we finally decided to use mixture C3.

For experiments, more cells are seeded in petri dishes with a growth area 2.5-times the size of a twelve-well entailing that the mixture was scaled up for the actual use.

Finally, 0.5×10^5 to 0.5×10^5 cells were seeded and transfected with 250 µl medium (no FBS), 2 µg DNA and 6 µl transfection reagent similar to the protocol used for HEK293 cells.

2.3 pH measurements in *E. coli* suspension

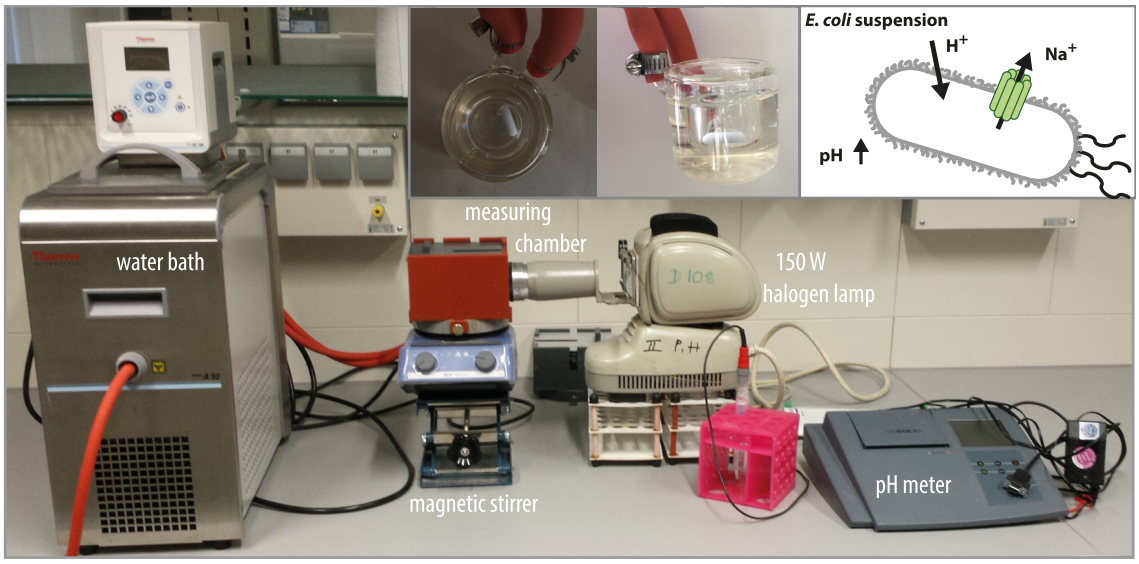

Figure 2.2: Setup for *E. coli* assay. Photograph of the setup used to asses light-induced changes of pH in solution of KR2-expressing *E.* Coli cell suspension. Insets show the temperature controlled measuring chamber (left) and a schematic representation of a bacterium expressing KR2 and the proposed way of pH change upon sodium outward-pumping (right).

KR2 (in pET-21a vector) transformation and expression in C41(DE3) chemocompetent *E. coli* cells was conducted according to protocols from Arita Silapetere adapted from Kato and colleagues[78]. First a pre-culture (4 ml medium, 100 µM ampicillin) was inoculated with transformed cells and grown at 37 °C and 180 rpm over night. Using 2 ml of the pre-culture 200 ml of medium (100 µM ampicillin) were inoculated the next day and grown at 37 °C and 180 rpm. At OD_{600}=0.6 protein expression was induced by addition of Isopropyl-β-D-thiogalactopyranosid (500 µM) and supplemented with 5 µM all-*t*rans-retinal. Cells were grown for three more hours, centrifuged down and washed once with the measuring solution containing 100 mM NaCl, KCl or choline chloride. Cells were gently resuspended in the intended measuring solution and OD_{600} was adjusted to similar values in all solutions (OD_{600} 8-9). To ensure equilibration of membrane processes in the suspension, cells were incubated for at least one hour in the respective solution (37 °C and 180 rpm) before measurements took place.

During the measurements the cell suspension was kept at 25 °C and pH was automatically monitored using a pH meter connected to a computer via a serial RS232

interface; white light illumination was provided by a 150 W halogen lamp and if indicated the protonophore carbonylcyanid-m-chlorophenylhydrazon (CCCP) was added. In all cases measurements with and without CCCP at the respective condition were done on samples from the same culture.

2.4 Imaging

2.4.1 Confocal imaging

Confocal images were taken using a FV1000 laser scanning microscope (Olympus, Japan) with a 60x/1.2 water immersion objective. If indicated, the cell membrane was labeled using octadecyl rhodamine B chloride (R18) for variants fused to a eYFP fluorophore or DiO for variants bearing an mKate2 fluorophore to minimize spectral overlap. The red dyes R18 and mKate2 were excited using a 559 nm diode laser, while a 515 nm argon laser and a 488 nm diode laser were used to excite eYFP and DiO, repectively.

A custom Fiji[182] macro (see appendix A.3) was used to extract the mean fluorescence either in the membrane area (identified by the membrane marker) or within the cell; average of three equatorial slices (0.5 µm) per cell (background subtracted). Afterwards, the membrane targeting was calculated as mean fluorescence of the membrane over mean fluorescence within the cell and then averaged for all cells.

2.4.2 pH imaging using pHluorin

To image potential local changes of the extracellular pH by putative proton pumping of KR2 the pH imaging assay originally devised by Johannes Vierock[183] was established again. Setup 1 was renewed by Jonas Wietek and equipped with a new monochromator (OptoScan, Cairn Research) and a new camera (pco.panda 4.2, pco).
All recordings were conducted in ND7/23 cells after one day of expression. The three measured constructs are displayed in figure 2.3A; with construct #2 and #3 kindly provided by Johannes Vierock. The respective ion pump was fused via a P2A ribosomal skip sequence[184] to the 105 N-terminal amino acids of the rat gastric ATPase β-subunit (UniProt: P18598) which tethered the superecliptic pHluorin (enhanced ecliptic pHluorin[185]; GenBank: AY533296.1) to the membrane. As all constructs did not contain another fluorophore besides pHluorin only residues 1-346 of eKR2 (C2C1_KR2_TS; no YFP and ER trafficking signal) were used for construct #1.

To monitor pHluorin fluorescence, images were taken at a 1 Hz frequency using 470 nm (full intensity, 7 nm bandpass, 25 % neutral density filter giving 0.22 $mW\,mm^{-2}$; 20 millis exposure time) light provided by the OptoScan for excitation (figure 2.3 B). Af-

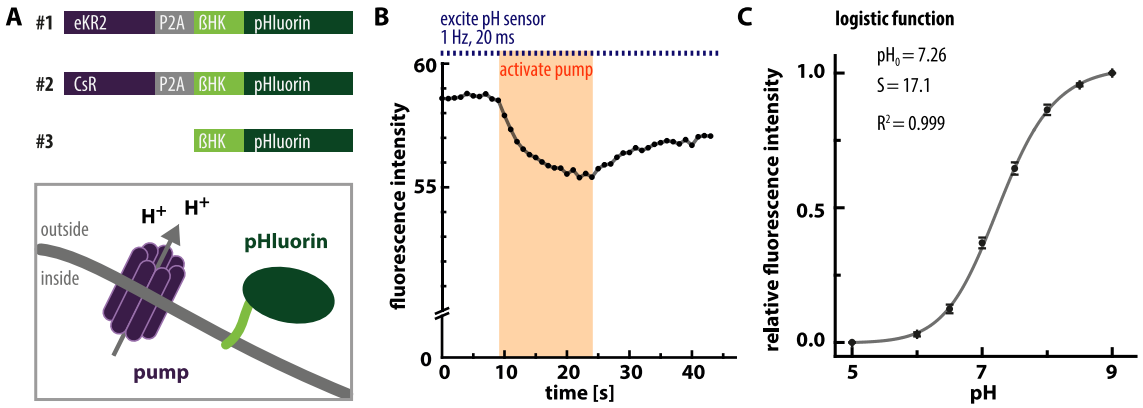

Figure 2.3: Constructs and calibration for pH imaging with superecliptic pHluorin. A Constructs used for pH imaging (top) and schematic representation of the construct in the cell membrane (bottom). **B** Representative time trace of the light-induced fluorescence changes evoked by outward proton pumping. Blue squares illustrate excitation of pHluorin fluorescence (10 Hz, 20 ms exposure time) while orange square indicates activation of the pump with 570 nm **C** Recorded pHluorin calibration curve (construct #3) to convert fluorescence intensity from B to pH changes; fitted with a logistic function (equation 2.1).

ter 10 s in the dark a second 560 nm illumination (0.66 mW mm^{-2}), provided by a xenon lamp using a bandpass filter (560 nm, FWHM 10 nm), was switched on to activate the pump for 15 s (figure 2.3 B). The new protocol allowed to pause the 560 nm activation of the pump while images were taken to avoid additional excitation of pHluorin by the 560 nm light. Both lights were combined by a 50/50 beam splitter, coupled into the epi-fluorescence port of the microscope and guided to the FLUAR 40x objective/1.3 oil (Zeiss, Germany) passing a dualband dichroic mirror (FF493/574, AHF Analysetechnik, Germany). All measurements were done at pH 7.5 in 10 mM, 1 mM, 0.1 mM HEPES in that sequence. After recording in the measuring solutions with different HEPES concentrations at pH 7.5, the fluorescence of cells was measured in the pH 5.0 and pH 9.0 calibration buffers to determine the upper and lower fluorescence boundaries for each cell, which is necessary for conversion of the fluorescence intensity into pH using the calibration curve (figure 2.3 C). The calibration curve was measured with the control construct #3 in buffered solutions of pH 5.0, 6.0 (20 mM MES), 6.5, 7.0, 7.5 (20 mM HEPES) and 8.0, 8.5, 9.0 (20 mM TRIS).

To evaluate the images a Fiji macro was written, which extracted the absolute fluorescence intensity of the cell over time (46 images) and thus determined the intensity values for the time trace (figure 2.3 B). The same region of interest was used to evaluate all recordings of the same cell. Time traces were baseline corrected by fitting the first ten points in the dark linearly and correcting for that decay, although bleaching was usually smaller than 1 %. A light dark difference was calculated by subtracting the average of the last three values in the light from the last three in the dark. To convert the observed

intensity changes to absolute pH values, the measured calibration curve was fitted with a logistic function (2.1), which yields the midpoint pH value and the steepness of the curve under the given conditions, while I_{low} and I_{high} were determined for each cell individually.

$$I = I_{high} + \frac{I_{low} - I_{high}}{1 + \left(\frac{pH}{pH_0}\right)^S} \tag{2.1}$$

with pH_0 - midpoint, I_{low} - intensity at lowest pH, I_{low} - intensity at highest pH, S - steepness of the curve.

Buffered solutions contained [mM]: 110 NaCl, 1 KCl, 2 $MgCl_2$, 2 $CaCl_2$, 1 CsCl and 10 mM, 1 mM, 0.1 mM HEPES for measuring and 20 mM MES (pH 5.0, 6.0), HEPES (pH 6.5, 7.0, 7.5) or TRIS (pH 8.0, 8.5, 9.0) for calibration. Osmolarity was adjusted to 310 mOsm using glucose.

2.5 Whole-cell patch-clamp recordings on cultured cells

All patch-clamp measurements conducted for this thesis were recorded in the whole-cell mode[186] either from HEK293 or ND7/23 cells or cultured hippocampal mouse neurons. For the immortalized cell lines, measurements took place 30 h to 50 h after transient transfection (see section 2.2). Primary cultures of hippocampal neurons were infected at one day *in vitro* (DIV) and recordings took place between 12 DIV to 15 DIV.

For HEK cells standard conditions were (ReaChR) (in [mM]): extracellular 140 NaCl, 1 KCl, 2 $MgCl_2$, 2 $CaCl_2$, 1 CsCl and 10 HEPES, pH 7.2 and intracellular 110 NaCl, 1 KCl, 2 $MgCl_2$, 2 $CaCl_2$, 1 CsCl, 10 EGTA and 10 HEPES, pH 7.2. For the KR2 measurements (ND7/23 cells) the extracellular standard buffer only contained 110 mM NaCl to have one condition (0 mV) without any electrochemical gradient. After establishment of the patch and before recording started, at least two minutes passed to ensure replacement of the cytosol by the intracellular buffer. For measurements with ReaChR, all cells were additionally illuminated with 530 nm (2 s) followed by at least 1 min in the dark to start each measurement from a similar dark-adapted state. If indicated, extracellular buffers were exchanged, all buffer compositions can be found in table 2.4.

2.5.1 Preparative procedures prior to measurements

Silver chloride electrodes For the two electrodes silver wire with different diameters was used (bath 0.64 mm; pipette 0.25 mm). To minimize offset potentials the silver was covered with an AgCl layer prior to measurements. If pipette and bath solution contain

Cl^-, this AgCl layer enables reversible electron flow according to:

$$Ag + Cl^- \leftrightarrow AgCl + e^-. \tag{2.2}$$

To obtain an AgCl layer, the wire was cleaned, connected to the positive pole of a voltage source (direct current), and dipped into a 3 M KCl solution with the reference electrode. When a voltage was applied, a current flew and a layer of AgCl deposited on the wire. To obtain a uniform AgCl layer a voltage of about 1 V was applied for 25 min.
To work properly the AgCl layer has to be intact and not oxidized. To guarantee that, it was renewed every two weeks or earlier in case the layer was apparently scratched.

Agar bridges To ensure a constant concentration of Cl^- near the bath electrode, an agar bridge was used to connect bath electrode and bath solution. They were made filling pipette tips with a 140 mM NaCl solution containing 1.5 % agar, and put over the bath electrode during measurements.

Micropipettes for electrophysiological measurements were made of standard wall (outer diameter 1.5 mm, inner diameter 0.86 mm) glass capillaries with filament (Warner Instruments, USA) using a horizontal micropipette puller (P-1000, Sutter Instrument, USA). After pulling, the shape of the pipettes was checked using a microscope, and they were fire polished with a microforge. Usually, the resistance of the pipettes ranged between 1.8 MΩ to 4 MΩ.

2.5.2 Voltage-clamp measuring protocols and data evaluation

Electrophysiology data was evaluated with Clampex 10.4.036 (Molecular Devices, USA), StimFit0.14[187] using custom python scripts (see A.3) using numpy and scipy[188], R software for statistics[189], Microsoft Excel 2013 (Microsoft Corporation), MATLAB (The MathWorks, Inc.) and Origin9.0 (OriginLab Corporation). Figures were composed using Adobe Illustrator 2015 (Adobe Systems Inc.).

Current-voltage relation and kinetics Microbial rhodopsins were excited at their maximal spectral sensitivity and the holding potential was varied from negative to positive voltages in 20 mV steps; a sufficient delay was included between the sweeps to ensure recovery of the protein prior to the next activation. After establishment of the whole-cell configuration at least two minutes passed before the measurement to guarantee replacement of the cytosol with the intracellular buffer. ReaChR recordings were filtered with a 2 kHz bessel filter at the amplifier and digitized at 10 kHz; eKR2 recordings were fil-

tered with a 5 kHz bessel filter at the amplifier and digitized at 20 kHz. To exchange the external buffered solution, it was either replaced manually (at least five times) with 1 ml of the new buffer (recordings on ReachR, setup 1) or superfused automatically (eKR2 measurements, setup 2) with at least 5 ml.

Peak and stationary photocurrents were determined relative to the current before illumination as the highest current during illumination or averaged over the last 20 ms of illumination, respectively.

If necessary (as indicated), liquid junction potentials (LJP) were calculated using Clampex software and corrected after the recordings (see section 2.5.4) before generation of the current-voltage plot.

From the current voltage-relation reversal potentials were calculated by linear interpolation between the two neighboring data points or, if reversal potentials were beyond the measuring range, by linear extrapolation from the two closest data points. Using the reversal potentials (E_{rev}) the Goldman-Hodgkin-Katz voltage equation (GHK):

$$E_{rev} = \frac{R \cdot T}{F} \cdot \ln\left(\frac{P_K[K]_e + P_{Na}[Na]_e + P_{Cl}[Cl]_e}{P_K[K]_i + P_{Na}[Na]_i + P_{Cl}[Cl]_i}\right) \tag{2.3}$$

allows the calculation of permeability ratios at a known ionic condition. In the GHK P_x denotes the permeability for ion x, while $[\mathrm{x}]_{\mathrm{i/e}}$ describes the intra- and extracellular concentration of ion x. Assuming that protons and monovalent ions are conducted it can give the permeability ratio of H^+ over Na^+:

$$\frac{P_H}{P_{Na}} = \frac{[Na]_e - \left(e^{\frac{z \cdot F}{R \cdot T} \cdot E_{rev}} \cdot [Na]_i\right)}{\left(e^{\frac{z \cdot F}{R \cdot T} \cdot E_{rev}} \cdot [H]_i\right) - [H]_e} \tag{2.4}$$

Inactivation kinetics and off-kinetics were determined by fitting the respective current decay with an exponential function using ClampFit. If two exponential components were needed for fitting, apparent time constants were calculated by averaging both time constants weighted by their amplitude:

$$\tau_{app} = \frac{A_1 \cdot \tau_1 + A_2 \cdot \tau_2}{A_1 + A_2} \tag{2.5}$$

Spectral sensitivity Action spectra were measured using a monochromator (Polychrome V 100 % intensity) as light source either at setup 1 (ReaChR) or setup 3 (eKR2) enabling to probe the photocurrent every 10 nm with a spectral resolution of 7 nm FHMW. For all measurements an automated neutral density filter wheel was used to adjust the pho-

ton flux to an equal count over the whole measured wavelength range. Spectra were either recorded using short 10 ms pulses to probe the dark state or with longer pulses of 300 ms to 1000 ms to obtain stationary action spectra. For flash-induced spectra of ReaChR, a neutral density filter was used to decrease intensity and resultant data points were corrected for the wavelength dependent transmission of the filter. If not indicated otherwise, resulting currents were normalized to the respective maximal value and if fitted a three-parametric Weibull function was used to determine the maximum:

$$I(\lambda) = I_0 + A\left(\frac{c-1}{c}\right)^{\frac{1-c}{c}}\left[\frac{\lambda-\lambda_{max}}{b}+\left(\frac{c-1}{c}\right)^{\frac{1}{c}}\right]^{c-1} e^{-\left[\frac{\lambda-\lambda_{max}}{b}+\left(\frac{c-1}{c}\right)^{\frac{1}{c}}\right]^{c}+\frac{c-1}{c}} \tag{2.6}$$

with I_0 - offset, A - amplitude, λ_{max} - wavelength at maximum, b/c - parameters of the function. Individual measurements were fitted independently and afterwards the average maximum and its standard deviation were calculated using Origin9.0.

Inactivation spectrum Inactivation spectra were recorded at setup 1 for ReaChR at standard conditions (see page 29) and a holding potential of −60 mV. The low intensity background illumination was provided by the Xenon lamp (528 nm bandpass and 50 % neutral density filter) and the secondary pulses (1 s) were provided by the Polychrome V operating at maximal intensity and 15 nm bandwidth; the neutral density filter wheel was used to adjust the photon flux of the secondary light pulses. Both light sources were combined by a 70/30 beam splitter and guided into the microscope. The green background illumination was switched on first and when the current inactivated to the stationary level the secondary pulses of varying wavelength (1 s) were additionally applied either individually or ranging from 380 nm to 670 nm.

Light titration Titrations of the photocurrents with the actinic light were recorded for ReaChR (setup1, Polychrome V) and eKR2 (setup2, Cool LED) under standard conditions (see page 29) at −60 mV and 0 mV, respectively. Using the Polychrome V operating at 100 %, 7 nm (ReaChR), light intensities were adjusted using neutral density filters inserted into the light path. For titration of eKR2 photocurrents, a combination of reducing the intensity of the LED (525 nm, FWHM 31 nm) and insertion of neutral density filters was used. In all cases absolute intensities were measured in the focal plane of the respective objective using the Optometer P9710 (Gigahertz Optik, Germany) and photon fluxes were calculated from that intensity using the illuminated area[c] (see table 2.6).

[c] The diameter of the circular spot was determined using a stage micrometer and the area was calculated from that.

Laser-induced single turnover measurements of the photocurrent The single turnover measurements were performed for eKR2 at setup 3. The laser was tuned to 525 nm operating at 100 % intensity with the attenuator set to 7 reducing the intensity to 6.6 µW per pulse which equals 1.8×10^{13} photons. To reach the highest possible time resolution series resistance was compensated up to 90 % (as detailed here[181]) for the laser measurements. All recordings were performed at symmetric buffer conditions to reduce LJPs and to improve comparability to spectroscopic measurements on the purified protein. During each measurement the holding potential was stepwise increased from −30 mV to 30 mV in 30 mV steps (see figure 2.4A), while the protein was kept in the dark for 1 s prior to the next sweep. The recording was repeated four times for each cell to increase signal to noise ratio. Resulting raw data was binned (averaging in the time domain) using a custom MATLAB script (written together with Jonas Wietek, see A.3) to have an equal number of data points (mostly 50) in each range of the time domain. After binning, the four recordings from the same cell were averaged further increasing the signal to noise ratio. Using Origin9.0 the binned and averaged (but non-normalized) data for each cell were fitted individually. Only the decay of the currents was fitted with a tri-exponential function starting the fit in the maximal amplitude (see figure 2.4B). Panel C of figure 2.4 illustrates that a bi-exponential function is not sufficient to fit the current decay. The used tri-exponential function is described by:

$$I = A_1 \cdot e^{-\frac{t}{\tau_1}} + A_2 \cdot e^{-\frac{t}{\tau_2}} + A_3 \cdot e^{-\frac{t}{\tau_3}} + I_0 \tag{2.7}$$

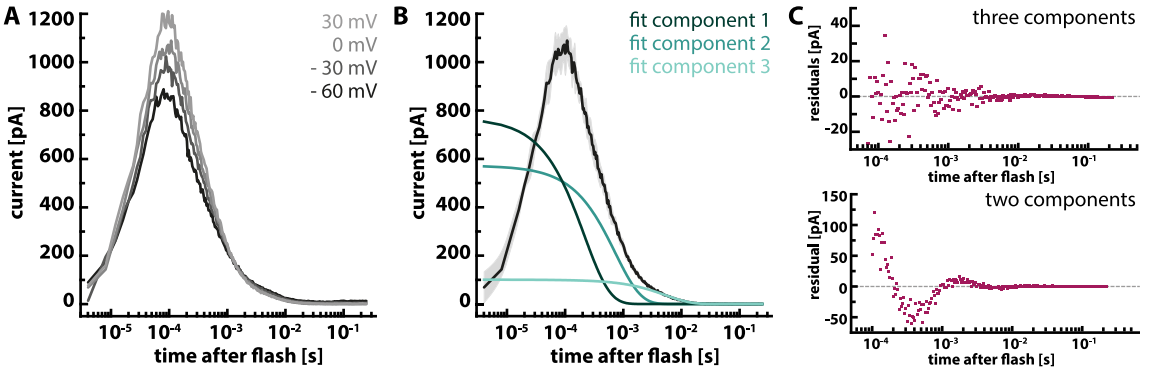

Figure 2.4: Evaluation of single turnover measurements. **A** Representative traces for laser-induced currents of eKR2 at different holding potentials varied in 30 mV steps from −30 mV to 30 mV at standard conditions; 110 mM $[Na^+]_{i/e}$, $pH_{i/e}$ 7.2. **B** Current trace at 0 mV holding potential with respective components of the tri-exponential fit of the current decay plotted onto the trace. **C** Residuals of the tri-exponential fit (top) displayed in B showing small and random scattering around zero in contrast to the residuals resulting from a bi-exponential fit of the same data (bottom) with large amplitude and non-random scattering implying the existence of more than two components.

With A - amplitude and τ - kinetic constant of the respective component, I - current and I_0 current offset, which was usually below 5 pA. Afterwards values resulting from the individual fits (each cell) like time constants or amplitudes were averaged. For display purposes individual recordings were normalized to the maximal amplitude of the current prior to averaging (figure 3.24). The integration of the individual fit components to access the area under the curve of the respective component was done on the non-normalized data using Origin9.0 and starting from the same time point as the exponential fit. Thus, it slightly varied within the cells (3.6×10^{-5} s to 1×10^{-4} s), but was kept the same for individual measurements on the same cell at different holding potentials.

2.5.3 Current-clamp recordings on cultured hippocampal neurons

The current-clamp recordings on cultured hippocampal mouse neurons infected with eKR2 (4.4×10^9 vector genome copies of adeno-associated virus, Viral core facility, Charite Berlin) were done under the supervision and together with Yinth Andrea Bernal Sierra and are described here[190]. The main components of the setup are listed in table 2.6. Measurements were performed in the whole-cell mode at room temperature (25 °C) after compensation of series resistance and pipette capacitance using the built-in circuits (bridge balance and capacitance neutralization) of the amplifier. Activation light was provided by a collimated 540 nm LED (Mightex, LCS-0540-14) coupled into the epifluorescence port of an inverted Olympus IX-73 microscope giving a maximum light intensity of 9.76 mW mm^{-2} in the focal plane. Standard solutions were [mM]: intracellular 17.8 HEPES, 135 KGluc, 4.6 $MgCl_2$, 4 MgATP, 0.3 NaGTP, 1 EGTA, 12 Na_2Phosphocreatine, and 50 phosphocreatine kinase, pH 7.3 and extracellular: 10 HEPES, 140 NaCl, 2.4 KCl, 2 CaCl2, 4 MgCl2, and 10 glucose, pH 7.4. The extracellular buffer also contained the synaptic transmission blockers NBQX (10 µM), Picrotoxin (100 µM), and CCPene (10 µM). The LJP (see section 2.5.4) was calculated using Clampex to be 17.2 mV and corrected post-recording if indicated.

2.5.4 Buffered solutions and junction potential correction

Table 2.4 summarizes electrophysiological buffers for recordings with ND7/23 cells expressing eKR2. For measurements with ReaChR (HEK293), the buffers were similar except that the extracellular solution contained 140 mM NaCl instead of 110 mM. Standard buffers for measurements on eKR2 expressing cells contained 110 mM NaCl and were adjusted to pH 7.2 (first column table 2.4) to have one condition without an electrochemical gradient (0 mV, symmetric buffers) for the pump. For ReaChR extracellular standard buffer contained 140 mM NaCl.

Table 2.4: Electrophysiology buffers used for recordings from ND7/23 cells expressing eKR2. pH values were adjusted using N-methyl-D-glucamine (NMG^+) and citric acid, while osmolarity was adjusted to 290 mM intracellularly and 320 mM extracellularly using glucose. All concentrations are given in mM and the first column contains the standard condition buffers.

intra KR2	**110 Na^+ pH 7.2**	**1 Na^+ pH 7.2**	**0.1 Na^+ pH 7.2**	**110 Na^+ pH 9.0**	**1 Na^+ pH 9.0**	**0.1 Na^+ pH 9.0**	**1 Na^+ pH 6.0**	**110 K^+ pH 7.2**
NaCl	110	1	0.1	110	1	0.1	1	1
KCl	1	1	1	1	1	1	1	110
$MgCl_2$	2	2	2	2	2	2	2	2
$CaCl_2$	2	2	2	2	2	2	2	2
CsCl	1	1	1	1	1	1	1	1
HCl	0	110	110	0	110	110	110	0
EGTA	10	10	10	10	10	10	10	10
HEPES	10	10	10	0	0	0	0	10
TRIS	0	0	0	10	10	10	0	0
MES	0	0	0	0	0	0	10	0
extra KR2	**110 Na^+ pH 7.2**	**1 Na^+ pH 7.2**	**110 Na^+ pH 9.0**	**1 Na^+ pH 9.0**	**110 Na^+ pH 5.0**	**1 Na^+ pH 5.0**	**110 K^+ pH 7.2**	**110 K^+ pH 9.0**
NaCl	110	1	110	1	110	1	1	1
KCl	1	1	1	1	1	1	110	110
$MgCl_2$	2	2	2	2	2	2	2	2
$CaCl_2$	2	2	2	2	2	2	2	2
CsCl	1	1	1	1	1	1	1	1
HCl	0	110	0	110	0	110	0	0
HEPES	10	10	0	0	0	0	10	0
TRIS	0	0	10	10	0	0	0	10
Citric acid	0	0	0	0	5	5	0	0

Table 2.5: Calculated LJPs (ClampFit software, Molecular Devices) for the used buffers (see table 2.4), corrected after measuring by using equation 2.8. Rows denote intracellular buffers while columns indicate combined extracellular solution. Upper part lists E_{init} for combinations of intra- and extracellular buffers without buffer change, while bottom part lists $E_{\text{init}}+E_{\text{ch}}$ for selectivity measurements when extracellular buffers were changed with the first and sixth column representing the starting condition at which the patch was established for KR2 and ReaChR, respectively. Numbers in names denote concentration of the indicated cation in mM.

	KR2						**ReaChR**			
E_{init} [mV] no change	**110 Na^+ pH 7.2**	**1 Na^+/K^+ pH 7.2**								
110 Na^+, pH 7.2	0.3	5.4								
1 Na^+/K^+, pH 7.2	-4.9	0.2								
0.1 Na^+, pH 7.2	-4.8	0.4								
1 Na^+/K^+, pH 9.0	-3.4	1.8								
1 Na^+/K^+, pH 6.0	-5.4	-0.3								
110 K^+, pH 7.2	4.0	-								
$E_{\text{init}}+E_{\text{ch}}$ [mV] extra. change	**110 Na^+ pH 7.2**	**1 Na^+/K^+ pH 7.2**	**110 Na^+ pH 9.0**	**1 Na^+/K^+ pH 9.0**	**1 Na^+/K^+ pH 5.0**	**110 Na^+ pH 5.0**	**140 Na^+ pH 7.2**	**1 Na^+ pH 7.2**	**140 Na^+ pH 9.0**	**1 Na^+ pH 9.0**
110 Na^+, pH 7.2	0.3	5.2	-0.4	-	-	-	0.6	5.7	-0.1	2.1
1 Na^+/K^+, pH 7.2	-4.9	0	-5.6	-	0.1	-4.5	-	-	-	-
110 Na^+, pH 9.0	0.9	5.6	0.1	4.7	5.3	-	-	-	-	-
1 Na^+/K^+, pH 9.0	-3.1	1.6	-3.9	0.7	1.3	-	-	-	-	-

LJP corrections were conducted for all eKR2 recordings and for the selectivity measurements on ReaChR. At standard conditions (almost symmetrical) LJPs are small (< 1 mV). The junction potentials were calculated using Clampex software (Molecular Devices, USA) according to[191] for a temperature of 23 °C and a 140 mM NaCl agar bridge, which is connecting the reference electrode to the bath solution. After recordings the holding

potential (E_{hold}) set during the measurement was corrected with the LJP according to:

$$E_{mem} = E_{hold} - (E_{init} + E_{ch}) \tag{2.8}$$

to give the membrane potential E_{mem} with E_{hold} - set holding potential, E_{init} - potential between first buffer pair and E_{ch} - potential between buffers after exchange of extracellular buffer. When the first measuring condition is symmetric, E_{init} is usually below 1 mV. The LJP for the buffers used in this thesis are given in table 2.5. If LJP were corrected, determined values like photocurrents or kinetic constants were linearly interpolated to the indicated voltage (*e.g.* −60 mV or 0 mV).

2.5.5 Statistics

All data in this thesis is presented as mean±standard deviation (SD) or mean±standard error of the mean (SEM) as indicated. All fits were performed for the individual measurements and afterwards values were averaged. Statistical tests (as indicated) were conducted in R (version 3.3.2) or Origin9.0 either performing a Wilcoxon Rank Sum or an unpaired two sample t-test. Significance levels were set to * $0.01 < p < 0.05$, ** $0.001 < p < 0.01$, *** $p < 0.001$ and ns - not significant.

2.5.6 The used patch-clamp setups

Four different patch-clamp setups were used and an overview of their main components with the respective supplier is given in table 2.6. Fundamentally, they were all built similarly, which is exemplified for setup 3 in figure 2.5 (modified[181]).

Table 2.6: Main devices at the four electrophysiological setups used during this thesis including respective illuminated areas in the focal plane and the respective manufacturer

	poly setup 1	**LED setup 2**	**laser setup 3**	**neuro setup 4**
light source	polychrome V, 75 W xenon lamp (Till Photonics, LOT-QuantumDesign)	CoolLED (CoolLED)	Polychrome V, laser, 150 W xenon lamp (Till Photonics, OPOTEC, LOT-QuantumDesign)	LEDs (Mightex)
objective	FLUAR 40x/1.3 (Carl Zeiss)	plan apochromat 40x/1.0 (Carl Zeiss)	plan apochromat 40x/1.0 (Carl Zeiss)	LUCPLFLN 60x/0.7 (Olympus)
illum. area	0.080 mm^2	0.035 mm^2	0.066 mm^2	0.102 mm^2
ND filter wheel	yes (Newport)	no	yes (Newport)	no
amplifier	AxoPatch 200 B (Molecular Devices)	ELC-03XS (npi electronics)	AxoPatch 200B (Molecular Devices)	AxoPatch 700B (Molecular Devices)
D/A converter	DigiData 1440A (Molecular Devices)	DigaData 1440A (Molecular Devices)	DigiData 1440A (Molecular Devices)	DigiData 1500 (Molecular Devices)
shutter	Uniblitz VS25 (Vincent Associates)	none	Uniblitz VS25 (Vincent Associates)	none
microscope	IX-70 (Olympus)	Axiovert 100 (Carl Zeiss)	Axiovert 100 (Carl Zeiss)	IX-73 (Olympus)
solution exchange	manually	Ringer bath handler (Lorenz Messgerätebau)	Ringer bath handler (Lorenz Messgerätebau)	none

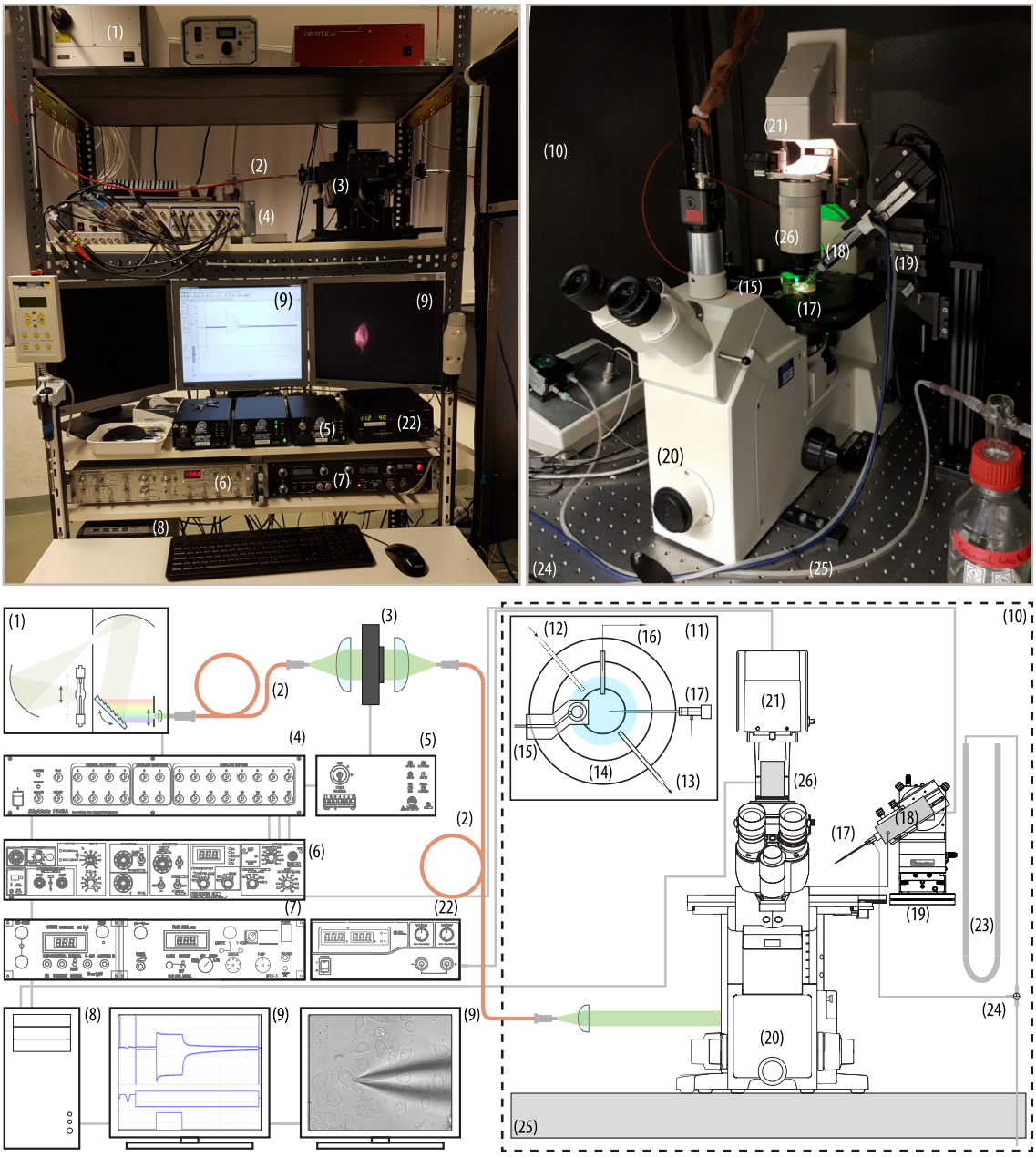

Figure 2.5: Patch-clamp setup. Photographs (top) and schematic representation of setup 3 with its components (bottom). The labeled items constitute all setup components in the photographs as well as the schemes and refer to (1) Light source (here Polychrome V), (2) optic fiber, (3) programmable shutter, (4) digitizer, (5) shutter driver, (6) amplifier, (7) perfusion system, (8) personal computer, (9) monitor, (10) faraday cage, (11) microscope stage, (12) perfusion inlet, (13) perfusion outlet, (14) recording chamber, (15) fluid level sensor, (16) bath electrode with agar bridge, (17) pipette holder, (18) headstage, (19) micromanipulator, (20) inverted microscope, (21) microscope lamp housing, (22) microscope lamp power supply, (23) water-filled U-tube , (24) three-way valve, (25) anti-vibration table, (26) CCD camera. Taken from [181]

3 Results

3.1 The red-light activatable channelrhodopsin ReaChR

When the chimeric ReaChR was published in 2013[150], it was the most red-shifted ChR together with the closely related chimera C1V1[117,147], which was reported earlier. In the neurosciences and to enhance versatility, red-light activated ChRs were a long sought goal after the emergence of the blue-light activated *Cr*ChR2 in 2002[37]. Both C1V1 and ReaChR are chimeric derivatives of *Vc*ChR1, which has a red-shifted activation maximum compared to *Cr*ChR2 but smaller photocurrents[147]. The overall helix architecture of both chimeras is similar with only small differences (figure 3.1). While ReaChR comprises only the N-terminus and parts of TM1 of *Cr*ChR1 for enhanced membrane targeting, C1V1 contains the whole TM1 and TM2 of *Cr*ChR1. Additionally, ReaChR has the L171I mutation (ChIEF position[100]) and TM6 of *Vc*ChR2, which only differs in five residues from TM6 of *Vc*ChR1 (figure 3.1 alignment). Both chimeras retained the red-shifted activation of the parental *Vc*ChR1 while showing drastically enhanced membrane targeting and higher photocurrent amplitudes[147,150]. However, Lin and colleagues claimed that ReaChR according to their head to head comparison has enhanced membrane targeting, higher currents and faster closing kinetics than C1V1 and C1V1 E122T[150], which were widely used before (see section 1.1.2).

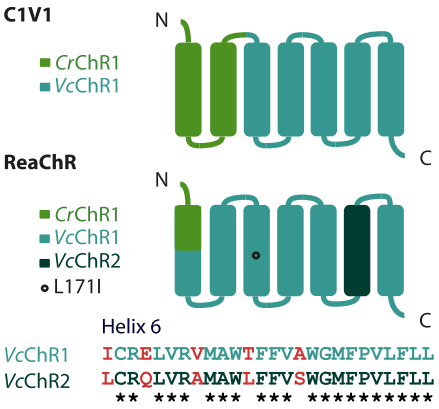

Figure 3.1: Helix architecture of ReaChR and C1V1. Comparison of helix composition of C1V1 and ReaChR with sequence alignment of TM6.

3.1.1 Spectral and light sensitivity of ReaChR

ReaChR was published with an unusual action spectrum[150], which was very broad in comparison to that of other ChRs and did not show a Gaussian shape as expected for a rhodopsin. Hence, the spectral sensitivity of ReaChR should be re-investigated. First, ac-

tion spectra were recorded with short (10 ms), low intensity light pulses to probe the dark state (see figure 3.2 A, top). This flash action spectrum peaked upon green-light activation at 531 ± 2 nm, exhibited a Gaussian shape and resembled the absorption spectrum of purified ReaChR (courtesy B. Krause, detergent pH 7.4) without any peculiarities (figure 3.2 B). However, when the action spectrum was measured with longer light pulses (1 s, see figure 3.2 A, bottom), the shape significantly deviated from a Gaussian shape as seen in figure 3.2 C. This stationary spectrum broadened and the maximal current was now observed upon orange illumination around 610 nm similar as described by Lin and co-workers[150]. Moreover, another interesting feature occurred, which was not reported by Lin and colleagues. In contrast to the flash spectrum[a], the stationary spectrum was dependent on the direction of measurement. It was broad regardless whether it was measured starting from longer (reverse direction) or from shorter wavelengths (forward direction), but the high currents upon orange illumination only occurred if it was measured reversely. In the forward measuring direction no real peak was observed and the currents were highest below 450 nm (figure 3.2 C).

When the stationary reverse spectrum was recorded at lower light intensities (50 %, 5 % and 1 %), its shape was considerably different than at full intensity as seen in figure 3.2 D. The unusual broad spectrum peaking around 600 nm only occurred at full[b] and 50 % light intensity, whereas at lower light doses currents peaked around 550 nm more similar to the flash action spectrum (*cf.* figure 3.2 D and B). Notably, the absolute stationary currents evoked with green light where highest at 5 % light intensity and decreased again at higher light doses (figure 3.2 D), which hints at a light-induced inactivation of green-light evoked photocurrents at higher light intensities. Additionally, panel E of figure 3.2 shows the non-normalized stationary action spectra in forward (left, squares) and reverse (right, circles) direction at 1 %, 10 % and 100 % light intensity measured from the same cell. They illustrate again the transition from the low to the high intensity spectrum and the influence of the measuring direction. Moreover, they emphasize that the highest absolute photocurrents were recorded upon orange-light activation in the reverse direction, which is harder to deduce from the normalized spectra.

Both for *Cr*ChR1 and for *Vc*ChR1, a dependence of the retinal absorption on the ambient pH was demonstrated[93,102] by either recording action spectra or absorption spectra of the purified protein. Thus, it was reasonable that for ReaChR such a pH dependence might exist as well. Hence, action spectra at different external pH_e values were recorded. Indeed the flash-induced action spectrum was on average 22 nm blue-shifted when pH_e

[a] The reverse flash spectrum is not shown here.

[b] Photon density is equal at all wavelengths and at 530 nm 100 % light intensity corresponds to 1.7 mW mm^{-2} s^{-1} or 1.6×10^{15} photons mm^{-2} s^{-1}. The same intensities are used in figure 3.4.

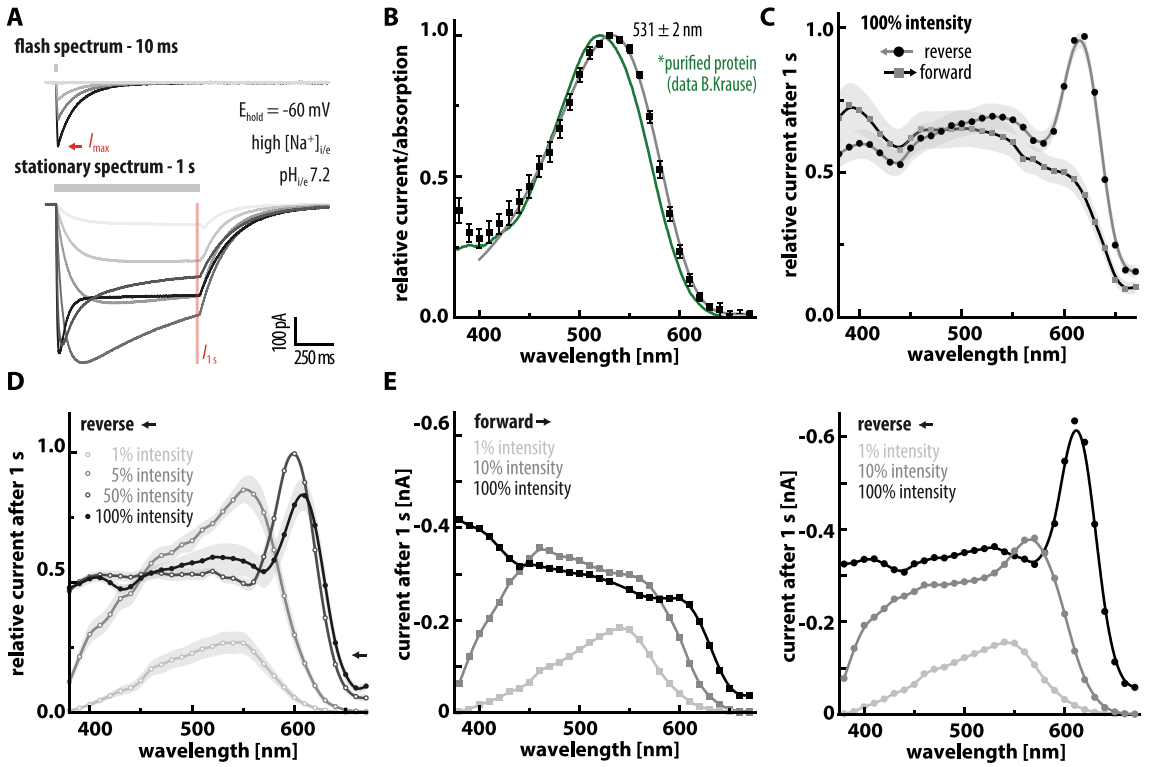

Figure 3.2: Spectral sensitivity of ReaChR. A Sample traces illustrating two ways of measuring action spectra in HEK293 cells with the currents either induced by 10 ms light pulses (top) or prolonged pulses of 1 s (bottom). Flash action spectra are fitted with a parametric Weibull function, while the stationary spectra are not fitted. All spectra are measured at standard conditions (see page 29) and E_{hold}=−60 mV. **B** Flash action spectrum at $pH_{i/e}$ 7.2 (mean±SEM, n=12) compared to the absorption spectrum of the purified protein (detergent pH 7.4, courtesy B.Krause) **C** Stationary action spectrum measured from 380 nm to 670 nm (forward, squares) and from 670 nm to 380 nm (reverse, circles). Data represented as mean±SEM (n=6) and normalized to highest current of respective cell with forward and reverse spectrum measured from the same cell, respectively. Photon density is equal at all wavelengths and at 530 nm 100 % light intensity corresponds to 1.7 mW mm^{-2} s^{-1} or 1.6 × 10^{15} photons mm^{-2} s^{-1} **D** Stationary reverse action spectra measured at 1 %, 5 %, 50 % and 100 % intensity activation light from the same cell respectively. Spectra normalized to the highest current of respective cell and presented as mean±SEM, n=6, n=6, n=6 and n=5. **E** Action spectra of absolute stationary currents at 1 %, 10 % and 100 % measured in forward and reverse direction from same cell.

was elevated to 9.0 and experienced a bathochromic shift of 9 nm at pH_e 5.0 as illustrated in figure 3.3 A. Also the stationary reverse action spectrum peaked at slightly different wavelengths upon variation of pH_e with the most red-shifted maximum at pH_e 5.0. The shape of the spectrum changed as well at different pH_e with different ratios of the highest current to the green-light evoked I_s (figure 3.3 B). This implied that the inactivation of the photocurrents evoked with green light occuring at high light intensities (*cf.* figure 3.2 D) was additionally dependent on the external pH_e. This phenomenon was even more complex as the current ratio I_{600}/I_{530} was highest at pH_e 5.0 and lowest at pH_e 7.2 with the value at pH_e 9.0 in between. Comparing the spectra qualitatively it is evident that they were similar at pH_e 5.0 and pH_e 7.2 but different at pH_e 9.0 with higher photocur-

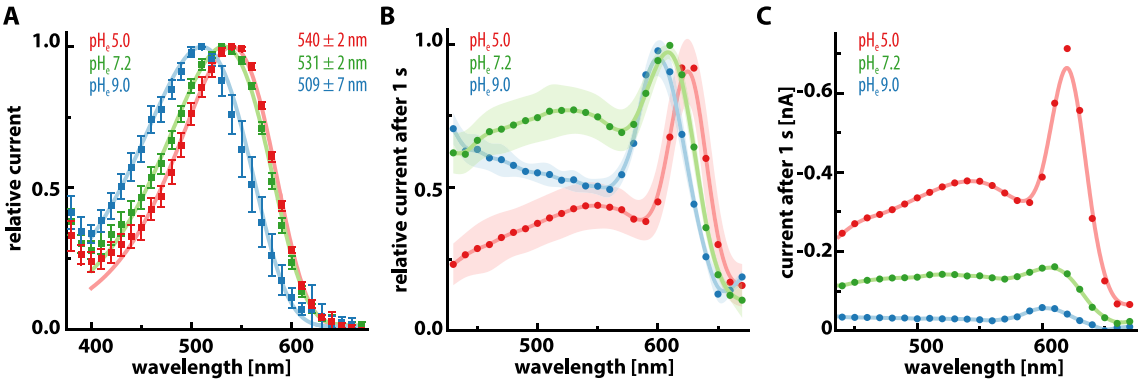

Figure 3.3: Spectral sensitivity of ReaChR at different extracellular pH$_e$ values. Action spectra recorded from HEK293 cells at pH$_i$ 7.2 and high $[Na^+]_{i/e}$ (pH$_e$ as indicated) at E_{hold}=−60 mV, normalized to maximal value and represented as mean±SEM. **A** Flash action spectra at pH$_e$ 5.0 (red), 7.2 (green) and 9.0 (blue). Represented as mean±SEM, n=7, n=12, n=8. **B** Stationary reverse action spectra at pH$_e$ 5.0, 7.2 and 9.0. Represented as mean±SEM, n=4, n=9, n=6 **C** Absolute currents of stationary action spectra presented in panel B from the same cell at different pH$_e$ as indicated.

rents below 450 nm (figure 3.3 B). Moreover, interpretation is complicated, because the photocurrent size rose strongly with the H^+-gradient as seen from the absolute stationary spectra at different pH$_e$ shown for the same cell in figure 3.3 C. To uncouple spectral properties from selectivity changes of the protein this recording should be repeated at symmetric conditions to isolate spectral changes from the influence of the H^+-gradient.

The flash action spectra of ReaChR demonstrated that it can be activated efficiently with green light but stationary photocurrents are highest upon activation with orange light. Hence, activation of ReaChR with 530 nm and 600 nm was directly compared with each other. For that, the photocurrents evoked with green (530 nm) and orange light (600 nm) were titrated with the intensity of the actinic light. For both activation wavelengths, the shape of the photocurrent trace - peak amplitude, time to peak, inactivation- strongly depended on the light intensity as seen in figure 3.4 A and B (upper row).

For activation with 530 nm, peak currents were half maximal already at a photon count of 2.7×10^{13} mm^{-2} s^{-1} (0.01 mW mm^{-2}) while I_{50} for I_s was at 0.005 mW mm^{-2} (figure 3.4 A, bottom). In contrast, activation with orange light using 600 nm was less efficient and I_p was half maximal only at 1.3×10^{14} mm^{-2} s^{-1} (0.04 mW mm^{-2}, figure 3.4 B, bottom), which is a four-times higher intensity than with 530 nm and in agreement with the reduced absorption coefficient at 600 nm already indicated in the flash action spectra (*cf.* figure 3.2 B and 3.4 A). I_p saturated at 100 % light intensity for both activation wavelengths, whereas the late current after 1 s underwent a significant reduction at higher light intensities. This inactivation at high intensities was more pronounced upon green-light activation, such that I_s was maximal already at 5 % intensity (similar to the stationary action spectra in figure 3.2 D) and decreased to 60 % of that amplitude at in-

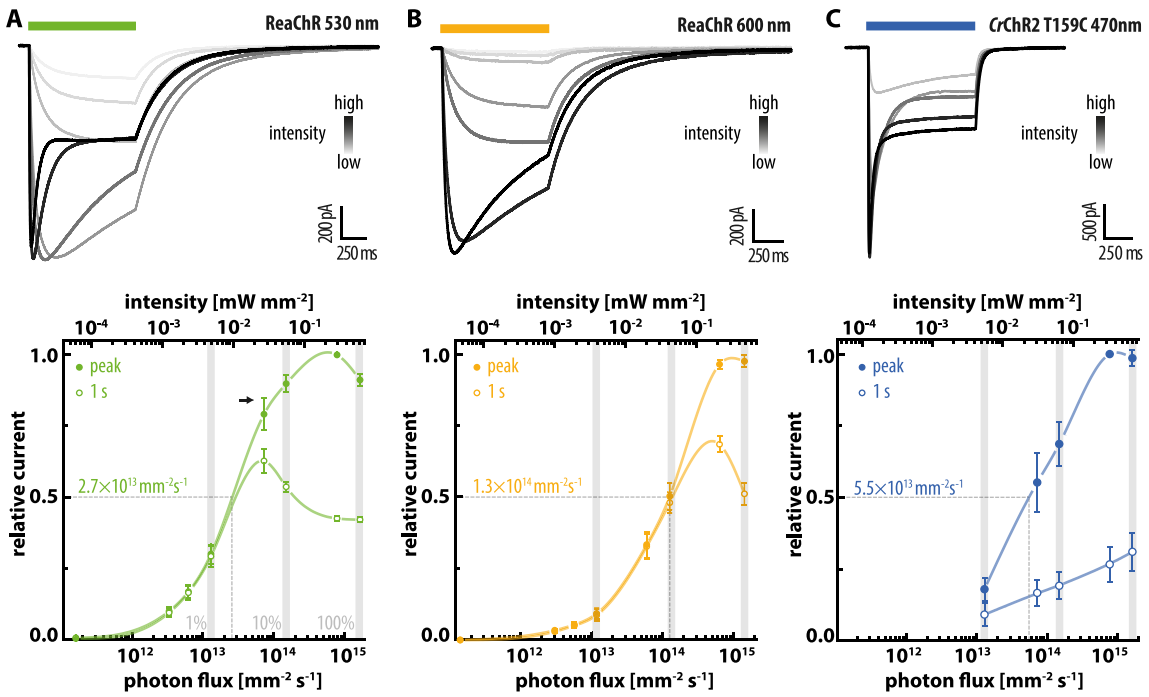

Figure 3.4: Light sensitivity at different activation wavelengths. Titration of photocurrents with the actinic light for ReaChR and *Cr*ChR2 T159C at standard conditions in HEK293 cells with the maximal intensities at all wavelength having equal photon flux. The filled and open circles correspond to the peak and the photocurrent at 1 s normalized to the maximal current, respectively; E_{hold} −60 mV. **A** Light titration for ReaChR using 530 nm activation light with photon counts ranging from 1.6×10^{11} mm^{-2} s^{-1} to 1.6×10^{15} mm^{-2} s^{-1}; mean±SEM and n=6. The line is visual guidance and no fit, but half-maximal light dose results from logistic fit. **B** Light titration curve for ReaChR using 600 nm activation light with photon counts ranging from 1.4×10^{11} mm^{-2} s^{-1} to 1.4×10^{15} mm^{-2} s^{-1}; mean±SEM, n = 6 and half-maximal light dose resulting from a logistic fit. **C** Light titration curve for *Cr*ChR2 T159C using 470 nm light ranging from 1.3×10^{13} mm^{-2} s^{-1} to 1.6×10^{15} mm^{-2} s^{-1}; mean±SEM and n=4, note that for *Cr*ChR2 T159C the half-maximal light dose was only estimated.

tensities above. Additionally, the 530 nm light titration curve showed a kink *e.g.* reduced slope (3.4 A, black arrow) already a decade away from saturation as well indicating light-induced inactivation of the currents at high intensities. This inactivation seems to be a feature af ReaChR and was not seen for *Cr*ChR2 T159C, which was measured in comparison. Contrary to ReaChR, I_p as well as I_s of *Cr*ChR2 T159C constantly rose till saturation upon rising intensities of the activation light as illustrated in figure 3.4 C.

To address which wavelength is suited best to activate ReaChR and sum up previous results, the current traces of the stationary action spectra (100 % intensity, reverse) were re-evaluated in a time dependent manner. The current size was not only plotted after 1 s like before but also at earlier time points of that same recording to see the temporal evolution of the stationary spectrum. This results in a contour plot showing the photocurrent size dependent on wavelength and duration of the pulse (figure 3.5 A).

Comparing time traces of the relative current at 530 nm and 600 nm plotted on a logarithmic scale, it becomes more evident which wavelength entails a higher current for

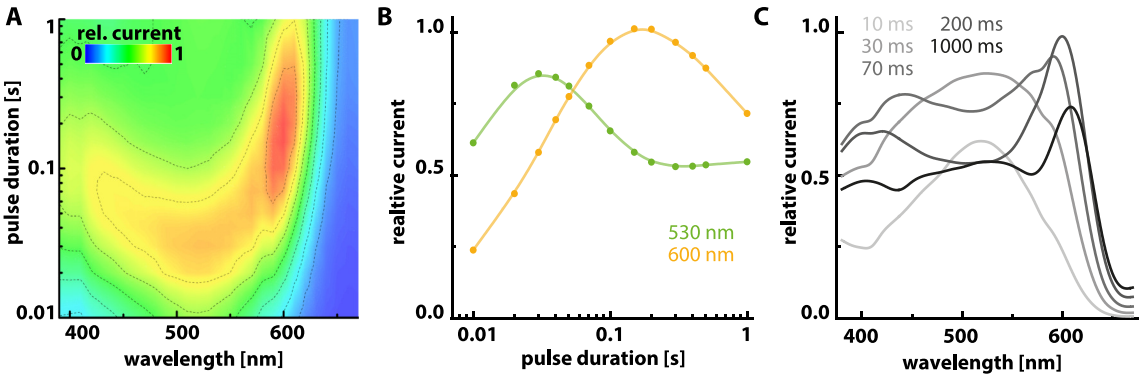

Figure 3.5: Temporal evolution of spectral sensitivity in ReaChR A Contour plot showing the relative photocurrent dependent on the activation wavelength and the duration of the light pulse at standard conditions and E_{hold}=−60 mV. The values for all time points were extracted from the same measurement respectively and the currents were normalized to the highest current of that recording. 10 s in the dark at E_{hold}=0 mV between sweeps; n=5. **B** Time traces of the current size at 530 nm and 600 nm extracted from the contour plot. Values at 0.01 s relate to the flash and at 1 s to the stationary action spectra. **C** Spectra extracted from A at different time points of the recording *e. g.* varying illumination length.

the respective illumination length. For pulses up to 40 ms, green-light activation resulted in higher currents than orange light, whereas it was *vice versa* for longer pulses (figure 3.5 B). As seen previously, the highest current was evoked with orange light and it was 15 % higher than the highest green-light evoked current. Additionally, the green-light induced current decreased again when the light pulse was longer than 40 ms.

When spectra were extracted from the contour plot (figure 3.5 A) for different pulse durations, those at 10 ms and 1 s expectedly resembled the flash and the stationary action spectrum, respectively (figure 3.5 C). The spectra at time points between 10 ms and 1 s illustrate several features occurring (in that sequence) during illumination *e. g.* with longer activation pulses: i) there is an early peak at 530 nm, ii) the spectrum gets broader, iii) the current around 530 nm decreases again and a peak rises at 600 nm iv) the peak around 600 nm decreases again. Remarkably, these spectra at different time points resemble the stationary action spectra (reverse) recorded at different intensities (*cf.* figure 3.2 D and 3.5 C), implying that rising activation intensity and prolonging the activation pulse have similar effects on the spectral shape.

3.1.2 Counter ion mutants

The homologue positions to the *Cr*ChR2 counter ions (E123 and D253) are E163 and D293 in ReaChR (see figure 3.6 A). To investigate their role in ReaChR, the residues were replaced individually by separate introduction of the mutations E163T and D293N.

The amplitudes of I_p as well as I_s of ReaChR D293N (figure 3.6 C) were significantly reduced to $-4 \pm 3\,pA\,pF^{-1}$ and $-2 \pm 1\,pA\,pF^{-1}$ in comparison to the wt, which showed

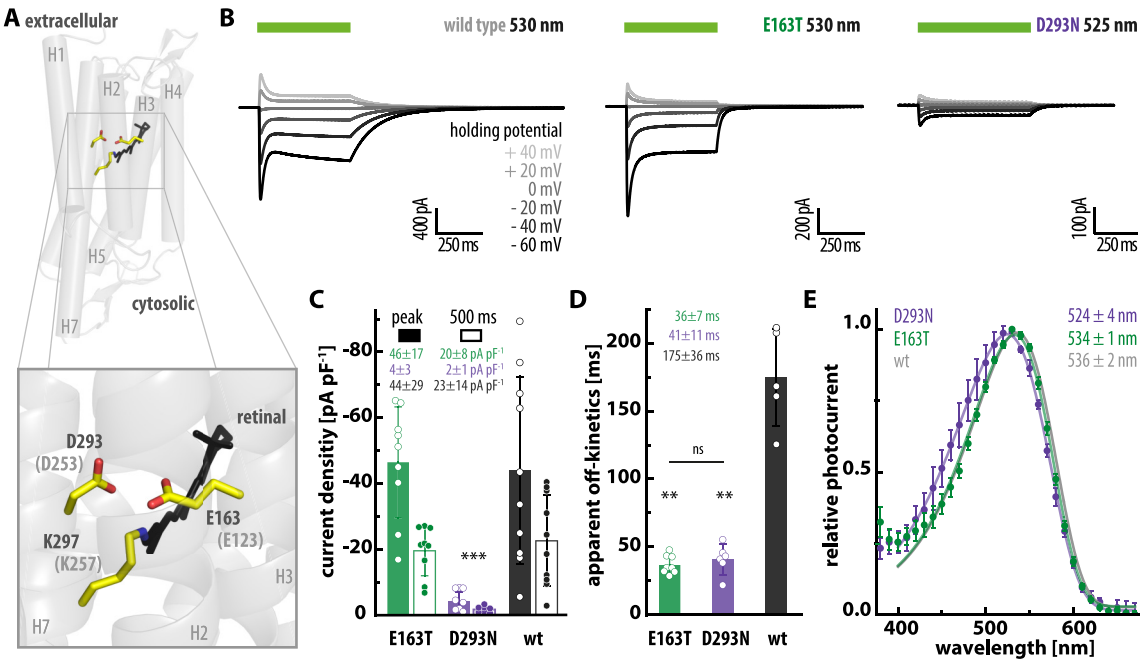

Figure 3.6: Counter ion mutants of ReaChR. A ReaChR homology structure model[192] based on C1C2 structure (PDB: 3UG9) highlighting the position of the counter ions E163 and D293 **B** Representative photocurrent traces at different E_{hold} for wt ReaChR, ReaChR E163T and ReaChR D293N mutant recorded at standard conditions upon 500 ms illumination with the indicated wavelength. **C** Comparison of current densities at E_{hold}=−60 mV from currents recorded in panel A; filled bars correspond to I_p and open bars to current at 500 ms represented as mean±SD and individual data points. Significance was tested using the Wilcoxon rank sum test comparing to the wt. **D** Apparent off-kinetics determined from the currents in C with the wt and E163T current decays fitted bi-exponentially and the D293N mutant mono-exponentially. Data represented as mean±SD with individual data points. Significance was tested using the Wilcoxon rank-sum test comparing to the wt or the indicated mutant. **E** Flash action spectra of wt ReaChR (gray), ReaChR E163T (green) and ReaChR D293N (purple) at standard conditions; represented as mean±SD with n=7, n=6 and n=6; D293N spectrum measured at higher intensity (without 25 % neutral density filter) because currents were small.

average current densities of $-44 \pm 29\,\mathrm{pA\,pF^{-1}}$ and $-23 \pm 14\,\mathrm{pA\,pF^{-1}}$ in that experiment. This was similar to the homologue *Cr*ChR2 D253N mutation, where replacement of that protonatable residue likewise impaired channel function[110]. The action spectrum of ReaChR D293N peaked at 524 ± 4 nm, which is 12 nm blue shifted (figure 3.6 E) compared to the wt and implies a higher energy difference between ground and excited state in that mutant. The observed hypsochromic shift of the action spectrum was inconsistent with spectroscopic results, which did not report an absorption shift for recombinant ReaChR D293N in detergent[193]. As the action spectrum of D293N had to be measured at higher intensity due to the small photocurrents, comparability to the wt spectrum is restricted, thus the hypsochromic shift might not be as big. Nevertheless, even a slightly blue or non-shifted spectrum compared to the wt was surprising as the reduced photocurrents of the D293N mutation supports that D293 is the proton acceptor to the RSB and thus deprotonated in the dark. Hence, it is surprising that neutralization of this

negative charge close to the RSB does not red-shift the absorption maximum like it was seen for the homologue mutation in *Cr*ChR2[114], *Ps*ChR[114]or C1C2[194]. One could speculate that in the ReaChR D293N mutant the other counter ion E163 is deprotonated in the dark and can likewise accept the proton and stabilize the protonated RSB. To explain the blue shift of the action spectrum in D293N the deprotonated E163 in the mutant would have to be closer to the RSB than the deprotonated D293 in the wt resulting in a more stable dark state and a hypsochromic shift of the spectrum.

Replacing the second counter ion residue by introduction of the E163T mutation did neither significantly affect the size of I_p nor I_s as seen in figure 3.6 C, which supports the role of D293 as primary proton acceptor to the RSB in ReaChR. However, like in *Cr*ChR2 E123T[112] off-kinetics were with 37 ± 7 ms five-fold faster than the wt kinetics as seen in figure 3.6 D. The fast-cycling ReaChR variant bReaChES[c] reported by Rajasethupathy *et al.* is based on introduction of a serine at this position[149]. Interestingly, the action spectrum of ReaChR E163T was not shifted in comparison to the wt (figure 3.6 E), in contrast to the corresponding mutation in *Cr*ChR2[114] or C1C2[194]. This indicates that introduction of the mutation is not eliminating a charge close to the RSB and hence that E163 might be protonated in the dark in wt ReaChR.

3.1.3 Ion selectivity of ReaChR

In *Cr*ChR2, E90 is located in the central gate and one of the major molecular determinants for ion selectivity as introduced earlier (see section 1.1.2). On the one hand introduction of a lysine or arginine at this position created Cl^--conductance[39], while on the other hand replacement of E90 by alanine or glutamine changed the permeability ratio for protons over sodium in *Cr*ChR2[106,108].

First, a red-shifted chloride-conducting ChR should be created from ReaChR. Thus, E130 (see figure 3.7 A) was replaced with a lysine or arginine in homology to an earlier selectivity-inversion approach for *Cr*ChR2[39]. ReaChR E130K and E130R both showed small currents (data not shown) and the action spectrum of E130R exhibited a 32 nm hypsochromic shift (figure 3.7 C).[d] However, when an outward-directed Cl^--gradient was applied, the reversal potential was at 3.7 ± 1.9 mV and did not shift compared to symmetric Cl^--conditions 4.2 ± 3.8 mV as illustrated for ReaChR E130R in figure 3.7 B. Hence, a Cl^--conductance of ReaChR E130K and E130R could not be achieved that way.

[c] bReaChES also contains a different N-terminus compared to ReaChR, which enhanced the photocurrents in mammalian cells[149].

[d] *Cr*ChR2 E90K T159C exhibits a red-shifted action spectrum compared to the wt *Cr*ChR2 (Personal communication with Jonas Wietek).

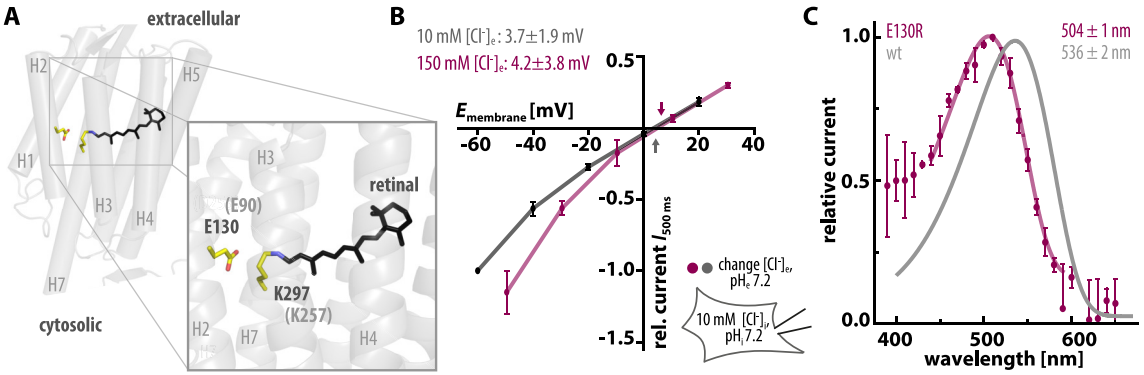

Figure 3.7: Chloride conductance of ReaChR E130R in HEK293 cells. **A** ReaChR homology structure model[192] based on C1C2 (PDB: 3UG9) highlighting the position of E130 in the putative ion conduction pathway. **B** Current-voltage relations for ReaChR E130R at external 10 mM (gray) and 150 mM [Cl^-] (purple) at symmetric pH 7.2$_{i/e}$ and 10 mM [Cl^-]$_i$; mean±SD and LJP-corrected, n=3 **C** Flash action spectrum of ReaChR E130R at 10 mM [Cl^-]$_{i/e}$ and pH$_{i/e}$ 7.2 in comparison to wt spectrum at standard conditions, both E_{hold}=−60 mV and represented as mean±SD with n=3 and n=7.

Finally, anion selectivity for ReaChR was achieved employing another conversion strategy, which was reported for the chimeric C1C2[40] and transferred to ReaChR yielding the Cl^--selective Aurora, which retained the red-shifted action spectrum of ReaChR[195].

Next, the E130Q mutation (see figure 3.7 A) was generated and the conductance of H^+ over Na^+ was investigated in detail in comparison to wt ReaChR. Figure 3.8 A shows representative photocurrent traces at varying holding potentials and different extracellular solutions (110 mM [Na^+]$_i$, pH$_i$ 7.2) for wt ReaChR (figure 3.8 A, left) and ReaChR E130Q (figure 3.8 A, right). The corresponding current-voltage relations after correction of the liquid junction potential (LJP) are displayed in figure 3.8 B. At standard conditions, I_p and I_s of ReaChR E130Q were reduced to 40 % and 20 % of the wt currents (see figure 3.8 A, table). Without a pH gradient and only a slight inward directed Na^+-gradient both variants showed small positive and similar E_{rev} with 8.7 ± 1.6 mV for the wt and 7.6 ± 1.4 mV for E130Q (figure 3.8 D). Upon reduction of extracellular [Na^+] the reversal potential shifted with ΔE_{rev} 14 ± 2 mV less for the wt than for the mutant with 41 ± 2 mV. When extracellular [H^+] was reduced at high [Na^+]$_e$ the opposite occurred with a larger ΔE_{rev} for the wt with 34 ± 4 mV than for the mutant with 6 ± 2 mV as seen in figure 3.8 E. Additionally, I_p and I_s were 2.3 and 1.2 times higher for E130Q than for the wt at this condition (figure 3.8 A, table). When extracellular [Na^+] and [H^+] were reduced, only outward-directed currents occured (figure 3.8 A) and E_{rev} shifted to −86 ± 6 mV in the wt and −104 ± 15 mV in the E130Q mutant (figure 3.8 D).

With the help of the Goldmann-Hodgkin-Katz voltage equation[196] (GHK) the determined reversal potentials were used to calculate the permeability ratio $\frac{P_H}{P_{Na}}$ of protons

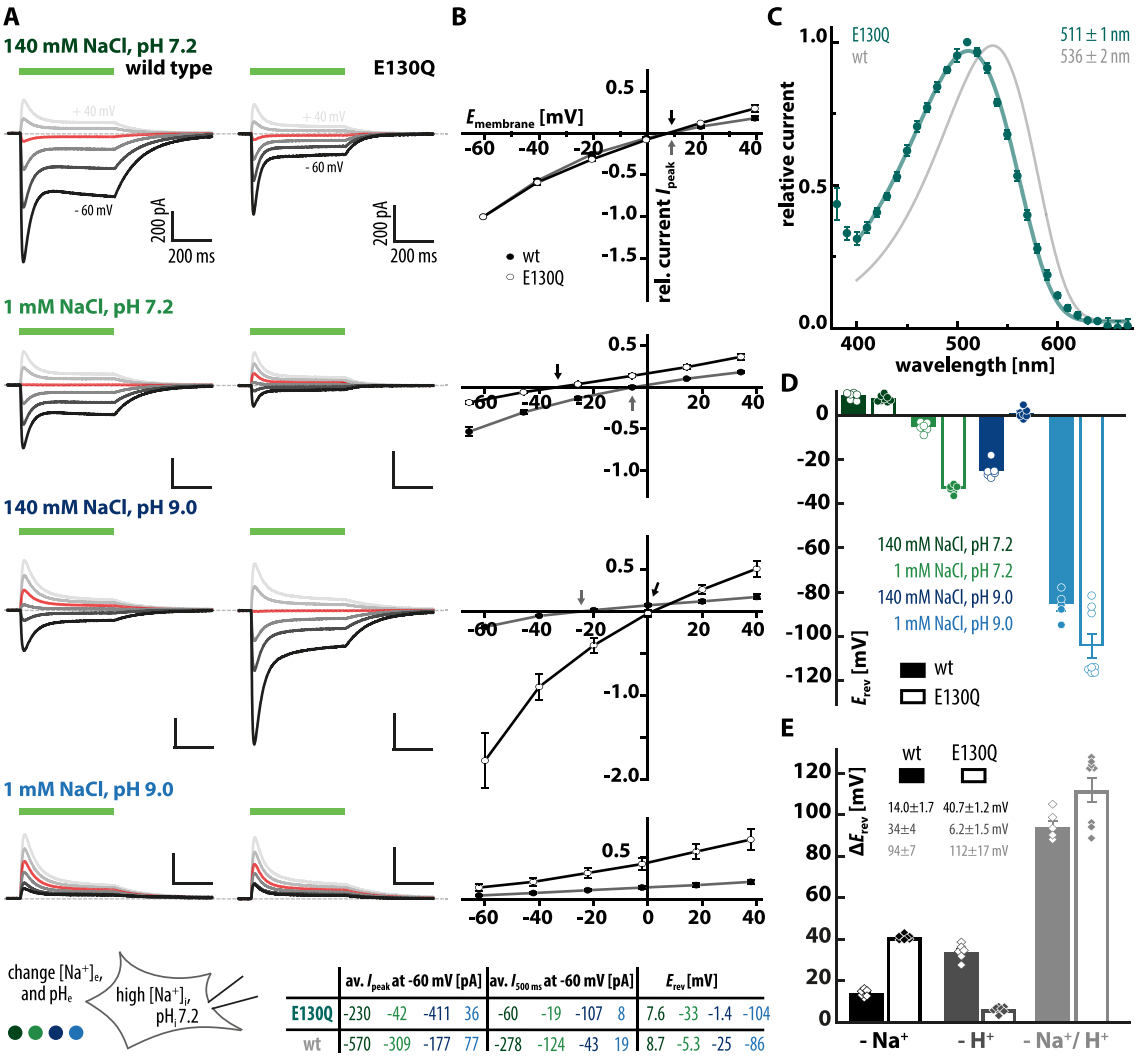

	av. I_{peak} at -60 mV [pA]				av. $I_{500\,ms}$ at -60 mV [pA]				E_{rev} [mV]			
E130Q	-230	-42	-411	36	-60	-19	-107	8	7.6	-33	-1.4	-104
wt	-570	-309	-177	77	-278	-124	-43	19	8.7	-5.3	-25	-86

Figure 3.8: Ion selectivity and spectral sensitivity of ReaChR E130Q in HEK293 cells. **A** Representative photocurrent traces of wt ReaChR (left) and ReaChR E130Q (right) at different E_{hold} from −60 mV to 40 mV and changing extracellular ionic conditions as indicated (110 mM $[Na^+]_i$ and pH 7.2$_i$); mean absolute currents at −60 mV for each condition are summarized in the table (bottom) **B** Current-voltage relations for wt (black) and E130Q (gray) corresponding to conditions in A (LJP corrected). Represented as mean±SEM. **C** Flash action spectrum of the E130Q mutant in comparison to wt ReaChR at standard conditions and E_{hold}=−60 mV. Represented as mean±SD with n=6 and n=7. **D** Absolute E_{rev} determined from B with numbers summarized in the table (bottom). Bars represent mean±SEM for wt (filled bars) and the E130Q mutant (open bars) supplemented by individual data points. **E** Reversal potential shifts compared to standard conditions after reducing extracellular Na^+ (black), H^+ (gray) or both (light gray). Data represented as mean±SEM and individual data points.

over sodium[e]. For the condition with the high sodium gradient, 1 mM $[Na^+]_e$ and pH_e 7.2, (figure 3.8 A and D) a ratio of $(9 \pm 4) \times 10^6$ was calculated for the wt and a one order of magnitude smaller ratio of $(6.4 \pm 0.6) \times 10^5$ for the E130Q mutant. Consistently, permeability ratios resulting from E_{rev} at asymmetric H^+-concentrations (high NaCl, pH 9.0; figure 3.8 A and D) resulted in similar ratios of $(4.4 \pm 0.8) \times 10^6$ for the wt and

[e] See materials and methods part page 31 for details on the calculation.

$(4 \pm 2) \times 10^5$ for the E130Q mutant. This conclusively showed that the ratio of H^+ over Na^+ permeability in the mutant was one order of magnitude smaller and shifted in favor of Na^+. For *Cr*ChR2 the permeability ratio for H^+ over Na^+ was calculated to be $(1 - 2.5) \times 10^6$ in earlier studies[100,151,197], which is in the range of the calculated ratio for wt ReaChR.

Bi-exponential fitting of the ReaChR E130Q current traces after light-off at standard conditions revealed a kinetic decay constant of 89 ± 18 ms for I_s, which is two-times faster in comparison to wt ReaChR. Moreover, the action spectrum of E130Q was 25 ± 1 nm blue shifted (figure 3.8 C), which was similarly reported for spectroscopic measurements of purified ReaChR E130Q[193], but not observed for the homologue E90Q mutation in *Cr*ChR2[109]. Together with the distinct blue shift of ReaChR E130R this indicates that replacement of E130 in ReaChR influences the counter ion configuration and stabilizes the dark state. Further, it implies that the structural arrangement of this central gate residue could be different in ReaChR and *Cr*ChR2, because hypsochromic shifts of the spectra were not observed in *Cr*ChR2 after replacement of E90.

3.1.4 Mutations in the DC-pair

Transferring one of the ChETA mutations[112] to ReaChR already generated a fast-cycling ReaChR variant (ReaChR E163T, see section 3.1.2). Now, through introduction of mutations in the DC-pair (figure 3.9 A), which comprises C168 and D196 in ReaChR, a slow down of the photocycle was aspired. Thus, the mutations D196N, D196C, C168T, C168A and C168S were introduced individually. All mutations retained functionality and decelerated the off-kinetics to varying extents as seen in figure 3.9 B. According to the different kinetics, wt, C168T and D196N where activated for 5 s and C168A/S and D196C where activated for 25 s and 20 s to reach a stationary current level in all cases. The off-kinetics were fitted from the beginning of the current decay on, but especially the slow variants showed a delay between light-off and current decrease (figure 3.9 B), which was not quantified here, but should be considered if the mutants are applied.

ReaChR C168T and D196N only showed 1.8- and 2.8-fold decelerated kinetics, but introducing C168A and C168S significantly slowed the photocycle and yielded two orders of magnitude slower off-kinetics with 22 ± 4 s and 28 ± 4 s, respectively (figure 3.9 D). Interestingly, elimination of D196 entailed a photocurrent without the transient I_p showing no inactivation, regardless whether the aspartic acid was replaced by asparagine or cysteine as seen from the representative current traces (figure 3.9 B). As not all mutants showed a real I_p in the current trace, only the current densities before the light was switched off were compared. Here, C168T and C168S showed 40 % and 53 % reduced

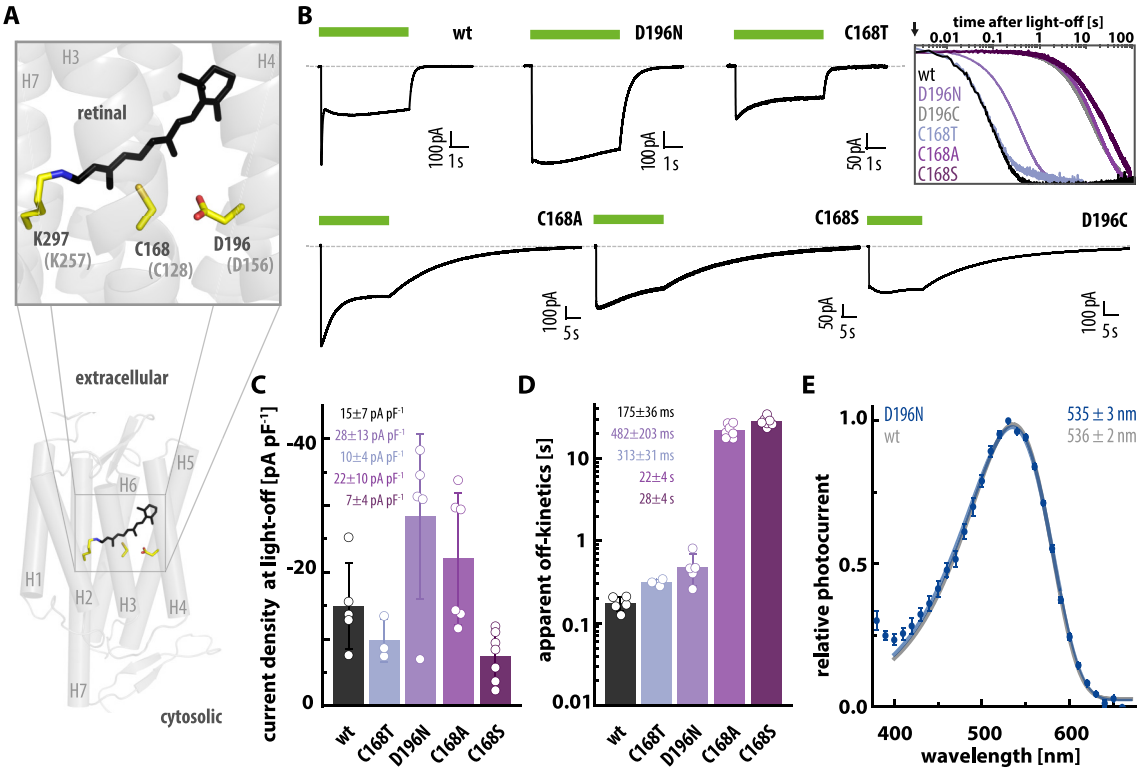

Figure 3.9: Slow-cycling mutants of ReaChR. A ReaChR homology structure model[192] based on the C1C2 structure (PDB: 3UG9) highlighting the position of the DC-pair with C168 in TM3 and D196 in TM4. **B** Representative photocurrent traces of mutations in the DC-pair at standard conditions upon illumination with 530 nm; E_{hold}=−60 mV. Inset shows a comparison of the off-kinetics of all mutants. The traces were normalized to the respective current at light-off indicated by the black arrow. **C** Average current densities (±SD) of indicated mutations before light-off extracted from B. **D** Average apparent off-kinetics (±SD) extracted from current traces recorded for C with mono-exponential fit for C168A, C168S and bi-exponential fit for wt, D196N and C168T. **E** Flash action spectrum for D196N mutant in comparison to wt ReaChR at standard conditions and E_{hold}=−60 mV, n=6.

photocurrent densities compared to the wt, whereas C168A and especially D196N exhibited 1.5- and 1.7-fold higher stationary current densities than wt ReaChR. For the slightly decelerated D196N an action spectrum was measured, which showed no shift in comparison to the wt, while a blue shift was reported for the absorption spectrum of purified ReaChR D196N[193,f].

3.1.5 Light-induced inactivation measurements

Exploiting the decelerated kinetics of the slow-cycling ReaChR variants an investigation of the open state and late photocycle intermediates became possible, because slow-cycling mutants accumulate the open state(s) under continuous illumination. The slow-

[f] For recombinant ReaChR D196N the spectrum of the initial dark state was 4 nm blue shifted, while the spectrum of the apparent dark state was 21 nm blue shifted[193]. As prior to all electrophysiological recordings with ReaChR the cells were illuminated (see section 2.5) the action spectra should be more comparable to the apparent dark state absorption spectra.

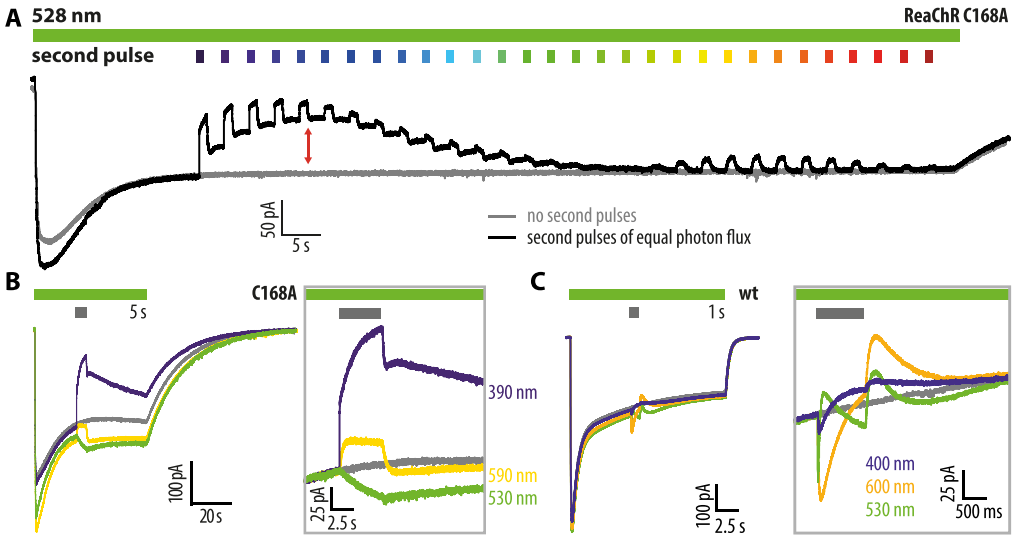

Figure 3.10: Light-induced inactivation of ReaChR. A Inactivation spectrum of ReaChR C168A recorded with a low intensity background illumination (528 nm) and additional pulses of higher intensity from 380 nm to 670 nm at E_{hold}=−60 mV and standard conditions. Duration of the additional light pulses was 1 s and the intensity was higher than that of the continuous green illumination. **B** Light-induced inactivation of I_s for ReaChR C168A with single light pulses of 5 s length, different wavelengths but equal photon flux. The inset shows a magnification with stationary currents aligned **C** Similar measurement to B but with wt ReaChR.

est kinetics were determined for ReaChR C168S (see section 3.1.4), but the mutation entailed a significant reduction of the current amplitude. Thus, ReaChR C168A, which showed wt-like current amplitudes, was used for inactivation measurements, as already performed for slow-cycling *Cr*ChR2 C128T and C1V1 E122T C167S[147].

First, an inactivation spectrum (figure 3.10) was measured. The open state was accumulated by a low intensity background illumination (528 nm) and when the stationary current was established, a series of second pulses (1 s) of different wavelengths but equal photon flux and higher intensity was applied. This tested which light qualities entail a photo-activated conversion of an intermediate thereby reducing the protein fraction in the open state(s). The light-induced inactivation of the stationary current with orange light was small and immediately reversed by the green background illumination (figure 3.10 A). However, the inactivation with UV or blue light pulses reduced the current to less than 50 % and only a small fraction recovered instantaneously under the green background illumination (figure 3.10, top). The prior steady state current level was only reached again within minutes, implying a partial conversion into a less or non-conducting product that only slowly re-entered the productive photocycle. The inactivation spectrum was similar if the series of second pulses was applied starting from the long wavelength range measuring from 670 nm to 380 nm (data not shown).

To test whether this slow recovery progressed thermally or was induced/enhanced

by the subsequent light pulses in the inactivation spectrum, the experiment was repeated with single additional light pulses (5 s) as illustrated in figure 3.10 B. Application of an additional green light (530 nm) pulse stably enlarged the current implying a shift of the steady state equilibrium towards the open state as best seen in the inset of figure 3.10 B. Orange light (590 nm) induced a small, reversible inactivation as already seen in the spectrum (figure 3.10 A) and a 390 nm pulse induced a bi-phasic reduction of the steady state current of more than 60 % with a fast and a slower component as evident in the inset (figure 3.10 B). The reversion of this inactivation was also bi-phasic with a small fraction recovering immediately in the green background light and another only slowly recovering over minutes.

The inactivation experiment was similarly performed with wt ReaChR as seen in figure 3.10 C. All light pulses (400 nm, 530 nm, 600 nm) gave qualitatively similar results evoking an additional activation in the first milliseconds, decreasing again during the pulse and a temporary inactivation, when the second light pulse is switched off again and only the green background illumination remains. This is explained by additional activation of protein from the dark state by the second pulse first enlarging the current because additional protein is activated. When the second pulse is switched off this additional fraction first has to complete the photocycle before it can be reactivated from the dark state by the green background illumination, which causes a transiently smaller stationary photocurrent. Surprisingly, this effect was most prominent for 600 nm showing the highest additional activation.

3.2 The green-light activated sodium pump KR2

In 2013 the family of microbial rhodopsins was enlarged by a new member, the light-driven Na^+-pump. The first publication reported KR2 from the marine flavobacterium *Krokinobacter eikastus*[48], which was quickly followed by identification of several homologues in other marine[43,72,73] or freshwater bacteria[74,80]. Already two years after its first report the crystal structure of KR2 was solved twice[78,79] rendering it the most interesting representative of that new class of microbial rhodopsin for mechanistic studies.

3.2.1 Assessing pump activity with the *E.coli* assay

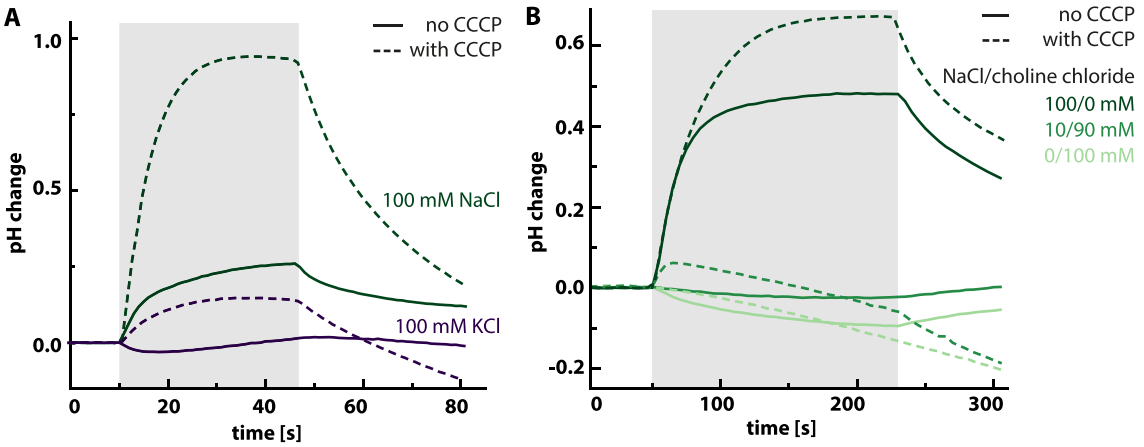

Figure 3.11: pH measurements in *E. coli* suspension expressing wt KR2. **A** Relative light-induced pH changes (normalized to initial value) monitored in a suspension of KR2-expressing *E. coli* in unbuffered NaCl or KCl solution, dotted lines represent measurements on the same sample after addition of CCCP (50 µM). The baseline was linearly corrected according to the ten points before illumination, pH at 0 s was 6.4 in NaCl (6.5 after addition of CCCP) and 6.5 in KCl (7.1). **B** Similar measurement as in A with 0 mM NaCl/100 mM choline chloride, 10 mM NaCl/90 mM choline chloride and 100 mM NaCl/0 mM choline chloride solution; initial pH 6.1 (6.1), 6.1 (6.1) and 6.8 (6.9), respectively.

The pH measurement in rhodopsin-expressing *E. coli* suspension was the assay of choice to monitor light-induced pump activity since the first report of KR2. Thus, this assay represented the starting point for this study and published results[48] should be reproduced first. Hence, *E. coli* suspensions (OD_{600} around 9) were incubated in unbuffered solution of 100 mM NaCl or KCl[g] (figure 2.2 A). In NaCl solution illumination with white light caused an elevation of the pH, which decreased again when the light was switched off. The effect was even more pronounced after addition of the protonophore carbonylcyanid-m-chlorophenylhydrazon (CCCP). In KCl solution a light-dependent acidification was observed, while after addition of CCCP the solution pH was elevated upon activation of the pump (figure 3.11 A). This was a significant difference

g Establishement of the assay and first experiments were done together with Arend Vogt.

compared to the published results, which reported the same behavior in NaCl but a loss of light-induced pH change upon addition of CCCP in the KCl solution.

Next, a similar experiment was performed with different Na^+-concentrations with NaCl replaced by choline chloride to ensure constant osmolarities (figure 2.2 B). In 100 mM NaCl expectedly similar results as before were observed (*cf.* figure 2.2 A and B). When Na^+ was completely replaced by choline chloride a light-dependent acidification was observed without CCCP and no light response was seen after the addition of CCCP, which would concur with a net outward H^+-transport and is similar to the reported results for KR2 in KCl[48]. Interestingly, at the intermediate [Na^+] (10 mM) the pH slightly decreased upon illumination without CCCP, but was elevated in the light when CCCP was present, meaning that opposite behavior was achieved although the [Na^+] was unchanged. Strikingly, this result was similar to that obtained in KCl, which could imply similar activity in high KCl concentrations and low NaCl concentrations.

3.2.2 Expression and membrane targeting in mammalian cells

To improve the poor membrane targeting of wt KR2 in mammalian cells, a multitude of different constructs was designed (figure 3.12). To evaluate their membrane targeting, confocal images of expressing cells were taken after membrane staining with commercially available dyes (see section 2.4.1 for details) with the membrane targeting calculated as ratio between mean fluorescence of the fusion protein in the membrane area and within the cell as shown in figure 3.13 A and B (for technical details see section 2.4.1). Additionally, photocurrents at standard conditions (110 mM $[Na^+]_{i/e}$, $pH_{i/e}$ 7.2) were recorded for all constructs to relate the determined targeting efficiency to pump activity of the respective construct (figure 3.13 C).

The membrane targeting of the unmodified wt KR2 was poor (figure 3.13 B) and accordingly for most of the cells no photocurrent was detected (figure 3.13 C). In a first round of constructs, different N-termini were fused to KR2. First a mixture of the N-termini of *Cr*ChR2 and *Cr*ChR1[149] (construct #075), second the N-terminus (23 amino acids) of subunit A of the mouse serotonine 5-HT_3 receptor, which is naturally expressed in dorsal root ganglion cells of mice (GeneBank: AAT37716.1) (construct #076) and third the Lynx secretion signal, a signaling peptide which was previously used to target membrane-tethered toxins to the cell membrane (construct #077)[198,199], were fused to KR2. The constructs are illustrated in figure 3.12. The latter two constructs #076 and #077 showed no significant improvement over the wt, with little membrane targeting and accordingly no photocurrents (figure 3.13 B and C). However, construct #075 with the ChR-N-terminus showed significantly higher photocurrents than the wt although

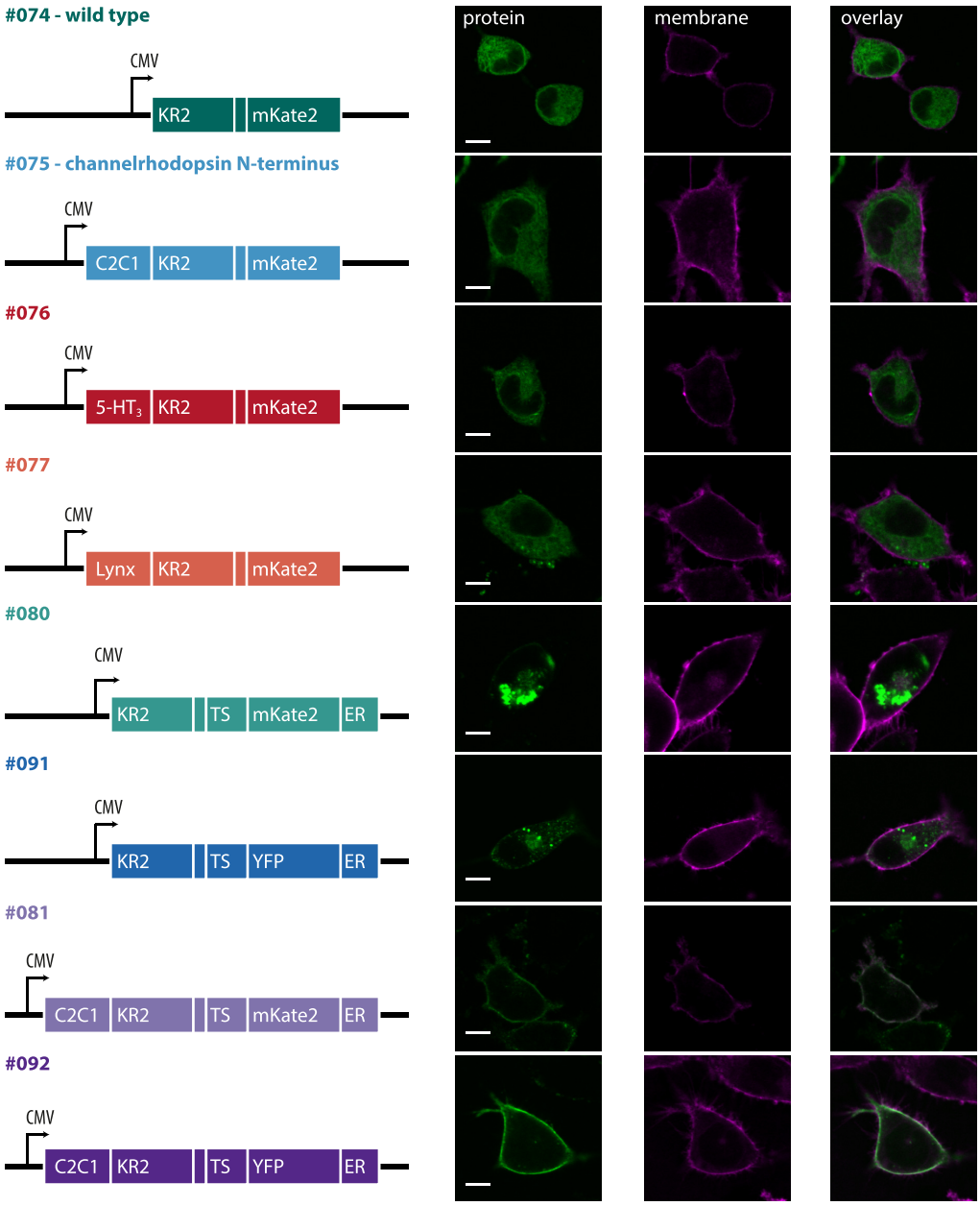

Figure 3.12: KR2 targeting constructs. Different sequences, reported to improve trafficking and membrane targeting of microbial rhodopsins, were fused to the N- and/or C-terminus of KR2 with KR2 always preserved in its entirety (left). Right: Confocal images (0.5 µm equatorial slice) of all constructs expressed in ND7/23 cells for two days. White bar corresponds to 10 µm. Protein fluorescence is shown in green (left), membrane marker in magenta (middle) and the overlay of both in white (right).

membrane targeting was in the same range. This is explained by an overall enhanced expression of construct #075 compared to the wt. Figure 3.13 A shows that the mean fluorescence in the membrane was higher than for wt KR2, which explains higher photocurrents (figure 3.13 C). As the average fluorescence within the cell was also higher compared to wt (figure 3.13 A), the membrane targeting was similar for both constructs. Next, two C-terminal targeting sequences were tested with two different fluorophores.

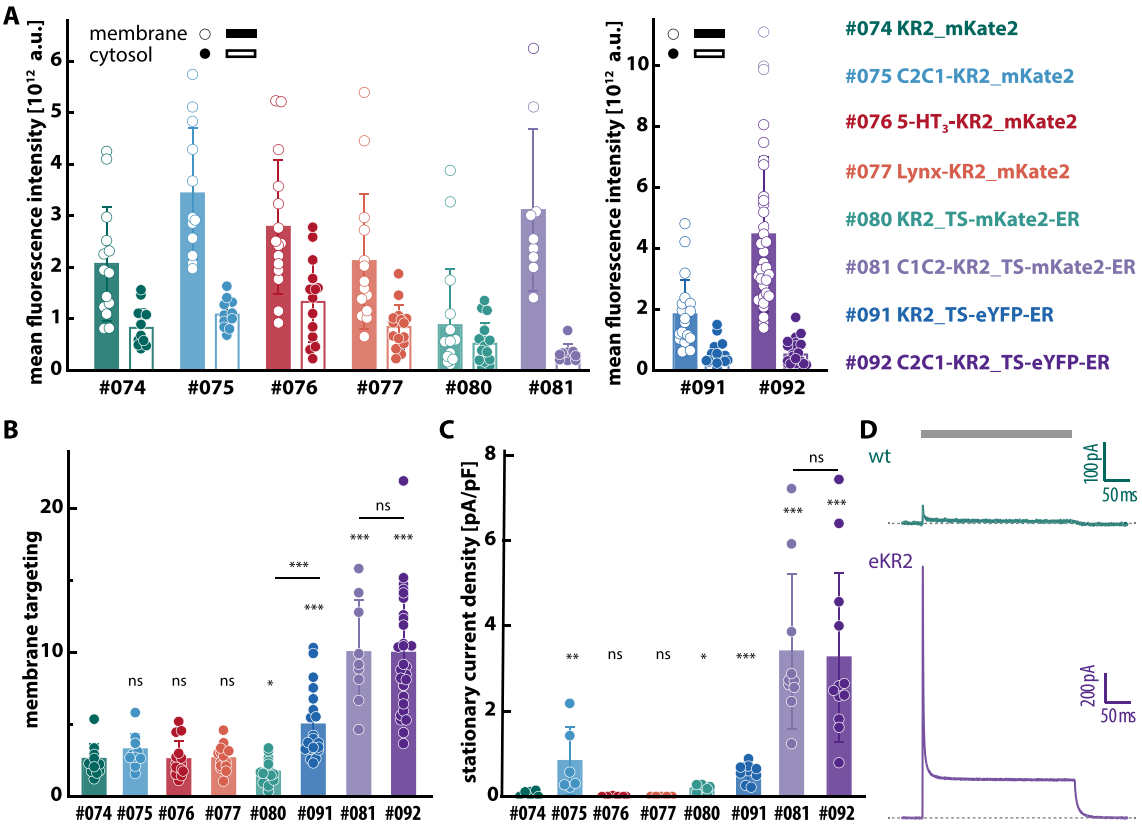

Figure 3.13: Expression, membrane targeting and photocurrents of targeting constructs in ND7/23 cells after two days of expression. A Averaged mean fluorescence (±SD) in the membrane (open circles) and within the cell (filled circles) for all targeting constructs. Constructs #074, #075, #076, #077, #080 and #081 bear an mKate2 fluorophore and #091 and #092 an eYFP. The absolute fluorescence intensities are only comparable for same fluorophore. **B** Membrane targeting (see figure 3.12 for corresponding confocal images) for all constructs as ratio of mean fluorescence in the membrane identified by membrane marker and within the cell. Values are determined as mean of three equatorial slices (0.5 µm) per cell. **C** Average stationary photocurrents (±SD) of the constructs at standard conditions and 0 mV after excitation with 525 nm (LED, 46 mW mm^{-2}). **D** Direct comparison of photocurrents recorded from cells expressing either wt KR2 (green) or eKR2 (purple) at standard conditions and 0 mV. All data is represented as mean±SD with single values as dots and significance was tested with the Wilcoxon rank-sum test comparing to the respective wt value or between the indicated pair.

Reported sequences to prevent aggregation in the endoplasmatic reticulum (ER) -FCEYENEV-[200] and to enhance trafficking to the membrane (TS) -KSRITSEGEYIPLDQIDINV-[201] were used. Both constructs bore the targeting sequences, but one was fused to mKate2[202,203] (#080) and the other to eYFP[204] (#091) as seen in figure 3.12. Construct #080 with flanked mKate2 surprisingly showed reduced membrane targeting compared to the unmodified KR2, which was accompanied by minimal photocurrents (figure 3.13 B and C). When the fluorophore was exchanged to eYFP flanked by the targeting sequences the so far highest membrane targeting was achieved and the photocurrents were significantly improved to the level observed for construct #075 (figure 3.13 B and C). Thus the fluorophore had a dramatic impact on trafficking and photocurrents in that context.

Consequently, in a last step, the targeting approaches of the two best constructs so far were combined yielding construct #092, which comprised the ChR N-terminus fused N-terminally and the TS and ER sequences flanking the eYFP at the C-terminus (figure 3.12). This construct was excellently targeted to the cell membrane with almost no protein retention in the cell (figure 3.13 B). Accordingly, the photocurrents were 60-fold enhanced in comparison to the unmodified wt protein (figure 3.13 C). Also at this stage, the fluorophore was replaced by mKate2 (construct #081), but here the exchange had no influence as currents and membrane targeting were similar to construct #092. In summary, the screening yielded a construct with excellent membrane targeting and 60-fold higher photocurrents than the unmodified KR2. Thus, it was termed enhanced KR2 (eKR2) and used for the electrophysiological investigation of the pumping activity.

3.2.3 Ion specificity of pumping activity of eKR2

One of the reported features of KR2 is the proposed switch from Na^+-pump activity in the presence of sodium to H^+-pumping in the absence of sodium, which was deduced from pH measurements in *E. coli* suspension[48]. As the poor membrane targeting of wt KR2 could be overcome through the design of eKR2, it was used to investigate the ion specificity of pumping activity in mammalian cells using whole-cell voltage-clamp measurements, which provides control over the intra- and extracellular ionic composition as well as the membrane voltage and additionally allows asymmetric ionic conditions to investigate the influence of ionic gradients.

Reference measurements with the proton pump *Cs*R

Only a limited number of studies in the past dealt with electrophysiological investigation and especially substrate specificity of the activity of microbial ion pumps. Thus, reference measurements were conducted with the reported outward H^+-pump from *Coccomyxa subellipsoidea* (*Cs*R)[205,206] to investigate photocurrent properties at different intracellular conditions and membrane voltages. Several photocurrent properties of *Cs*R were determined at different intracellular pH values, thus at varying substrate concentrations for the outward-directed H^+-pump. At 0 mV holding potential the currents were statistically influenced by the intracellular H^+-concentration (figure 3.14 A). While the peak current density did not significantly depend on the substrate concentration *e. g.* the intracellular pH (figure 3.14 B), the stationary photocurrent density gradually decreased from $13 \pm 6\,\mathrm{pA\,pF^{-1}}$ over $7.1 \pm 2.3\,\mathrm{pA\,pF^{-1}}$ to $1 \pm 1\,\mathrm{pA\,pF^{-1}}$ when pH_i was elevated from 6.0 over 7.2 to 9.0 (figure 3.14 C). A reduction of I_s with the substrate concentration was similarly reported for the fungal H^+-pump CarO[207] or the Cl^--pump

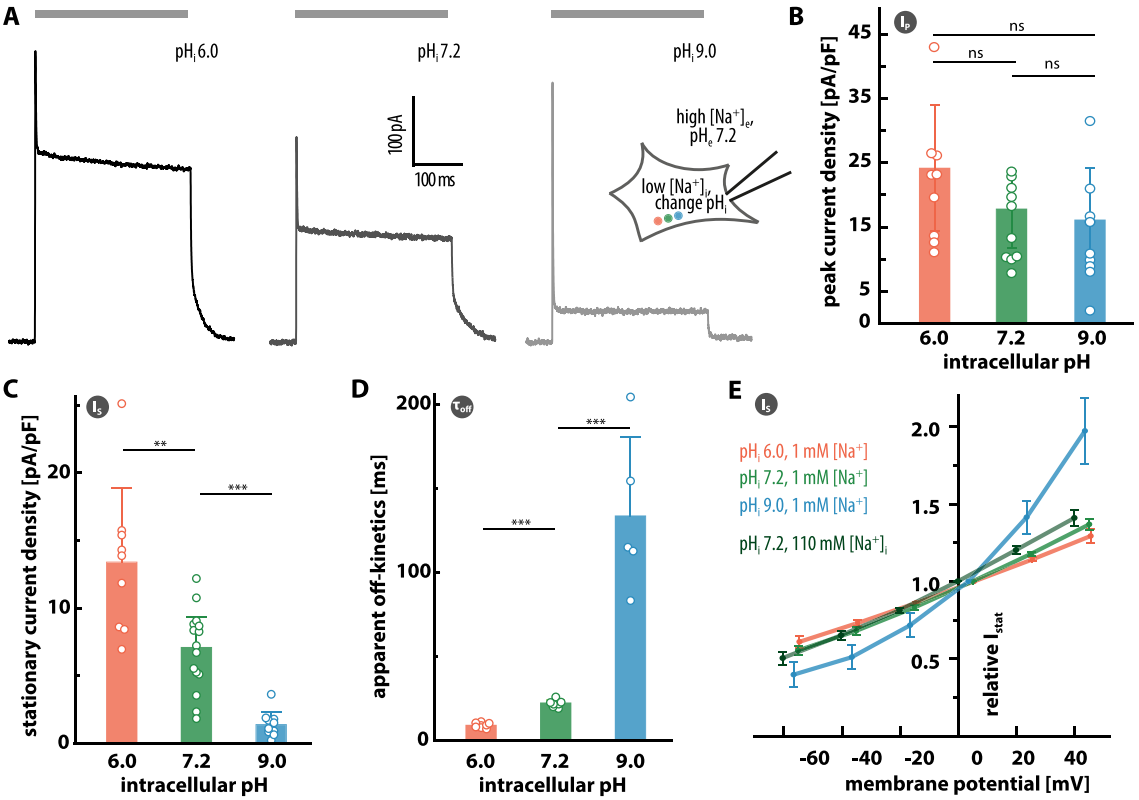

Figure 3.14: Reference measurements with the H$^+$-pump *Cs*R in ND7/23 cells. **A** Representative photocurrent traces of *Cs*R at 0 mV in ND7/23 cells after one day of expression at different intracellular [H$^+$] as indicated. Illumination for 300 ms with 525 nm LED; [Na$^+$]$_e$=110 mM, pH$_e$=7.2, [Na$^+$]$_i$=1 mM. **B** Average peak current densities at different intracellular pH values determined from measurements in A. **C** Corresponding average stationary current densities at different intracellular pH values. **D** Corresponding average apparent decay kinetics of the I_s after light-off resulting from bi-exponential fit. **E** Current-voltage relations of I_s at different intracellular proton concentrations (conditions from A). Additionally, the current voltage relation at standard conditions (dark green) is displayed. Currents are normalized to symmetric 0 mV current with LJP corrected, n=9, n=10, n=8, n=17. All data is represented as mean±SD with individual data points in bar graphs and significance was tested for indicated pairs with the unpaired Wilcoxon rank-sum test.

*Np*HR of *Natromonas pharaonis*[162]. Additionally, together with the photocurrent decline the apparent off-kinetics slowed from 9.0 ± 1.5 ms at pH$_i$ 6.0 over 22.3 ± 2.1 ms at neutral pH to 134 ± 47 ms at pH$_i$ 9.0 (figure 3.14 D). The voltage dependence of I_s from −60 mV to 40 mV was linear and similar for intracellular pH 6.0 and 7.2 (at 1 mM [Na$^+$]$_i$) and not affected when intracellular [Na$^+$] was elevated to 110 mM. However, the I-V curve deviated from linearity and became steeper at pH$_i$ 9.0 *e.g.* reduced substrate concentration.

Influence of the intracellular ionic condition on eKR2 photocurrents

Photocurrents were recorded at seven different intracellular ionic conditions at three Na$^+$-concentrations (110 mM, 1 mM, 0.1 mM) and three pH values (6.0, 7.2 , 9.0). For the recorded photocurrent traces, peak and stationary current densities as well as the kinetic

constant of the decay of I_s after light-off were determined at 0 mV (figure 3.15 A-D).

The peak current density was similar at all conditions with one exception; it was significantly higher at 110 mM $[Na^+]_i$ and pH_i 9.0 than at all other conditions (except for 110 mM $[Na^+]_i$, pH_i 7.2) as seen in figure 3.15 B. For the stationary current densities a more systematic dependence on the intracellular condition was observed (figure 3.15 B). The average stationary current density decreased stepwise when intracellular $[Na^+]$ was lowered from 110 mM over 1 mM to 0.1 mM at pH_i 7.2. At intracellular pH 9.0 there was only a significant difference between 110 mM and 1 mM $[Na^+]_i$, but the current was not further decreased at 0.1 mM $[Na^+]_i$ (figure 3.15 C). In contrast, when the intracellular $[H^+]$ was changed at 110 mM and 1 mM $[Na^+]_i$ the stationary current density was not significantly affected. Only at 0.1 mM $[Na^+]_i$ the stationary current densities were differing between pH_i 7.2 and 9.0 with the latter 2.1-fold higher (figure 3.15 C).

In accord with the current densities of I_s, the off-kinetics slowed from 6.8 ± 0.6 ms at 110 mM over 14.4 ± 1.9 ms at 1 mM to 17 ± 4 ms at 0.1 mM when intracellular $[Na^+]$ was lowered at pH_i 7.2 (figure 3.15 D) and were unaffected when the pH_i was changed, both at 110 mM and 1 mM $[Na^+]_i$ (figure 3.15 D). Although the correlation between I_s and the off-kinetics was preserved at 0.1 mM $[Na^+]_i$ and pH_i 9.0, the results at this condition were unexpected. Surprisingly, the stationary current densities increased and the decay after light-off accelerated in comparison to 0.1 mM $[Na^+]_i$ and pH_i 7.2 and was rather similar to 1 mM $[Na^+]_i$ and pH_i 9.0. Also at 1 mM intracellular $[Na^+]$ the closing kinetics were significantly accelerated at higher pH_i (figure 3.15 D).

Interestingly, the current traces (figure 3.15 A) showed a fast transient increase (overshot) of the stationary current after the light is switched off, but only at low intracellular $[Na^+]$ (1 mM and 0.1 mM). This feature will be investigated in more detail later (see section 3.1.5). Current-voltage relations show that I_p was only slightly dependent on the membrane voltage but not affected by any change of the intracellular buffer as seen in figure 3.15 E (left). Surprisingly, also the stationary current was not at all voltage dependent at 110 mM $[Na^+]_i$ and pH_i 7.2 (figure 3.15 E), which was similar at pH_i 9.0 (not shown). The voltage independence of I_s distinguishes eKR2 from Cl^--pumps[42,162] or H^+-pumps[206–210]. However, at low intracellular sodium concentration (1 mM $[Na^+]_i$) I_s became linearly voltage dependent, but was not affected by the intracellular $[H^+]$ and similar at pH_i 6.0, 7.2 and 9.0. There was no additional effect on the voltage dependence upon further decrease of the intracellular $[Na^+]$ to 0.1 mM (data not shown).

As demonstrated, decreasing intracellular $[Na^+]$ systematically reduced the stationary current density and slowed the off-kinetics. However, as the recordings were performed at high extracellular $[Na^+]$, one could argue that this decrease was caused by a rising Na^+-gradient against the pump rather than a substrate limitation and that the

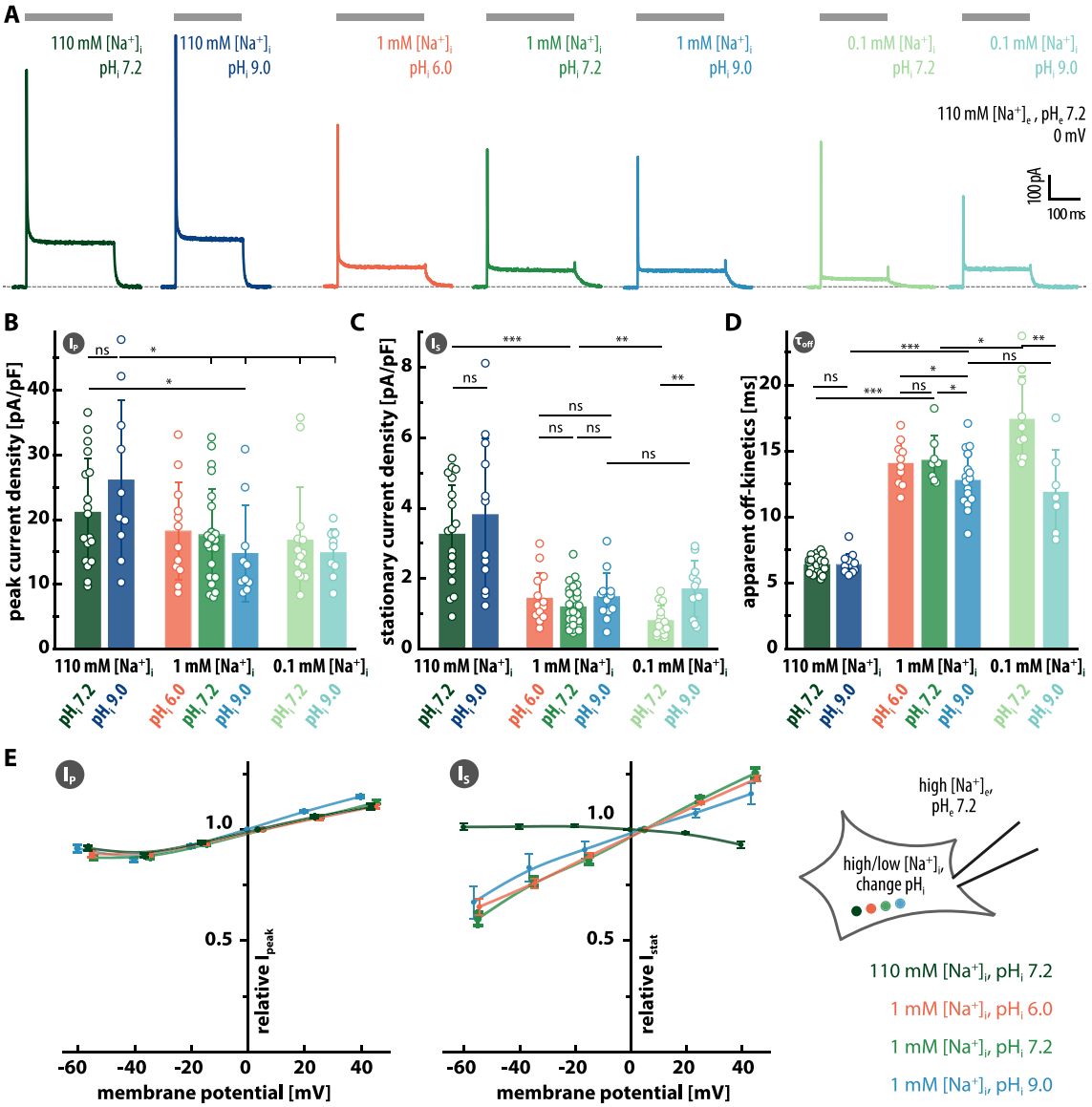

Figure 3.15: Variation of intracellular sodium and protons at 110 mM $[Na^+]_e$ and pH_e 7.2. **A** Representative photocurrent traces of eKR2 at 0 mV after two days of expression in ND7/23 cells at indicated intracellular pH values and $[Na^+]$. Activation with 525 nm LED is indicated by the gray bar. **B** Averaged peak current densities at conditions from A. **C** Average stationary current densities. **D** Corresponding average apparent kinetics of the current decay after light-off resulting from bi-exponential fit. For B, C and D selected significance levels (Wilcoxon rank-sum test) are indicated, for complete list of all p values see appendix A.1. All values were determined after LJP correction from linear interpolation to 0 mV and are represented as mean±SD with individual values as dots. **E** Voltage dependence of I_p (left) and I_s (right) at indicated intracellular conditions. Values are given relative to the respective 0 mV current and LJP are corrected. Data represented as mean±SEM and for I_p n=9, n=14, n=11, n=12 and for I_s n=9, n=14, n=12, n=8.

Na^+-gradient also obscured the measurement of the H^+-dependence. Hence, selected conditions from figure 3.15 were re-measured at low extracellular $[Na^+]$ to have no or even an outward directed Na^+-gradient. Although there are slight differences in the overall results, they were qualitatively similar. The stationary current density was re-

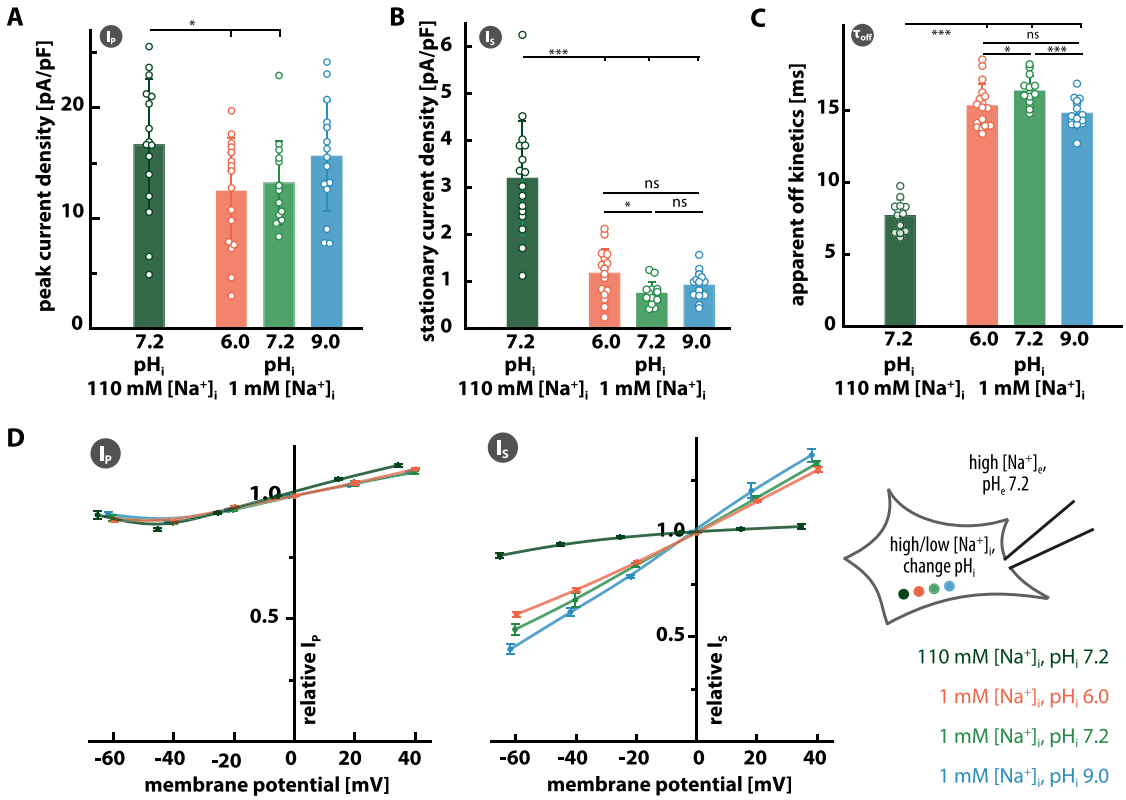

Figure 3.16: pH dependence of the eKR2 photocurrents at 1 mM [Na$^+$]$_e$ and pH$_e$ 7.2. Influence of intracellular [H$^+$] (pH$_i$ 6.0, 7.2 and 9.0) at 1 mM intracellular [Na$^+$] represented by **A** peak photocurrent density, **B** stationary current density and **C** apparent off-kinetics. All values were obtained through linear interpolation after LJP correction and are represented as mean±SD with individual data points as dots **D** Voltage dependence of I_p (left) and I_s (right) at same conditions as A-C. Values relative to the respective 0 mV value and represented as mean±SEM with n=16, n= 17, n=13, n=15 for I_p and n=16, n= 17, n=14, n=17 for I_s.

duced 4.2-fold when the [Na$^+$]$_i$ was lowered from 110 mM to 1 mM and the closing kinetics slowed from 7.7 ± 1.1 ms to 16.3 ± 1.1 ms as seen in figure 3.16. Additionally, the current densities at 110 mM [Na$^+$]$_i$ were with 3.3 ± 1.4 pF at high and 3.2 ± 1.3 pF at low similar (p = 0.93) at both external Na$^+$-concentrations, which is seen by comparing figure 3.15 C and 3.16 B. The independence of the average I_s density from the extracellular [Na$^+$] was preserved at 1 mM intracellular [Na$^+$] with values of 1.1 ± 0.6 pF at high and 0.7 ± 0.3 pF at low extracellular [Na$^+$] (p = 0.08). This supports that the Na$^+$-gradient is not affecting these photocurrent features.

Likewise, the independence of the stationary current density from the intracellular [H$^+$] was mostly preserved (figure 3.16) at low extracellular [Na$^+$]. The currents and off-kinetics were statistically indistinguishable at intracellular pH 6.0 and 9.0 (figure 3.16 B and C) and kinetics at low intracellular [Na$^+$] were fastest at pH 9.0, which argues against H$^+$-pumping. However some aspects were surprising. The density of I_s was 1.6-fold lower at pH 7.2 compared to pH 6.0 with 6 % faster kinetics at pH$_i$ 6.0 (figure 3.16

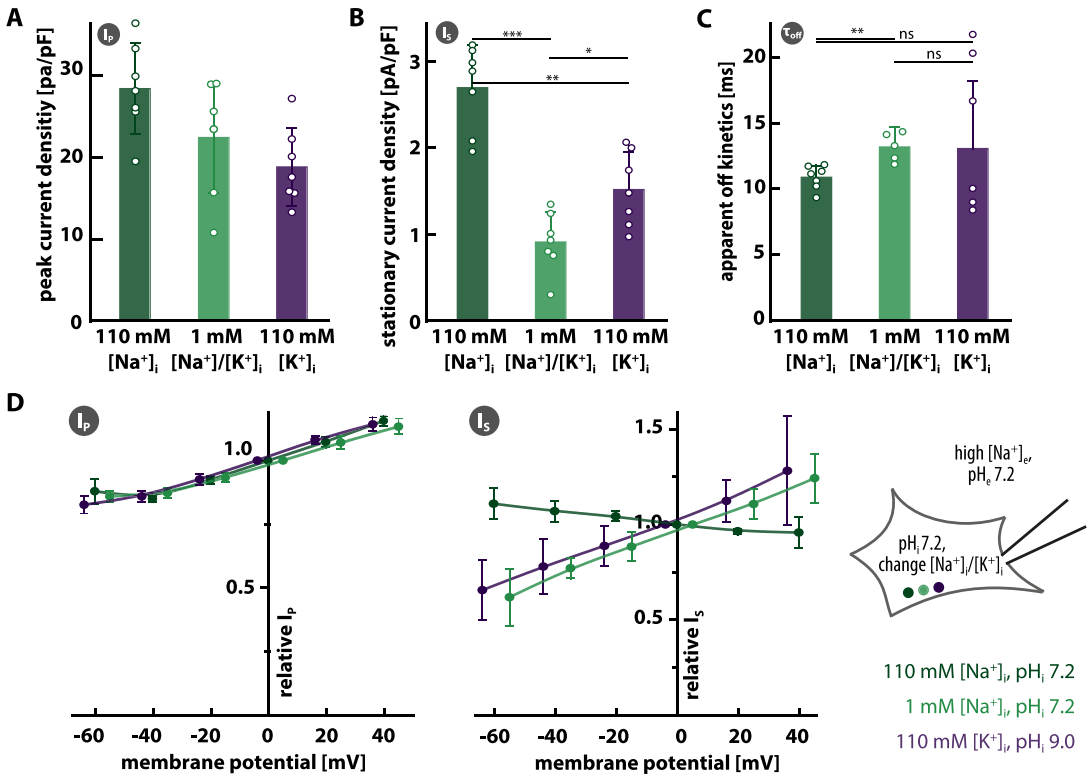

Figure 3.17: Variation of intracellular [K^+] at pH_i 7.2. **A** Average peak current densities at different intracellular [K^+] at −20 mV. pH_i=7.2, 110 mM $[Na^+]_e$ and pH_e=7.2. Currents were evoked with an 525 nm LED for 500 ms. **B** Corresponding average stationary current densities at −20 mV. **C** Corresponding average kinetics of the current decay after light off resulting from a bi-exponential fit. All values were obtained after correction of the LJP and interpolation to −20 mV and are represented as mean±SD with individual data points. Significance was tested with the unpaired Wilcoxon rank-sum test. **D** Current voltage relation for I_p (left) and I_s (right). Values given relative to respective 0 mV value and presented as mean±SEM. For I_p n=13, n=11, n=14 and for I_s n=13, n=11, n=14

C). Additionally, with 16.3 ± 1.1 ms at low *vs.* 14.3 ± 1.9 ms at high $[Na^+]_e$ (p = 0.006) kinetics at 1 mM $[Na^+]_i$ and pH_i 7.2 were also slower than at the corresponding high $[Na^+]_e$ condition (*cf.* figures 3.15 D and 3.16 C).

The voltage dependence of I_s slightly differed compared to high extracellular $[Na^+]$. With the voltage independence at high intracellular $[Na^+]$ and an emerging voltage dependence at low intracellular $[Na^+]$ (figure 3.16), the most evident features were conserved. But at low $[Na^+]_i$ the voltage dependence of I_s was systematically dependent on the pH_i getting steeper with decreasing $[H^+]$ (figure 3.16 D). Taken together, this implies that the Na^+-dependence and the H^+-independence of the pumping activity is preserved at low extracellular $[Na^+]$ and thus not induced by the Na^+-gradient. Still it is evident that the extracellular $[Na^+]$ influences the photocurrents as results were not exactly the same compared to high extracellular $[Na^+]$.

While in most of the published spectroscopic measurements the Na^+-free condition was achieved by a replacement of Na^+ with K^+, here it was replaced by the non-

transported N-methyl-D-glucamine (NMG) whenever Na^+ was reduced. Nevertheless, it should be investigated whether eKR2 pumps K^+ or not, which is why recordings at 110 mM intracellular [K^+] were performed and compared to 1 mM $[Na^+]_i$/1 mM $[K^+]_i$ and 110 mM intracellular Na^+. Whenever the patch was established at asymmetric K^+-concentrations the measurements became more noisy and less stable, which increased at positive holding potentials. Thus, current densities and off-kinetics were not extracted at 0 mV like before but at −20 mV instead, because it was reasonable that the noise is evoked by endogenous voltage-gated potassium channels, which open at positive membrane voltages. Similar to all previous changes of the intracellular ionic condition, the peak current density was not significantly altered by a change in $[K^+]_i$ (figure 3.17 A). In contrast, the stationary current density was affected, and with $1.5 \pm 0.5\,pA\,pF^{-1}$ significantly ($p = 0.017$) higher than at low intracellular [K^+] with $0.9 \pm 0.4\,pA\,pF^{-1}$. Nevertheless, it was 1.8 times smaller ($p = 0.002$) than at high $[Na^+]_i$ where current densities reached $2.7 \pm 0.5\,pA\,pF^{-1}$ (figure 3.17 B).

Consistent with previous results (*cf.* figure 3.15 D), kinetics were slowed upon reduction of intracellular Na^+ from 10.8 ± 0.9 ms to 13 ± 1 ms ($p = 0.002$). Upon increase of the K^+ the average kinetics were 13 ± 5 ms similar to those at low Na^+/K^+ but significantly slower than at high Na^+. However, the kinetics spread over a wider range with some similar to high intracellular $[Na^+]_i$ and some even slower than at the low Na^+ condition (3.17 C), which makes these results difficult to interpret. In conclusion, the stationary current densities rose significantly upon increased intracellular K^+ and kinetics were slower than at high intracellular Na^+ hinting at a K^+-transport, which is less effective than the Na^+-transport. However, the experiment could be repeated in the presence of a K^+-channel blocker like tetraethylammonium to block endogenous channels.[h]

Again also the voltage dependence of the photocurrents was investigated with I_p showing mild dependence on the membrane voltage and unaffected by the intracellular [K^+] (figure 3.17 D, left). However, the stationary photocurrents at high intracellular K^+ were more voltage dependent similar to the currents at low intracellular Na^+ (figure 3.17 D, right).

Probing proton pumping by pH imaging

The electrophysiological recordings showed no evidence for a contribution of protons to the stationary photocurrent of eKR2. Nevertheless, the possibility of proton pumping was further explored via pH imaging, because potential proton pumping of eKR2, should be accompanied by local pH changes at the cell membrane. A fluorescence assay

[h] 2 mM $BaCl_2$ in the extracellular buffer was tried, which did not have the desired effect.

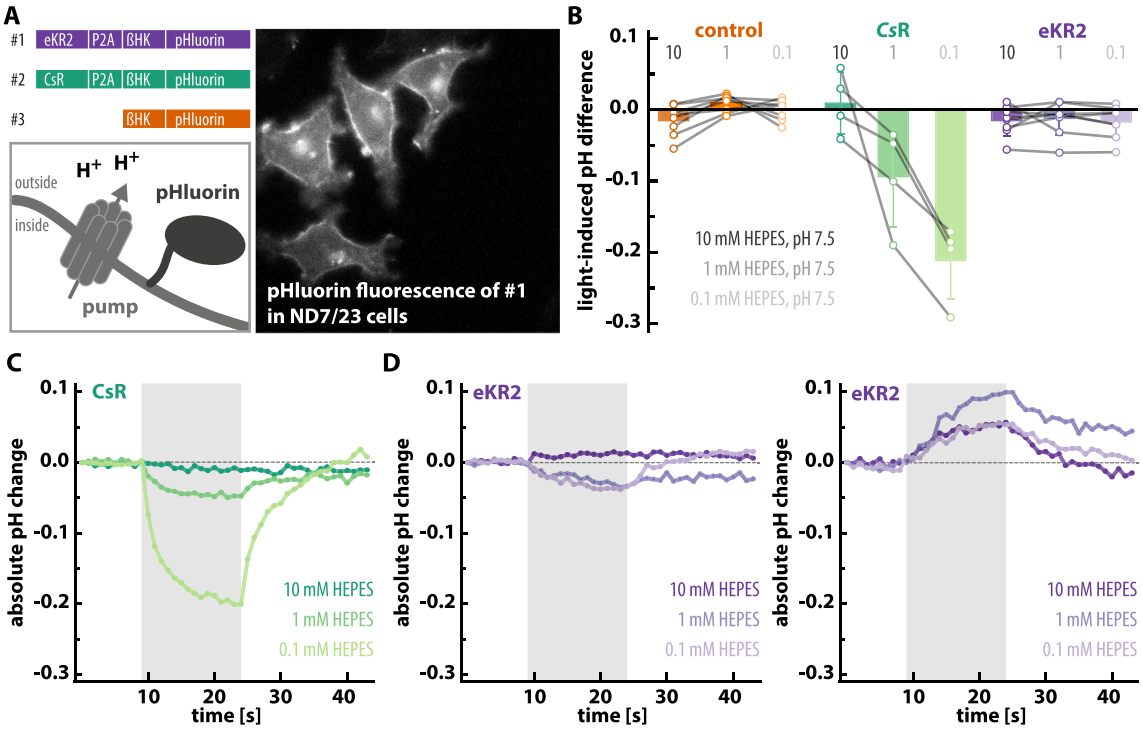

Figure 3.18: pH imaging to determine local changes in extracellular pH. A Construct design and schematic representation of the construct expressed at the cell membrane and sample image of ND7/23 cells expressing construct #1 for one day **B** Calculated average changes of the pH at the extracellular surface of the cell evoked by light-induced pumping activity of the control construct (orange), H^+-pump *Cs*R (green) and eKR2 (purple) at three different external buffer concentrations, respectively (10 mM, 1 mM and 0.1 mM HEPES). Data is presented as mean±SD with individual data points as dots. **C** Representative time traces of the local pH changes on the extracellular surface induced by H^+-pumping of *Cs*R at three different HEPES concentrations. **D** Two distinct responses for cells expressing the eKR2 construct (#1) were observed one implying acidification (seen for 3 cells) and one suggesting alkalinization (seen for 2 cells). Half of the cells showed no light response and n=10.

to monitor the extent of extracellular acidification by outward-directed H^+-pumps was devised by Johannes Vierock in our group[183]. In principle, superecliptic pHluorin is tethered to the extracellular side of the membrane (figure 3.18 A) and its pH-dependent fluorescence is used to monitor the local pH changes induced by activation of a co-expressed H^+-pump. Reversing this principle, the assay can also be used to investigate whether an ion pump is transporting H^+ at a given condition. In case of eKR2, a systematic dependence of the photocurrents on intracellular [H^+] like for the H^+-pump CsR was never seen (see figures 3.14 and 3.15). However, the affinity of eKR2 for H^+ could be much higher than for Na^+ rendering it effectively insensitive to the performed pH changes, because it always pumps a proton together with the sodium ion (co-transport). A co-transport like this, should in turn modify the local pH on the extracellular surface rendering it accessible via pH imaging. Together with Jonas Wietek[i] the imaging setup

[i] Thanks!

was equipped with a new light source and CCD camera and the recording protocol was improved to avoid simultaneous illumination of pHluorin and the pump. For experimental details see section 2.4.2.

Control measurements with construct #3 without any pump and the H^+-pump *Cs*R (construct #2 [j]) verified the assay. There was no signal without a pump (figure 3.18 B) and a light-dependent acidification, which got more pronounced the lower the extracellular solution was buffered, induced by H^+-pumping of *Cs*R (figure 3.18 B and C). Interpretation of eKR2 results was difficult as opposing results were observed for some cells. For five out of ten cells no light-induced pH change was observed regardless of the HEPES concentration. For two cells a light-dependent elevation of the extracellular pH was recorded, which was independent of the HEPES concentration. For three cells there was a slight light-induced and reversible acidification of the extracellular surface most evident at 0.1 mM HEPES (figure 3.18 D). On average, even excluding the two cells with the unexpected alkalinization, there was no light-dependent acidification observed for the eKR2 construct under this condition (figure 3.18 B), which could prove H^+-pumping of eKR2. It is still interesting that for some cells, albeit only observed at 0.1 mM HEPES, a light-dependent acidification was observed. Nevertheless, there are several aspects hindering conclusive interpretation of the experiment, which will be discussed in more detail later (see section 4.2.1).

3.2.4 Influence of extracellular condition, membrane potential and gradients

Next, influences of the applied membrane potential on the stationary photocurrents of eKR2 should be investigated. Current-voltage relations were recorded at different extracellular Na^+- (110 mM or 1 mM $[Na^+]_e$) and H^+-concentrations (pH_e 7.2 or 9.0) at selected intracellular conditions to additionally see the influence of Na^+- and H^+-gradients.

At 110 mM intracellular $[Na^+]$ and pH_i 7.2 stationary photocurrents were largely independent of the membrane voltage (figure 3.19 A). Moreover, I_s was barely affected by changing the external $[Na^+]$ or pH_e (figure 3.19 A). In contrast, I_s was slightly affected by the external buffer composition but remained largely voltage independent when intracellular $[H^+]$ was reduced at high intracellular $[Na^+]$ (110 mM $[Na^+]_i$, pH_i 9.0) as seen in figure 3.19 C. Here, I_s at 0 mV was 10 % decreased upon removal of extracellular $[Na^+]$ and stationary currents were highest at pH_e 9.0 and high $[Na^+]_e$ (figure 3.19 C).

In contrast, at low internal $[Na^+]$ (1 mM $[Na^+]_i$, pH_i 7.2) I_s became linearly voltage-dependent increasing 0.2 pA mV^{-1} with the membrane voltage at all external conditions (figure 3.19 B). Even more pronounced I_s was again enhanced at high pH_e and reduced

[j] Construct design and #2 and #3 kindly provided by Johannes Vierock.

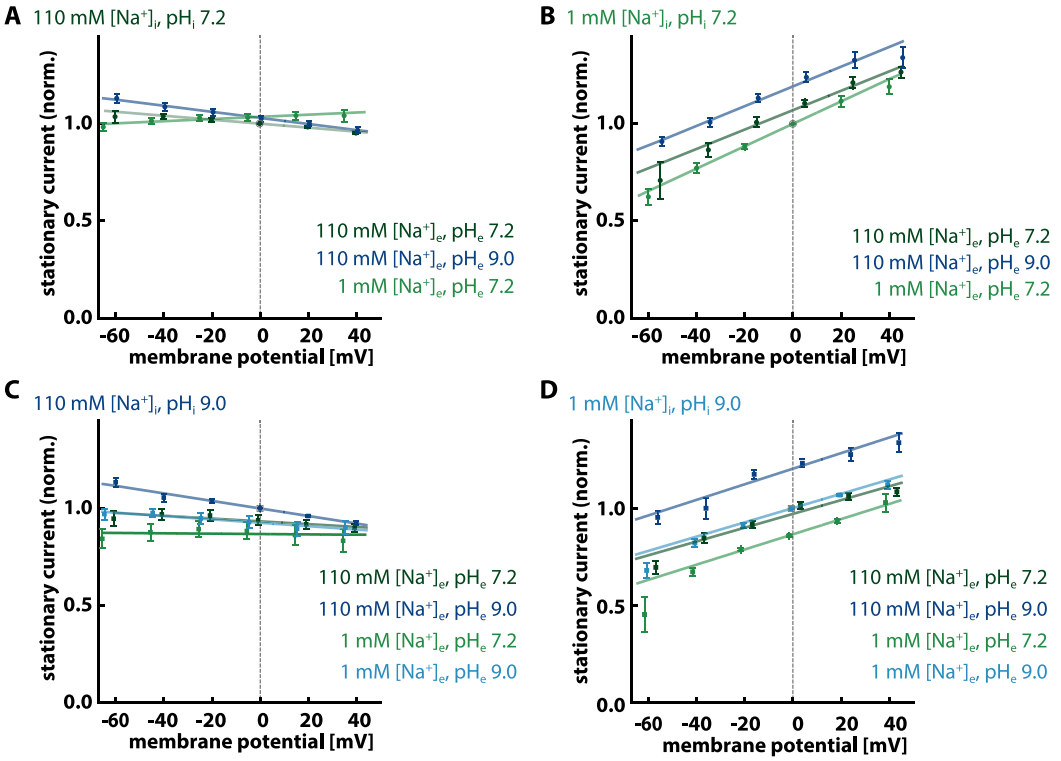

Figure 3.19: Voltage dependence of the stationary current at different ionic gradients and substrate concentrations. Current voltage relations for eKR2 at different extracellular ionic conditions and varying intracellular conditions as indicated. All values are LJP corrected and displayed as mean±SEM. Values are normalized to the respective symmetric 0 mV for each intracellular condition (gray frame). **A** 110 mM $[Na^+]_i$, pH_i 7.2 (n=6, n=5, n=6). **B** 110 mM $[Na^+]_i$, pH_i 9.0 (n=7, n=7, n=7). **C** 1 mM $[Na^+]_i$, pH_i 7.2 (n=8, n=11, n=8, n=6). **D** 1 mM $[Na^+]_i$, pH_i 9.0 (n=6, n=5, n=6, n=6).

at low external $[Na^+]$ (figure 3.19 B). Also at low intracellular $[Na^+]$ a reduction of the intracellular $[H^+]$ did neither qualitatively change the voltage dependence nor the dependence on the extracellular condition (figure 3.19 D). In summary I_s of eKR2 i) was independent of the membrane voltage when intracellular $[Na^+]$ was abundant, ii) became voltage dependent when intracellular $[Na^+]$ was low and iii) was promoted by external $[Na^+]_e$ and alkaline pH_e 9.0 – regardless of the ionic/pH gradient.

Although there was no evidence so far, the possibility that eKR2 pumps H^+ should be further explored. When H^+-pumps like bacteriorhodopsin face a high H^+-gradient against their pumping direction they shut down and pumping activity is inhibited, a phenomenon called the back pressure effect[211,212]. Thus, eKR2 photocurrents were recorded at different pH and Na^+-gradients against the pumping direction to further explore the influence of gradients on the currents. The patch was established at symmetric conditions (figure 3.20 A-C, left column) and then the external pH was reduced to 5.0, followed by an additional change of the extracellular Na^+-concentration to create gradients. When intracellular Na^+ was abundant (figure 3.20 A), change from extracellular

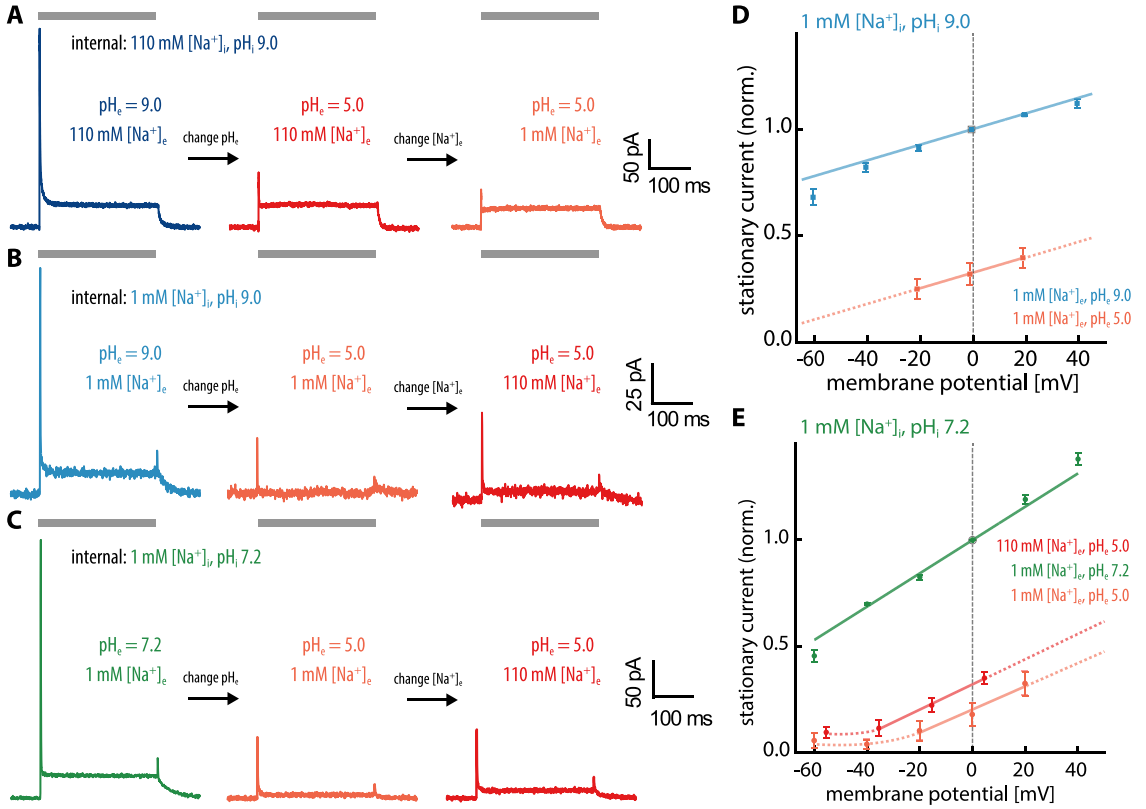

Figure 3.20: Effect of H^+- and Na^+ gradients on eKR2 photocurrents. Photocurrent traces of eKR2 at 0 mV with the patch established at symmetric conditions (left) followed by a change of pH_e to 5.0 (middle) and by a change of $[Na^+]_e$ to create proton and sodium gradients. At intracellular **A** 110 mM $[Na^+]$ and pH_i 9.0, **B** 1 mM $[Na^+]$ and pH_i 9.0 and **C** 1 mM $[Na^+]$ and pH_i 7.2. **D** Voltage dependence of I_s at intracellular pH 9.0 and 1 mM $[Na^+]$ at extracellular conditions as indicated. Values are LJP corrected and represented as mean±SD relative to symmetric current at 0 mV, n=2. **E** Voltage dependence of I_s at intracellular pH 7.2 and 1 mM $[Na^+]$ at extracellular conditions as indicated. Values are LJP corrected and represented as mean±SD relative to symmetric current at 0 mV, n=6 each.

pH 9.0 to 5.0 reduced I_p to 30 % but left I_s unaffected (figure 3.20 A middle). When extracellular Na^+ was removed additionally, I_p and I_s were only marginally further reduced (figure 3.20 A right column). In contrast, at low intracellular $[Na^+]$ (1 mM $[Na^+]_i$) I_s was reduced together with I_p upon establishment of the H^+-gradient (figure 3.20 B middle). When in addition to the H^+-gradient a Na^+-gradient was applied at low intracellular Na^+ both I_p and I_s increased again (figure 3.20 B, right). Qualitatively, results were similar at low intracellular $[Na^+]$ and pH_i 7.2 as seen in figure 3.20 C indicating that the observed reduction of the currents was not evoked by the pH-gradient, but rather the extracellular acidification. This conclusion is supported, when the current-voltage relation at acidic extracellular conditions is compared at intracellular pH 9.0 and 7.0 (figure 3.20 D and E). Although the pH-gradient is higher at intracellular pH 9.0 than 7.2, the reduced I_s after extracellular acidification is with 11 ± 10 % and 18 ± 10 % comparable in both cases.

3.2.5 Spectral properties and their dependence on the ionic condition

In addition to the specificity of the ion transport, the spectral properties of eKR2 that are accessible by electrophysiological measurements were investigated. Separately, the spectroscopic investigation of the purified protein was performed by Arita Silapetere in our lab. The action spectrum of eKR2 at standard conditions peaked at 525 ± 1 nm (figure 3.21 A) similar to the absorption spectrum of the purified protein, which revealed a maximal sensitivity at 527 nm (detergent, pH 8.0)[190].

Titration of the photocurrents with the intensity of the activation light showed that the amplitude of I_p, I_s and the inactivation from the transient to the stationary current level depended on the activation light. For I_s half-maximal currents were observed at an irradiance of $0.58 \pm 0.10\,\mathrm{mW\,mm^{-2}}$. Additionally an inactivation of I_s for intensities higher than $7\,\mathrm{mW\,mm^{-2}}$ (figure 3.21 B), which reached 25 % at the highest intensity, was revealed. Under continuous illumination the transient I_p decayed bi-exponentially to I_s with a fast (80 %) and a slow component (20 %). Similar to the extent of the inactivation, both kinetic constants were light dependent as seen in figure 3.21 B (inset) and accelerated with rising light intensities. The fast component was 2.9-fold and the slow component 3.4-fold accelerated comparing $7\,\mathrm{mW\,mm^{-2}}$ and $46\,\mathrm{mW\,mm^{-2}}$, respectively (figure 3.21 C). At the highest intensity ($46\,\mathrm{mW\,mm^{-2}}$) the slow component of the inactivation was with a time constant of 6.8 ± 1.2 ms similar to the apparent off-kinetics at this intensity and ionic condition 6.8 ± 0.6 ms (*cf.* figure 3.21 C and 3.15 D).

Similar to the off-kinetics (see section 3.2.3), the bi-exponential inactivation from I_p to I_s depended on intracellular $[Na^+]$. Whereas the dominating (80 %) fast component accelerated from 0.90 ± 0.15 ms to 0.56 ± 0.14 ms upon reduction of $[Na^+]_i$, the slow component (20 %) slowed from 6.7 ± 1.8 ms to 15 ± 7 ms and almost completely vanished with a fraction of only 2 % at low $[Na^+]_i$. As seen before for the intensity dependence, the slow component of the inactivation kinetics behaved similar to the apparent off-kinetics and slowed upon reduction of intracellular $[Na^+]$.

Another feature of the photocurrents became evident when the intracellular $[Na^+]$ was lowered to 1 mM. In contrast to high intracellular $[Na^+]$, a fast-rising and transient increase of I_s (overshot) was observed after the light was switched off as seen in figure 3.22 A. This overshot was also observed at 0.1 mM intracellular $[Na^+]$ and preserved at all pH_i values (see figure 3.15 A). The ratio of I_p to I_s (*e. g.* the extend of inactivation) was 6.8 ± 1.1 at high intracellular $[Na^+]$ and increased to 16 ± 4 at 1 mM intracellular $[Na^+]$ (figure 3.22 C) . Interestingly, the ratio from I_p to the current overshot only appearing at low $[Na^+]_i$ was 7.0 ± 1.5 and thus similar to the high $[Na^+]$ ratio of I_p to I_s (figure 3.22 C). This suggested that the overshot might not be an additional activation but rather a

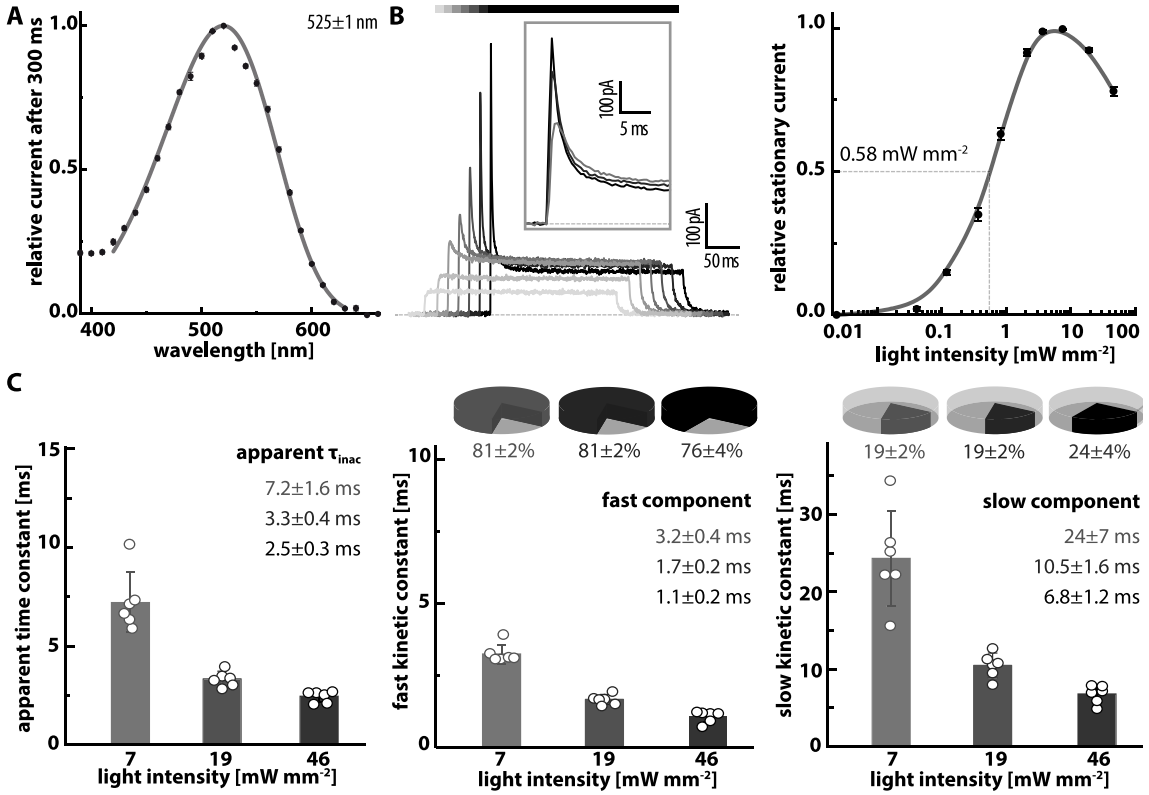

Figure 3.21: Spectral and light sensitivity of eKR2 at standard conditions. **A** Action spectrum of I_s at 0 mV after 300 ms illumination with varying wavelength light of equal photon flux. Data is presented as mean±SEM and n=6. **B** Left: Representative current traces from titration of the photocurrents with the intensity of the activation light. Right: Relative I_s at different light intensities, normalized to respective maximal current and represented as mean±SEM with n=6. **C** Time constants of the inactivation kinetics from I_p to I_s under continuous illumination resulting from bi-exponential fit with apparent (left), fast (middle) and slow (right) kinetic constants at the three highest light intensities. Data are represented as mean±SD with individual data points as dots. Pie charts indicate the amplitude of the respective component; conditions like A and B.

light-induced inactivation for the duration of the light pulse, which disappeared when illumination was terminated.

To elucidate that, the photocurrents were titrated with the intensity of the actinic light again, but at low intracellular [Na^+], where the overshot occurred (figure 3.22 D). Similar to standard conditions, I_p and I_s rose light-dependent with a half-maximal I_s at $0.6 \pm 0.4\,\mathrm{mW\,mm^{-2}}$ (figure 3.22 D). Interestingly, the overshot was first visible at $18\,\mathrm{mW\,mm^{-2}}$, the same intensity were inactivation of I_s started (figure 3.22 D). From a light intensity of $18\,\mathrm{mW\,mm^{-2}}$ on, the amplitude of the overshot increased with rising intensities (3.22 D, inset). Interestingly, the highest overshot, which was observed at $50\,\mathrm{mW\,mm^{-2}}$, was still higher than the highest I_s, which was observed at $12\,\mathrm{mW\,mm^{-2}}$ light intensity. Thus, the overshot cannot be completely explained by an inactivation over the course of illumination. Taken together, the overshot was only present when the photocycle was slow due to low $[Na^+]_i$ and it was dependent on the intensity of the

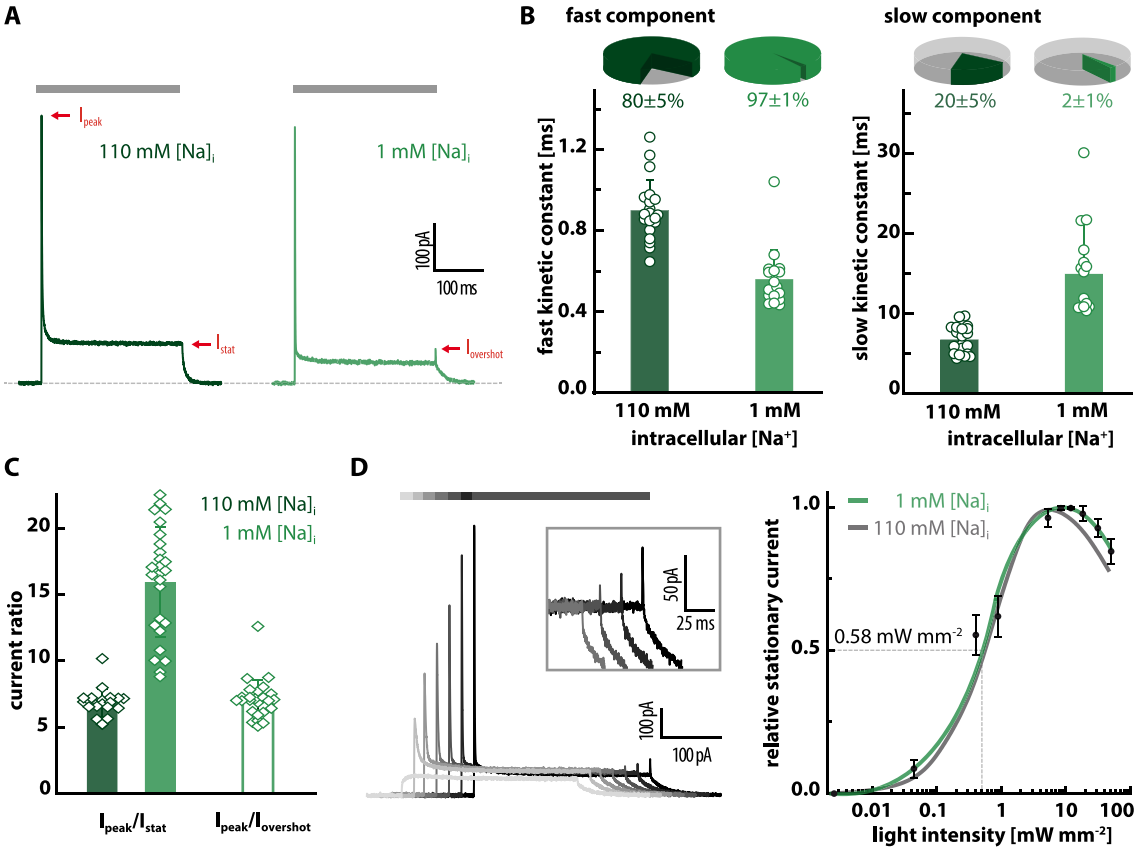

Figure 3.22: Na^+-dependence of inactivation and light sensitivity. **A** Sample traces of eKR2 at high and low $[Na^+]_i$ at 0 mV with the current overshot after light-off visible at low $[Na^+]_i$; 110 mM $[Na^+]_e$, $pH_{i/e}$ 7.2. **B** Fast (left) and slow (right) time constants of inactivation kinetics from I_p to I_s at conditions from A and maximal intensity. The pie charts indicate amplitude ratio of the two components resultant from bi-exponential fit. Data represent mean±SD with individual values as dots. **C** Ratio of I_p to I_s at high and low $[Na^+]_i$ and I_p to current overshot at low $[Na^+]_i$. **D** Representative photocurrent traces at different light intensities at low $[Na^+]_i$ with average light titration (±SEM) curve (right, n=6) in comparison to titration at high intracellular Na^+ (gray).

activation light. This implies that it was mainly caused by a photoactivated conversion of an intermediate in the photocycle by-passing the pumping intermediate and thereby reducing I_s in the light.

Previous results showed that the amplitude of I_p was largely unaffected by changes of the intracellular ionic condition ($[Na^+]$ and $[H^+]$, *cf.* figure 3.15 B). Nevertheless, the kinetics of the recovery of I_p after previous activation can serve as indicator for the photocycle turnover time[213,214]. Thus, double pulse experiments (figure 3.23 A) at different intracellular ionic conditions were conducted to estimated influences of the substrate concentration on the photocycle turnover time.

Although the absolute values were systematically slower at all conditions, recovery of I_p was similarly dependent on the intracellular ion concentration as the off-kinetics (see figure 3.15 D for comparison). The recovery kinetics slowed when intracellular

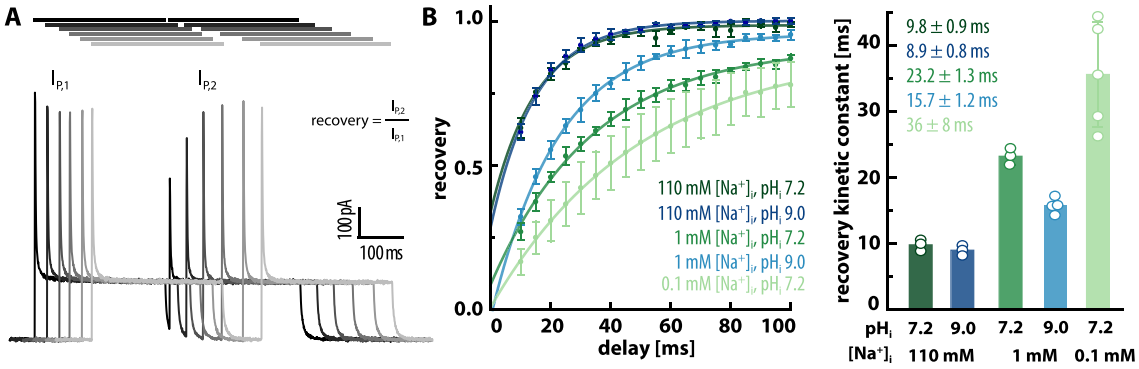

Figure 3.23: Recovery of I_p for eKR2 at different intracellular conditions. **A** Sample traces at 0 mV with prolonging delay between repetitive activation to determine the recovery of I_p as ratio of I_{p2} over I_{p1}. Extracellular condition was always the same with 110 mM $[Na^+]_e$, pH_e 7.2. **B** Recovery curve at indicated intracellular conditions with varying Na^+- and H^+-concentrations. Data displayed as mean±SD with n=3, n=3, n=3, n=4 and n=5. Data was fitted with a mono-exponential function and resultant time constants displayed in the bar graph, mean±SD with individual data points (right).

$[Na^+]$ was lowered at pH_i 7.2 from 9.8 ± 0.9 ms at 110 mM over 23.2 ± 1.3 ms at 1 mM to 36 ± 8 ms at 0.1 mM $[Na^+]_i$ (figure 3.23 B). At pH_i 9.0 the kinetics were similar to pH_i 7.2 at 110 mM $[Na^+]_i$ with 8.9 ± 0.8 ms at pH 9.0 and 9.8 ± 0.9 ms at pH 7.2 and thus merely influenced by the pH at high $[Na^+]_i$. At reduced intracellular $[Na^+]$ the recovery got 2.3 times slowed at pH_i 7.2 and 1.8-times slowed at pH_i 9.0 in comparison to the respective high $[Na^+]_i$ value. Overall, the photocycle was always faster at pH_i 9.0 than at the respective pH_i 7.2 condition, which was most evident at 1 mM $[Na^+]_i$ (figure 3.23). This was similar to the off-kinetics, which were as well faster at pH_i 9.0 (figure 3.15 D).

3.2.6 Laser-induced single turnover measurements

To improve the resolution of fast kinetic components, photocurrents were recorded under single turnover conditions induced by a nanosecond laser pulse. Moreover, single turnover conditions eliminate the possibility of secondary photochemistry events, which may occur under continuous illumination rendering single turnover photocurrents more representative for the electrical steps in the photocycle. Additionally, they are more comparable to spectroscopic flash photolysis measurements, which monitor absorption changes of the protein as well under single turnover conditions. We recorded photocurrents of eKR2 upon activation with a nanosecond laser pulse of 525 nm wavelength at three different symmetric ion conditions: 110 mM $[Na^+]_{i/e}$ at $pH_{i/e}$ 7.2, 1 mM $[Na^+]_{i/e}$ at $pH_{i/e}$ 7.2, and 1 mM $[Na^+]_{i/e}$ at $pH_{i/e}$ 9.0. At all ionic conditions photocurrents rose to their maximum within 70 µs, which is beyond our time resolution in ND7/23 cells. Thus, only the decay of the current was fitted with a tri-exponential function and the resulting components were plotted onto the current (figure 3.24 A-C).

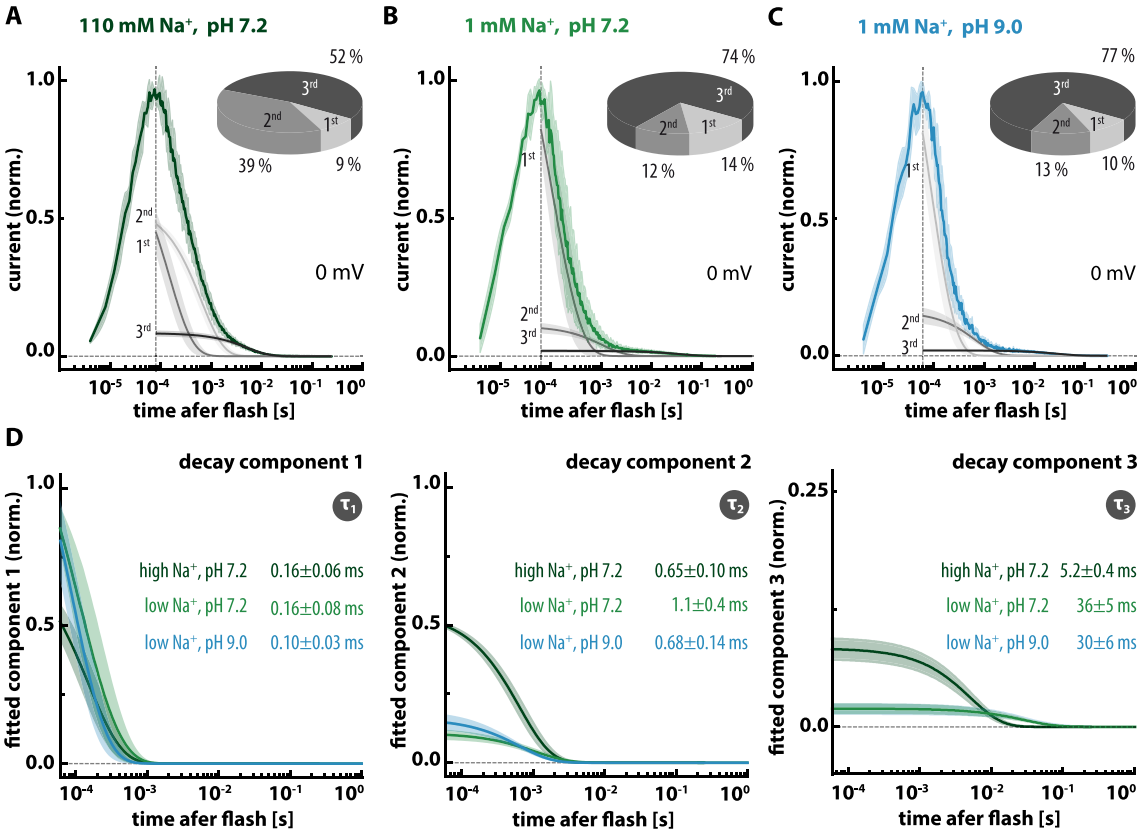

Figure 3.24: Laser-induced single turnover photocurrents of eKR2 at 0 mV in ND7/23. Normalized single turnover photocurrent displayed as mean±SD of eKR2 at symmetric **A** 110 mM $[Na^+]_{i/e}$ and $pH_{i/e}$ 7.2 (n=3) **B** 1 mM $[Na^+]_{i/e}$ and $pH_{i/e}$ 7.2 (n=4) and **C** 1 mM $[Na^+]_{i/e}$ and $pH_{i/e}$ 9.0 (n=5). Resultant components of the tri-exponential fit of the current decay are plotted onto the currents. Pie charts indicate the integrals for the respective decay component resulting from the fit. **D** 1st (left), 2nd (middle) and 3rd decay component compared at the three different ionic conditions. Data is presented as mean±SD and the kinetics constants resulting from the exponential fit are given. Note the 4-fold upscaled y-axis for the slowest component.

At standard conditions (figure 3.24 A) two sub-millisecond (1st and 2nd) components with similar relative amplitudes were identified, which decayed with time constants τ_1 0.16 ± 0.06 ms and τ_2 0.65 ± 0.10 ms (figure 3.24 A). From the millisecond time regime on the current was carried by the 3rd component with smaller relative amplitude decaying with τ_3 5.2 ± 0.4 ms (figure 3.24 A). Although, the slow component contributed only 6 ± 1 % to the amplitude under single turnover conditions it carried 53 ± 1 % of the charge as illustrated by the relative integrals of the individual components (figure 3.24 A, pie chart). Based on the kinetic constants it can be concluded that the 3rd component dominates I_s evoked by continuous illumination.

Symmetric reduction $[Na^+]$ at $pH_{i/e}$ 7.2 did neither affect the relative integral (9 ± 2 % *vs.* 14 ± 4 %, p=0.1, unpaired t-test) nor τ_1 of the 1st component (0.16 ± 0.60 ms *vs.* 0.16 ± 0.80 ms, p = 0.9, unpaired t-test). The 2nd component was likewise not affected

regarding its kinetics with 0.65 ± 0.10 ms at high and 1.1 ± 0.4 ms at low [Na^+] (p=0.08, unpaired t-test). However, the relative amplitude and integral were reduced 5.7- and 3.2-fold, respectively (p<0.0001, unpaired t-test) (figure 3.24 B and D). The sole influence of Na^+-reduction on a kinetic constant was observed for the 3rd component, where τ_3 slowed 7-fold from 5.2 ± 0.4 ms to 36 ± 5 ms (p<0.0001, unpaired t-test). Consequently, the 3rd component can be considered the rate limiting step. In accordance, the relative amplitude of the 3rd component was reduced to 1.3 ± 1.0 % when Na^+ was reduced.

When H^+-concentration was reduced along with the Na^+-concentration (figure 3.24 C), the photocurrents showed no significant qualitative changes compared to low [Na^+] at pH 7.2, which was surprising as accelerated off-kinetics and faster recovery of I_p upon reduction of intracellular [H^+] was seen before for continuous illumination. However, as well in the single turnover currents there were tendencies of acceleration of all three components although not significant (figure 3.24 D) and in the single turnover experiment [H^+] was reduced symmetrically in contrast to previous measurements, were it was only changed on the substrate side.

So far single turnover photocurrents at 0 mV were discussed, which is the preferential holding potential for a comparison to spectroscopic single turnover experiments, because there is no membrane potential for spectroscopic measurements in detergent. In addition to that, the voltage dependence of the single turnover photocurrents was investigated in the range from −60 mV to 30 mV at high and low [Na^+] at pH 7.2 (figure 3.25 A and B). None of the kinetic constants showed voltage dependence at high [Na^+], (figure 3.25 C), while at low [Na^+] the slow kinetic component accelerated with increasing voltage (figure 3.25 D). This voltage dependence of the single turnover kinetics explains the voltage dependence observed for I_s. At high Na^+-concentrations, where the slow kinetic constant of the single turnover currents was unaffected by the membrane voltage (figure 3.25 C), no voltage dependence was observed for I_s. In contrast, at low [Na^+] the accelerated turnover at increased membrane voltages in the single turnover currents (figure 3.25 D) mediates higher currents and thus voltage dependence of I_s under continuous illumination, which was indeed observed at low [Na^+].

Surprisingly and in contrast to the low Na^+-conditions, the relative integral of the 2nd and slow component were both voltage dependent at high [Na^+][k]. While the integral of the 1st component was unaffected by the voltage, the slowest and the 2nd component contributed different amounts to the overall charge movement depending on the membrane voltage (figure 3.25 C). At −60 mV the 2nd component carried 30 % of the charge, while the slowest component accounted for 65 %. With an increase of the membrane voltage

[k] This was not observed for *Cs*R, there the integrals were constant over the voltage range, similar to the low [Na^+] conditions for eKR2 (personal communication with Johannes Vierock).

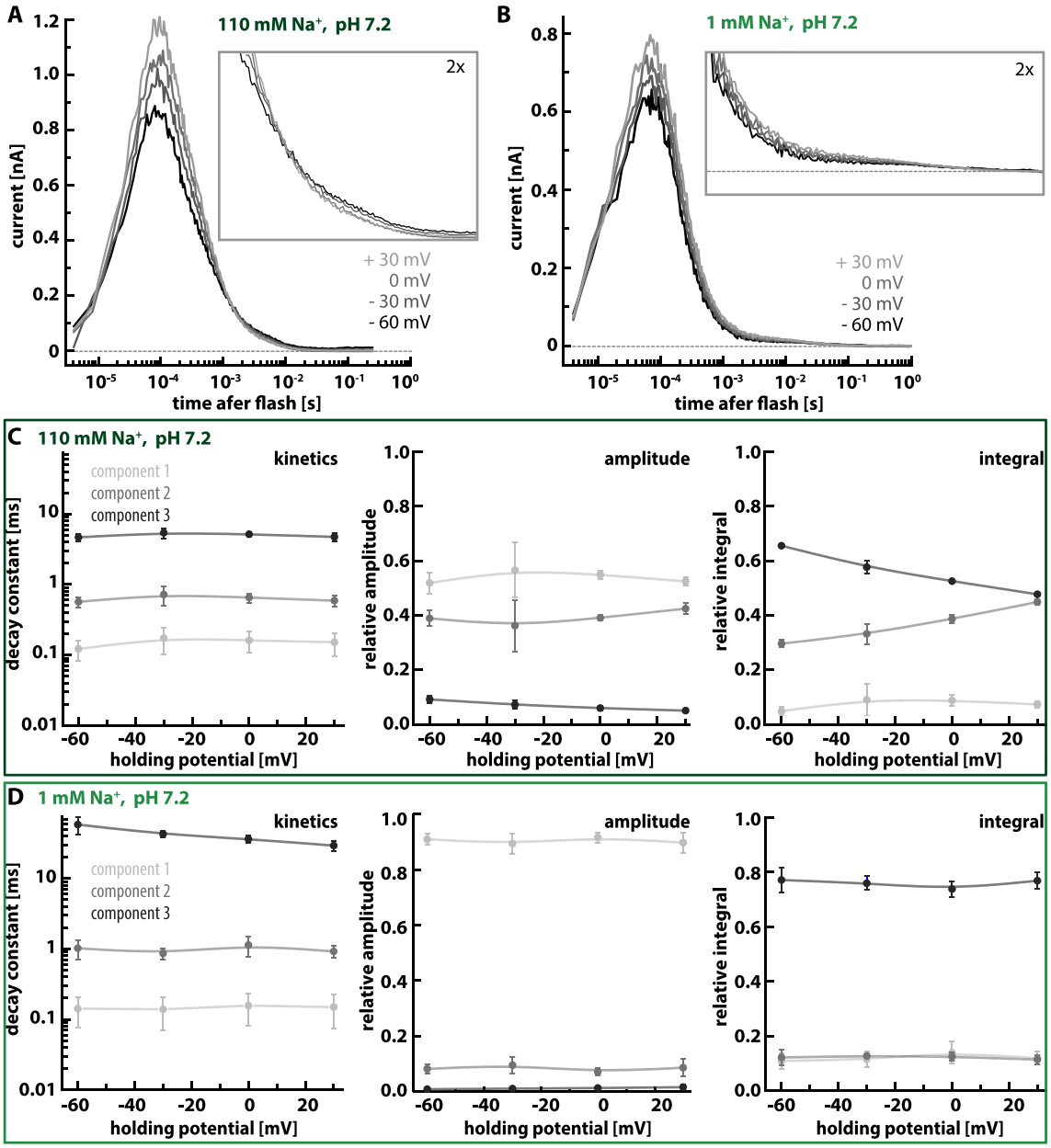

Figure 3.25: Voltage dependence in single turnover currents of eKR2. **A** Representative single turnover photocurrents of eKR2 at different membrane potentials at pH $7.2_{i/e}$ and high symmetric [Na^+]. **B** Voltage dependence of single turnover currents at low symmetric [Na^+] (pH $7.2_{i/e}$). Corresponding time constants (left), relative amplitudes (middle) and relative integrals of individual decay components resulting from tri-exponential fit at **C** high (n=3) and **D** low symmetric [Na^+] (n=4), $pH_{i/e}$ 7.2. Data is represented as mean±SD.

the contribution of the 2nd component linearly increased to 45 %, while it linearly decreased to 47 % for the slowest component. Assuming that each component represents the same charge movement (same amount and distance) at the different voltages, this is an unexpected result. Kinetics could change and entail different amplitudes but the integral should be constant. The most straight forward explanation would be that not

always the same charge movement is observed. This could be explained by two different protein conformations populated in different ratios depending on the membrane voltage or two different pathways of the charge in this electrogenic step, which are preferred in varying ratios depending on the membrane voltage.

3.2.7 Neuronal inhibition with eKR2

Finally, the optogenetic potential of eKR2 should be demonstrated in neuronal cell culture[1] and be compared to construct #091 (KR2_TS-YFP_ER), which is capable of light-induced neuronal inhibition as demonstrated before[215]. Hippocampal mouse neurons were transduced with adeno-associated virus encoding for eKR2 (#092), construct #091 and a control only expressing a fluorescent protein. Expression of all three constructs did not significantly alter the resting membrane potential of the neurons (#092 76 ± 7 mV, #091 75 ± 6 mV, control 75 ± 5 mV), which shows that expression itself is non-toxic.

The enhanced expression of eKR2 was preserved in neurons (figure 3.26 A), it was located to the soma and also trafficked to the neurites and did not show intracellular aggregation like #091 (not shown, but also reported here[215]). The rheobase is the minimal sustained somatic current injection sufficient to drive action potentials. Upon hyperpolarization of the membrane the rheobase is shifted, because a higher current is needed to drive spiking (rheobase shift). The light-induced rheobase shift caused by outward sodium pumping was determined for eKR2 and compared to #091. Already at 0.5 mW mm^{-2} the rheobase in eKR2-expressing neurons was significantly shifted in the light compared to the dark and the rheobase shift evoked by activation of eKR2 was significantly higher than for #091 (figure 3.26 B). This effect increased for eKR2 upon rising light intensities to reach a rheobase shift of 378 ± 234 pA at 10 mW mm^{-2}, while it saturated already at 1 mW mm^{-2} for #091 at a five-fold smaller value.

Another way of evaluating the optical silencing capabilities is the injection of a ramp current pulse (0.44 pA ms^{-1}), which was combined with continuous illumination throughout the ramp and compared to the dark (figure 3.26 C). In the light both constructs increased the latency to the first action potential and thereby reduced the relative number of action potentials fired during the ramp in comparison to the dark (figure 3.26 C). At 10 mW mm^{-2} construct #091 decreased the number of action potentials on average by 24 %, whereas eKR2 achieved a light-induced reduction of 74 % and for some cells completely abolished firing during the ramp. From the ramp protocol the average hyperpolarization induced by eKR2 activation was extracted as well, which was with 30 ± 11 mV three-fold higher than that of construct #091 with 9 ± 7 mV (figure 3.26 D).

[1] All neuronal recordings were performed under the supervision and together with Yinth Andrea Bernal Sierra and are presented here with her consent.

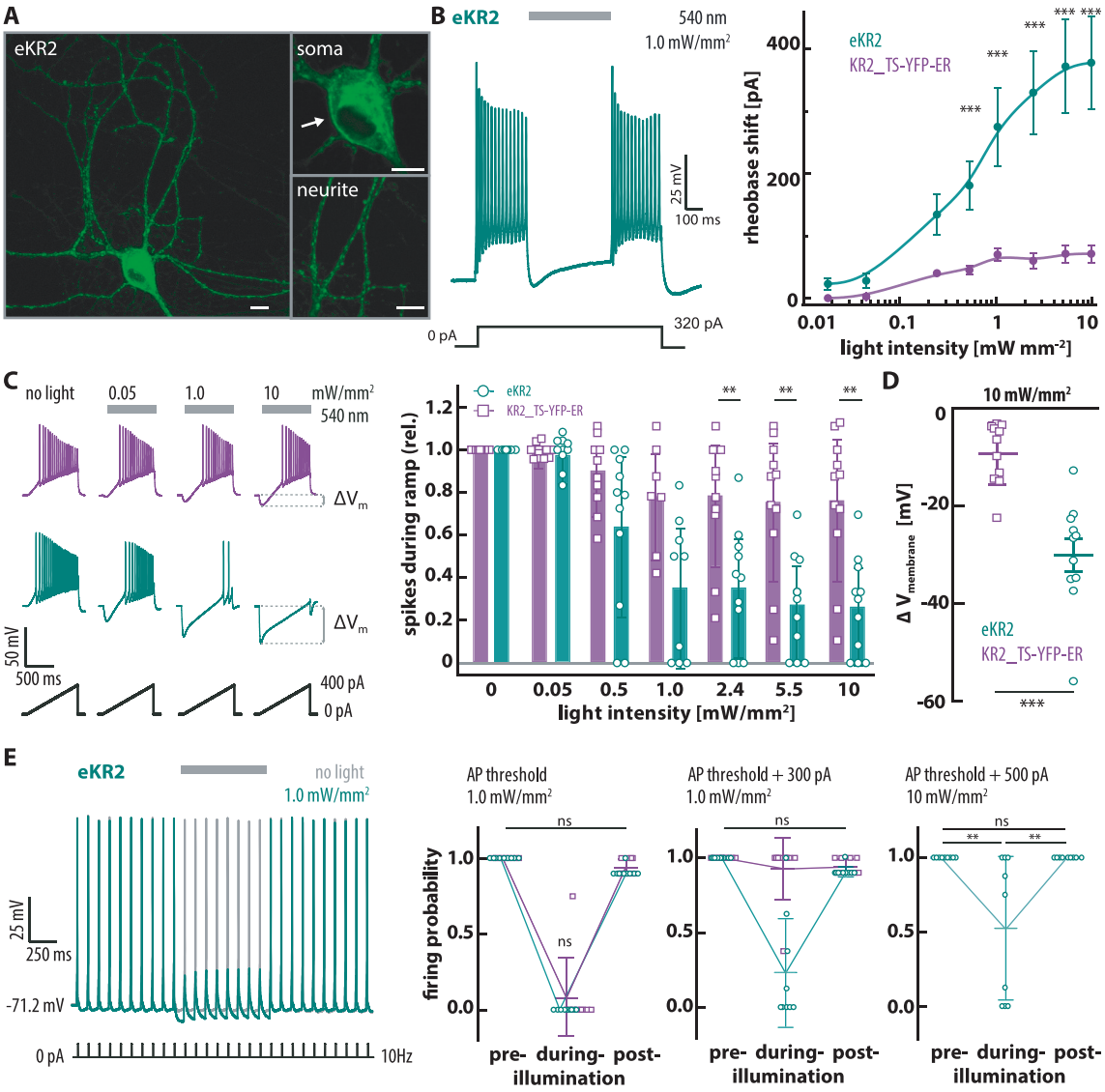

Figure 3.26: Optogenetic potential of eKR2 (#092, green) compared to C-terminally targeted KR2 (#091, purple) in cultured neurons. **A** Confocal image of eKR2-expressing hippocampal mouse neuron (z-stack) with zoom-in on neurites and soma (equatorial slice), scale bar corresponds to 10 µm. **B** Representative voltage-clamp trace showing light-induced inhibition of current-induced (square pulse) action potential firing by eKR2 (left). Light-induced rheobase shift entailed by eKR2 expression (green) or expression of only C-terminally targeted KR2 (purple). **C** Voltage traces upon injection of ramp currents ($0.44\,\mathrm{pA\,ms^{-1}}$) at different intensities (illumination starts with ramp) for both constructs with corresponding light-induced reduction of number of spikes during ramp (right). **D** Light-induced hyperpolarization of the membrane at $10\,\mathrm{mW\,mm^{-2}}$ extracted from the ramp protocols in C. **E** Inhibition of single action potentials induced by repetitive (10 Hz) 10 ms, high current injections with illumination period and calculated firing probabilities pre-, during and post that illumination. All data is represented as mean±SD with individual data points.

Lastly, a pulse trail protocol was used to drive single action potentials with repetitive (10 Hz), short (10 ms) but intense[m] somatic current injections and an illumination period

[m] High enough to drive APs with 10 ms current injection at 10 Hz; the value was determined for each neuron individually.

in the middle of the pulse trail (figure 3.26 E). At the AP threshold and using 1 mW mm^{-2} both constructs reliably inhibited AP firing upon illumination and returned to the pre-illumination firing pattern when light was switched off (figure 3.26 E). When current injections were raised 300 pA above the AP threshold, eKR2 still reliably reduced the firing probability in the light to 0.07 compared to 0.72 for the control. Even at current injections 500 pA above AP threshold eKR2 was still capable of reducing firing probability to 0.38 when light intensity was raised to 10 mW mm^{-2} as seen in figure 3.26 E.

4 Discussion

4.1 ReaChR

4.1.1 Photocycle and complex photochemistry

The photocycle of ReaChR A major objective of this thesis was to characterize the spectral sensitivity and photochemistry of ReaChR. Together with Benjamin Krause, who performed protein purification and spectroscopic measurements on the recombinant protein, the photocycle of ReaChR was investigated and elucidated. Using flash photolysis experiments and stationary spectroscopy, the photocycle in figure 4.1 D was determined. Overall, many similarities to the *Cr*ChR2 photocycle (see section 1.1.2) were identified. However, in contrast to *Cr*ChR2[128,129,216] an L-like intermediate rising on the µs time-scale after the laser flash was identified for ReaChR (figure 4.1 D). A similar L state was proposed for natural anion-conducting ChRs[217,218] and the more sodium-selective[151] *Ps*ChR of *Platymonas subcordiformis*[219]. Further, L states were identified in the photocycles of Cl^--pumps[220,221] like *Np*HR or halorhodopsin and H^+-pumps like *Hs*BR[59,62,222]. This L state exhibits a still protonated RSB and absorbs maximally at 495 nm at pH 5.0 in case of ReaChR[223] (figure 4.1 C), where it was most prominent in flash photolysis experiments. The L state is succeeded by the M state, which features a deprotonated RSB. During the transition from M state to N state channel opening is supposed to happen in analogy to *Cr*ChR2[116,129]. The N-state absorption difference is barely visible in the contour plot from flash photolysis recordings at pH 7.4, because it has an absorption maximum similar to the dark state and is masked by the dark state bleach (figure 4.1 A and C). However, it is more evident at pH 5.0[223] (figure 4.1 C). Additionally, stationary absorption spectra of recombinant slow-cycling ReaChR C168S showed the rise of one species with an absorption at 400 nm after photoactivation, but no complete bleach of the absorption at 525 nm. The remaining absorption at 525 nm even after prolonged green illumination indicates that after photoactivation an intermediate absorbing similar to the dark state, *e. g.* the N state, arises[223], which causes the persisting absorption around 525 nm.

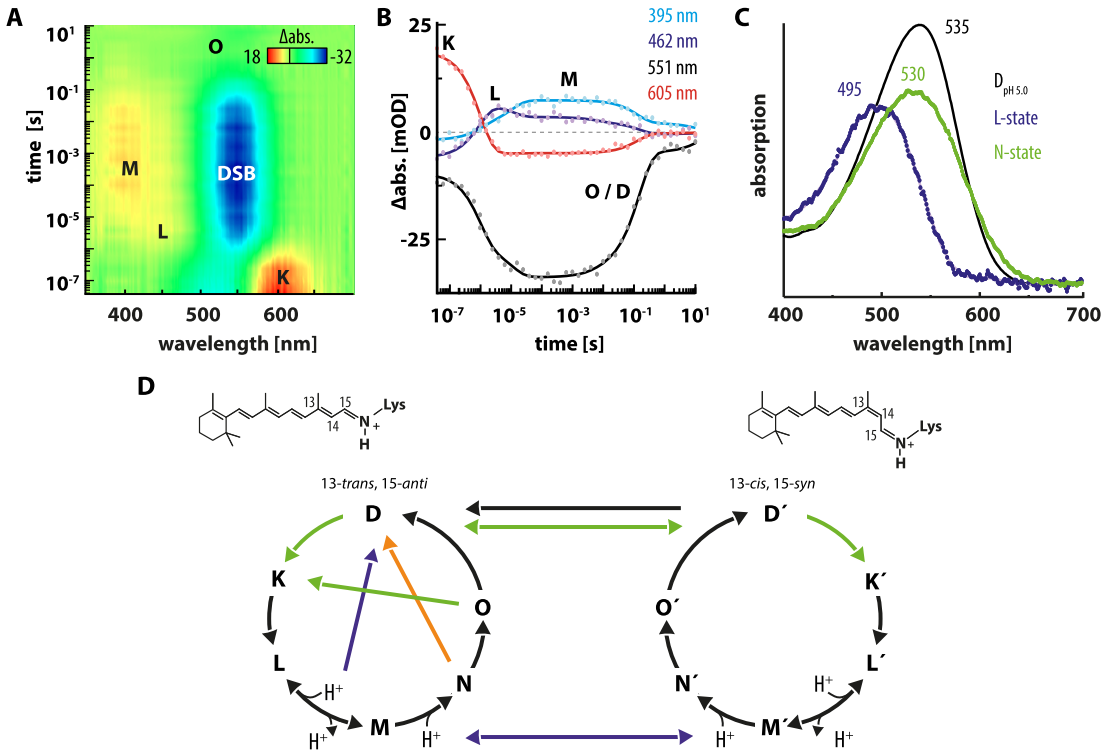

Figure 4.1: The photocycle of ReaChR. A Flash photolysis data of recombinant ReaChR at pH 7.4 represented by a contour plot showing the transient absorption changes after a 10 ns laser flash (530 nm). Data from [223]. **B** Time traces of the absorption changes at indicated wavelengths extracted from A. Data from [193]. **C** Calculated absorption spectra of the L- and N-state of ReaChR at pH 5.0, where the N-state absorption difference was most prominent. Taken from [223]. **D** Proposed photocycle for ReaChR with black arrows indicating thermal transitions and colored arrows corresponding to light-induced transitions between the intermediates.

Additionally, retinal extraction from the dark adapted wt and subsequent HPLC of the retinoids revealed that the dark state of ReaChR comprises a 78:22 all-*trans*:13-*cis* isomer mixture [223]. This led to extension of the photocycle similarly as proposed for *Cr*ChR2 [140] to feature one cycle based on the 13-*trans*, 15-*anti* retinal conformation, referred to as *anti*-cycle, and another starting from the 13-*cis*, 15-*syn* dark state conformation of the retinal termed *syn*-cycle (figure 4.1 D). In *Cr*ChR2, two conducting states with different conductivities are needed to explain all properties of the photocurrents (see section 1.1.2 "Photocycle models"). However, so far it is not consistently shown, whether those two conducting states occur subsequent in the same cycle or one is part of the *anti*- and one part of the *syn*-cycle or even both, which would imply the existence of more than two conducting states.

Photoconversion of intermediate states was already demonstrated for *Cr*ChR2 [116,128] and its slow-cycling mutants [115,117,216]. With the aim to investigate the photosensitivity of the open states and cross-reactions in the photocycle of ReaChR, inactivation measurements were performed on the slow-cycling mutant ReaChR C168A (see section 3.1.5). Under

constant illumination with green light the open state(s) were accumulated and could be photo-converted by additional application of blue (380 nm to 430 nm) and orange (580 nm to 630 nm) light pulses. The inactivation induced by orange light was small (15 %) and immediately reversed by the green background illumination. Thus, it was concluded to end in the dark state and start from the N state (figure 4.1 D). This inactivation is possible due to the small shoulder in the N-state absorption, which is not overlapping with the dark state spectrum (figure 4.1 C). Blue light inactivated the stationary photocurrent more than 60 %. The blue-light induced inactivation was more complex as both the inactivation and the recovery to the prior steady state current proceeded in a bi-phasic manner. One fraction of the inactivation progressed slowly and was instantaneously reversed by the green background illumination. Hence, it was attributed to a M-D photoconversion (figure 4.1 D). This conversion would not only include the *cis-trans* isomerization of the retinal but also the re-protonation of the RSB. Indeed, FT-IR measurements indicated that the primary proton acceptor D293 in ReaChR deprotonates during that light-induced M-D conversion[193], which most likely reprotonates the RSB.

For the second component of that inactivation, reduction of the photocurrent was fast, on the timescale of milliseconds, but recovery of the stationary current level under the green illumination was very slow on the time scale of minutes. As the stationary current was not recovered by the green light for an extended period of time, it was concluded that inactivation could not occur to the dark state in that case (figure 4.1 D) and rather takes place into another non- or less-conducting species. This transition could for example go into the *syn*-cycle as the open state of the *syn*-cycle could be less-conductive in analogy to *Cr*ChR2[131]. A transition between M and M' would then be accompanied by a 13-*cis*, 15-*anti* to 13-*trans*, 15-*syn* double isomerization (figure 4.1 D, purple arrow). The possibility to have a light-driven double isomerization between these two retinal conformations was already demonstrated for the histidine kinase rhodopsin 1 of *Chlamydomonas reinhardtii*[34]. Additionally, a photo-induced conversion between the two dark state isomers was proposed[136], which as well requires a double isomerization. Finally, as well a single *syn-anti* isomerization is conceivable, but was to my knowledge not shown for a microbial rhodopsin so far. This would offer the possibility of a transition from the M state of the *anti*-cycle to D' of the *syn*-cycle, which would similarly transfer the protein to the less-conducting *syn*-cycle and could as well explain the data.

Complex photochemistry in ReaChR The electrophysiological investigation of the spectral sensitivity revealed that the photochemistry of ReaChR is complex and distinct from that of *Cr*ChR2. When action spectra were measured with short light pulses or with intensities in the linear range of the dose response curve (*cf.* figure 3.4), they

peaked between 530 nm to 550 nm similar to the absorption spectrum of the recombinant protein and the spectral shape did not show any differences compared to other ChRs (*cf.*figure 3.2). However, at higher light intensities the spectrum became broad and complex with a sharp peak arising around 600 nm (figure 4.1 E). A shape like this may either be indicative for a difference spectrum caused by activation of the dark state and simultaneous photoinactivation of an intermediate or for the photoactivation from two different dark states with overlapping spectra. The latter explanation seems unlikely here, because i) the 600 nm peak is very sharp with an estimated full width at half maximum of 50 nm and ii) the relative absorption coefficients suggested by the flash action spectrum were consistent with the light sensitivities to 530 nm and 600 nm light. This supports that photoactivation primarily occurs from one green-light sensitive dark state rather than two with one activated by green and one by orange light. Additionally, the change in spectral shape was dependent on the light intensity as well supporting secondary photochemistry to cause the shape change of the spectrum. This suggests the spectral shape is based on a difference spectrum evoked by photoinactivation, which immediately raises the question on the nature of the photo-activated intermediate.

As the photocurrents are reduced by this photoconversion it either takes place from the conducting state(s) or a photointermediate prior to that, which would both reduce the amount of protein in the open state and thereby the photocurrents. The photocurrents are not effectively reduced around 600 nm, thus the inactivated intermediate should have an absorption maximum blue shifted to the dark state. The K state is already half-decayed within 1 µs after excitation rendering it a rather unlikely candidate to absorb another photon. Moreover, it has a red shifted absorption compared to the dark state. The succeeding L state maximally absorbs at 495 nm at pH 5.0 and seems to be present up to the millisecond time regime[193] (figure 4.1 B) rendering it a possible candidate to absorb a second photon. However, the L and M state are spectrally not well separated making it hard to judge whether the absorption difference at 462 nm prevailing into the millisecond time scale belongs to the L state or is rather caused by the shoulder of the M-state absorption (figure 4.1 B). However, in cryogenic UV-vis measurements, the L state was identified in the photostationary state[a] at temperatures from 200 K to 298 K[223] supporting that it prevails under continuous illumination at ambient temperatures. The photoinactivation was more pronounced at acidic pH_e 5.0 (*cf.* figure 3.3 B) and the L-state absorption difference was more pronounced at pH 5.0 in the flash photolysis data[223], which as well supports the L state as the photo-converted species. Fi-

[a] The recombinant protein was illuminated until the amplitude of the strongest IR absorption band at 1660 cm^{-1} reached saturation, which was termed photostationary state. Otherwise the state was not defined and can include a mixture of photointermediates.

nally, an L state was not identified in the *Cr*ChR2 photocycle[110,128], potentially explaining why the secondary photochemistry is more pronounced in ReaChR than in *Cr*ChR2.

Nevertheless, it is also possible that the N state, which has a similar absorption to the dark state (figure 4.1 C) is the photo-converted species with different absorption cross-sections of the dark and the N state enabling efficient inactivation only around the peak absorption of the N state. It was present into the late millisecond time range and as well more pronounced at acidic than at neutral pH[223]. Moreover, the absorption maxima of dark and conducting N state are very similar in ReaChR (figure 4.1 C), in contrast to *Cr*ChR2 where they are spectrally separated by about 50 nm[110,128]. This could also explain, why inactivation of the photocurrents by the activation light is more pronounced in ReaChR than in *Cr*ChR2.

Another peculiarity of the 600 nm peak in the stationary action spectra was that it only arose when the spectrum was measured reversely starting from longer wavelengths and not present when it was measured *vice versa* (*cf.* figure 3.2 C). Albeit less pronounced, differences in the spectral shape depending on the measuring direction were as well observed at lower light intensities. This issue was not entirely resolved during the course of this work and would need further clarification. A similar phenomenon was neither reported for *Cr*ChR2 nor in the initial publication for ReaChR[150].

A dependence of the spectral shape of the direction of measurement can in principle rely on different effects. On the one hand it is possible that repetitive activation reduced the ionic gradient, which is not fully re-established in the 10 s delay between the individual pulses, resulting in currents that are decreased continuously over the course of measurement. In general, changing the intracellular pH by ChR activation is possible, but needs long continuous illumination for several seconds[151], which was not used here. Moreover, the effect would progress over the course of measurement entailing that each current is smaller than the one before. This was not the case as for some conditions the current size decreased and rose again within the same spectrum. Finally, the depletion of the gradient should largely depend on the size of the cell and the expression level of the ChR[151]. This would evoke a different shape of the spectrum for every cell, but the recorded spectra were qualitatively consistent. Thus, depletion of the gradient as main cause for the discrepancy between forward and reverse measuring direction is unlikely.

On the other hand, dependence of the spectral shape on the measuring direction could be caused by the respective pre-illumination, which is different in both cases. Hence, the 600 nm peak might either be suppressed by prior blue or green light activation or it is enhanced, when red light is applied before. In principle, this could as well speak for a transition to the *syn*-cycle with a weakly conducting open state as discussed

earlier. Nevertheless, the question remains how the effect is mediated *e. g.* whether the pre-illumination influences the dark state composition or the secondary photochemistry of ReaChR. Influences on the dark state composition could be potentially unraveled using spectroscopic techniques with recombinant protein like Resonance Raman, while a discrimination in the flash action spectra is only possible when both states are spectrally well-separated and even more importantly (meta-) stable. If the differences only occur during the photocycle and are caused by secondary photochemistry they would be even harder to investigate. As already mentioned, the molecular determinants of this effect were not completely elucidated here, but the effect itself was also present in the chloride-conducting ReaChR variant Aurora[195,b] and thus seems to be an inherent property of ReaChR, which has to be taken into account when it is used for optogenetic experiments.

4.1.2 Applicability of ReaChR in optogenetics

Investigation of the spectral sensitivity revealed that ReaChR is a green-light activated ChR, which also generates high photocurrents upon illumination with orange light. While for short activation pulses green light is more suitable because activation is more efficient, orange light evokes higher currents if a longer pulse can be delivered for activation. At a photon flux of $1.6 \times 10^{15}\,s^{-1}\,mm^{-2}$, which equals $0.6\,mW\,mm^{-2}$ for 530 nm and was the maximal intensity used in the experiments with ReaChR, green-light evoked higher currents up to a pulse duration of 40 ms (*cf.* figure 3.5). However, that value will also depend on the light intensity and consequently, the activation wavelength of choice will depend on the respective application context. Thus, it is even more important to know the photochemical properties in detail to set up an experiment purposefully.

After investigating the distinct photochemistry of ReaChR, the question arises: Is ReaChR a good choice for your optogenetic experiment? There are several things in favor of ReaChR supporting its application. It can be activated red-shifted compared to *Cr*ChR2 enabling higher tissue penetration depth. ReaChR was used to drive spiking through the intact skull of mice[150] and was applied to control behavior in freely moving flies[224]. Hooks and colleagues used ReaChR and *Cr*ChR2 *in vivo* in the primary motor cortex of mice to investigate signal integration from the somatosensory cortex and thalamus into single motor cortex neurons[225]. To restore light responses in blind mice ReaChR provided an advantage over *Cr*ChR2, because it could be activated by light red-shifted compared to *Cr*ChR2 activation at less damaging light intensities[226]. Further on, ReaChR-mediated pacing of rat cardiomyocytes was demonstrated[227], which all underline its applicability *in vivo*. Additionally, there are a lot of variants of ReaChR available

[b] Personal communication with Jonas Wietek

tailoring the protein to the respective demands of the experiment. There are slow-cycling variants, which were presented in this thesis (see figure 3.9), which usually provide a higher light sensitivity to the cell[115,195]. There are fast-cycling variants like bReaChES with τ_{off}=50 ms[149], the recently reported ReaChR F259Y closing with a kinetic constant of 30 ms[228] or ReaChR E163T as investigated here[c] with τ_{off}=40 ms. The more Na^+-selective mutant ReaChR E130Q investigated here, could help to reduce adverse effects of proton transport during ChR activation. Although it exhibited a blue-shifted action spectrum compared to the wild type, it is still considerably red-shifted compared to *Cr*ChR2. Finally, as well a chloride-selective variant is available[195] enabling red-light induced neuronal inhibition.

The number of available ReaChR variants emphasizes the versatility of ReaChR and likewise the importance of engineering approaches to tailor the microbial rhodopsin to the experimental demandings. However, todays optogenetic experiments often demand complex illumination protocols with multiple wavelengths. For example in cases where two different ChR should be combined or when actuators like ReaChR are used together with sensors for pH, calcium or voltage changes to perform all optical experiments. Here, using ReaChR would provide a serious drawback. Despite the red-light activatability, which ReaChR undoubtedly provides, it retains a very high sensitivity to blue and green light as deduced from the broad stationary action spectrum. According to the spectra measured here (*cf.* figure 3.2), you get at least half maximal stationary currents over the whole wavelength range from 380 nm to 620 nm rendering it highly unlikely to combine ReaChR with another photoreceptor without cross-talk. Additionally, pre-illumination effects as discussed above, potentially even compromise the activity upon orange illumination. Consequently, in cases demanding multicolor illumination the red-light sensitivity might not outweigh the mentioned adverse effects anymore. Moreover, the discovery of the red-light activated Chrimson renders ReaChR dispensable for many applications, because its flash action spectrum peaks at 590 nm[95,151] more than 50 nm red-shifted compared to ReaChR. However, according to the selectivity measurements performed in this thesis and in a recent study[151] the permeability ratio of H^+ over Na^+ is significantly higher for Chrimson as for ReaChR, which might render ReaChR more attractive in some cases. On the other hand there are as well Chrimson variants like ChrimsonS (E143S) with highly reduced proton selectivity[151].

One possibility to circumvent the remaining blue-light sensitivity of ReaChR is to use it with two-photon activation, which has been demonstrated with the closely related C1V1[229–232] and also explored for ReaChR[233]. For ReaChR maximal two-photon

[c] The ReaChR E163T mutant was already reported earlier[150], but the kinetics were not investigated.

currents were reached with excitation wavelength in the range from 975 nm to 1030 nm with photocurrents high enough to drive single action potentials[233]. Combining actuators and sensors with two-photon activation largely enhances penetration depth and enables all-optical approaches. For example, light-induced neuronal stimulation with 1064 nm light using C1V1 was combined with a read out of activity based on calcium imaging at 940 nm using GCaMP[234] in freely moving mice[231,232].

4.2 eKR2

There are two main obstacles impeding in-depth electrophysiological characterization of microbial ion pumps. On the one hand expression levels are usually low and often combined with poor membrane targeting in vertebrate cells entailing small photocurrents. On the other hand most pumps are outward-directed, which demands control over the intracellular solution to change the substrate concentration. Accessibility of the substrate concentration in combination with voltage control is provided by whole-cell voltage-clamp measurements on mammalian cells, which requires good expression and membrane targeting.

As microbial light-driven Cl^--pumps are inward-directed, they were already characterized electrophysiologically in more detail in *Xenopus* oocytes[42] and also neuronal cell culture[162]. For the outward-directed H^+-pumps electrophysiological characterization in vertebrate cells was pioneered by Nagel and colleagues, who recorded *Hs*BR photocurrents after heterologeous expression in *Xenopus* oocytes[70]. Additionally, electrophysiological investigations of the H^+-pumps of the marine alga *Acetabularia acetabulum*[214] and the cyanobacterium *Gloeobacter violaceus*[213] as well as the bacterial proteorhodopsin[209], the algal *Cs*R[206] and the fungal CarO rhodopsin[207] were reported. However, except for the latter two reports, which include patch-clamp recordings in mammalian cells, all these studies base on the heterologeous expression of the respective pump in *Xenopus* oocytes hampering control over the ionic condition on the substrate side of the outward pumps.

Pioneered by Gradinaru and co-workers for the Cl^--pump *Np*HR[200,235], it was demonstrated that expression and especially membrane targeting of microbial pumps in mammalian cells can be significantly enhanced by molecular engineering via C- and N- terminal fusion of targeting sequences. The targeting approach was transferable to other pumps[236] and rendered molecular investigation of the pumping mechanism and optogenetic application of microbial ion pumps more feasible. Similar to other pumps,

photocurrents of the unmodified Na^+-pump KR2 were small in *Xenopus* oocytes[d] and also mammalian cells as investigated in this study (figure 3.13). Initially, KR2 photocurrents were enhanced by C-terminal targeting as reported during the course of this work[76,78,237] and also found in experiments here (figure 3.13). However, the combination of C-terminal targeting with N-terminal fusion of an earlier reported ChR-derived N-terminus[149,238] further enhanced the membrane targeting and the photocurrents (figure 3.13). The final eKR2 construct exhibited 6-times higher photocurrent densities than the construct with only C-terminal targeting. Additionally, eKR2 showed 66 % higher stationary photocurrent densities than a chimeric Na^+-pump[e], which was reported recently[237]. Hence, eKR2 was well-suited for an in-depth electrophysiological characterization of the pumping mechanism and exploration of the optogenetic potential of Na^+-pumps.

4.2.1 Substrate specificity of eKR2

Interestingly, a substrate switch from Na^+ to H^+ was proposed for KR2[48], which is unusual for microbial pumps and motivated the thorough investigation of the substrate specificity. Initially, this conclusion was based on pH-measurements in suspension of KR2-expressing *E. coli* cells. Inoue and colleagues observed a light-dependent pH elevation in unbuffered NaCl solution, which was enhanced in presence of CCCP and hence interpreted as sodium pumping[48]. This finding was reproduced within this thesis as seen in figure 3.11. Further, published studies reported a light-dependent acidification in unbuffered KCl solution, which was abolished in presence of CCCP and thus explained by proton pumping[48,76,78,239]. This result could not be confirmed here, as the light-dependent acidification observed in KCl was not abolished after addition of CCCP but rather reversed to a light-dependent alkalinization (figure 3.11 A). This argues for a secondary inward-directed H^+-movement induced by extrusion of positive charges other than H^+ in presence of CCCP. The same result was obtained at an intermediate Na^+-concentration (10 mM). Here, the pH changes as well switched from slow light-induced acidification without CCCP to light-induced alkalinization in presence of CCCP (figure 3.11 B).

In principle the switch from acidification without to alkalinization with CCCP is an unexpected outcome for this assay, but a similar result was observed in proteoliposomes

[d] Personal communication with Arend Vogt

[e] Hoque and colleagues used 120 mM intracellular sodium compared to 110 mM here; intensity was 99 mW mm^{-2} (534 nm-600 nm)[237].

for another Na^+-pump *Nd*NaR by Zhao *et al.*[81]. This *in-vitro* reproduction of the switch[f] argues against some endogenous response of the *E. coli* cells, but rather for an intrinsic property of the pump, which causes this effect. This leaves the result hard to explain. In principle, it could originate from a substrate switch of KR2 from H^+ without CCCP to Na^+ in presence of CCCP, although it remains unclear how this would be mediated on a molecular level. Although hard to explain, the switch does not argue for H^+-pumping. Nevertheless, the measurements in choline chloride, which were performed here to have one condition with no Na^+ or K^+ added to the extracellular solution, could be explained by H^+-pumping, because the light-dependent reduction of the solution pH was abolished after addition of CCCP. In summary, the measurements performed here reproduced the published results in NaCl[48], but did not hint at H^+-transport in KCl. Nevertheless, measurements in choline chloride can indeed be interpreted by H^+-pumping (figure 3.11).

Conclusive interpretation of results from the *E. coli* assay regarding substrate specificity of an ion pump is challenging, because *E. coli* cells have a lot of endogenous transporters, which can interfere with the measurements. Additionally, in most cases the measured pH change is caused by a secondary H^+-movement over the membrane (*cf.* figure 2.2) impeding selectivity conclusions for the investigated transporter. Further, the substrate side of the outward-directed pump is not accessible and it is not known in what intracellular ion concentration extracellular replacement by an ionic species actually results. Moreover, it is uncertain whether the intracellular adaption of the ion concentration would be similar for all tested ions, such that the measurements in different ionic solutions might *per se* only be poorly comparable to each other. In conclusion, this assay presents a quick and easy way to assess light-driven pump activity, for example to screen mutants, but certainly it is not the assay of choice to investigate the substrate specificity of a pump.

The investigations of the eKR2 photocurrents at different intracellular ionic conditions (*cf.* section 3.2.3), which is the substrate side of the outward-directed pump, yielded new insights into the substrate specificity of eKR2 and also revealed mechanistic aspects for ion pumps in general. As expected for a Na^+-pump the stationary photocurrent of eKR2 was largely dependent on the intracellular Na^+-concentration and decreased with reduced substrate availability. This was demonstrated for H^+-[207] and also Cl^--pumps before[162]. Additionally, it was observed that significant changes in the stationary current

[f] The results are similar, but difficult to interpret conclusively as the authors report the preparation of the proteoliposomes in a solution containing 100 mM K_2SO_4, but it is not clear whether this is still present in the measuring solution. Further the orientation of the protein in the membrane is not investigated and only indirectly deduced from the results[81].

densities, were virtually always accompanied by a change in the respective kinetics of the current decay after light-off τ_{off} (figure 3.15). Seeing the pump as an enzyme that catalyzes transport of ions over the membrane this seems reasonable, because reduced substrate availability renders an enzyme less efficient reducing kinetics and turnover rate[240]. As microbial ion pumps transport only one charge per photon, a reduced turnover entails a reduction in the stationary current amplitude. Most importantly, pumping kinetics are not dependent on the expression level in contrast to the whole-cell photocurrent, which makes the apparent τ_{off} a more sensitive variable to characterize pumping efficiency than the amplitude of the photocurrent. This is also seen in the data presented here, as in some cases (*e. g.* figure 3.16 *vgl.* 1 mM $[Na^+]_i$ pH_i 7.2 with 9.0) the kinetic constants are significantly different, while the current densities are not (yet), due to the relatively higher standard deviation evoked by cell-to-cell differences in expression.

Stationary photocurrents not only increased at higher intracellular Na^+- but also K^+-concentrations, which hints at potential K^+ transport activity of eKR2. This would be in-line with the results of the *E. coli* assay in KCl solution measured here, which can be explained by K^+-pumping, but contradicts previously reported data for wt KR2[78,79]. Gushchin *et al.*[84] directly investigated the K^+-dependence of the currents recorded in an experiment with liposomes attached to BLMs and concluded no K^+-pump activity of wt KR2. Kato and colleagues[78] did only investigate the K^+-pump activity of the wild type via the *E. coli* assay, but also excluded K^+-pumping[78] similar to other studies[48,80]. Additionally to the direct photocurrent measurements, the spectroscopic data recorded by Arita Silapetere support a potential transport activity of KR2 for potassium as discussed later (see here 4.2.4). Earlier studies reported a pumping activity for Li^+[48,241], which was not investigated here.

The initial key question regarding the substrate specificity of eKR2 was: Is there a transport activity for H^+? A general problem with the investigation of H^+ selectivity is that H^+ are no ion in a classical sense and that they can also modify the rhodopsin. Changing the pH does not only change the proton concentration as potential substrate, but can as well modify protein features by altering the protonation state of key residues. Thus, kinetic changes upon pH variation would not necessarily be an evidence for H^+-transport itself at least not for a Na^+-pump, where both Na^+-translocation and protonation changes of key residues occur during the photocycle. Still, the photocurrent measurements for *Cs*R revealed that for H^+-pumps stationary currents are decreasing with increasing pH_i and the apparent τ_{off} changes accordingly.

For eKR2 neither increasing nor decreasing the intracellular H^+-concentration even at 1 mM $[Na^+]_i$, did affect the stationary photocurrents (figure 3.15). Also the apparent

τ_{off} was not affected when pH_i was elevated from 6.0 to 7.2 and the off-kinetics were even accelerated at pH_i 9.0. This was different for the H^+-pump *Cs*R and contradicts a H^+-transport hypothesis for eKR2. At 0.1 mM $[Na^+]_i$ the enhancing effect of alkaline pH_i was even larger and the apparent off-kinetics was 1.5-times faster at pH_i 9.0 than at pH 7.2. At pH_i 9.0 - in contrast to pH_i 7.2 - no differences in the stationary current densities or apparent τ_{off} were observed upon reduction of $[Na^+]_i$ from 1 mM to 0.1 mM, which hints at a pH dependence of the Na^+-affinity. This was further supported by the results for the recovery kinetics of the peak current, which is a more accurate indicator for the photocycle turnover time than the apparent τ_{off}. Here, the kinetics were likewise enhanced by a reduction of the H^+-concentration on the substrate side indicating an enhancing effect of alkaline pH but contradicting H^+-concentration as rate limiting for pumping activity as observed for $[Na^+]_i$.

At first glance, interpretation of the pH_i-dependence of the stationary photocurrents measured here in ND7/23 cells contradicts H^+-transport of eKR2 at the investigated ionic conditions. However, the selectivity of eKR2 for H^+ could be so high that the photocurrents were not (yet) affected by the pH changes in the observed range between pH_i 6.0 and 9.0. As the Na^+-transport of eKR2 was consistently shown here, this explanation would demand a co-transport of both ions. In principle it would be possible that in every photocycle a H^+ is co-transported with the Na^+ ion with different affinities for both ionic species. In general, a co-transport would as well comply with the published results from the *E. coli* assay. In NaCl solution a H^+ and a Na^+-ion would be transported causing alkalinization on the outside. When CCCP is added the electrical gradient established by the H^+-transport would be abolished but Na^+-transport would still drive alkalinization. In KCl on the other hand only H^+ would be transported due to the absence of Na^+ resulting in a CCCP sensitive acidification as seen by Ionue and colleagues[48,g]. A co-transport of both ions was already proposed for the Na^+-pump *Nd*NaR by Zhao and colleagues[81]. Although, the paper is not clear whether co-transport means simultaneous transport of both ions by one protein or parallel occurrence of rhodopsins pumping H^+ and rhodopsins pumping Na^+ in the observed protein ensemble. To further elucidate the possibility of co-transport by eKR2, the pH imaging experiments were conducted (figure 3.18), because an extrusion of protons from the cell, will locally acidify the extracellular lumen[183]. Reference measurements with the H^+-pump *Cs*R verified the assay and showed that outward H^+-pumping decreases the pHluorin fluorescence intensity reporting the pH change, which was more pronounced the less the extracellular solution

g Although a co-transport would not be contradicted by the electrical data measured here and would comply with the published *E. coli* measurements it does not explain the different results in KCl from the *E. coli* assay performed here (see figure 3.11).

was buffered. In contrast, results obtained for eKR2 were ambiguous. On average eKR2 activation caused no acidification at the extracellular surface, but for some cells a slight light-dependent pH decrease was observed in the most weakly buffered solution.

However, there are several aspects rendering these results rather premature and demanding further experiments. For example, construct #3 with KR2 was not exactly eKR2, because the fluorophore and therefore the ER targeting sequence were omitted, because a fluorophore additionally to pHluorin could compromise the imaging. Hence, for a conclusive comparison similar expression levels and membrane targeting of the imaging construct and eKR2 has to be verified. As the construct only contained the fluorescent pHluorin and this is separated by a P2A site from the pump, the membrane fluorescence of the cells does not reflect the amount of KR2 located to the membrane. As the amount of protein in the membrane is uncertain, the average size of the photocurrents evoked by construct #3 and whether those are comparable to *Cs*R is unknown[h]. Further, simultaneous imaging and electrical recording, which would be the desired way to perform this experiment, was technically not (yet) possible. Without electrical recording the intracellular ionic condition is uncontrolled and pH and sodium concentration might undergo cell-to-cell variation. Further, it is not reported whether and how a local change of the sodium concentration, which would be evoked by Na^+-pumping, might affect the pHluorin fluorescence. Hence, control measurements with a Na^+-free extracellular buffer would be necessary to test for a potential influence of the sodium concentration.

In the future, pH imaging could be complemented with sodium imaging for example with a ratiometric, soluble sodium sensor like sodium-binding benzofuran isophthalate (SBFI)[242] a commercially available[i] chemical Na^+-sensor. One advantage of this dye is that its emission and excitation maxima are at $\lambda_{ex,1}$=340 nm, $\lambda_{ex,2}$=380 nm and λ_{em}=500 nm similar to the Ca^{2+}-sensor FURA-2[243], which would allow an easy implementation of Na^+-imaging at a setup where Ca^{2+}-imaging is already possible. However, it is questionable whether the changes in the sodium concentration would be high enough to be detected in an experimental setup like this. In comparison to ChR photocurrents, where detection of changes in $[Ca^{2+}]$ with FURA-2 was demonstrated before[151,244], the eKR2 photocurrents are small. Further, FURA-2 has a sensitivity for $[Ca^{2+}]$ in the nanomolar range[242] while SFBI has a dissociation constant for Na^+ in the millimolar range[242,j]. Thus, the combination of a supposedly smaller change in the ion

[h] Construct #3 was tested for functionality, but a systematic characterization of the current amplitude is still needed.

[i] SBFI is available as tetraammonium salt or alternatively as cell permeant acetoxymethyl ester.

[j] The actual dissociation constant depends on multiple factors in the experimental setup (pH, concentration of other cations *etc.*), but in a solution containing Na^+ and K^+ (pH 7.05) like it is to expect for a physiological setup the effective K_d was determined to be 17 mM.

concentration with a reduced sensitivity of the dye could impair monitoring of the transport activity by sodium imaging in this case. Additionally, SFBI is also sensitive to K^+, albeit with a reduced affinity compared to Na^+ [242], and as eKR2 supposedly pumps K^+ to a certain extent this could distort the measurement as well.

Taken together the selectivity measurements on eKR2 demonstrated that the stationary photocurrent is mainly carried by Na^+ and to a smaller extent potentially also K^+. However, although not fully excluded, evidence for a substantial contribution of protons under the investigated ionic conditions was not gathered, here. Even if in a setup without any Na^+, which was not established here, eKR2 would pump H^+, it is expected to exclusively pump Na^+ and K^+ in a physiological context, which is the most relevant for application purposes.

4.2.2 Voltage independence of steady state pump activity

As seen in figure 3.19 stationary eKR2 photocurrents displayed no pronounced voltage dependence when intracellular sodium was abundant. Similar results were obtained by Hoque and colleagues, who saw no voltage dependence of stationary KR2 photocurrents in ND7/23 cells [237,k]. In comparison, other microbial ion pumps like H^+- or Cl^--pumps reportedly have voltage dependent photocurrents and show increasing amplitudes with more positive membrane potentials [42,70,162,207,245]. In animal cells Na^+-extrusion is provided by Na^+,K^+ ATPases (NKA), which consume ATP to transport three Na^+ ions out of the cell in exchange for two K^+ ions [246–248]. NKAs are a long known and extensively studied class of ion translocating proteins [246,249] and their importance was emphasized by the awarding of the Nobel Prize in Chemistry to Jens Skou in 1997 for their discovery [249,l]. Electrophysiological studies revealed that for NKAs stationary photocurrents are usually dependent on the membrane voltage [250–252], which was as well extensively studied theoretically [251,253–256]. In principle, voltage dependence of stationary photocurrents is mediated by the turnover rate of the transporter, which is determined by the kinetics of the individual transport steps [251,253,254]. Individual transport steps involving charge movement, should in principle depend on the membrane voltage as charges are moved within an electric field [251,253–255]. However, the over all turnover rate might only exhibit voltage sensitivity if the voltage dependent steps are rate limiting [251].

For eKR2 the single turnover photocurrents revealed that none of the kinetic components showed voltage dependence in the observed range from −60 mV to 30 mV (figure 3.25) at high sodium concentrations agreeing with the voltage independence of the sta-

k Kato and colleagues reported a voltage independence of the peak photocurrent [78].

l "Jens C. Skou-Facts". Nobelprize.org. Nobel Media AB 2014. Web. 19 Jun 2018. http://www.nobelprize.org/nobel_prizes/chemistry/laureates/1997/skou-facts.html

tionary photocurrents at this condition. At low sodium concentration, however, the slow kinetic constant in the single turnover currents became voltage dependent together with the current-voltage relations of the stationary photocurrents. An increase of the steepness of the current-voltage relation was similarly observed for *Cs*R (figure 3.14) when pH_i was changed from 7.2 to 9.0 *e. g.* the substrate concentration was reduced. At high substrate availability neither uptake, nor translocation within the protein nor release of the Na^+ seem to be voltage dependent, as all the kinetic constants were voltage independent. Hence, all transport steps are progressed at their respective maximal rate constants regardless of the membrane potential. Possibly, this could imply that the ion is not moved by local electric potentials within the protein but rather "pushed" through by conformational changes, which are not necessarily dependent on the membrane potential. At low substrate availability ion uptake might be less effective and slowed, but can be accelerated by negative membrane potentials rendering the whole turnover rate voltage sensitive.

Irrespective of the molecular explanation for the voltage-independent pump activity of eKR2 at high substrate concentrations, it presents an advantage for the optogenetic application of eKR2. All ion pumps are used to hyperpolarize the cell membrane to reduce the excitability of neurons (see section 4.2.5). As their activation entails a reduction of the membrane potential and H^+- as well as Cl^--pumps show decreasing activity at negative membrane potentials[162,164], their activity and thus inhibition potential will decrease the lower the membrane potential gets. In contrast, eKR2 should provide constant photocurrents over a wide voltage range, when enough substrate is present[78].

4.2.3 Modulation of pump activity by the ambient pH and ionic gradients

For eKR2, elevation of the intra- and extracellular pH entailed a promotion of the pumping activity. Independent of the sodium concentration and ionic gradients the stationary photocurrents were always slightly higher at pH_e 9.0 than at the respective pH_e 7.2 condition (figure 3.19). Similarly, reduction of the intracellular proton concentration enhanced the stationary photocurrent amplitude and accelerated τ_{app} for the current decay after light-off. The promotion by alkaline pH values was especially evident in the measurements of the recovery of I_p, where regardless of $[Na^+]_i$ kinetics were always faster at pH_i 9.0 than at the respective pH_i 7.2 condition. Additionally, an enhancing effect of a high extracellular sodium concentration was observed. Regardless of the pH_e or the intracellular ionic condition, stationary photocurrents were always higher at high than at low external sodium concentrations (figure 3.19). This slight activity enhancement by extracellular sodium could be mediated by the external sodium binding site[79,85] (see

figure 1.5), which has a K_d of 11 mM and is therefore occupied at 110 mM but not 1 mM $[Na^+]_e$. One could speculate that occupation of the binding site induces oligomerization as discussed in the introduction (*cf.* page 8) and/or stabilizes the protein slightly enhancing activity. When D102, which is part of this extracellular sodium binding site is replaced by asparagine to abolish sodium binding ability, the thermostability of the protein was reduced[78], which supports a stabilizing function of this external sodium binding.[m]

Reduction of the extracellular pH_e to 5.0 drastically decreased the photocurrents. At high substrate concentration only I_p was reduced, while both I_p and I_s where diminished at low substrate concentrations (figure 3.20). In contrast, a reduction of the intracellular pH_i to 6.0, did not affect the photocurrents (figure 3.15). In line with that observation Arend Vogt in our lab saw a photocurrent reduction at external pH 5.0 in electrophysiological measurements with *Xenopus* oocytes[190]. Further, Gushchin *et al.* observed a significantly reduced pumping activity of KR2 in the *E. coli* assay at pH 5.6[79]. In ND7/23 cells, the photocurrent reduction by extracellular acidification was similar at high (pH_i 9.0) and lower (pH_i 7.2) proton gradient against the pumping direction (figure 3.20), which led to the conclusion that it is not induced by the proton gradient but rather by the extracellular acidification itself. As the kinetics of the photocurrent decay after light-off were unaffected by the acidification-caused inactivation, it seems reasonable that not the photocycle is modulated but a fraction of the protein is inactivated.

The KR2 crystal structure was resolved under acidic conditions too[78,79]. Here, the primary proton acceptor D116[78] is not facing the RSB[78,79] like it would be necessary according to the proposed transport mechanism (see section 1.1.1) potentially hinting at non-functionality of this acidic dark state conformation. D116 should be interacting with the RSB at neutral pH, where the protein is functional, because introduction of D116N red-shifted the absorption spectrum[78]. A less pronounced but still significant bathochromic shift of the absorption spectrum of wt KR2 was observed upon acidification from pH 7.0 to 4.0[78] indicating that a stabilizing negative charge close to the RSB got neutralized or flips away. Consequently, one way to explain the acidification-induced inactivation would be a protonation of the primary proton acceptor D116. Nevertheless, this can not be the complete explanation for the inactivation upon extracellular acidification, because it would not explain, why it only occurs at low substrate concentrations. It seems as if the presence of sodium reduces this acidification-induced inactivation. It could either be that i) the protonation state of another residue is involved (additionally), ii) a sodium ion is already bound in the dark state preventing protonation or iii)

[m] Control measurements with the recombinant wt in absence of sodium, which should similarly reduce thermostability, were not conducted in the paper[78].

it implies that the inactivation is not happening in the dark state but after photoactivation. Initially, sodium binding in the dark state was excluded, because the absorption maximum is insensitive to the sodium concentration[48], which was supported by the spectroscopic measurements of Arita Silapetere in our lab[190].

Taken together, it can be concluded that eKR2 is not inhibited by strong sodium or proton gradients and is optimized to perform in alkaline environments, when sodium as substrate is abundant. From an evolutionary perspective this seems plausible, because it originates from a marine flavobacterium living in sea water, which typically has a pH between 7.8-8.2[257] and sodium concentrations above 400 mM[258,259]. An interesting, yet unanswered question is whether a sodium pump in marine bacteria is only used for the generation of an ionic gradient to produce ATP or it is also needed for sodium homeostasis of the bacterium. Taking into account that eKR2 still showed pumping activity against a strong, inward-directed sodium gradient (0.1 mM $[Na^+]_i$ and 110 mM $[Na^+]_e$), the latter seems at least feasible.

4.2.4 Complementation of single turnover photocurrents with spectroscopic flash photolysis

Single turnover measurements of the photocurrents and the absorption changes of recombinant protein present a unique opportunity to correlate spectroscopic with electrophysiological results. For KR2, electrophysiological single turnover recordings on eKR2 (figures 3.24 and 3.25) presented here, were complemented by flash photolysis measurements on recombinant KR2 at similar ionic conditions performed by Arita Silapetere in our lab[n]. As resulting kinetic constants for absorption and electrical changes were both recorded under single turnover conditions, they are more comparable and useful for a correlation of the spectroscopic photocycle to the activity of the protein. Nevertheless, the protein was expressed in ND7/23 cells for the electrical recordings and reconstituted in detergent micelles for the spectroscopic analysis. This entails profound differences in the lipid environment of the protein comparing both measurements, which reportedly can influence recorded kinetics[241,260]. This can only be avoided, if electric measurements and spectroscopic recordings are performed on the exact same sample as recently demonstrated by Henrich and colleagues[261], who recorded spectral and electrical light-induced changes of KR2 reconstituted in lipid nanodiscs. For the electrical measure-

[n] For the exact experimental procedures for purification and the spectroscopic recordings the reader is referred to the methods section of Grimm *et al.*[190].

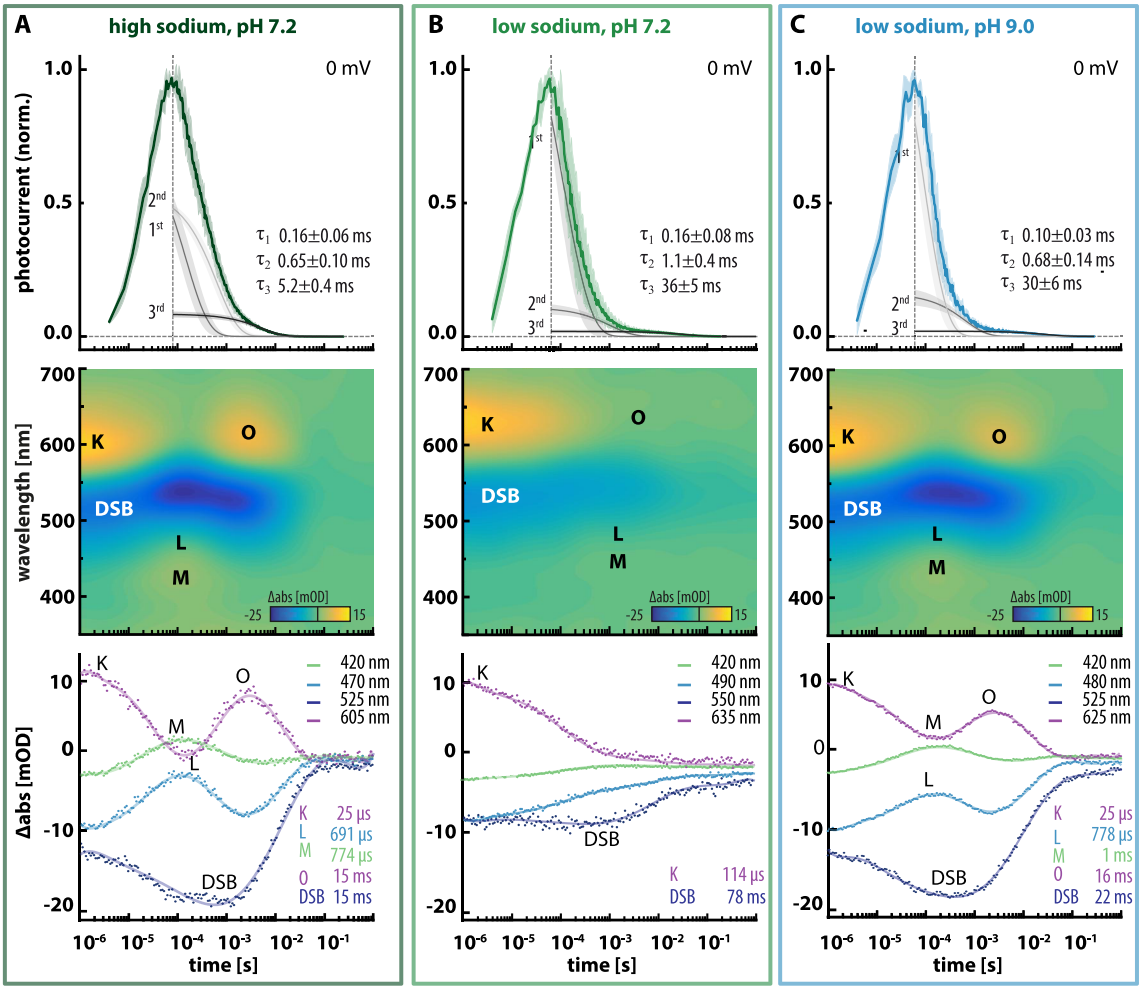

Figure 4.2: Correlation of single turnover photocurrents with spectroscopic changes monitored with flash photolysis. Single turnover photocurrents are compared to spectroscopic changes at similar ionic conditions at **A** 110 mM $[Na^+]_{i/e}$ and $pH_{i/e}$ 7.2, **B** 1 mM $[Na^+]_{i/e}$ and $pH_{i/e}$ 7.2, and **C** 1 mM $[Na^+]_{i/e}$ and $pH_{i/e}$ 9.0. Top row shows the single turnover photocurrents with the individual components of the tri-exponential fit and their corresponding kinetic constants, E_{rev}=0 mV and symmetric buffer conditions. Contour plots (middle row) represent the absorption changes after a laser flash and the bottom row displays the kinetic traces of the absorption changes at the indicated wavelengths. Kinetic constants result from exponential fit of respective absorption decay. Spectroscopic data Grimm *et al.*[190].

ments, however, the nanodiscs were adsorbed to a solid-supported membrane[261], which does not allow control over the membrane voltage presenting a drawback in comparison to measurements on mammalian cells using whole-cell voltage-clamp recordings.

In our experiments, flash photolysis measurements at pH 7.2 and high sodium concentration revealed a sequence and kinetic evolution of photointermediates similar to the published photocycle of KR2[48] (figure 4.2 A, middle and bottom). The K state decayed with a time constant of 25 µs and was, therefore, already decayed when the single turnover photocurrent started rising. The maximum of the single turnover photocurrent coincided with the spectroscopic L/M state equilibrium (figure 4.2 A) and the electric

τ_2 decayed with 0.65 ms on a similar timescale as the L/M equilibrium (0.77 ms). The late O state rose in the millisecond timescale and its decay τ_O=15 ms paralleled the 3rd electric component, which decayed with τ_3=5.2 ms. Interestingly, a recent step-scan FTIR study on KR2 revealed that the retinal still adopts a 13-*cis* conformation in the so-called O state, which would actually imply that it is rather an N state[82].

When only sodium was reduced (figure 4.2 B), the L, M and O state absorption differences were barely visible in the spectroscopic measurements, but as the K state emerged and the dark state bleached, KR2 nevertheless seemed to go through a photocycle. Still the kinetics decelerated significantly and the photocycle turnover was five-fold slower at low than at high sodium (pH 7.2). In accordance with the spectroscopically observed slow down, the 3rd electrical component of the single turnover photocurrents was slowed by a factor of 6, which could be attributed to the reduced substrate availability.

Interestingly, when the sodium concentration was kept low and the proton concentration was reduced likewise (figure 4.2 C) the distinct O-state absorption difference became visible again in the contour plot, although the sodium concentration was unchanged. This was a surprising result in the light of earlier studies where the accumulation of the spectroscopic O state was taken as indication for sodium uptake and pumping[48,261] and the O-state-less photocycle of KR2 was assigned to proton pumping[48,261]. According to that theory, the photocycle in figure 4.2 A would represent sodium pumping and that in 4.2 B would represent proton pumping. Further following that train of thoughts, a reduction of protons at a low sodium concentration (transition from panel B to C) should slow down the photocycle because the substrate is reduced. However, according to the spectroscopic analysis the photocycle was accelerated 3.5-fold and all three electric kinetic components were slightly acceler-

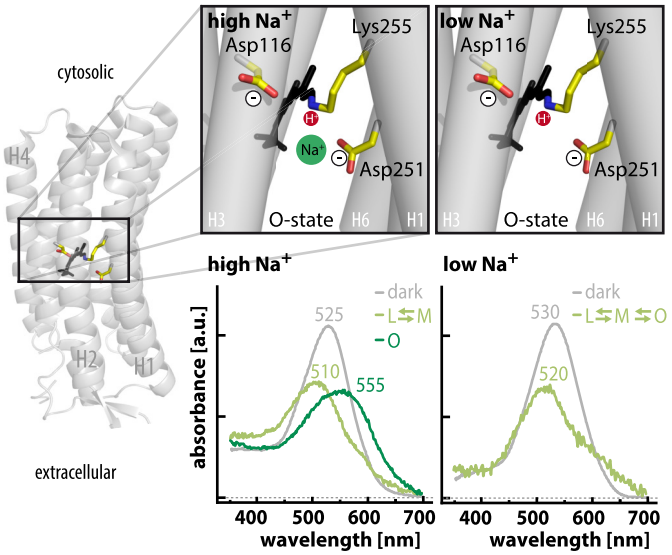

Figure 4.3: Bathochromic shift of O-state absorption Dark state structure of KR2 (PDB:4XTL) with inset showing the proposed transient sodium binding site at D251[78,79,83]. In the O state the sodium ion is presumably located close to the RSB as indicated. No implications on the retinal isomer conformation intended and TM 2 was removed for visibility. Bottom row shows the calculated absorption spectra of the photointermediates extracted from spectroscopic flash photolysis experiments. Taken from Grimm *et al.*[190].

ated as well[o]. Overall, the photocycle at low sodium and low proton concentration was spectroscopically similar to high sodium pH 7.2, but electrically similar to low sodium and pH 7.2. Hence, judging from the single turnover photocurrents the transport process was not significantly different at low sodium pH 9.0 and pH 7.2, despite the pronounced spectroscopic changes.

This led to the conclusion that although the dark state absorption of KR2 is largely independent of the sodium concentration[48,190], the O-state absorption is red-shifted by transient sodium binding (figure 4.3). Accordingly, the transient binding of the positively charged sodium close to the RSB causes a bathochromic shift of the O-state absorption, while the sodium-less O state would absorb similar to the dark state masking it in the spectroscopic measurements of the absorption differences. The reduced bleach of the dark state at low sodium pH 7.2 in the ms time regime (figure 4.2 B), could further support the rise of a photointermediate absorbing similar to the dark state. Kato and colleagues observed different red-shifts of the O-state absorption in LiCl and NaCl and similarly concluded a transient localization of the ion close to the RSB[78]. This transient sodium binding is further modified by the proton concentration, such that the affinity for sodium is increased at alkaline pH, red-shifting O-state absorption more at low sodium pH 9.0 than pH 7.2[p]. However, if sodium would be transported in one and protons in the other case, a change in the electrogenic steps would be reasonable as it is hard to imagine that an ion and a proton would be transported along the exact same pathway. Nevertheless, the single turnover photocurrents were very similar at both pH values and low sodium indicating no major changes in ion translocation.

Qualitatively similar to high Na^+ (figure 4.2 A), a rise of the O-state absorption difference was observed when flash photolysis experiments were performed in a solution containing 110 mM K^+ and 1 mM Na^+[190]. In contrast, recordings with only 1 mM Na^+ (NMG buffer) did, not show an O-state related absorption difference as discussed above (figure 4.2 B). Regarding the above-discussed mechanism causing a red-shift of the O-state absorption by an ion close to the RSB, a transient location of a K^+ in proximity of the RSB can be deduced. Consequently, this implies a transport activity of KR2 for K^+, which agrees with the photocurrent increase observed upon raised $[K^+]_i$. Likewise, this emphasizes that generation of the Na^+-free condition by a replacement with K^+, as done in several previous studies[48,80], might be unfavorable and a replacement by a non-transported ion would be preferable.

[o] Changes were not significant (yet), but acceleration at alkaline pH would be in agreement with the observed promotion of the stationary photocurrents at low proton concentration.

[p] The slight dark state absorption shift comparing pH 7.2 and 9.0 at low sodium[190] would not be enough to explain the pronounced change in O-state absorption difference.

4.2.5 Optogenetic potential of eKR2

Today, the toolbox to inhibit neuronal activity is extremely versatile as recently nicely reviewed by Wiegert *et al.*[262]. Complementing optogenetic approchaches there are other strategies using chemogenetic silencing tools like designer receptors exclusively activated by a designer drug (DREADD)[263], non-light controlled genetic silencing approaches[264,265] or non-genetic methods like cooling, administration of tetrodotoxin or muscimol to inhibit neuronal activity[262,266,267]. However, in this section the silencing potential of eKR2 will be discussed in the context of other light-induced, mainly genetically-encoded inhibitory tools.

Within the group of optogenetic tools for neuronal silencing two kinds of tool exist with one group based on microbial rhodopsins and the other one not. The alternative light-controlled inhibition approaches, which are mainly[q] genetically-encoded but not based on microbial rhodopsins, were explored extensively over the last years. Earlier attempts include a synthetic photoisomerizable azobenzene-regulated K^+ (SPARK) channel[159]. Here, the conductance of a voltage-gated potassium channel was modulated by a tethered synthetic compound, which reversibly switches light-induced from *trans* to *cis* configuration thereby establishing or releasing a channel block[159]. In 2010, Janovjak and colleagues reported the hyperpolarizing light-gated channel HyLighter[268], which makes the pore of a bacterial K^+-channel light sensitive by fusion to a photoswitchable ligand-binding domain of an ionotropic glutamate receptor (iGluR), which was engineered earlier[269]. Additionally, the possibility to render endogenous inhibitory GPCR-induced pathways light-sensitive was explored[155,270] and following the 'optoXR'-approach[271] a chimera from a rat rhodopsin and a rat opoid-like receptor was created yielding a light-induced opioid-like receptor[272]. In 2015, the group of Anna Moroni created a blue-light induced K^+-channel (BLINK1) via the fusion of a LOV-domain to a viral K^+-channel[273].

All of the afore-mentioned approaches enabled the light-induced silencing of neuronal activity. Nevertheless, they present several drawbacks especially in comparison to microbial rhodopsin-based silencing tools. For example constructs depending on light-switchable synthetic compounds like SPARK and HyLighter need supplementation of the compound, which could potentially be toxic especially *in vivo* and additionally leaves the construct not fully genetically encoded. The GPCR related approaches yielded light-control of endogenous inhibitory pathways and are for that reason mostly limited to investigate those and their related inhibitory responses. A light-activated K^+-

[q] Strictly speaking the approaches using tethered photoswitchable compounds are not completely genetically encoded, because the synthetic compound has to be added.

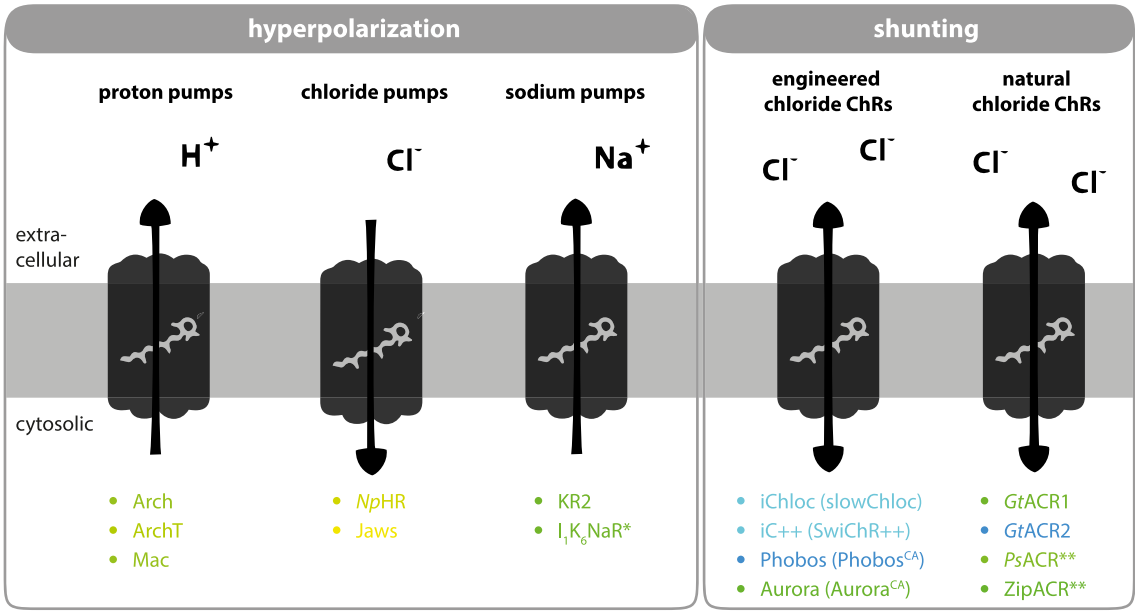

Figure 4.4: Overview of rhodopsin-based inhibitory optogenetic tools. Inhibitory optogenetic tools based on microbial rhodopsins can be divided into two groups according to their inhibition mechanism. Active ion pumps transport one charge per absorbed photon and hyperpolarize the membrane rendering it less excitable (left). Chloride-conducting ChRs shunt the neurons and clamp the membrane potential to the Cl^--reversal potential impeding the generation of APs (right). Listed below are examples of natural or engineered microbial rhodopsin belonging to the respective group colored according to their activation wavelength. * indicates missing demonstration of inhibitory potential *in-vivo* and ** indicates that silencing of APs has not been demonstrated in neurons *in vitro*. For references regarding the constructs, the reader is referred to the text.

channel would present a physiological way of hyperpolarizing the cell via clamping the membrane potential to the K^+ reversal potential thus impeding AP firing. However, expression of BLINK1 itself seems to be challenging in mammalian cells as the authors report that currents above the dark level were only observed in 10 % of the transfected cells[273] reducing the applicability of BLINK1.

In contrast, all advantages of microbial rhodopsins introduced before in the context of optogenetics (see page 16) as well apply for inhibitory microbial rhodopsins. They are small proteins, fully genetically-encoded, need no supplementation of retinal in mammals, they act reversibly and on the timescale of milliseconds[262]. Available rhodopsin-based optogenetic silencing tools include H^+-pumps like Arch[164], ArchT[274] or Mac[164] showing maximal sensitivities between 545 nm to 560 nm and their expression-optimized versions eArch 3.0, eArchT 3.0 eMac 3.0 with wild-type like action spectra[236]. Additionally, Cl^--pumps like *Np*HR[164] or e*Np*HR 2.0/3.0[200,201] activated best by 570 nm light and the slightly red-shifted Jaws[275] (λ_{max}=580 nm) were used to inhibit AP firing *in vitro* and *in vivo*. For all known light-driven ion pumps neuronal inhibition is achieved through hyperpolarization of the membrane due to the transported charges, which shifts the

rheobase to higher values and reduces excitability of the cell (figure 4.4). In contrast, the ACRs mediate light-induced neuronal inhibition through another mechanism. Allowing the passage of Cl^- along its electrochemical gradient upon illumination they shunt the cell clamping it to the reversal potential of Cl^-, which is close to the cells resting potential in mature neurons (figure 4.4). On the one hand there are engineered ACRs like ChloC[39] and iC1C2[40] and their enhanced successors iChloc[276] and iC++[238] all activated best with 490 nm light. Additionally, there are ACRs with differing activation wavelength like the blue-shifted Phobos absorbing maximally at 470 nm[195] and the red-shifted Aurora (λ_{max}=520 nm)[195]), which are both available as slow-cycling bi-stable variants allowing to be switched on and off with light[195]. On the other hand there are natural ACRs like *Gt*ACR1/2 maximally sensitive to 530 nm and 470 nm light[41], the slightly red-shifted *Ps*ChR (λ_{max}=540 nm)[218] and the fast ZipACR with closing kinetics below 1 ms[277] and a peak absorption at λ_{max}=515 nm[96].

Despite their evident usefulness for the light-triggered cessation of neuronal firing, established rhodopsin-based silencing tools possess several drawbacks. All ACRs present a passive system and hence depend on the ambient Cl^--gradient. It was shown that the Cl^--concentration can vary within different compartments of the neuron rendering ACRs inhibitory in the soma but excitatory in axons or synaptic termini[262,278,279]. Additionally, it is known that the intracellular Cl^--concentration can vary during the developmental stages of a neuron[280–283] entailing that ACRs might not be inhibitory at all stages of neuronal maturation. In contrast, hyperpolarization by active pumping would not depend on the ionic gradient, but could affect the distribution of the respective ion. In case of the Cl^--pump *Np*HR it was demonstrated that activation of the pump elevates the intracellular Cl^--concentration such that the $GABA_A$ reversal potentials can be shifted[284] and synaptic transmission is altered beyond the actual time of inhibition[284]. A similar effect was not observed after silencing with a H^+-pump[284]. However, Mahn and colleagues demonstrated that hyperpolarization via H^+-extrusion can significantly alter the pH especially in small compartments[278].

Regarding the above detailed drawbacks of inhibitory microbial rhodopsins, Na^+-extrusion could present a less invasive way of neuronal silencing as neither the Cl^--concentration nor pH are altered. Additionally, an outward-directed Na^+-pump is not changing the strong inward directed Na^+-gradient naturally present in neurons but rather enlarging it. Moreover, the sodium gradient should be tightly regulated by the NKAs, because it is essential for AP firing. Hence, potential influences on the Na^+-concentration might be rather transient reducing harming effects beyond the intended silencing. One additional advantage of eKR2 is that the pumping activity is not reduced at negative membrane potentials as discussed earlier (see page 92) in contrast to

H^+- and Cl^--pumps, which should enable a stable hyperpolarization not decreasing over time[78]. Earlier approaches to enhance the performance of sodium pumps included the generation of a chimeric pump[237] and the screen of the silencing capabilities of natural pumps[76]. However, expressed in neurons the variants reached hyperpolarizations of the membrane potential around 10 mV[76,237], while eKR2 hyperpolarized the membrane on average by 30 mV at 10 mW mm^{-2} intensity of the activation light. Already at 0.5 mW mm^{-2} eKR2 activation reliably inhibited AP generation and entailed a significantly stronger rheobase shift than the first-used KR2 variant for silencing[78] with C-terminal targeting sequences (figure 3.26). Experiments demonstrating the applicability of eKR2 for neuronal silencing and investigating its compatibility *in vivo* still have to be done. Nevertheless, eKR2 is adding to the optogenetic tool box providing a complementary way of non-invasive, ms-precise neuronal silencing in contexts were the use of established tools based on H^+ or Cl^- transport is unfavorable or even impossible.

Although, the choice of optogenetic tools was initially rather limited, the optogenetic tool box became extremely versatile today. Over the last decade extensive genome mining approaches revealed a myriad of microbial rhodopsins with different properties with the protein family comprising more than 7000 members today[12]. The discovery of new types of microbial rhodopsins with desired properties was complemented by engineering approaches tailoring the known proteins to the experimental needs or even creating new features. Future challenges might therefore not be the availability of a certain tool, but rather the appropriate choice of tool for the intended experiment. Nevertheless, a thorough understanding of the molecular mechanisms of microbial rhodopsins will always be needed both for engineering attempts and for a purposeful setup of an optogenetic experiment.

Appendix

A.1 Statistics

This section summarizes all calculated p values for figure 3.15 -also those not mentioned in text or figure- using the non-parametric Wilcoxon rank sum test (unpaired) to determine whether and to what extent differences were statistically significant.

Table 1: Table lists the pairwise (all combinations) caculated (Wilcoxon rank-sum test) p values and the deduced significance levels for data represented in figure 3.15. First number in column one and two indicates intracellular Na^+-concentration in mM while the second number indicates the pH value. Extracellular buffer is the same for all conditions as stated in the figure legend of figure 3.15.

condition		peak current density		stationary current density		off-kinetics	
1	2	p value	sign. level	p value	sign. level	p value	sign. level
110, 7.2	110, 9.0	0.286	ns	0.577	ns	0.737	ns
	1, 6.0	0.346	ns	$8*10^{-5}$	***	$1*10^{-8}$	***
	1, 7.2	0.279	ns	$1*10^{-7}$	***	$1*10^{-7}$	***
	1, 9.0	0.202	*	$2*10^{-4}$	***	$3*10^{-12}$	***
	0.1, 7.2	0.115	ns	$6*10^{-8}$	***	$1.*10^{-8}$	***
	0.1, 9.0	0.075	ns	0.0025	**	$5*10^{-7}$	***
110, 9.0	1, 6.0	0.140	ns	$5*10^{-4}$	***	$3*10^{-6}$	***
	1, 7.2	0.0382	*	$1*10^{-5}$	***	$1*10^{-5}$	***
	1, 9.0	0.0232	*	0.0011	**	$2*10^{-8}$	***
	0.1, 7.2	0.0305	*	$2*10^{-6}$	***	$3*10^{-6}$	***
	0.1, 9.0	0.022	*	0.012	*	$8*10^{-5}$	***
1, 6.0	1, 7.2	0.797	ns	0.332	ns	0.896	ns
	1, 9.0	0.282	ns	0.595	ns	0.11	ns
	0.1, 7.2	0.526	ns	0.004	**	0.011	*
	0.1, 9.0	0.382	ns	0.466	ns	0.108	ns
1, 7.2	1, 9.0	0.167	ns	0.218	ns	0.102	ns
	0.1, 7.2	0.466	ns	0.024	*	0.011	*
	0.1, 9.0	0.509	ns	0.055	ns	0.072	ns
1, 9.0	0.1, 7.2	0.235	ns	0.0044	**	$2*10^{-4}$	***
	0.1, 9.0	0.447	ns	0.525	ns	0.389	ns
0.1, 7.2	0.1, 9.0	0.975	ns	$1.7*10^{-3}$	**	$4.6*10^{-3}$	**

A.2 Sequence alignment of NaRs

Figure 5 shows a complete sequence alignment of putative sodium pumping rhodopsins with the NDQ motif with the proton pump *Hs*BR and the chloride pump *Np*HR.

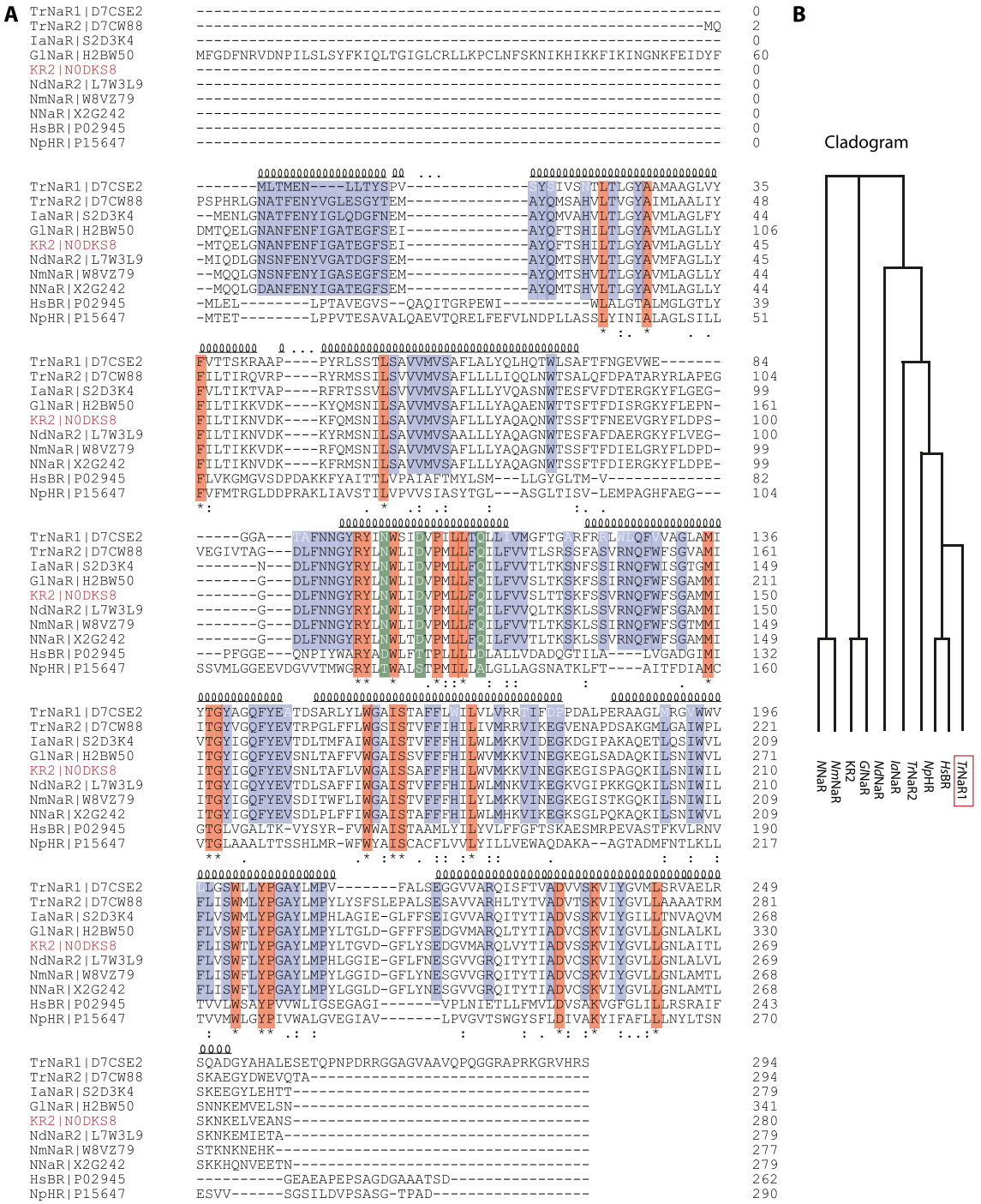

Figure 5: Primary sequence alignment of putative NaRs. A Sequence alignment of *Hs*BR (DTD motif), *Np*HR (TSA motif) and microbial rhodopsins with NDQ motif putatively pumping Na^+ with name and UniProt ID. *Tr*NaR1 and 2 of *Truepera radiovictrix*, *Ia*NaR of *Indibacter alkaliphilus*, *Gl*NaR of *Gillisia limnaea*, *Nd*NaR2 of *Nonlabens dokdonensis*, *Nm*NaR of *Nonlabens marinus*, *N*NaR of *Nonlabens* sp. YIK11, KR2 of *Krokinobacter eikastus*. Residues similar in all pumps are marked in red, while blue indicates residues conserved within NaRs but different in *Hs*BR and *Np*HR. The putative NaR *Tr*NaR1 distinguishes from the other pumps in several positions indicated by white letters on blue background. **B** Cladogram of all aligned pumps underlining that *Tr*NaR1 despite having the NDQ motif is closer related to *Hs*BR and *Np*HR than to the other NaRs.

A.3 Source code

Python: Automatic extraction of basic values from a recorded photocurrent

When the number of recorded files grew I wrote a small Python script (heavily relying on the stf Python package[187]) to automatically evaluate basic parameters of the recorded photocurrents, which was used for the evaluation of the KR2 data. The code extracts some basic values of the traces like cell capacitance, seal resistance, peak current, stationary current, ratio of peak to stationary current. Peak and stationary current are additionally given normalized to the respective cell size using the cell capacitance. The script works for multiple sweeps in one file (like in an I-V measurement) and determines the sampling rate of the file and the respective command voltage of the evaluated sweep automatically. Certain values like the position to extract peak and stationary current as well as to determine the baseline have to be adapted to the respective recording protocol.

```
1  import numpy
2  import stf
3  import scipy
4
5  #script extracts basic values of a current trace
6  #printing and giving back the return
7  #parameters are the minimum seal resistance chosen to evaluate a trace
       (quality of the patch)
8
9  def get_BasicValues(RSealMin):
10 SamplingInterval = stf.get_sampling_interval() #in micro sec
11 VoltageStepRamp = 50 #in mV; necessary to calculate C_p
12 stf.set_channel(0)
13 NumberOfSweeps = stf.get_size_channel()
14 stf.set_baseline_method("mean") #average points within baseline cursors
15 CurrentTrace = 0
16 SumCellCapacitance = 0
17
18 #calculates average C_p from all recorded sweeps using the voltage ramp
19 for n in range(0, NumberOfSweeps):
20 DataPoints = stf.get_trace(n, 0)
21 Q1a = 148/SamplingInterval
22 Q1b = 196/SamplingInterval
23 Q2a = 198/SamplingInterval
```

```
24 Q2b = 246/SamplingInterval
25 Q1 = numpy.trapz(DataPoints[Q1a:Q1b], None, SamplingInterval, -1)
26 Q2 = numpy.trapz(DataPoints[Q2a:Q2b], None, SamplingInterval, -1)
27 CellCapacitance = -(Q1-Q2)/(2*VoltageStepRamp)
28 SumCellCapacitance = SumCellCapacitance+CellCapacitance
29 MeanCapacitance = SumCellCapacitance/NumberOfSweeps
30
31 print (stf.get_filename())
32 Output="R_membrane"+"\t"+"I_peak"+"\t"+"I_stat"+"\t"+"I_peak/I_stat"+"\
       t"+"C_cell␣="+str(round(MeanCapacitance, 2))+"\t"+"norm.␣I_peak"+"\t
       "+"norm.␣I_stat"+"\n"
33
34 while CurrentTrace < stf.get_size_channel():
35 stf.set_trace(CurrentTrace)
36
37 # calculates command voltage
38 stf.set_channel(1) #channel with command voltage
39 stf.set_base_start(290, True)
40 stf.set_base_end(330, True)
41 stf.set_peak_start(410, True)
42 stf.set_peak_end(470, True)
43 stf.set_peak_mean(-1)
44 stf.measure()
45 CommandVoltage = stf.get_peak()-stf.get_base()
46
47 # calculates SealResistance in GigaOhm
48 stf.set_channel(0) #channel with recorded current
49 stf.set_base_start(290, True)
50 stf.set_base_end(330, True)
51 stf.set_peak_start(1240, True)
52 stf.set_peak_end(1340, True)
53 stf.set_peak_mean(-1)
54 stf.measure()
55 SealResistance = CommandVoltage /(stf.get_peak()-stf.get_base())
56 CommandVoltage = round(CommandVoltage)
57
58 if SealResistance>=RSealMin:
59 #peak current (1 pt) with respect to baseline
60 stf.set_base_start(1240, True)
61 stf.set_base_end(1340, True)
62 stf.set_peak_start(1340, True)
```

```
63 stf.set_peak_end(1400, True)
64 stf.set_peak_mean(1)
65 stf.measure()
66 PeakCurrent = stf.get_peak()-stf.get_base()
67
68 #stationary current (all pts between peak cursors)
69 stf.set_peak_start(1625,True)
70 stf.set_peak_end(1645,True)
71 stf.set_peak_mean(-1)
72 stf.measure()
73 StationaryCurrent = stf.get_peak()-stf.get_base()
74 Ratio = PeakCurrent/StationaryCurrent
75
76 CurrentTrace += 1
77 intermediate = str(SealResistance)+"\t"+str(PeakCurrent)+"\t"+str(
       StationaryCurrent)+"\t"+str(Ratio)+"\t"+"␣"+"\t"+str(PeakCurrent/
       MeanCapacitance)+"\t"+str(StationaryCurrent/MeanCapacitance)+"\n"
78 Output = Output + intermediate
79
80 elif CommandVoltage == 0.0:
81 #peak current (1 pt) with respect to baseline
82 stf.set_base_start(1240, True)
83 stf.set_base_end(1340, True)
84 stf.set_peak_start(1340, True)
85 stf.set_peak_end(1400, True)
86 stf.set_peak_mean(1)
87 stf.measure()
88 PeakCurrent = stf.get_peak()-stf.get_base()
89
90 #stationary current (all pts between peak cursors)
91 stf.set_peak_start(1625,True)
92 stf.set_peak_end(1645,True)
93 stf.set_peak_mean(-1)
94 stf.measure()
95 StationaryCurrent = stf.get_peak()-stf.get_base()
96 Ratio = PeakCurrent/StationaryCurrent
97
98 CurrentTrace += 1
99 SealResistance = float('nan')
```

```
intermediate = str(SealResistance)+"\t"+str(PeakCurrent)+"\t"+str(
    StationaryCurrent)+"\t"+str(Ratio)+"\t"+"␣"+"\t"+str(PeakCurrent/
    MeanCapacitance)+"\t"+str(StationaryCurrent/MeanCapacitance)+"\n"
Output = Output + intermediate

else:
CurrentTrace += 1
PeakCurrent = StationaryCurrent = Ratio = float('nan')
intermediate = str(SealResistance)+"\t"+str(PeakCurrent)+"\t"+str(
    StationaryCurrent)+"\t"+str(Ratio)+"\t"+"␣"+"\t"+str(PeakCurrent/
    MeanCapacitance)+"\t"+str(StationaryCurrent/MeanCapacitance)+"\n"
Output = Output + intermediate
print Output
return (Output)
```

The following code was used to run the above code on multiple files at once, but it could also be adapted to run other methods multiple times.

```
import os
import numpy as np
import stf
import Basics

def more():
#path to folder containing files in 'fileList'
Path = "E:\SodiumPumps_sorted\LightTitration" #adapt
#list of files to be evaluated (.abf); all in one folder (with 'Path')
fileList = ["file1", "file2", "file3", "file4", "etc."] #adapt

for file in fileList:
stf.file_open(Path + os.path.sep + file)
Basics.get_BasicValues(0.4) #set cutoff for evaluation in gigaOhm
#(recordings with R_m smaller than this will be irgnored)
stf.close_this()
return ('tada')
```

ImageJ: Evaluate membrane targeting

This Fiji macro was used to automate and facilitate the evaluation of membrane targeting in confocal images. After determining the average fluorescence in the cell membrane, in the cell and in the background, membrane targeting was calculated in Microsoft Excel.

```
1  #macro opens selected images containing the fluorescence of the
       membrane protein and the membrane marker
2  #set the threshold and converts the image to a binary picture; 1 in
       membrane and 0 elsewhere
3  #binary image is mutiplied with the original image of the protein
       fluorescence (now only in the membrane) and then averaged over the
       membrane area
4  pathMembrane = File.openDialog("Select the image with the membrane
       marker fluorescence")
5  open(pathMembrane);
6  membraneImageID = getImageID()
7  pathProtein = File.openDialog("Select the image with the protein
       fluorescence")
8  open(pathProtein);
9  proteinImageID = getImageID()
10 selectImage(membraneImageID);
11 setAutoThreshold("Default dark");
12 run("Threshold...");
13 waitForUser("Set threshold and press ok")
14 run("Make Binary");
15 run("Divide...", "value=255.000");
16 imageCalculator("Multiply create", proteinImageID, membraneImageID);
17 newID = getImageID()
18 selectImage(newID);
19 pathSave = File.openDialog("Select the file name to save")
20 saveAs("Tiff", pathSave);
21 selectImage(membraneImageID)
22 close();
23 run("ROI Manager...");
24 selectImage(newID)
25 setTool("wand");
26 waitForUser("Select membrane area")
27 run("Measure");
28 close();
29 roiManager("Delete");
30 selectImage(proteinImageID);
31 setTool("rectangle");
32 waitForUser("Select background area")
33 run("Measure");
```

The following code was run afterwards to determine the average fluorescence within the cell using the image created with the above script.

```
pathMerge = File.openDialog("Select␣the␣image␣with␣the␣merged␣protein␣
    and␣mebrane␣fluorescence")
open(pathMerge);
mergeImageID = getImageID()
pathProtein = File.openDialog("Select␣the␣image␣with␣the␣protein")
open(pathProtein);
proteinImageID = getImageID()
selectImage(mergeImageID);
run("ROI␣Manager...");
setTool("freehand");
waitForUser("Select␣cytosolic␣area␣and␣add␣to␣ROI␣manager")
close();
selectImage(proteinImageID)
run("Measure");
waitForUser("Delete␣old␣ROI␣and␣select␣background␣area")
run("Measure");
close();
String.copyResults();
waitForUser("Paste␣results␣now")
run("Clear␣Results");
```

MatLAB: Isologarithmic binning

The following Matlab code was generated together with Jonas Wietek and used to process the photocurrent data obtained during single turnover measurements upon illumination with a ns-laser flash. To have maximal time resolution data was measured at a sampling rate of 250 kHz resulting in large files. Therefore, we needed a way to bin the data such that each time regime is represented by the same number of data points (isologarithmic binning).

```
function [BinnedData] = logbinning(RawData, bins)
%LOGBINNING
%time must be ms!
%bins sets binning per decade (usually 50)

time=RawData(:,1)/1000; %extract time in seconds
data1=RawData(:,2); %extract datapoints
data2=RawData(:,3);
```

```
9  data3=RawData(:,4);
10 data4=RawData(:,5);
11
12 %find min and max decade
13 t_expmax=floor(log10(time(length(time)))); %max decade
14 t_expmin=floor(log10(time(2))); %min decade / time(1) usually 0
15 NODec=abs(t_expmin-t_expmax)+1; %no of decades incl boundaries
16
17 noOfPoints=bins*NODec;
18
19 spacing=logspace(log10(1),log10(length(time)+1),noOfPoints);
20 [~, binidx] = histc(1:length(time),spacing);
21
22 timemeans = accumarray(binidx.', time', [], @mean);
23 datameans1 = accumarray(binidx.', data1', [], @mean);
24 datameans2 = accumarray(binidx.', data2', [], @mean);
25 datameans3 = accumarray(binidx.', data3', [], @mean);
26 datameans4 = accumarray(binidx.', data4', [], @mean);
27
28 BinnedData =horzcat(timemeans,datameans1,datameans2,datameans3,
       datameans4);
29 BinnedData( all(~BinnedData,2), : ) = []; % remove zero rows time
30 BinnedData=BinnedData(2:end,:); %del firt row time=0
31
32 end
```

List of Figures

List of Tables

Bibliography

[1] L. Rizzini, J.-J. Favory, C. Cloix, D. Faggionato, A. O'Hara, E. Kaiserli, R. Baumeister, E. Schafer, F. Nagy, G. I. Jenkins, and R. Ulm. Perception of UV-B by the *Arabidopsis* UVR8 Protein. *Science*, 332 (6025):103–106, (**2011**). doi: 10.1126/science.1200660. 1

[2] J. Gong, Y. Yuan, A. Ward, L. Kang, B. Zhang, Z. Wu, J. Peng, Z. Feng, J. Liu, and X. S. Xu. The *C. elegans* Taste Receptor Homolog LITE-1 Is a Photoreceptor. *Cell*, 167(5):1252–1263, (**2016**). doi: 10.1016/j.cell.2016.10.053. 1, a

[3] J. R. Wagner, J. Zhang, J. S. Brunzelle, R. D. Vierstra, and K. T. Forest. High Resolution Structure of *Deinococcus* Bacteriophytochrome Yields New Insights into Phytochrome Architecture and Evolution. *Journal of Biological Chemistry*, 282(16):12298–12309, (**2007**). doi: 10.1074/jbc.M611824200. 1

[4] N. C. Rockwell, D. Duanmu, S. Shelley, C. Bachy, D. C. Price, D. Bhattacharya, A. Z. Worden, J. C. Lagarias, N. C. Rockwell, D. Duanmu, S. S. Martin, C. Bachy, D. C. Price, and D. Bhattacharya. Eukaryotic algal phytochromes span the visible spectrum. *Proceedings of the National Academy of Sciences*, 112(9):E1051–E1051, (**2015**). doi: 10.1073/pnas.1501871112. 1

[5] J. L. Spudich, C. S. Yang, K. H. Jung, and E. N. Spudich. RETINYLIDENE PROTEINS: Structures and Functions from Archaea to Humans. *Annu. Rev. Cell Dev. Biol.*, 16:365–392, (**2000**). doi: 10.1146/annurev.cellbio.16.1.365. 1, 1.1

[6] N. G. BROWN, C. FOWLES, R. SHARMA, and M. AKHTAR. Mechanistic studies on rhodopsin kinase. Light-dependent phosphorylation of C-terminal peptides of rhodopsin. *European Journal of Biochemistry*, 208(3):659–667, (**1992**). doi: 10.1111/j.1432-1033.1992.tb17232.x. 1

[7] K. Palczewski, T. Kumasaka, T. Hori, C. A. Behnke, H. Motoshima, B. A. Fox, I. Le Trong, D. C. Teller, T. Okada, R. E. Stenkamp, M. Yamamoto, and M. Miyano. Crystal Structure of Rhodopsin: A G Protein-Coupled Receptor. *Science*, 289(5480):739–745, (**2000**). doi: 10.1126/science.289.5480.739.

[8] T. Okada, Y. Fujiyoshi, M. Silow, J. Navarro, E. M. Landau, and Y. Shichida. Functional role of internal water molecules in rhodopsin revealed by x-ray crystallography. *Proceedings of the National Academy of Sciences*, 99(9):5982–5987, (**2002**). doi: 10.1073/pnas.082666399.

[9] D. Salom, D. T. Lodowski, R. E. Stenkamp, I. L. Trong, M. Golczak, B. Jastrzebska, T. Harris, J. A. Ballesteros, and K. Palczewski. Crystal structure of a photoactivated deprotonated intermediate of rhodopsin. *Proceedings of the National Academy of Sciences*, 103(44):16123–16128, (**2006**). doi: 10.1073/pnas.0608022103. 1

[10] T. Okano, T. Yoshizawa, and Y. Fukada. Pinopsin is a chicken pineal photoreceptive molecule. *Nature*, 372(6501):94–97, (**1994**). doi: 10.1038/372094a0. 1

[11] I. Provencio, I. R. Rodriguez, G. Jiang, W. P. Hayes, E. F. Moreira, and M. D. Rollag. A Novel Human Opsin in the Inner Retina. *The Journal of Neuroscience*, 20(2):600–605, (**2000**). doi: 10.1523/JNEUROSCI.20-02-00600.2000. 1

[12] E. G. Govorunova, O. A. Sineshchekov, H. Li, and J. L. Spudich. Microbial Rhodopsins: Diversity, Mechanisms, and Optogenetic Applications. *Annual Review of Biochemistry*, 86(1):845–872, (**2017**). doi: 10.1146/annurev-biochem-101910-144233. 1.1, 1.3, 4.2.5

[13] O. P. Ernst, D. T. Lodowski, M. Elstner, P. Hegemann, L. S. Brown, and H. Kandori. Microbial and Animal Rhodopsins: Structures, Functions, and Molecular Mechanisms. *Chemical Reviews*, 114(1):126–163, (**2014**). doi: 10.1021/cr4003769. 1.1, 1.1.1, 1.2, 1.1.1, 1.3

[14] W. Stoeckenius. The rhodopsin-like pigments of halobacteria: light-energy and signal transducers in an archaebacterium. *Trends in Biochemical Sciences*, 10(12):483–486, (**1985**). doi: 10.1016/0968-0004(85)90210-5. 1.1

[15] H. Tomioka, T. Takahashi, N. Kamo, and Y. Kobatake. Flash spectrophotometric identification of a fourth rhodopsin-like pigment in Halobacterium halobium. *Biochemical and Biophysical Research Communications*, 139(2):389–395, (**1986**). doi: 10.1016/S0006-291X(86)80003-1. 1.1

[16] K.-H. Jung, V. D. Trivedi, and J. L. Spudich. Demonstration of a sensory rhodopsin in eubacteria. *Molecular Microbiology*, 47(6):1513–1522, (**2003**). doi: 10.1046/j.1365-2958.2003.03395.x. 1.1

[17] M. Luck, T. Mathes, S. Bruun, R. Fudim, R. Hagedorn, T. M. Tran Nguyen, S. Kateriya, J. T. M. Kennis, P. Hildebrandt, and P. Hegemann. A photochromic histidine kinase rhodopsin (HKR1) that is bimodally switched by ultraviolet and blue light. *Journal of Biological Chemistry*, 287(47):40083–40090, (**2012**). doi: 10.1074/jbc.M112.401604. 1.1

[18] K. Yoshida, S. P. Tsunoda, L. S. Brown, and H. Kandori. A unique choanoflagellate enzyme rhodopsin exhibits light-dependent cyclic nucleotide phosphodiesterase activity. *Journal of Biological Chemistry*, 292(18):7531–7541, (**2017**). doi: 10.1074/jbc.M117.775569. 1.1

[19] G. M. Avelar, R. I. Schumacher, P. A. Zaini, G. Leonard, T. A. Richards, and S. L. Gomes. A Rhodopsin-Guanylyl Cyclase Gene Fusion Functions in Visual Perception in a Fungus. *Current Biology*, 24(11):1234–1240, (**2014**). doi: 10.1016/j.cub.2014.04.009. 1.1

[20] D. Oesterhelt and W. Stoeckenius. Rhodopsin-like protein from the purple membrane of *Halobacterium halobium*. *Nature New Biology*, 233(39):149–152, (**1971**). doi: 10.1038/newbio233149a0. 1.1, 1.1, 1.1.1

[21] M. Kolbe, H. Besir, L.-O. Essen, and D. Oesterhelt. Structure of the Light-Driven Chloride Pump Halorhodopsin at 1.8 Å Resolution. *Science*, 288(5470):1390–1396, (**2000**). doi: 10.1126/science.288.5470.1390. 1.1, 1.1

[22] R. A. Bogomolni, W. Stoeckenius, I. Szundi, E. Perozo, K. D. Olson, and J. L. Spudich. Removal of transducer HtrI allows electrogenic proton translocation by sensory rhodopsin I. *Proceedings of the National Academy of Sciences*, 91(21):10188–10192, (**1994**). doi: 10.1073/pnas.91.21.10188. b

[23] J. Sasaki and J. L. Spudich. Proton Circulation During the Photocycle of Sensory Rhodopsin II. *Biophysical Journal*, 77(4):2145–2152, (**1999**). doi: 10.1016/S0006-3495(99)77055-4. 1.1

[24] G. Schmies, B. Lüttenberg, I. Chizhov, M. Engelhard, A. Becker, and E. Bamberg. Sensory Rhodopsin II from the Haloalkaliphilic *Natronobacterium pharaonis*: Light-Activated Proton Transfer Reactions. *Biophysical Journal*, 78(2):967–976, (**2000**). doi: 10.1016/S0006-3495(00)76654-9. b

[25] R. Seidel, B. Scharf, M. Gautel, K. Kleine, D. Oesterhelt, and M. Engelhard. The primary structure of sensory rhodopsin II: a member of an additional retinal protein subgroup is coexpressed with its transducer, the halobacterial transducer of rhodopsin II. *Proceedings of the National Academy of Sciences*, 92(7):3036–3040, (**1995**). doi: 10.1073/pnas.92.7.3036. 1.1

[26] J. L. Spudich. Protein-protein interaction converts a proton pump into a sensory receptor. *Cell*, 79(5): 747–750, (**1994**). doi: 10.1016/0092-8674(94)90064-7. 1.1

[27] J. L. Spudich. Variations on a molecular switch: transport and sensory signalling by archaeal rhodopsins. *Molecular Microbiology*, 28(6):1051–1058, (**1998**). doi: 10.1046/j.1365-2958.1998.00859.x. 1.1

[28] S. Hippler-Mreyen, J. P. Klare, A. A. Wegener, R. Seidel, C. Herrmann, G. Schmies, G. Nagel, E. Bamberg, and M. Engelhard. Probing the Sensory Rhodopsin II Binding Domain of its Cognate Transducer by Calorimetry and Electrophysiology. *Journal of Molecular Biology*, 330(5):1203–1213, (**2003**). doi: 10.1016/S0022-2836(03)00656-9. 1.1

[29] U. Scheib, K. Stehfest, C. E. Gee, H. G. Körschen, R. Fudim, T. G. Oertner, and P. Hegemann. The rhodopsin – guanylyl cyclase of the aquatic fungus *Blastocladiella emersonii* enables fast optical control of cGMP signaling. *Science Signalling*, 8(389):1–9, (**2015**). 1.1

[30] A. Greiner. *CRISPR / Cas9 und Zinkfinger-Nukleasen für die gezielte Genstilllegung in Chlamydomonas reinhardtii*. PhD thesis, 2015.

[31] L. B. Lamarche, R. P. Kumar, M. M. Trieu, E. L. Devine, L. E. Cohen-Abeles, D. L. Theobald, and D. D. Oprian. Purification and Characterization of RhoPDE, a Retinylidene/Phosphodiesterase Fusion Protein and Potential Optogenetic Tool from the Choanoflagellate *Salpingoeca rosetta*. *Biochemistry*, 56(43): 5812–5822, (**2017**). doi: 10.1021/acs.biochem.7b00519. 1.1

[32] M. M. Trieu, E. L. Devine, L. B. Lamarche, A. E. Ammerman, J. A. Greco, R. R. Birge, D. L. Theobald, and D. D. Oprian. Expression, purification, and spectral tuning of RhoGC, a retinylidene/guanylyl cyclase fusion protein and optogenetics tool from the aquatic fungus *Blastocladiella emersonii*. *Journal of Biological Chemistry*, 292(25):10379–10389, (**2017**). doi: 10.1074/jbc.M117.789636. 1.1

[33] A. Greiner, S. Kelterborn, H. Evers, G. Kreimer, I. Sizova, and P. Hegemann. Targeting of Photoreceptor Genes in *Chlamydomonas reinhardtii* via Zinc-finger Nucleases and CRISPR/Cas9. *The Plant Cell*, page tpc.00659.2017, (**2017**). doi: 10.1105/tpc.17.00659. 1.1

[34] M. Luck, S. Bruun, A. Keidel, P. Hegemann, and P. Hildebrandt. Photochemical chromophore isomerization in histidine kinase rhodopsin HKR1. *FEBS Letters*, 589(10):1067–1071, (**2015**). doi: 10.1016/j.febslet.2015.03.024. 1.1, 4.1.1

[35] Y. Tian, S. Gao, S. Yang, and G. Nagel. A novel rhodopsin phosphodiesterase from Salpingoeca rosetta shows light-enhanced substrate affinity. *Biochemical Journal*, 475(6):1121–1128, (**2018**). doi: 10.1042/BCJ20180010. 1.1

[36] G. Nagel, D. Ollig, M. Fuhrmann, S. Kateriya, A. M. Musti, E. Bamberg, and P. Hegemann. Channelrhodopsin-1: a light-gated proton channel in green algae. *Science*, 296(5577):2395–2398, (**2002**). doi: 10.1126/science.1072068. 1.1, 1.1.2

[37] G. Nagel, T. Szellas, W. Huhn, S. Kateriya, N. Adeishvili, P. Berthold, D. Ollig, P. Hegemann, and E. Bamberg. Channelrhodopsin-2, a directly light-gated cation-selective membrane channel. *Proceedings of the National Academy of Sciences*, 100(24):13940–5, (**2003**). doi: 10.1073/pnas.1936192100. 1.1.2, 1.1.2, 1.2, 3.1

[38] E. G. Govorunova, O. A. Sineshchekov, and J. L. Spudich. Structurally Distinct Cation Channelrhodopsins from Cryptophyte Algae. *Biophysical Journal*, 110(11):2302–2304, (**2016**). doi: 10.1016/j.bpj.2016.05.001. 1.1, 1.2

[39] J. Wietek, J. S. Wiegert, N. Adeishvili, F. Schneider, H. Watanabe, S. P. Tsunoda, A. Vogt, M. Elstner, T. G. Oertner, and P. Hegemann. Conversion of Channelrhodopsin into a Light-Gated Chloride Channel. *Science*, 344(6182):409–412, (**2014**). doi: 10.1126/science.1249375. 1.1, 1.1.2, 1.1.2, 1.2, 3.1.3, 4.2.5

[40] A. Berndt, S. Y. Lee, C. Ramakrishnan, and K. Deisseroth. Structure-Guided Transformation of Channelrhodopsin into a Light-Activated Chloride Channel. *Science*, 344(April):420–424, (**2014**). doi: 10.5061/dryad.9r0p6. 1.1.2, 1.2, 3.1.3, 4.2.5

[41] E. G. Govorunova, O. A. Sineshchekov, R. Janz, X. Liu, and J. L. Spudich. Natural light-gated anion channels: A family of microbial rhodopsins for advanced optogenetics. *Science*, 349:647–650, (**2015**). doi: 10.1126/science.aaa7484. 1.1, 1.1.2, 1.2, 4.2.5

[42] A. Seki, S. Miyauchi, S. Hayashi, T. Kikukawa, M. Kubo, M. Demura, V. Ganapathy, and N. Kamo. Heterologous Expression of *Pharaonis* halorhodopsin in *Xenopus laevis* oocytes and electrophysiological characterization of its light-driven Cl- pump activity. *Biophysical Journal*, 92(7):2559–2569, (**2007**). doi: 10.1529/biophysj.106.093153. 1.1, 3.2.3, 4.2, 4.2.2

[43] S. Yoshizawa, Y. Kumagai, H. Kim, Y. Ogura, T. Hayashi, W. Iwasaki, E. F. DeLong, and K. Kogure. Functional characterization of flavobacteria rhodopsins reveals a unique class of light-driven chloride pump in bacteria. *Proceedings of the National Academy of Sciences*, 111(18):6732–6737, (**2014**). doi: 10.1073/pnas.1403051111. 1.1, 1.1.1, 3.2

[44] O. Béjà, L. Aravind, E. V. Koonin, M. T. Suzuki, A. Hadd, L. P. Nguyen, S. B. Jovanovich, C. M. Gates, R. A. Feldman, J. L. Spudich, N. Elena, and E. F. Delong. Bacterial Rhodopsin : Evidence for a New Type of Phototrophy in the Sea Bacterial Rhodopsin : Evidence for a New Type of Phototrophy in the Sea. *Science*, 289(5486):1902–1906, (**2000**). doi: 10.1126/science.289.5486.1902. 1.1, 1.1.1

[45] A. Harris, M. Ljumovic, A. N. Bondar, Y. Shibata, S. Ito, K. Inoue, H. Kandori, and L. S. Brown. A new group of eubacterial light-driven retinal-binding proton pumps with an unusual cytoplasmic proton donor. *Biochimica et Biophysica Acta - Bioenergetics*, 1847(12):1518–1529, (**2015**). doi: 10.1016/j.bbabio.2015.08.003. 1.1, 1.1.1

[46] K. Inoue, S. Ito, Y. Kato, Y. Nomura, M. Shibata, T. Uchihashi, S. P. Tsunoda, and H. Kandori. A natural light-driven inward proton pump. *Nature Communications*, 7(May):1–7, (**2016**). doi: 10.1038/ncomms13415. 1.1

[47] V. Shevchenko, T. Mager, K. Kovalev, V. Polovinkin, A. Alekseev, J. Juettner, I. Chizhov, C. Bamann, C. Vavourakis, R. Ghai, I. Gushchin, V. Borshchevskiy, A. Rogachev, I. Melnikov, A. Popov, T. Balandin, F. Rodriguez-Valera, D. J. Manstein, G. Bueldt, E. Bamberg, and V. Gordeliy. Inward H^+ pump xenorhodopsin: Mechanism and alternative optogenetic approach. *Science Advances*, 3(9):e1603187, (**2017**). doi: 10.1126/sciadv.1603187. 1.1

[48] K. Inoue, H. Ono, R. Abe-Yoshizumi, S. Yoshizawa, H. Ito, K. Kogure, and H. Kandori. A light-driven sodium ion pump in marine bacteria. *Nature communications*, 4:1678, (**2013**). doi: 10.1038/ncomms2689. 1.1, 1.1.1, 1.1.1, 1.4, 1.1.1, 1.1.1, 1.3, 3.2, 3.2.1, 3.2.3, 4.2.1, 4.2.3, 4.2.4, 4.2.4

[49] W. Stoeckenius and R. Rowen. A MORPHOLOGICAL STUDY OF HALOBACTERIUM HALOBIUM AND ITS LYSIS IN MEDIA OF LOW SALT CONCENTRATION. *The Journal of Cell Biology*, 34(1):365 – 393, (**1967**). 1.1.1

[50] C. W. F. McClare. Bonding between Proteins and Lipids in the Envelopes of Halobacterium halobium. *Nature*, 216:766–771, (**1967**). 1.1.1

[51] K. Inoue, Y. Nomura, and H. Kandori. Asymmetric Functional Conversion of Eubacterial Light-driven Ion Pumps. *Journal of Biological Chemistry*, 291(19):9883–9893, (**2016**). doi: 10.1074/jbc.M116.716498. 1.1.1, 1.1.1

[52] S. P. Balashov, E. S. Imasheva, V. A. Boichenko, J. Antón, J. M. Wang, and J. K. Lanyi. Xanthorhodopsin: A Proton Pump with a Light-Harvesting Carotenoid Antenna. *Science*, 309(5743):2061–2064, (**2005**). doi: 10.1126/science.1118046. 1.1.1

[53] Y. Sudo and S. Yoshizawa. Functional and Photochemical Characterization of a Light-Driven Proton Pump from the Gammaproteobacterium Pantoea vagans. *Photochemistry and Photobiology*, 92(3):420–427, (**2016**). doi: 10.1111/php.12585. 1.1.1

[54] L. E. Petrovskaya, E. P. Lukashev, V. V. Chupin, S. V. Sychev, E. N. Lyukmanova, E. A. Kryukova, R. H. Ziganshin, E. V. Spirina, E. M. Rivkina, R. A. Khatypov, L. G. Erokhina, D. A. Gilichinsky, V. A. Shuvalov, and M. P. Kirpichnikov. Predicted bacteriorhodopsin from *Exiguobacterium sibiricum* is a functional proton pump. *FEBS Letters*, 584(19):4193–4196, (**2010**). doi: 10.1016/j.febslet.2010.09.005. 1.1.1

[55] S. P. Balashov, L. E. Petrovskaya, E. S. Imasheva, E. P. Lukashev, A. K. Dioumaev, J. M. Wang, S. V. Sychev, D. A. Dolgikh, A. B. Rubin, M. P. Kirpichnikov, and J. K. Lanyi. Breaking the carboxyl rule lysine 96 facilitates reprotonation of the schiff base in the photocycle of a retinal protein from exiguobacterium sibiricum. *Journal of Biological Chemistry*, 288(29):21254–21265, (**2013**). doi: 10.1074/jbc.M113.465138.

[56] V. H. Albarracin, I. Kraiselburd, C. Bamann, P. G. Wood, E. Bamberg, M. E. Farias, and W. Gärtner. Functional Green-Tuned Proteorhodopsin from Modern Stromatolites. *PLOS ONE*, 11(5):e0154962, (**2016**). doi: 10.1371/journal.pone.0154962. 1.1.1

[57] J. Heberle, J. Fitter, H. J. Sass, and G. Büldt. Bacteriorhodopsin: the functional details of a molecular machine are being resolved. *Biophysical Chemistry*, 85:229–248, (**2000**). doi: 10.1016/S0301-4622(99)00154-4. 1.2, 1.1.1

[58] H. G. Khorana. Two light-transducing membrane proteins: bacteriorhodopsin and the mammalian rhodopsin. *Proceedings of the National Academy of Sciences*, 90(4):1166–1171, (**1993**). doi: 10.1073/pnas.90.4.1166. 1.1.1

[59] H. G. Khorana. Bacteriorhodopsin, a membrane protein that uses light to translocate protons. *Journal of Biological Chemistry*, 263(16):7439–42, (**1988**). 1.1.1, 4.1.1

[60] K. Gerwert, G. Souvignier, and B. Hess. Simultaneous monitoring of light-induced changes in protein side-group protonation, chromophore isomerization, and backbone motion of bacteriorhodopsin by time-resolved Fourier-transform infrared spectroscopy. *Proceedings of the National Academy of Sciences*, 87(24):9774–9778, (**1990**). doi: 10.1073/pnas.87.24.9774. 1.1.1

[61] M. S. Braiman, O. Bousche, and K. J. Rothschild. Protein dynamics in the bacteriorhodopsin photocycle: submillisecond Fourier transform infrared spectra of the L, M, and N photointermediates. *Proceedings of the National Academy of Sciences*, 88(6):2388–2392, (**1991**). doi: 10.1073/pnas.88.6.2388.

[62] M. P. Krebs and H. G. Khorana. Mechanism of light-dependent proton translocation by bacteriorhodopsin. *Journal of Bacteriology*, 175(6):1555–1560, (**1993**). doi: 10.1128/jb.175.6.1555-1560.1993. 1.1.1, 4.1.1

[63] S. P. Fodor, J. B. Ames, R. Gebhard, E. M. Van Den Berg, J. Lugtenburg, and R. A. Mathies. Chromophore Structure In Bacteriorhodopsin's N Intermediate: Implications For The Proton-pumping Mechanism. *Biochemistry*, 27(18):7097–7101, (**1988**). doi: 10.1021/bi00418a064. 1.1.1

[64] S. O. Smith, B. Curry, R. Mathies, J. A. Pardoen, P. P. Mulder, and J. Lugtenburg. Chromophore Structure in Bacteriorhodopsin's O^{640} Photointermediate. *Biochemistry*, 22(26):6141–6148, (**1983**). doi: 10.1021/bi00295a016. 1.1.1

[65] A. K. Dioumaev, L. S. Brown, R. Needleman, and J. K. Lanyi. Coupling of the reisomerization of the retinal, proton uptake, and reprotonation of Asp-96 in the N photointermediate of bacteriorhodopsin. *Biochemistry*, 40(38):11308–11317, (**2001**). doi: 10.1021/bi011027d. 1.1.1

[66] S. P. Balashov, M. Lu, E. S. Imasheva, R. Govindjee, T. G. Ebrey, B. Othersen, Y. Chen, R. K. Crouch, and D. R. Menick. The proton release group of bacteriorhodopsin controls the rate of the final step of its photocycle at low pH. *Biochemistry*, 38(7):2026–2039, (**1999**). doi: 10.1021/bi981926a. 1.1.1

[67] L. P. Kayushin and V. P. Skulachev. Bacteriorhodopsin as an electrogenic proton pump: Reconstitution of bacteriorhodopsin proteoliposomes generating $\Delta\psi$ and ΔpH. *FEBS Letters*, 39(1):39–42, (**1974**). doi: 10.1016/0014-5793(74)80011-6. 1.1.1

[68] L. A. Drachev, A. A. Jasaitis, A. D. Kaulen, A. A. Kondrashin, E. A. Liberman, I. B. Nemecek, S. A. Ostroumov, A. Y. Semeov, and V. P. Skulachev. Direct measurement of electric current generation by cytochrome oxidase, H^+-ATPase and bacteriorhodopsin. *Nature*, 249:321–324, (**1974**).

[69] T. R. Herrmann and G. W. Rayfield. A measurement of the proton pump current generated by bacteriorhodopsin in black lipid membranes. *BBA - Biomembranes*, 443(3):623–628, (**1976**). doi: 10.1016/0005-2736(76)90482-X. 1.1.1

[70] G. Nagel, B. Mockel, G. Buldt, and E. Bamberg. Functional expression of bacteriorhodopsin in oocytes allows direct measurement of voltage-dependence of light-induced H^+ pumping. *FEBS Letters*, 377 (N2):263–266, (**1995**). 1.1.1, 4.2, 4.2.2

[71] J. H. Yoon, S. J. Kang, S. Park, and T. K. Oh. Reclassification of the three species of the genus *Krokinobacter* into the genus *Dokdonia* as *Dokdonia genika* comb. nov., *Dokdonia diaphoros* comb. nov. and *Dokdonia eikasta* comb. nov., and emended description of the genus . *International Journal of Systematic and Evolutionary Microbiology*, 62(8):1896–1901, (**2012**). doi: 10.1099/ijs.0.035253-0. c

[72] S. K. Kwon, B. K. Kim, J. Y. Song, M. J. Kwak, C. H. Lee, J. H. Yoon, T. K. Oh, and J. F. Kim. Genomic makeup of the marine flavobacterium Nonlabens *(Donghaeana) dokdonensis* and identification of a novel class of rhodopsins. *Genome Biology and Evolution*, 5(1):187–199, (**2013**). doi: 10.1093/gbe/evs134. 1.1.1, 3.2

[73] Y. M. Kwon, S. Y. Kim, K. H. Jung, and S. J. Kim. Diversity and functional analysis of light-driven pumping rhodopsins in marine Flavobacteria. *MicrobiologyOpen*, 5(2):212–223, (**2016**). doi: 10.1002/mbo3.321. 1.1.1, 3.2

[74] S. P. Balashov, E. S. Imasheva, A. K. Dioumaev, J. M. Wang, K. H. Jung, and J. K. Lanyi. Light-driven Na^+ pump from Gillisia limnaea: A high-affinity Na^+ binding site is formed transiently in the photocycle. *Biochemistry*, 53(48):7549–7561, (**2014**). doi: 10.1021/bi501064n. 1.1.1, 3.2

[75] K. Inoue, Y. Kato, and H. Kandori. Light-driven ion-translocating rhodopsins in marine bacteria. *Trends in Microbiology*, 23(2):91–98, (**2015**). doi: 10.1016/j.tim.2014.10.009. 1.1.1, 1.1.1

[76] S. P. Tsunoda, M. Prigge, R. Abe-Yoshizumi, K. Inoue, Y. Kozaki, T. Ishizuka, H. Yawo, O. Yizhar, and H. Kandori. Functional characterization of sodium-pumping rhodopsins with different pumping properties. *PLOS ONE*, 12(7):e0179232, (**2017**). doi: 10.1371/journal.pone.0179232. e, 1.1.1, 4.2, 4.2.1, 4.2.5

[77] F. Sievers, A. Wilm, D. Dineen, T. J. Gibson, K. Karplus, W. Li, R. Lopez, H. McWilliam, M. Remmert, J. Soding, J. D. Thompson, and D. G. Higgins. Fast, scalable generation of high-quality protein multiple sequence alignments using Clustal Omega. *Molecular Systems Biology*, 7(1):539–539, (**2014**). doi: 10.1038/msb.2011.75. 1.3

[78] H. E. Kato, K. Inoue, R. Abe-Yoshizumi, Y. Kato, H. Ono, M. Konno, S. Hososhima, T. Ishizuka, M. R. Hoque, H. Kunitomo, J. Ito, S. Yoshizawa, K. Yamashita, M. Takemoto, T. Nishizawa, R. Taniguchi, K. Kogure, A. D. Maturana, Y. Iino, H. Yawo, R. Ishitani, H. Kandori, and O. Nureki. Structural basis for Na^+ transport mechanism by a light-driven Na^+ pump. *Nature*, 521(7550):48–53, (**2015**). doi: 10.1038/nature14322. 1.1.1, 1.1.1, 1.5, 2.3, 3.2, 4.2, 4.2.1, k, 4.2.2, 4.2.3, m, 4.3, 4.2.4, 4.2.5

[79] I. Gushchin, V. Shevchenko, V. Polovinkin, K. Kovalev, A. Alekseev, E. Round, V. Borshchevskiy, T. Balandin, A. Popov, T. Gensch, C. Fahlke, C. Bamann, D. Willbold, G. Büldt, E. Bamberg, and V. Gordeliy. Crystal structure of a light-driven sodium pump. *Nature structural & molecular biology*, 22 (5):390–395, (**2015**). doi: 10.1038/nsmb.3002. 1.1.1, 1.1.1, 1.5, 3.2, 4.2.1, 4.2.3, 4.3

[80] H. Li, O. A. Sineshchekov, G. F. Z. Da Silva, and J. L. Spudich. In vitro demonstration of dual light-driven Na^+/H^+ pumping by a microbial rhodopsin. *Biophysical Journal*, 109(7):1446–1453, (**2015**). doi: 10.1016/j.bpj.2015.08.018. 1.1.1, 3.2, 4.2.1, 4.2.4

[81] H. Zhao, B. Ma, L. Ji, L. Li, H. Wang, and D. Chen. Coexistence of light-driven Na^+ and H^+ transport in a microbial rhodopsin from Nonlabens dokdonensis. *Journal of Photochemistry and Photobiology B: Biology*, 172:70–76, (**2017**). doi: 10.1016/j.jphotobiol.2017.05.004. 1.1.1, 4.2.1, f

[82] H.-F. Chen, K. Inoue, H. Ono, R. Abe-Yoshizumi, A. Wada, and H. Kandori. Time-Resolved FTIR Study of Light-Driven Sodium Pump Rhodopsins. *Physical Chemistry Chemical Physics*, (**2018**). doi: 10.1039/C8CP02599A. 1.1.1, 4.2.4

[83] C.-M. Suomivuori, A. P. Gamiz-Hernandez, D. Sundholm, and V. R. I. Kaila. Energetics and dynamics of a light-driven sodium-pumping rhodopsin. *Proceedings of the National Academy of Sciences*, 114(27): 7043–7048, (**2017**). doi: 10.1073/pnas.1703625114. 1.1.1, 1.5, 4.3

[84] I. Gushchin, V. Shevchenko, V. Polovinkin, V. Borshchevskiy, P. Buslaev, E. Bamberg, and V. Gordeliy. Structure of the light-driven sodium pump KR2 and its implications for optogenetics. *FEBS Journal*, 283(7):1232–1238, (**2015**). doi: 10.1111/febs.13585. 1.1.1, 1.5, 4.2.1

[85] Y. Hontani, K. Inoue, M. Kloz, Y. Kato, H. Kandori, and J. T. M. Kennis. The photochemistry of sodium ion pump rhodopsin observed by watermarked femto- to submillisecond stimulated Raman spectroscopy. *Physical chemistry chemical physics : PCCP*, 18(35):24729–24736, (**2016**). doi: 10.1039/C6CP05240A. 1.1.1, 4.2.3

[86] M. Shibata, K. Inoue, K. Ikeda, M. Konno, M. Singh, C. Kataoka, R. Abe-Yoshizumi, H. Kandori, and T. Uchihashi. Oligomeric states of microbial rhodopsins determined by high-speed atomic force microscopy and circular dichroic spectroscopy. *Scientific Reports*, 8(1):8262, (**2018**). doi: 10.1038/s41598-018-26606-y. 1.1.1

[87] K. W. Foster and R. D. Smyth. Light Antennas in phototactic algae. *Microbiological reviews*, 44(4): 572–630, (**1980**). 1.1.2

[88] K. W. Foster, J. Saranak, N. Patel, G. Zarilli, M. Okabe, T. Kline, and K. Nakanishi. A rhodopsin is the functional photoreceptor for phototaxis in the inicellular eukaryote *Chlomydomonas*. *Nature*, 311: 756–759, (**1984**).

[89] P. Kröger and P. Hegemann. Photophobic responses and phototaxis in *Chlamydomonas* are triggered by a single rhodopsin photoreceptor. *FEBS Letters*, 341(1):5–9, (**1994**). doi: 10.1016/0014-5793(94)80229-7. 1.1.2

[90] H. Harz and P. Hegemann. Rhodopsin-regulated calcium currents in *Chlamydomonas*. *Nature*, 351 (6326):489–491, (**1991**). doi: 10.1038/351489a0. 1.1.2

[91] F. J. Braun and P. Hegemann. Two Light-Activated Conductances in the Eye of the Green Alga *Volvox carteri*. *Biophysical Journal*, 76(3):1668–1678, (**1999**). doi: 10.1016/S0006-3495(99)77326-1.

[92] O. A. Sineshchekov, K.-H. Jung, and J. L. Spudich. Two rhodopsins mediate phototaxis to low- and high-intensity light in *Chlamydomonas reinhardtii*. *Proceedings of the National Academy of Sciences*, 99(13): 8689–8694, (**2002**). doi: 10.1073/pnas.122243399. 1.1.2, f

[93] A. Kianianmomeni, K. Stehfest, G. Nematollahi, P. Hegemann, and A. Hallmann. Channelrhodopsins of Volvox carteri Are Photochromic Proteins That Are Specifically Expressed in Somatic Cells under Control of Light, Temperature, and the Sex Inducer. *Plant Physiology*, 151(1):347–366, (**2009**). doi: 10.1104/pp.109.143297. 1.1.2, 1.1.2, 1.1, 3.1.1

[94] S.-Y. Hou, E. G. Govorunova, M. Ntefidou, C. E. Lane, E. N. Spudich, O. A. Sineshchekov, and J. L. Spudich. Diversity of *Chlamydomonas* channelrhodopsins. *Photochemistry and Photobiology*, 88(1):119–128, (**2012**). doi: 10.1111/j.1751-1097.2011.01027.x. 1.1.2, 1.1, 1.1.2

[95] N. C. Klapoetke, Y. Murata, S. S. Kim, S. R. Pulver, A. Birdsey-Benson, Y. K. Cho, T. K. Morimoto, A. S. Chuong, E. J. Carpenter, Z. Tian, J. Wang, Y. Xie, Z. Yan, Y. Zhang, B. Y. Chow, B. Surek, M. Melkonian, V. Jayaraman, M. Constantine-Paton, G. K.-S. Wong, and E. S. Boyden. Independent optical excitation of distinct neural populations. *Nature methods*, 11(3):338–46, (**2014**). doi: 10.1038/nmeth.2836. 1.1.2, 1.1, 1.1.2, i, 4.1.2

[96] E. G. Govorunova, O. A. Sineshchekov, E. M. Rodarte, R. Janz, O. Morelle, M. Melkonian, G. K.-S. Wong, and J. L. Spudich. The Expanding Family of Natural Anion Channelrhodopsins Reveals Large Variations in Kinetics, Conductance, and Spectral Sensitivity. *Scientific Reports*, 7(January):43358, (**2017**). doi: 10.1038/srep43358. 1.1.2, 4.2.5

[97] F. Schneider, C. Grimm, and P. Hegemann. Biophysics of Channelrhodopsin. *Annual Review of Biophysics*, 44(1):167–186, (**2015**). doi: 10.1146/annurev-biophys-060414-034014. 1.1.2, 1.1.2

[98] J. Wietek and M. Prigge. Enhancing Channelrhodopsins: An Overview. In *Methods in Molecular Biology*, volume 1408, pages 141–165. 2016. doi: 10.1007/978-1-4939-3512-3_10. 1.1.2, 1.1.2

[99] M. Müller, C. Bamann, E. Bamberg, and W. Kühlbrandt. Projection structure of channelrhodopsin-2 at 6 Å resolution by electron crystallography. *Journal of Molecular Biology*, 414(1):86–95, (**2011**). doi: 10.1016/j.jmb.2011.09.049. 1.1.2

[100] J. Y. Lin, M. Z. Lin, P. Steinbach, and R. Y. Tsien. Characterization of Engineered Channelrhodopsin Variants with Improved Properties and Kinetics. *Biophysical Journal*, 96(5):1803–1814, (**2009**). doi: 10.1016/j.bpj.2008.11.034. 1.1.2, 1.3, 3.1, 3.1.3

[101] H. Wang, Y. Sugiyama, T. Hikima, E. Sugano, H. Tomita, T. Takahashi, T. Ishizuka, and H. Yawo. Molecular Determinants Differentiating Photocurrent Properties of Two Channelrhodopsins from Chlamydomonas. *Journal of Biological Chemistry*, 284(9):5685–5696, (**2009**). doi: 10.1074/jbc.M807632200. 1.1.2

[102] S. P. Tsunoda and P. Hegemann. Glu 87 of Channelrhodopsin-1 Causes pH-dependent Color Tuning and Fast Photocurrent Inactivation. *Photochemistry and Photobiology*, 85(2):564–569, (**2008**). doi: 10.1111/j.1751-1097.2008.00519.x. 1.1.2, 3.1.1

[103] H. E. Kato, F. Zhang, O. Yizhar, C. Ramakrishnan, T. Nishizawa, K. Hirata, J. Ito, Y. Aita, T. Tsukazaki, S. Hayashi, P. Hegemann, A. D. Maturana, R. Ishitani, K. Deisseroth, and O. Nureki. Crystal structure of the channelrhodopsin light-gated cation channel. *Nature*, 482(7385):369–374, (**2012**). doi: 10.1038/nature10870. 1.1.2, g, 1.1.2, 1.7

[104] O. Volkov, K. Kovalev, V. Polovinkin, V. Borshchevskiy, C. Bamann, R. Astashkin, E. Marin, A. Popov, T. Balandin, D. Willbold, G. Büldt, E. Bamberg, and V. Gordeliy. Structural insights into ion conduction by channelrhodopsin 2. *Science*, 358(6366):eaan8862, (**2017**). doi: 10.1126/science.aan8862. 1.1.2, 1.1.2, 1.7, 1.1.2

[105] T. Suzuki, K. Yamasaki, S. Fujita, K. Oda, M. Iseki, K. Yoshida, M. Watanabe, H. Daiyasu, H. Toh, E. Asamizu, S. Tabata, K. Miura, H. Fukuzawa, S. Nakamura, and T. Takahashi. Archaeal-type rhodopsins in *Chlamydomonas*: model structure and intracellular localization. *Biochemical and Biophysical Research Communications*, 301(3):711–717, (**2003**). doi: 10.1016/S0006-291X(02)03079-6.

[106] K. Ruffert, B. Himmel, D. Lall, C. Bamann, E. Bamberg, H. Betz, and V. Eulenburg. Glutamate residue 90 in the predicted transmembrane domain 2 is crucial for cation flux through channelrhodopsin 2. *Biochemical and Biophysical Research Communications*, 410(4):737–743, (**2011**). doi: 10.1016/j.bbrc.2011.06.024. 1.1.2, 3.1.3

[107] H. C. Watanabe, K. Welke, F. Schneider, S. Tsunoda, F. Zhang, K. Deisseroth, P. Hegemann, and M. Elstner. Structural model of channelrhodopsin. *Journal of Biological Chemistry*, 287(10):7456–7466, (**2012**). doi: 10.1074/jbc.M111.320309. 1.1.2

[108] K. Eisenhauer, J. Kuhne, E. Ritter, A. Berndt, S. Wolf, E. Freier, F. Bartl, P. Hegemann, and K. Gerwert. In channelrhodopsin-2 Glu-90 is crucial for ion selectivity and is deprotonated during the photocycle. *Journal of Biological Chemistry*, 287(9):6904–6911, (**2012**). doi: 10.1074/jbc.M111.327700. 1.1.2, 3.1.3

[109] A. Berndt. *Mechanismus und anwendungsbezogene Optimierung von Channelrhodopsin-2*. PhD thesis, 2011. 1.1.2, 3.1.3

[110] V. A. Lórenz-Fonfría, T. Resler, N. Krause, M. Nack, M. Gossing, G. Fischer von Mollard, C. Bamann, E. Bamberg, R. Schlesinger, and J. Heberle. Transient protonation changes in channelrhodopsin-2 and their relevance to channel gating. *Proceedings of the National Academy of Sciences*, 110(14):E1273–81, (**2013**). doi: 10.1073/pnas.1219502110. 1.1.2, 1.1.2, 3.1.2, 4.1.1

[111] J. Kuhne, K. Eisenhauer, E. Ritter, P. Hegemann, K. Gerwert, and F. Bartl. Early Formation of the Ion-Conducting Pore in Channelrhodopsin-2. *Angewandte Chemie International Edition*, 54(16):4953–4957, (**2015**). doi: 10.1002/anie.201410180. 1.1.2

[112] L. A. Gunaydin, O. Yizhar, A. Berndt, V. S. Sohal, K. Deisseroth, and P. Hegemann. Ultrafast optogenetic control. *Nature Neuroscience*, 13(3):387–392, (**2010**). doi: 10.1038/nn.2495. 1.1.2, 3.1.2, 3.1.4

[113] A. Berndt, P. Schoenenberger, J. Mattis, K. M. Tye, K. Deisseroth, P. Hegemann, and T. G. Oertner. High-efficiency channelrhodopsins for fast neuronal stimulation at low light levels. *Proceedings of the National Academy of Sciences*, 108(18):7595–600, (**2011**). doi: 10.1073/pnas.1017210108. 1.1.2

[114] E. G. Govorunova, O. A. Sineshchekov, H. Li, R. Janz, and J. L. Spudich. Characterization of a highly efficient blue-shifted channelrhodopsin from the marine alga Platymonas subcordiformis. *Journal of Biological Chemistry*, 288(41):29911–29922, (**2013**). doi: 10.1074/jbc.M113.505495. 1.1.2, 3.1.2

[115] A. Berndt, O. Yizhar, L. A. Gunaydin, P. Hegemann, and K. Deisseroth. Bi-stable neural state switches. *Nature Neuroscience*, 12(2):229–234, (**2009**). doi: 10.1038/nn.2247. 1.1.2, 4.1.1, 4.1.2

[116] C. Bamann, T. Kirsch, G. Nagel, and E. Bamberg. Spectral Characteristics of the Photocycle of Channelrhodopsin-2 and Its Implication for Channel Function. *Journal of Molecular Biology*, 375(3):686–694, (**2008**). doi: 10.1016/j.jmb.2007.10.072. 1.1.2, 1.1.2, 1.1.2, 4.1.1, 4.1.1

[117] O. Yizhar, L. E. Fenno, M. Prigge, F. Schneider, T. J. Davidson, D. J. O'Shea, V. S. Sohal, I. Goshen, J. Finkelstein, J. T. Paz, K. Stehfest, R. Fudim, C. Ramakrishnan, J. R. Huguenard, P. Hegemann, and K. Deisseroth. Neocortical excitation/inhibition balance in information processing and social dysfunction. *Nature*, 477(7363):171–178, (**2011**). doi: 10.1038/nature10360. 1.1.2, 1.1.2, 3.1, 4.1.1

[118] I. Radu, C. Bamann, M. Nack, G. Nagel, E. Bamberg, and J. Heberle. Conformational Changes of Channelrhodopsin-2. *Journal of the American Chemical Society*, 131(21):7313–7319, (**2009**). doi: 10.1021/ja8084274. 1.1.2

[119] M. Nack, I. Radu, M. Gossing, C. Bamann, E. Bamberg, G. F. von Mollard, and J. Heberle. The DC gate in Channelrhodopsin-2: crucial hydrogen bonding interaction between C128 and D156. *Photochemical & Photobiological Sciences*, 9(2):194–198, (**2010**). doi: 10.1039/b9pp00157c. 1.1.2

[120] H. C. Watanabe, K. Welke, D. J. Sindhikara, P. Hegemann, and M. Elstner. Towards an understanding of channelrhodopsin function: simulations lead to novel insights of the channel mechanism. *Journal of molecular biology*, 425(10):1795–1814, (**2013**). doi: 10.1016/j.jmb.2013.01.033. 1.1.2

[121] K. Welke, H. C. Watanabe, T. Wolter, M. Gaus, and M. Elstner. QM/MM simulations of vibrational spectra of bacteriorhodopsin and channelrhodopsin-2. *Physical chemistry chemical physics : PCCP*, 15 (18):6651–6659, (**2013**). doi: 10.1039/c3cp44181d. 1.1.2

[122] H. Luecke, B. Schobert, H. T. Richter, J. P. Cartailler, and J. K. Lanyi. Structure of bacteriorhodopsin at 1.55 Å resolution. *Journal of Molecular Biology*, 291(4):899–911, (**1999**). doi: 10.1006/jmbi.1999.3027. 1.1.2, 1.1.2

[123] A. Perálvarez-Marín, M. Márquez, J. L. Bourdelande, E. Querol, and E. Padrós. Thr-90 Plays a Vital Role in the Structure and Function of Bacteriorhodopsin. *Journal of Biological Chemistry*, 279(16):16403–16409, (**2004**). doi: 10.1074/jbc.M313988200. 1.1.2

[124] I. K. McDonald and J. M. Thornton. Satisfying hydrogen bonding potential in proteins. *Journal of Molecular Biology*, 238(5):777–793, (**1994**). doi: 10.1006/jmbi.1994.1334. 1.1.2

[125] S. Ito, H. E. Kato, R. Taniguchi, T. Iwata, O. Nureki, and H. Kandori. Water-Containing Hydrogen-Bonding Network in the Active Center of Channelrhodopsin. *Journal of the American Chemical Society*, 136(9):3475–3482, (**2014**). doi: 10.1021/ja410836g. h

[126] M. K. Neumann-Verhoefen, K. Neumann, C. Bamann, I. Radu, J. Heberle, E. Bamberg, and J. Wachtveitl. Ultrafast infrared spectroscopy on channelrhodopsin-2 reveals efficient energy transfer from the retinal chromophore to the protein. *Journal of the American Chemical Society*, 135(18): 6968–6976, (**2013**). doi: 10.1021/ja400554y. 1.1.2, 1.1.2

[127] L. Vogeley, O. A. Sineshchekov, V. D. Trivedi, J. Sasaki, J. L. Spudich, and H. Luecke. *Anabaena* sensory rhodopsin: A photochromic color sensor at 2.0 Å. *Science*, 306(5700):1390–1393, (**2004**). doi: 10.1126/science.1103943. 1.1.2

[128] E. Ritter, K. Stehfest, A. Berndt, P. Hegemann, and F. J. Bartl. Monitoring light-induced structural changes of Channelrhodopsin-2 by UV-visible and Fourier transform infrared spectroscopy. *Journal of Biological Chemistry*, 283(50):35033–35041, (**2008**). doi: 10.1074/jbc.M806353200. 1.1.2, 1.8, 4.1.1, 4.1.1

[129] V. A. Lórenz-Fonfría and J. Heberle. Channelrhodopsin unchained: structure and mechanism of a light-gated cation channel. *Biochimica et biophysica acta*, 1837(5):626–642, (**2014**). doi: 10.1016/j.bbabio.2013.10.014. 1.1.2, 4.1.1

[130] V. A. Lórenz-Fonfría, C. Bamann, T. Resler, R. Schlesinger, E. Bamberg, and J. Heberle. Temporal evolution of helix hydration in a light-gated ion channel correlates with ion conductance. *Proceedings of the National Academy of Sciences*, 112(43):E5796–E5804, (**2015**). doi: 10.1073/pnas.1511462112. 1.1.2

[131] K. Nikolic, N. Grossman, M. S. Grubb, J. Burrone, C. Toumazou, and P. Degenaar. Photocycles of channelrhodopsin-2. *Photochemistry and Photobiology*, 85(1):400–411, (**2009**). doi: 10.1111/j.1751-1097.2008.00460.x. 1.1.2, 4.1.1

[132] K. Stehfest and P. Hegemann. Evolution of the Channelrhodopsin Photocycle Model. *ChemPhysChem*, 11(6):1120–1126, (**2010**). doi: 10.1002/cphc.200900980. 1.1.2

[133] O. P. Ernst, P. A. Sánchez Murcia, P. Daldrop, S. P. Tsunoda, S. Kateriya, and P. Hegemann. Photoactivation of channelrhodopsin. *Journal of Biological Chemistry*, 283(3):1637–1643, (**2008**). doi: 10.1074/jbc.M708039200. 1.1.2

[134] A. Berndt, M. Prigge, D. Gradmann, and P. Hegemann. Two open states with progressive proton selectivities in the branched channelrhodopsin-2 photocycle. *Biophysical Journal*, 98(5):753–761, (**2010**). doi: 10.1016/j.bpj.2009.10.052. 1.1.2

[135] P. Hegemann, S. Ehlenbeck, and D. Gradmann. Multiple photocycles of channelrhodopsin. *Biophysical Journal*, 89(6):3911–3918, (**2005**). doi: 10.1529/biophysj.105.069716. 1.1.2

[136] S. Bruun, D. Stoeppler, A. Keidel, U. Kuhlmann, M. Luck, A. Diehl, M.-A. Geiger, D. Woodmansee, D. Trauner, P. Hegemann, H. Oschkinat, P. Hildebrandt, and K. Stehfest. Light–Dark Adaptation of Channelrhodopsin Involves Photoconversion between the all- trans and 13- cis Retinal Isomers. *Biochemistry*, 54(35):5389–5400, (**2015**). doi: 10.1021/acs.biochem.5b00597. 1.1.2, 4.1.1

[137] P. Scherrer, M. K. Mathew, W. Sperling, and W. Stoeckenius. Retinal Isomer Ratio in Dark-Adapted Purple Membrane and Bacteriorhodopsin Monomers. *Biochemistry*, 28(2):829–834, (**1989**). 1.1.2

[138] H. Patzelt, B. Simon, A. TerLaak, B. Kessler, R. Kühne, P. Schmieder, D. Oesterhelt, H. Oschkinat, and R. Ku. The structures of the active center in dark-adapted bacteriorhodopsin by solution-state NMR spectroscopy. *Proceedings of the National Academy of Sciences*, 99(15):9765–70, (**2002**). doi: 10.1073/pnas.132253899. 1.1.2

[139] M. Nack, I. Radu, C. Bamann, E. Bamberg, and J. Heberle. The retinal structure of channelrhodopsin-2 assessed by resonance Raman spectroscopy. *FEBS Letters*, 583(22):3676–3680, (**2009**). doi: 10.1016/j.febslet.2009.10.052. 1.1.2

[140] E. Ritter, P. Piwowarski, P. Hegemann, and F. J. Bartl. Light-dark adaptation of channelrhodopsin C128T mutant. *Journal of Biological Chemistry*, 288(15):10451–10458, (**2013**). doi: 10.1074/jbc.M112.446427. 1.1.2, 4.1.1

[141] B. J. Tromberg, N. Shah, R. Lanning, A. Cerussi, J. Espinoza, T. Pham, L. Svaasand, and J. Butler. Non-Invasive *In Vivo* Characterization of Breast Tumors Using Photon Migration Spectroscopy. *Neoplasia*, 2(1-2):26–40, (**2000**). doi: 10.1038/sj.neo.7900082. 1.1.2

[142] S. L. Jacques. Corrigendum: Optical properties of biological tissues: a review. *Physics in Medicine and Biology*, 58(14):5007–5008, (**2013**). doi: 10.1088/0031-9155/58/14/5007.

[143] T. Ziegler and A. Moeglich. Photoreceptor engineering. *Frontiers in Molecular Biosciences*, 2(June):1–25, (**2015**). doi: 10.3389/fmolb.2015.00030. 1.1.2

[144] F. Zhang, M. Prigge, F. Beyrière, S. P. Tsunoda, J. Mattis, O. Yizhar, P. Hegemann, and K. Deisseroth. Red-shifted optogenetic excitation: a tool for fast neural control derived from *Volvox carteri*. *Nature neuroscience*, 11(6):631–633, (**2008**). doi: 10.1038/nn.2120. 1.1.2, 1.1, 1.1.2

[145] E. G. Govorunova, E. N. Spudich, C. E. Lane, O. A. Sineshchekov, and J. L. Spudich. New Channelrhodopsin with a Red-Shifted Spectrum and Rapid Kinetics from Mesostigma viride. *mBio*, 2(3):1–9, (**2011**). doi: 10.1128/mBio.00115-11. 1.1.2, 1.1

[146] H. Tomita, E. Sugano, N. Murayama, T. Ozaki, F. Nishiyama, K. Tabata, M. Takahashi, T. Saito, and M. Tamai. Restoration of the majority of the visual spectrum by using modified *Volvox* channelrhodopsin-1. *Molecular Therapy*, 22(8):1434–40, (**2014**). doi: 10.1038/mt.2014.81. 1.1.2

[147] M. Prigge, F. Schneider, S. P. Tsunoda, C. Shilyansky, J. Wietek, K. Deisseroth, and P. Hegemann. Color-tuned channelrhodopsins for multiwavelength optogenetics. *Journal of Biological Chemistry*, 287 (38):31804–31812, (**2012**). doi: 10.1074/jbc.M112.391185. 1.1.2, 3.1, 3.1.5

[148] K. Erbguth, M. Prigge, F. Schneider, P. Hegemann, and A. Gottschalk. Bimodal Activation of Different Neuron Classes with the Spectrally Red-Shifted Channelrhodopsin Chimera C1V1 in Caenorhabditis elegans. *PLOS ONE*, 7(10):e46827, (**2012**). doi: 10.1371/journal.pone.0046827. 1.1.2

[149] P. Rajasethupathy, S. Sankaran, J. H. Marshel, C. K. Kim, E. Ferenczi, S. Y. Lee, A. Berndt, C. Ramakrishnan, A. Jaffe, M. Lo, C. Liston, and K. Deisseroth. Projections from neocortex mediate top-down control of memory retrieval. *Nature*, 526(7575):653–659, (**2015**). doi: 10.1038/nature15389. 1.1.2, 3.1.2, c, 3.2.2, 4.1.2, 4.2

[150] J. Y. Lin, P. M. Knutsen, A. Muller, D. Kleinfeld, and R. Y. Tsien. ReaChR: a red-shifted variant of channelrhodopsin enables deep transcranial optogenetic excitation. *Nature Neuroscience*, 16(10): 1499–1508, (**2013**). doi: 10.1038/nn.3502. 1.1.2, 1.3, 3.1, 3.1.1, 4.1.1, 4.1.2, c

[151] J. Vierock, C. Grimm, N. Nitzan, and P. Hegemann. Molecular determinants of proton selectivity and gating in the red-light activated channelrhodopsin Chrimson. *Scientific Reports*, 7(1):1–15, (**2017**). doi: 10.1038/s41598-017-09600-8. 1.1.2, 3.1.3, 4.1.1, 4.1.1, 4.1.2, 4.2.1

[152] A. Bi, J. Cui, Y.-P. Ma, E. Olshevskaya, M. Pu, A. M. Dizhoor, and Z.-H. Pan. Ectopic expression of a microbial-type rhodopsin restores visual responses in mice with photoreceptor degeneration. *Neuron*, 50(1):23–33, (**2006**). doi: 10.1016/j.neuron.2006.02.026. 1.2

[153] E. S. Boyden, F. Zhang, E. Bamberg, G. Nagel, and K. Deisseroth. Millisecond-timescale, genetically targeted optical control of neural activity. *Nature neuroscience*, 8(9):1263–1268, (**2005**). doi: 10.1038/nn1525. 1.9, 1.2

[154] G. Nagel, M. Brauner, J. F. Liewald, N. Adeishvili, E. Bamberg, and A. Gottschalk. Light Activation of Channelrhodopsin-2 in Excitable Cells of *Caenorhabditis elegans* Triggers Rapid Behavioral Responses. *Current biology : CB*, 15(24):2279–2284, (**2005**). doi: 10.1016/j.cub.2005.11.032. 1.2, 1.2

[155] X. Li, D. V. Gutierrez, M. G. Hanson, J. Han, M. D. Mark, H. Chiel, P. Hegemann, L. T. Landmesser, and S. Herlitze. Fast noninvasive activation and inhibition of neural and network activity by vertebrate rhodopsin and green algae channelrhodopsin. *Proceedings of the National Academy of Sciences*, 102(49):17816–17821, (**2005**). doi: 10.1073/pnas.0509030102. 1.2, 4.2.5

[156] T. Ishizuka, M. Kakuda, R. Araki, and H. Yawo. Kinetic evaluation of photosensitivity in genetically engineered neurons expressing green algae light-gated channels. *Neuroscience Research*, 54(2):85–94, (**2006**). doi: 10.1016/j.neures.2005.10.009. 1.2

[157] K. Deisseroth, G. Feng, A. K. Majewska, G. Miesenböck, A. Ting, and M. J. Schnitzer. Next-generation optical technologies for illuminating genetically targeted brain circuits. *The Journal of Neuroscience*, 26 (41):10380–10386, (**2006**). doi: 10.1523/JNEUROSCI.3863-06.2006. 1.2

[158] B. V. Zemelman, G. A. Lee, M. Ng, and G. Miesenböck. Selective Photostimulation of Genetically ChARGed Neurons. *Neuron*, 2002(1):15–22, (**2002**). doi: 10.1016/S0896-6273(01)00574-8. 1.2

[159] M. Banghart, K. Borges, E. Isacoff, D. Trauner, and R. H. Kramer. Light-activated ion channels for remote control of neuronal firing. *Nature Neuroscience*, 7(12):1381–1386, (**2004**). doi: 10.1038/nn1356. 1.2, 4.2.5

[160] Method of the Year 2015. *Nature Methods*, 13(1):1–1, (**2016**). doi: 10.1038/nmeth.3730. 1.2

[161] C. Schroll, T. Riemensperger, D. Bucher, J. Ehmer, T. Völler, K. Erbguth, B. Gerber, T. Hendel, G. Nagel, E. Buchner, and A. Fiala. Light-Induced Activation of Distinct Modulatory Neurons Triggers Appetitive or Aversive Learning in *Drosophila* Larvae. *Current Biology*, 16(17):1741–1747, (**2006**). doi: 10.1016/j.cub.2006.07.023. 1.2

[162] F. Zhang, L.-P. Wang, M. Brauner, J. F. Liewald, K. Kay, N. Watzke, P. G. Wood, E. Bamberg, G. Nagel, A. Gottschalk, and K. Deisseroth. Multimodal fast optical interrogation of neural circuitry. *Nature*, 446:633–639, (**2007**). doi: 10.1038/nature05744. 1.2, 3.2.3, 3.2.3, 4.2, 4.2.1, 4.2.2

[163] S. Zhao, C. Cunha, F. Zhang, Q. Liu, B. Gloss, K. Deisseroth, G. J. Augustine, and G. Feng. Improved expression of halorhodopsin for light-induced silencing of neuronal activity. *Brain Cell Biology*, 36 (1-4):141–154, (**2008**). doi: 10.1007/s11068-008-9034-7.

[164] B. Y. Chow, X. Han, A. S. Dobry, X. Qian, A. S. Chuong, M. Li, M. A. Henninger, G. M. Belfort, Y. Lin, P. E. Monahan, and E. S. Boyden. High-performance genetically targetable optical neural silencing by light-driven proton pumps. *Nature*, 463(7277):98–102, (**2010**). doi: 10.1038/nature08652. 1.2, 4.2.2, 4.2.5

[165] A. S. Mauss, C. Busch, and A. Borst. Optogenetic Neuronal Silencing in *Drosophila* during Visual Processing. *Scientific Reports*, 7(1):1–12, (**2017**). doi: 10.1038/s41598-017-14076-7. 1.2

[166] F. Mohammad, J. C. Stewart, S. Ott, K. Chlebikova, J. Y. Chua, T. W. Koh, J. Ho, and A. Claridge-Chang. Optogenetic inhibition of behavior with anion channelrhodopsins. *Nature Methods*, 14(3): 271–274, (**2017**). doi: 10.1038/nmeth.4148.

[167] Y. C. Wei, S. R. Wang, Z. L. Jiao, W. Zhang, J. K. Lin, X. Y. Li, S. S. Li, X. Zhang, and X. H. Xu. Medial preoptic area in mice is capable of mediating sexually dimorphic behaviors regardless of gender. *Nature Communications*, 9(1), (**2018**). doi: 10.1038/s41467-017-02648-0. 1.2

[168] M. Stierl, P. Stumpf, D. Udwari, R. Gueta, R. Hagedorn, A. Losi, W. Gärtner, L. Petereit, M. Efetova, M. Schwarzel, T. G. Oertner, G. Nagel, and P. Hegemann. Light Modulation of Cellular cAMP by a Small Bacterial Photoactivated Adenylyl Cyclase, bPAC, of the Soil Bacterium *Beggiatoa*. *Journal of Biological Chemistry*, 286(2):1181–1188, (**2011**). doi: 10.1074/jbc.M110.185496. 1.2

[169] A. Möglich, R. a. Ayers, and K. Moffat. Design and Signaling Mechanism of Light-Regulated Histidine Kinases. *Journal of Molecular Biology*, 385(5):1433–1444, (**2009**). doi: 10.1016/j.jmb.2008.12.017. 1.2

[170] C. Gasser, S. Taiber, C.-M. Yeh, C. H. Wittig, P. Hegemann, S. Ryu, F. Wunder, and A. Moglich. Engineering of a red-light-activated human cAMP/cGMP-specific phosphodiesterase. *Proceedings of the National Academy of Sciences*, 111(24):8803–8808, (**2014**). doi: 10.1073/pnas.1321600111. 1.2

[171] M. Jinek, K. Chylinski, I. Fonfara, M. Hauer, J. A. Doudna, and E. Charpentier. A Programmable Dual-RNA-Guided DNA Endonuclease in Adaptive Bacterial Immunity. *Science*, 337(6096):816–821, (**2012**). doi: 10.1126/science.1225829. 1.2

[172] F. Richter, I. Fonfara, B. Bouazza, C. H. Schumacher, M. Bratovic, E. Charpentier, and A. Möglich. Engineering of temperature- and light-switchable Cas9 variants. *Nucleic Acids Research*, 44(20):gkw930, (**2016**). doi: 10.1093/nar/gkw930. 1.2

[173] X. X. Zhou, X. Zou, H. K. Chung, Y. Gao, Y. Liu, L. S. Qi, and M. Z. Lin. A Single-Chain Photoswitchable CRISPR-Cas9 Architecture for Light-Inducible Gene Editing and Transcription. *ACS Chemical Biology*, 13(2):443–448, (**2018**). doi: 10.1021/acschembio.7b00603. 1.2

[174] W. Wang, C. P. Wildes, T. Pattarabanjird, M. I. Sanchez, G. F. Glober, G. A. Matthews, K. M. Tye, and A. Y. Ting. A light- and calcium-gated transcription factor for imaging and manipulating activated neurons. *Nature Biotechnology*, 35(9):864–871, (**2017**). doi: 10.1038/nbt.3909. 1.2

[175] D. Niopek, D. Benzinger, J. Roensch, T. Draebing, P. Wehler, R. Eils, and B. Di Ventura. Engineering light-inducible nuclear localization signals for precise spatiotemporal control of protein dynamics in living cells. *Nature Communications*, 5:1–11, (**2014**). doi: 10.1038/ncomms5404. 1.2

[176] D. Niopek, P. Wehler, J. Roensch, R. Eils, and B. Di Ventura. Optogenetic control of nuclear protein export. *Nature Communications*, 7:1–9, (**2016**). doi: 10.1038/ncomms10624. 1.2

[177] C. Ellis. The state of GPCR research in 2004. *Nature Reviews Drug Discovery*, 3(7):577–626, (**2004**). doi: 10.1038/nrd1458. 1.3

[178] A. S. Hauser, M. M. Attwood, M. Rask-Andersen, H. B. Schiöth, and D. E. Gloriam. Trends in GPCR drug discovery: new agents, targets and indications. *Nature Reviews Drug Discovery*, 16(12):829–842, (**2017**). doi: 10.1038/nrd.2017.178. 1.3

[179] J. N. Wood, S. J. Bevan, P. R. Coote, P. M. Dunn, A. Harmar, P. Hogan, D. S. Latchman, C. Morrison, G. Rougon, M. Theveniau, and S. Wheatley. Novel Cell Lines Display Properties of Nociceptive Sensory Neurons. *Proceedings of the Royal Society B: Biological Sciences*, 241(1302):187–194, (**1990**). doi: 10.1098/rspb.1990.0084. 2.2, 2.2.2

[180] S. Kaech and G. Banker. Culturing hippocampal neurons. *Nature Protocols*, 1(5):2406–2415, (**2006**). doi: 10.1254/fpj.119.163. 2.2.1

[181] C. Grimm, J. Vierock, P. Hegemann, and J. Wietek. Whole-cell Patch-clamp Recordings for Electrophysiological Determination of Ion Selectivity in Channelrhodopsins. *Journal of Visualized Experiments*, (123), (**2017**). doi: 10.3791/55497. b, 2.5.2, 2.5.6, 2.5

[182] J. Schindelin, I. Arganda-Carreras, E. Frise, V. Kaynig, M. Longair, T. Pietzsch, S. Preibisch, C. Rueden, S. Saalfeld, B. Schmid, J. Y. Tinevez, D. J. White, V. Hartenstein, K. Eliceiri, P. Tomancak, and A. Cardona. Fiji: An open-source platform for biological-image analysis. *Nature Methods*, 9(7):676–682, (**2012**). doi: 10.1038/nmeth.2019. 2.4.1

[183] E. A. Ferenczi, J. Vierock, K. Atsuta-Tsunoda, S. P. Tsunoda, C. Ramakrishnan, C. Gorini, K. Thompson, S. Y. Lee, A. Berndt, C. Perry, S. Minniberger, A. Vogt, J. Mattis, R. Prakash, S. Delp, K. Deisseroth, and P. Hegemann. Optogenetic approaches addressing extracellular modulation of neural excitability. *Scientific Reports*, 6(23947):1–20, (**2016**). doi: 10.1038/srep23947. 2.4.2, 3.2.3, 4.2.1

[184] J. H. Kim, S. R. Lee, L. H. Li, H. J. Park, J. H. Park, K. Y. Lee, M. K. Kim, B. A. Shin, and S. Y. Choi. High cleavage efficiency of a 2A peptide derived from porcine teschovirus-1 in human cell lines, zebrafish and mice. *PLOS ONE*, 6(4):1–8, (**2011**). doi: 10.1371/journal.pone.0018556. 2.4.2

[185] G. Miesenböck, D. A. De Angelis, and J. E. Rothman. Visualizing secretion and synaptic transmission with pH-sensitive green fluorescent proteins. *Nature*, 394(6689):192–195, (**1998**). doi: 10.1038/28190. 2.4.2

[186] O. P. Hamill, A. Marty, E. Neher, B. Sakmann, and F. J. Sigworth. Improved patch-clamp techniques for high-resolution current recording from cells and cell-free membrane patches. *Pflügers Archiv : European journal of physiology*, 391(2):85–100, (**1981**). doi: 10.1007/BF00656997. 2.5

[187] S. J. Guzman, A. Schlögl, and C. Schmidt-Hieber. Stimfit: quantifying electrophysiological data with Python. *Frontiers in neuroinformatics*, 8(February):1–10, (**2014**). doi: 10.3389/fninf.2014.00016. 2.5.2, A.3

[188] T. E. Oliphant. Python for Scientific Computing. *Computing in Science & Engineering*, 9(90), (**2007**). 2.5.2

[189] R Core Team. R: A Language and Environment for Statistical Computing. (**2013**). 2.5.2

[190] C. Grimm, A. Silapetere, A. Vogt, Y. A. Bernal Sierra, and P. Hegemann. Electrical properties, substrate specificity and optogenetic potential of the engineered light-driven sodium pump eKR2. *Scientific Reports*, 8(1):9316, (**2018**). doi: 10.1038/s41598-018-27690-w. 2.5.3, 3.2.5, 4.2.3, n, 4.2, 4.3, 4.2.4, p

[191] P. H. Barry. JPCalc, a software package for calculating liquid junction potential corrections in patch-clamp, intracellular, epithelial and bilayer measurements and for correcting junction potential measurements. *Journal of Neuroscience Methods*, 51(1):107–116, (**1994**). doi: 10.1016/0165-0270(94)90031-0. 2.5.4

[192] K. Arnold, L. Bordoli, J. Kopp, and T. Schwede. The SWISS-MODEL workspace: a web-based environment for protein structure homology modelling. *Bioinformatics*, 22(2):195–201, (**2006**). doi: 10.1093/bioinformatics/bti770. 3.6, 3.7, 3.9

[193] J. C. D. Kaufmann, B. S. Krause, C. Grimm, E. Ritter, P. Hegemann, and F. J. Bartl. Proton transfer reactions in the red light-activatable channelrhodopsin variant ReaChR and their relevance for its function. *Journal of Biological Chemistry*, 292(34):14205–14216, (**2017**). doi: 10.1074/jbc.M117.779629. 3.1.2, 3.1.3, 3.1.4, f, 4.1, 4.1.1

[194] H. Li, E. G. Govorunova, O. A. Sineshchekov, and J. L. Spudich. Role of a helix B lysine residue in the photoactive site in channelrhodopsins. *Biophysical Journal*, 106(8):1607–1617, (**2014**). doi: 10.1016/j.bpj.2014.03.002. 3.1.2

[195] J. Wietek, S. Rodriguez-Rozada, J. Tutas, F. Tenedini, C. Grimm, T. G. Oertner, P. Soba, P. Hegemann, and J. Simon Wiegert. Anion-conducting channelrhodopsins with tuned spectra and modified kinetics engineered for optogenetic manipulation of behavior. *Scientific Reports*, 7(1):1–18, (**2017**). doi: 10.1038/s41598-017-14330-y. 3.1.3, 4.1.1, 4.1.2, 4.2.5

[196] B. Hille. *Ion Channels of Excitable Membranes*. Sinauer Associates, Inc., 3 edition, 2001. 3.1.3

[197] S. Kleinlogel, K. Feldbauer, R. E. Dempski, H. Fotis, P. G. Wood, C. Bamann, and E. Bamberg. Ultra light-sensitive and fast neuronal activation with the Ca^{2+}-permeable channelrhodopsin CatCh. *Nature Neuroscience*, 14(4):513–518, (**2011**). doi: 10.1038/nn.2776. 3.1.3

[198] I. Ibañez-Tallon, J. M. Miwa, H.-L. Wang, N. C. Adams, G. W. Crabtree, S. M. Sine, and N. Heintz. Novel Modulation of Neuronal Nicotinic Acetylcholine Receptors by Association with the Endogenous Prototoxin lynx1. *Neuron*, 33(6):893–903, (**2002**). doi: 10.1016/S0896-6273(02)00632-3. 3.2.2

[199] I. Ibañez-Tallon and M. N. Nitabach. Tethering toxins and peptide ligands for modulation of neuronal function. *Current opinion in neurobiology*, 22(1):72–78, (**2012**). doi: 10.1016/j.conb.2011.11.003. 3.2.2

[200] V. Gradinaru, K. R. Thompson, and K. Deisseroth. eNpHR: a *Natronomonas* halorhodopsin enhanced for optogenetic applications. *Brain cell biology*, 36(1-4):129–139, (**2008**). doi: 10.1007/s11068-008-9027-6. 3.2.2, 4.2, 4.2.5

[201] V. Gradinaru, F. Zhang, C. Ramakrishnan, J. Mattis, R. Prakash, I. Diester, I. Goshen, K. R. Thompson, and K. Deisseroth. Molecular and Cellular Approaches for Diversifying and Extending Optogenetics. *Cell*, 141(1):154–165, (**2010**). doi: 10.1016/j.cell.2010.02.037. 3.2.2, 4.2.5

[202] D. Shcherbo, E. M. Merzlyak, T. V. Chepurnykh, A. F. Fradkov, G. V. Ermakova, E. A. Solovieva, K. A. Lukyanov, E. A. Bogdanova, A. G. Zaraisky, S. Lukyanov, and D. M. Chudakov. Bright far-red fluorescent protein for whole-body imaging. *Nature Methods*, 4(9):741–746, (**2007**). doi: 10.1038/nmeth1083. 3.2.2

[203] D. Shcherbo, C. S. Murphy, G. V. Ermakova, E. A. Solovieva, T. V. Chepurnykh, A. S. Shcheglov, V. V. Verkhusha, V. Z. Pletnev, K. L. Hazelwood, P. M. Roche, S. Lukyanov, A. G. Zaraisky, M. W. Davidson, and D. M. Chudakov. Far-red fluorescent tags for protein imaging in living tissues. *Biochemical Journal*, 418(3):567–574, (**2009**). doi: 10.1042/BJ20081949. 3.2.2

[204] M. Orm, A. B. Cubitt, K. Kallio, L. A. Gross, R. Y. Tsien, and S. J. Remington. Crystal Structure of the *Aequorea victoria* Green Fluorescent Protein. *Science*, 273(5280):1392–1395, (**1996**). doi: 10.1126/science.273.5280.1392. 3.2.2

[205] F. Zhang, J. Vierock, O. Yizhar, L. E. Fenno, S. Tsunoda, A. Kianianmomeni, M. Prigge, A. Berndt, J. Cushman, J. Polle, J. Magnuson, P. Hegemann, and K. Deisseroth. The Microbial Opsin Family of Optogenetic Tools. *Cell*, 147(7):1446–1457, (**2011**). doi: 10.1016/j.cell.2011.12.004. 3.2.3

[206] A. Vogt, Y. Guo, S. P. Tsunoda, S. Kateriya, M. Elstner, and P. Hegemann. Conversion of a light-driven proton pump into a light-gated ion channel. *Scientific Reports*, 5:16450, (**2015**). doi: 10.1038/srep16450. 3.2.3, 3.2.3, 4.2

[207] J. García-Martínez, M. Brunk, J. Avalos, and U. Terpitz. The CarO rhodopsin of the fungus Fusarium fujikuroi is a light-driven proton pump that retards spore germination. *Scientific Reports*, 5(1):1–11, (**2015**). doi: 10.1038/srep07798. 3.2.3, 4.2, 4.2.1, 4.2.2

[208] G. Nagel, B. Kelety, B. Möckel, G. Büldt, and E. Bamberg. Voltage dependence of proton pumping by bacteriorhodopsin is regulated by the voltage-sensitive ratio of M^1 to M^2. *Biophysical journal*, 74(1): 403–12, (**1998**). doi: 10.1016/S0006-3495(98)77797-5.

[209] É. Lörinczi, M. K. Verhoefen, J. Wachtveitl, A. C. Woerner, C. Glaubitz, M. Engelhard, E. Bamberg, and T. Friedrich. Voltage- and pH-Dependent Changes in Vectoriality of Photocurrents Mediated by Wild-type and Mutant Proteorhodopsins upon Expression in *Xenopus* Oocytes. *Journal of Molecular Biology*, 393(2):320–341, (**2009**). doi: 10.1016/j.jmb.2009.07.055. 4.2

[210] S. Geibel, È. Lörinczi, E. Bamberg, and T. Friedrich. Voltage Dependence of Proton Pumping by Bacteriorhodopsin Mutants with Altered Lifetime of the M Intermediate. *PLOS ONE*, 8(9):1–11, (**2013**). doi: 10.1371/journal.pone.0073338. 3.2.3

[211] K. J. Hellingwerf, J. C. Arents, B. J. Scholte, and H. V. Westerhoff. Bacteriorhodopsin in Liposomes II. Experimental Evidence in Support of a Theoretical Model. *Biochimica et Biophysica Acta*, 547:561–582, (**1979**). 3.2.4

[212] H. V. Westerhoff and Z. Dancsházy. Keeping a light-driven proton pump under control. *Trends in Biochemical Sciences*, 9(3):112–117, (**1984**). doi: 10.1016/0968-0004(84)90107-5. 3.2.4

[213] A. Vogt, J. Wietek, and P. Hegemann. Gloeobacter rhodopsin, limitation of proton pumping at high electrochemical load. *Biophysical Journal*, 105(9):2055–2063, (**2013**). doi: 10.1016/j.bpj.2013.08.031. 3.2.5, 4.2

[214] S. P. Tsunoda, D. Ewers, S. Gazzarrini, A. Moroni, D. Gradmann, and P. Hegemann. H^+-pumping rhodopsin from the marine alga Acetabularia. *Biophysical Journal*, 91(4):1471–1479, (**2006**). doi: 10.1529/biophysj.106.086421. 3.2.5, 4.2

[215] Y. Kato, K. Inoue, and H. Kandori. Kinetic Analysis of H^+-Na^+ Selectivity in a Light-Driven Na^+-Pumping Rhodopsin. *Journal of Physical Chemistry Letters*, 6(24):5111–5115, (**2015**). doi: 10.1021/acs.jpclett.5b02371. 3.2.7

[216] C. Bamann, R. Gueta, S. Kleinlogel, G. Nagel, and E. Bamberg. Structural guidance of the photocycle of channelrhodopsin-2 by an interhelical hydrogen bond. *Biochemistry*, 49(2):267–278, (**2010**). doi: 10.1021/bi901634p. 4.1.1, 4.1.1

[217] O. A. Sineshchekov, H. Li, E. G. Govorunova, and J. L. Spudich. Photochemical reaction cycle transitions during anion channelrhodopsin gating. *Proceedings of the National Academy of Sciences*, 113(14): E1993–E2000, (**2016**). doi: 10.1073/pnas.1525269113. 4.1.1

[218] J. Wietek, M. Broser, B. S. Krause, and P. Hegemann. Identification of a Natural Green Light Absorbing Chloride Conducting Channelrhodopsin from Proteomonas sulcata. *Journal of Biological Chemistry*, 291 (8):4121–4127, (**2016**). doi: 10.1074/jbc.M115.699637. 4.1.1, 4.2.5

[219] I. Szundi, H. Li, E. Chen, R. Bogomolni, J. L. Spudich, and D. S. Kliger. Platymonas Subcordiformis Channelrhodopsin-2 Function. Part I: The Photochemical Reaction Cycle. *Journal of Biological Chemistry*, 290(27):16573–16584, (**2015**). doi: 10.1074/jbc.M114.631614. 4.1.1

[220] A. Kulcsar, G. Groma, J. K. Lanyi, and G. Váró. Characterization of the Proton-Transporting Photocycle of Pharaonis Halorhodopsin. *Biophysical Journal*, 79:2705–2713, (**2000**). doi: 10.1016/S0006-3495(00)76508-8. 4.1.1

[221] K. Inoue, F. H. M. Koua, Y. Kato, R. Abe-Yoshizumi, and H. Kandori. Spectroscopic study of a light-driven chloride ion pump from marine bacteria. *The Journal of Physical Chemistry B*, 118(38):11190–11199, (**2014**). doi: 10.1021/jp507219q. 4.1.1

[222] R. H. R. Lozier, R. A. R. R. A. Bogomolni, W. Stoeckenius, , and W. Stoeckenius. BACTERIORHODOPSIN: A LIGHT-DRIVEN PROTON PUMP IN *HALOBACTERIUM HALOBIUM*. *Biophysical Journal*, 15(9):955–962, (**1975**). doi: 10.1016/S0006-3495(75)85875-9. 4.1.1

[223] B. S. Krause, C. Grimm, J. C. D. Kaufmann, F. Schneider, T. P. Sakmar, F. J. Bartl, and P. Hegemann. Complex Photochemistry within the Green-Absorbing Channelrhodopsin ReaChR. *Biophysical Journal*, 112(6):1166–1175, (**2017**). doi: 10.1016/j.bpj.2017.02.001. 4.1.1, 4.1, 4.1.1

[224] H. K. Inagaki, Y. Jung, E. D. Hoopfer, A. M. Wong, N. Mishra, J. Y. Lin, R. Y. Tsien, and D. J. Anderson. Optogenetic control of Drosophila using a red-shifted channelrhodopsin reveals experience-dependent influences on courtship. *Nature methods*, 11(3):325–332, (**2014**). doi: 10.1038/Nmeth.2765. 4.1.2

[225] B. M. Hooks, J. Y. Lin, C. Guo, and K. Svoboda. Dual-Channel Circuit Mapping Reveals Sensorimotor Convergence in the Primary Motor Cortex. *Journal of Neuroscience*, 35(10):4418–4426, (**2015**). doi: 10.1523/JNEUROSCI.3741-14.2015. 4.1.2

[226] A. Sengupta, A. Chaffiol, E. Mace, R. Caplette, M. Desrosiers, M. Lampic, V. Forster, O. Marre, J. Y. Lin, J. Sahel, S. Picaud, D. Dalkara, and J. Duebel. Red-shifted channelrhodopsin stimulation restores light responses in blind mice, macaque retina, and human retina. *EMBO Molecular Medicine*, 8(11):1248–1264, (**2016**). doi: 10.15252/emmm.201505699. 4.1.2

[227] E. C. Nyns, A. Kip, C. I. Bart, J. J. Plomp, K. Zeppenfeld, M. J. Schalij, A. A. De Vries, and D. A. Pijnappels. Optogenetic termination of ventricular arrhythmias in the whole heart: Towards biological cardiac rhythm management. *European Heart Journal*, 38(27):2132–2136, (**2017**). doi: 10.1093/eurheartj/ehw574. 4.1.2

[228] T. Mager, D. Lopez de la Morena, V. Senn, J. Schlotte, A. D'Errico, K. Feldbauer, C. Wrobel, S. Jung, K. Bodensiek, V. Rankovic, L. Browne, A. Huet, J. Jüttner, P. G. Wood, J. J. Letzkus, T. Moser, and E. Bamberg. High frequency neural spiking and auditory signaling by ultrafast red-shifted optogenetics. *Nature Communications*, 9(1):1750, (**2018**). doi: 10.1038/s41467-018-04146-3. 4.1.2

[229] A. M. Packer, D. S. Peterka, J. J. Hirtz, R. Prakash, K. Deisseroth, and R. Yuste. Two-photon optogenetics of dendritic spines and neural circuits. *Nature Methods*, 9(12):1202–1205, (**2012**). doi: 10.1038/nmeth.2249. 4.1.2

[230] A. Begue, E. Papagiakoumou, B. Leshem, R. Conti, L. Enke, D. Oron, and V. Emiliani. Two-photon excitation in scattering media by spatiotemporally shaped beams and their application in optogenetic stimulation. *Biomedical Optics Express*, 4(12):2869, (**2013**). doi: 10.1364/BOE.4.002869.

[231] J. P. Rickgauer, K. Deisseroth, and D. W. Tank. Simultaneous cellular-resolution optical perturbation and imaging of place cell firing fields. *Nature Neuroscience*, 17(12):1816–1824, (**2014**). doi: 10.1038/nn.3866. 4.1.2

[232] L. Carrillo-Reid, W. Yang, Y. Bando, D. S. Peterka, and R. Yuste. Imprinting Cortical Ensembles. *Science*, 353(6300):691–694, (**2016**). doi: 10.1126/science.aaf7560. 4.1.2

[233] E. Chaigneau, E. Ronzitti, M. A. Gajowa, G. J. Soler-Llavina, D. Tanese, A. Y. B. Brureau, E. Papagiakoumou, H. Zeng, and V. Emiliani. Two-Photon Holographic Stimulation of ReaChR. *Frontiers in Cellular Neuroscience*, 10(October):1–13, (**2016**). doi: 10.3389/fncel.2016.00234. 4.1.2

[234] J. Nakai, M. Ohkura, and K. Imoto. A high signal-to-noise Ca^{2+} probe composed of a single green fluorescent protein. *Nature Biotechnology*, 19(2):137–141, (**2001**). doi: 10.1038/84397. 4.1.2

[235] V. Gradinaru, M. Mogri, K. R. Thompson, J. M. Henderson, and K. Deisseroth. Optical Deconstruction of Parkinsonian Neural Circuitry. *Science*, 324(5925):354–359, (**2009**). doi: 10.1126/science.1167093. 4.2

[236] J. Mattis, K. M. Tye, E. A. Ferenczi, C. Ramakrishnan, D. J. O'Shea, R. Prakash, L. A. Gunaydin, M. Hyun, L. E. Fenno, V. Gradinaru, O. Yizhar, and K. Deisseroth. Principles for applying optogenetic tools derived from direct comparative analysis of microbial opsins. *Nature Methods*, 9, (**2012**). doi: 10.1038/NMeth.1808. 4.2, 4.2.5

[237] M. R. Hoque, T. Ishizuka, K. Inoue, R. Abe-Yoshizumi, H. Igarashi, T. Mishima, H. Kandori, and H. Yawo. A Chimera Na^+-Pump Rhodopsin as an Effective Optogenetic Silencer. *PLOS ONE*, 11(11):e0166820, (**2016**). doi: 10.1371/journal.pone.0166820. 4.2, e, 4.2.2, 4.2.5

[238] A. Berndt, S. Y. Lee, J. Wietek, C. Ramakrishnan, E. E. Steinberg, A. J. Rashid, H. Kim, S. Park, A. Santoro, P. W. Frankland, S. M. Iyer, S. Pak, S. Ährlund-Richter, S. L. Delp, R. C. Malenka, S. A. Josselyn, M. Carlén, P. Hegemann, and K. Deisseroth. Structural foundations of optogenetics: Determinants of channelrhodopsin ion selectivity. *Proceedings of the National Academy of Sciences*, 113(4):822–829, (**2016**). doi: 10.1073/pnas.1523341113. 4.2, 4.2.5

[239] M. Konno, Y. Kato, H. E. Kato, K. Inoue, O. Nureki, and H. Kandori. Mutant of a Light-Driven Sodium Ion Pump Can Transport Cesium Ions. *Journal of Physical Chemistry Letters*, 7(1):51–55, (**2016**). doi: 10.1021/acs.jpclett.5b02385. 4.2.1

[240] K. A. Johnson and R. S. Goody. The original Michaelis constant: Translation of the 1913 Michaelis-Menten Paper. *Biochemistry*, 50(39):8264–8269, (**2011**). doi: 10.1021/bi201284u. 4.2.1

[241] K. Inoue, H. Ono, and H. Kandori. Na^+ Transport by a Sodium Ion Pump Rhodopsin is Resistant to Environmental Change: A Comparison of the Photocycles of the Na^+ and Li^+ Transport Processes. *Chemistry Letters*, 44(3):294–296, (**2015**). doi: 10.1246/cl.141023. 4.2.1, 4.2.4

[242] A. Minta and R. Y. Tsien. Fluorescent Indicators for Cytosolic Sodium. *Journal of Biological Chemistry*, 264:19449–19457, (**1989**). 4.2.1

[243] G. Grynkiewicz, M. Poenie, and R. Y. Tsien. A new generation of Ca^{2+} indicators with greatly improved fluorescence properties. *Journal of Biological Chemistry*, 260(6):3440–3450, (**1985**). doi: 3838314. 4.2.1

[244] F. Schneider. *Design and electrophysiological characterization of rhodopsin-based optogenetic tools*. PhD thesis, Humboldt-Universität zu Berlin, 2013. 4.2.1

[245] A. Vogt. *Elektrophysiologische Untersuchung des gerichteten Protonentransportes in mikrobiellen Rhodopsinen*. 2017. 4.2.2

[246] J. C. Skou. The influence of some cations on an adenosine triphosphatase from peripheral nerves. *Biochimica et Biophysica Acta*, 23:394–401, (**1957**). doi: 10.1016/0006-3002(57)90343-8. 4.2.2

[247] J. P. Morth, B. P. Pedersen, M. S. Toustrup-Jensen, T. L. M. Sorensen, J. Petersen, J. P. Andersen, B. Vilsen, and P. Nissen. Crystal structure of the sodium-potassium pump. *Nature*, 450(7172):1043–1049, (**2007**). doi: 10.1038/nature06419.

[248] L. D. Faller. Mechanistic studies of sodium pump. *Archives of Biochemistry and Biophysics*, 476(1):12–21, (**2008**). doi: 10.1016/j.abb.2008.05.017. 4.2.2

[249] C. Toyoshima, R. Kanai, and F. Cornelius. First crystal structures of Na^+,K^+-ATPase: New light on the oldest ion pump. *Structure*, 19(12):1732–1738, (**2011**). doi: 10.1016/j.str.2011.10.016. 4.2.2

[250] D. Mogul, H. Rasmussen, D. Singer, and R. T. Eick. Inhibition of Na, K-pump current in Guinea pig ventricular myocytes by dihydroouabain occurs at both high and low afinity sites. *Biophysical Journal*, 53:1063–1069, (**1988**). 4.2.2

[251] D. C. GADSBY and M. NAKAO. Steady-state current-voltage relationship of the Na/K pump in guinea pig ventricular myocytes. *The Journal of General Physiology*, 94(3):511–537, (**1989**). doi: 10.1085/jgp.94.3.511. 4.2.2

[252] J. M. Argüello, R. D. Peluffo, J. B. Lingrel, J. R. Berlin, R. D. Peluffo, J. Feng, J. B. Lingrel, and J. R. Berlin. Substitution of Glutamic 779 with Alanine in the Na , K-ATPase α Subunit Removes Voltage Dependence of Ion Transport. *The Journal of Biological Chemistry*, 271(40):24610–24616, (**1996**). 4.2.2

[253] U. P. Hansen, D. Gradmann, D. Sanders, and C. L. Slayman. Interpretation of Current-Voltage Relationships for "Active" Ion Transport Systems: I. Steady-state Reaction Kinetic Analysis of Class-I Mechanisms. *The Journal of Membrane Biology*, 63:165–190, (**1981**). doi: 10.1007/BF01995634. 4.2.2

[254] J. A. Reynolds, E. A. Johnson, and C. Tanford. Incorporation of membrane potential into theoretical analysis of electrogenic ion pumps. *Proceedings of the National Academy of Sciences of the United States of America*, 82(20):6869–73, (**1985**). doi: 10.1073/pnas.82.20.6869. 4.2.2

[255] J. B. Chapman, E. A. Johnson, and J. M. Kootsey. Electrical and Biochemical Properties of an Enzyme Model of the Sodium Pump. *The Journal of Membrane Biology*, 74(2):139–153, (**1983**). doi: 10.1007/BF01870503. 4.2.2

[256] R. GOLDSCHLEGGER, S. J. D. KARLISH, A. REPHAELI, and W. D. STEIN. THE EFFECT OF MEMBRANE POTENTIAL ON THE MAMMALIAN SODIUM-POTASSIUM PUMP RECONSTITUTED INTO PHOSPHOLIPID VESICLES. *Journal of Physiology*, 387:331–355, (**1987**). 4.2.2

[257] G. E. Hofmann, J. E. Smith, K. S. Johnson, U. Send, L. A. Levin, F. Micheli, A. Paytan, N. N. Price, B. Peterson, Y. Takeshita, P. G. Matson, E. de Crook, K. J. Kroeker, M. C. Gambi, E. B. Rivest, C. A. Frieder, P. C. Yu, and T. R. Martz. High-frequency dynamics of ocean pH: A multi-ecosystem comparison. *PLoS ONE*, 6(12), (**2011**). doi: 10.1371/journal.pone.0028983. 4.2.3

[258] H. Barnes. Some Tables for the Ionic Composition of Sea Water. *Journal of Experimental Biology*, 31(4): 582–588, (**1954**). 4.2.3

[259] K. Grasshoff, K. Kremling, and M. Ehrhardt, editors. *Methods of Seawater Analysis*. WILEY-VCH, 3 edition, 1999. 4.2.3

[260] M. Jawurek, C. Glaubitz, and K. Hauser. Impact of the lipid environment on the protonation dynamics of bacteriorhodopsin studied with time-resolved step-scan FTIR spectroscopy. *Biomedical Spectroscopy and Imaging*, 5(2):167–174, (**2016**). doi: 10.3233/BSI-160135. 4.2.4

[261] E. Henrich, J. Sörmann, P. Eberhardt, O. Peetz, J. Mezhyrova, N. Morgner, K. Fendler, V. Dötsch, J. Wachtveitl, F. Bernhard, and C. Bamann. From Gene to Function: Cell-Free Electrophysiological and Optical Analysis of Ion Pumps in Nanodiscs. *Biophysical Journal*, 113(6):1331–1341, (**2017**). doi: 10.1016/j.bpj.2017.03.026. 4.2.4, 4.2.4

[262] J. S. Wiegert, M. Mahn, M. Prigge, Y. Printz, and O. Yizhar. Silencing Neurons: Tools, Applications, and Experimental Constraints. *Neuron*, 95(3):504–529, (**2017**). doi: 10.1016/j.neuron.2017.06.050. 4.2.5, 4.2.5

[263] B. N. Armbruster, X. Li, M. H. Pausch, S. Herlitze, and B. L. Roth. Evolving the lock to fit the key to create a family of G protein-coupled receptors potently activated by an inert ligand. *Proceedings of the National Academy of Sciences*, 104(12):5163–5168, (**2007**). doi: 10.1073/pnas.0700293104. 4.2.5

[264] I. Ibanez-Tallon, H. Wen, J. M. Miwa, J. Xing, A. B. Tekinay, F. Ono, P. Brehm, N. Heintz, I. Ibañez-Tallon, H. Wen, J. M. Miwa, J. Xing, A. B. Tekinay, F. Ono, P. Brehm, and N. Heintz. Tethering naturally occurring peptide toxins for cell-autonomous modulation of ion channels and receptors in vivo. *Neuron*, 43(3):305–311, (**2004**). doi: 10.1016/j.neuron.2004.07.015. 4.2.5

[265] S. Auer. *Development of new membrane-tethered toxins as genetic tools for in vitro and in vivo silencing of ion channels by*. PhD thesis, 2010. 4.2.5

[266] W. A. Catterall. Neurotoxins that Act on Voltage-Sensitive Sodium Channels in Excitable Membranes. *Annual Review of Pharmacology and Toxicology*, 20(1):15–43, (**1980**). doi: 10.1146/annurev.pa.20.040180.000311. 4.2.5

[267] T. Yamauchi, T. Hori, and T. Takahashi. Presynaptic inhibition by muscimol through $GABA^B$ receptors. *European Journal of Neuroscience*, 12(9):3433–3436, (**2000**). doi: 10.1046/j.1460-9568.2000.00248.x. 4.2.5

[268] H. Janovjak, S. Szobota, C. Wyart, D. Trauner, and E. Y. Isacoff. A light-gated, potassium-selective glutamate receptor for the optical inhibition of neuronal firing. *Nature Neuroscience*, 13(8):1027–1032, (**2010**). doi: 10.1038/nn.2589. 4.2.5

[269] M. Volgraf, P. Gorostiza, R. Numano, R. H. Kramer, E. Y. Isacoff, and D. Trauner. Allosteric control of an ionotropic glutamate receptor with an optical switch. *Nature Chemical Biology*, 2(1):47–52, (**2006**). doi: 10.1038/nchembio756. 4.2.5

[270] O. A. Masseck, K. Spoida, D. Dalkara, T. Maejima, J. M. Rubelowski, L. Wallhorn, E. S. Deneris, and S. Herlitze. Vertebrate cone opsins enable sustained and highly sensitive rapid control of gi/osignaling in anxiety circuitry. *Neuron*, 81(6):1263–1273, (**2014**). doi: 10.1016/j.neuron.2014.01.041. 4.2.5

[271] R. D. Airan, K. R. Thompson, L. E. Fenno, H. Bernstein, and K. Deisseroth. Temporally precise *in vivo* control of intracellular signalling. *Nature*, 458(7241):1025–1029, (**2009**). doi: 10.1038/nature07926. 4.2.5

[272] E. R. Siuda, B. A. Copits, M. J. Schmidt, M. A. Baird, R. Al-Hasani, W. J. Planer, S. C. Funderburk, J. G. McCall, R. W. Gereau, and M. R. Bruchas. Spatiotemporal Control of Opioid Signaling and Behavior. *Neuron*, 86(4):923–935, (**2015**). doi: 10.1016/j.neuron.2015.03.066. 4.2.5

[273] C. Cosentino, L. Alberio, S. Gazzarrini, M. Aquila, E. Romano, S. Cermenati, P. Zuccolini, J. Petersen, M. Beltrame, J. L. Van Etten, J. M. Christie, G. Thiel, and A. Moroni. Engineering of a light-gated potassium channel. *Science*, 348(6235):707–710, (**2015**). doi: 10.1126/science.aaa2787. 4.2.5

[274] X. Han, B. Y. Chow, H. Zhou, N. C. Klapoetke, A. Chuong, R. Rajimehr, A. Yang, M. V. Baratta, J. Winkle, R. Desimone, and E. S. Boyden. A High-Light Sensitivity Optical Neural Silencer: Development and Application to Optogenetic Control of Non-Human Primate Cortex. *Frontiers in Systems Neuroscience*, 5(April):1–8, (**2011**). doi: 10.3389/fnsys.2011.00018. 4.2.5

[275] A. S. Chuong, M. L. Miri, V. Busskamp, G. A. C. Matthews, L. C. Acker, A. T. Sørensen, A. Young, N. C. Klapoetke, M. A. Henninger, S. B. Kodandaramaiah, M. Ogawa, S. B. Ramanlal, R. C. Bandler, B. D. Allen, C. R. Forest, B. Y. Chow, X. Han, Y. Lin, K. M. Tye, B. Roska, J. A. Cardin, and E. S. Boyden. Noninvasive optical inhibition with a red-shifted microbial rhodopsin. *Nature neuroscience*, 17(8):1123–1129, (**2014**). doi: 10.1038/nn.3752. 4.2.5

[276] J. Wietek, R. Beltramo, M. Scanziani, P. Hegemann, T. G. Oertner, and J. Simon Wiegert. An improved chloride-conducting channelrhodopsin for light-induced inhibition of neuronal activity in vivo. *Scientific Reports*, 5:1–11, (**2015**). doi: 10.1038/srep14807. 4.2.5

[277] W. Jonas. *Anionen leitende Kanalrhodopsine*. PhD thesis, Humboldt Universität zu Berlin, 2018. 4.2.5

[278] M. Mahn, M. Prigge, S. Ron, R. Levy, and O. Yizhar. Biophysical constraints of optogenetic inhibition at presynaptic terminals. *Nature Neuroscience*, 19(4):554–6, (**2016**). doi: 10.1038/nn.4266. 4.2.5

[279] A. Y. Malyshev, M. V. Roshchin, G. R. Smirnova, D. A. Dolgikh, and P. M. Balaban. Neuroscience Letters Chloride conducting light activated channel GtACR2 can produce both cessation of firing and generation of action potentials in cortical neurons in response to light. *Neuroscience Letters*, 640:76–80, (**2017**). doi: 10.1016/j.neulet.2017.01.026. 4.2.5

[280] Y. Ben-Ari, E. Cherubini, R. Corradetti, and J.-L. Gaiarsa. Giant Synaptic Potentialsin Immature Rat CA3 Hippocampal Neurons. *Journal of Physiology*, 416:303–325, (**1989**). 4.2.5

[281] D. F. Owens, L. H. Boyce, M. B. E. Davis, and A. R. Kriegstein. Excitatory GABA Responses in Embryonic and Neonatal Cortical Slices Demonstrated by Gramicidin Perforated-Patch Recordings and Calcium Imaging. *The Journal of Neuroscience*, 16(20):6414–6423, (**1996**). doi: 10.1523/JNEUROSCI.16-20-06414.1996.

[282] M. D. Plotkin, E. Y. Snyder, S. C. Hebert, and E. Delpire. Expression of the Na-K-2Cl Co-transporter Is Developmentally Regulated in Postnatal Rat Brains : A Possible Mechanism Underlying GABA's Excitatory Role in Immature Brain. *J Neurobiol.*, 33(6):781–795, (**1997**). doi: 10.1002/(SICI)1097-4695(19971120)33.

[283] C. Rivera, J. Voipio, J. A. Payne, E. Ruusuvuori, H. Lahtinen, K. Lamsa, U. Pirvola, M. Saarma, and K. Kaila. The K^+/Cl^- co-transporter KCC2 renders GABA hyperpolarizing during neuronal maturation. *Nature*, 397(6716):251–255, (**1999**). doi: 10.1038/16697. 4.2.5

[284] J. V. Raimondo, L. Kay, T. J. Ellender, and C. J. Akerman. Optogenetic silencing strategies differ in their effects on inhibitory synaptic transmission. *Nature Neuroscience*, 15(8):1102–1104, (**2012**). doi: 10.1038/nn.3143. 4.2.5

Acknowledgments

First and foremost I would like to thank my supervisor Peter Hegemann who supported me in the last years and enabled my work on these interesting topics. Thanks for all the scientific discussions, for challenging and pushing me, for the numerous conferences I could visit, and for your support when things did not work out as planned.
I am as well thankful to Franz Bartl, not only for reviewing this work, but also for the wonderful collaboration on ReaChR and his kind supervision throughout these years.
I would like to express my gratitude to Georg Nagel, who agreed to review this thesis.

This work would not have been possible without the help of my colleagues in the lab, who always made coming to work a pleasure. Johannes - I am grateful for all the discussions we had related to work or other stuff :) Thanks for challenging me and your never ending willingness to debate scientific questions.
Jonas - thanks a lot for proof reading, sharing the office, for advice on so many occasions, for several conferences together and for welcoming me into your wonderful family.
I thank Benni Krause for proof reading, working together in the ReaChR project and all the fun conferences - my pleasure! Roman Fudim, not only for proof reading but also for numerous discussions about spectroscopy and bacteriorhodopsin - thanks a lot. I am thankful to Arita Silapetere who supported me with her spectroscopy measurements in the KR2 project. And Arend Vogt for proof reading and Arend and Yinth Bernal Sierra for the nice collaboration on KR2. Lastly, my deepest gratitude goes to Shatanik Mukherjee for proof reading the whole thesis, manuscripts, abstracts... and all your support - thanks a lot!
Nothing would be like it is without the technical support of Maila, Altina and Tharsana, thanks for all your help in the everyday lab life. Moreover, I thank all electrophysiologists, especially Joe and Rodrigo, and all other lab members for the nice working environment in our lab.

Further I would like to acknowledge the help of the group of Andreas Herrmann in particular Thomas Korte for the measuring time and the support with confocal microscopy. Moreover, I acknowledge the funding of the DFG through the SFB1078 over all the years, together with the nicely organized annual retreats.

I thank my dearest fellow students Ivan and Jens and further Peter Müller for their support and always having a sympathetic ear.

I am very thankful for my friends, who supported and encouraged me in endless ways throughout all the years - Jule, Jule, Marian, Nils, Holger for more than one and a half decade now. Franzi, Sabrina, Kati and Robert, thanks, you are great! And what would I have done without you, Anni, most valuable advisor in all questions of life - Danke!

Finally, my biggest and deepest thanks goes to my family, who always supported me and provided advice and comfort whenever it was needed. Thanks for helping and guiding me, thanks for tolerating my absence too often, thanks for believing in me when I did not, for celebrating the small and big successes- thanks for everything!

Eigenständigkeitserklärung

Hiermit versichere ich, dass ich die vorliegende Arbeit mit dem Titel »Electrophysiological characterization of the microbial rhodopsins ReaChR and KR2 and their optogenetic potential« eigenständig verfasst und keine weiteren als die angegeben Hilfmittel und Quellen verwendet habe.

Berlin, den 22.08.2018

Christiane Grimm